PROMINENCES: THE PHANTOM MENACE

Rosie Waugh

A Thesis Submitted for the Degree of PhD
at the
University of St Andrews

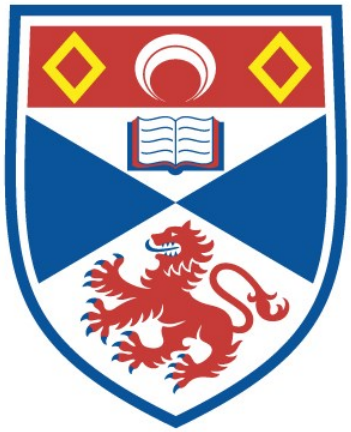

2023

Prominences: The phantom menace

Rosie Waugh

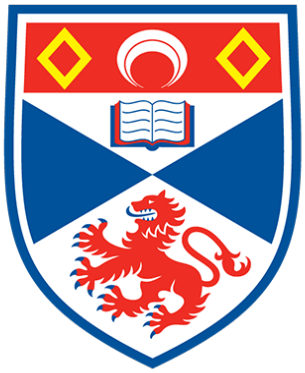

University of
St Andrews

This thesis is submitted in partial fulfilment for the degree of

Doctor of Philosophy (PhD)

at the University of St Andrews

May 2023

Candidate's declaration

I, Rosie Waugh, do hereby certify that this thesis, submitted for the degree of PhD, which is approximately 72,000 words in length, has been written by me, and that it is the record of work carried out by me, or principally by myself in collaboration with others as acknowledged, and that it has not been submitted in any previous application for any degree. I confirm that any appendices included in my thesis contain only material permitted by the 'Assessment of Postgraduate Research Students' policy.

I was admitted as a research student at the University of St Andrews in September 2017.

I received funding from an organisation or institution and have acknowledged the funder(s) in the full text of my thesis.

Date Signature of candidate

Supervisor's declaration

I hereby certify that the candidate has fulfilled the conditions of the Resolution and Regulations appropriate for the degree of PhD in the University of St Andrews and that the candidate is qualified to submit this thesis in application for that degree. I confirm that any appendices included in the thesis contain only material permitted by the 'Assessment of Postgraduate Research Students' policy.

Date Signature of supervisor

Permission for publication

In submitting this thesis to the University of St Andrews we understand that we are giving permission for it to be made available for use in accordance with the regulations of the University Library for the time being in force, subject to any copyright vested in the work not being affected thereby. We also understand, unless exempt by an award of an embargo as requested below, that the title and the abstract will be published, and that a copy of the work may be made and supplied to any bona fide library or research worker, that this thesis will be electronically accessible for personal or research use and that the library has the right to migrate this thesis into new electronic forms as required to ensure continued access to the thesis.

I, Rosie Waugh, have obtained, or am in the process of obtaining, third-party copyright permissions that are required or have requested the appropriate embargo below.

The following is an agreed request by candidate and supervisor regarding the publication of this thesis:

Printed copy

No embargo on print copy.

Electronic copy

No embargo on electronic copy.

Date Signature of candidate

Date Signature of supervisor

Underpinning Research Data or Digital Outputs

Candidate's declaration

I, Rosie Waugh, understand that by declaring that I have original research data or digital outputs, I should make every effort in meeting the University's and research funders' requirements on the deposit and sharing of research data or research digital outputs.

Date Signature of candidate

Permission for publication of underpinning research data or digital outputs

We understand that for any original research data or digital outputs which are deposited, we are giving permission for them to be made available for use in accordance with the requirements of the University and research funders, for the time being in force.

We also understand that the title and the description will be published, and that the underpinning research data or digital outputs will be electronically accessible for use in accordance with the license specified at the point of deposit, unless exempt by award of an embargo as requested below.

The following is an agreed request by candidate and supervisor regarding the publication of underpinning research data or digital outputs:

No embargo on underpinning research data or digital outputs.

Date Signature of candidate

Date Signature of supervisor

General acknowledgements

Behind every scientist is a village of people who have supported them, without whom that science would never have been realised.

My supervisor, Moira Jardine, has my eternal gratitude and appreciation. I'd like to thank her for all her support and guidance over the past many years of my research journey. Before starting my PhD, I was told at the STFC Introductory Summer School that “life would start happening” during my PhD. Boy, they weren't wrong. I can't thank her enough for supporting me throughout everything over these past 5 years. I hope Moira chooses easier PhD students to supervise in future intakes!

I'm very grateful to Jonathan Keeling for being an incredibly supportive Director of Postgraduate Studies. I appreciate all his help throughout my time here, from taking parental leave to organising extensions to my studies. Getting to the point of writing this thesis would likely have been very stressful and potentially impossible without his help.

Thanks to my husband, Elliott, for always pretending to listen to my grievances on broken code or radius of curvature - a venting partner that I would recommend to anyone. I'm also thankful for (and at times terribly jealous of) his ability to visualise. I'm grateful for the many evenings he spent lending me this ability - much of this work would have taken longer without his explanations and diagrams of what something would look like.

I owe thanks to my toddler, for regularly re-igniting my curiosity and showing me what an amazing place this universe is. I hope one day to be as proficient at naming solar system bodies as they are!

Funding

This work was supported by the Science and Technology Facilities Council [grant number STFC/R000824/1].

Research Data/Digital Outputs access statement

Research data underpinning this thesis are available at https://doi.org/10.17630/2c93b181-0a7b-46b0-9b26-5a3d26622d6c

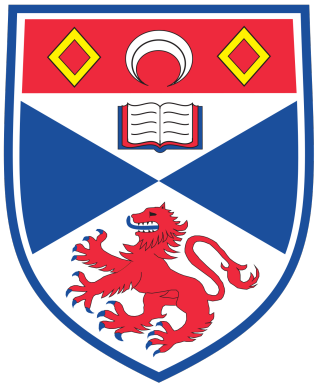

University of St. Andrews

Ph.D. Thesis

Prominences: The Phantom Menace

Rose F.P. Waugh

supervised by
Prof. Moira M. Jardine

August 18, 2023

Associated publications

Waugh, R.F.P. & Jardine, M.M, **"Magnetic support of stellar slingshot prominences"**, Monthly Notices of the Royal Astronomical Society, vol. 483, no. 2, pp. 1513-1522, 2019.

Waugh, R.F.P. & Jardine, M.M & Morin, J. & Donati, J.-F., **"Slingshot prominences: a hidden mass loss mechanism"**, Monthly Notices of the Royal Astronomical Society, vol. 505, no. 4, pp. 5104–5116, 2021.

Waugh, R.F.P. & Jardine, M.M, **"Magnetic confinement in the wind of low mass stars"**, Proceedings of the International Astronomical Union, 17(S370), 198-199, 2021.

Waugh, R.F.P. & Jardine, M.M, **"Magnetic confinement of dense plasma inside (and outside) stellar coronae"**, Monthly Notices of the Royal Astronomical Society, vol. 514, no. 4, pp. 5465–5477, 2022.

Contents

The work in this thesis was funded by STFC, grant number ST/R000824/1.

Abstract

It has been proposed that slingshot prominences may be a mass and angular momentum loss mechanism for rapidly rotating young stars. Stellar evolution models currently rely only on the wind as the angular momentum loss mechanism and do not include prominences. These models often require more angular momentum to be removed than the wind allows, and prominence ejection may hold at least part of the answer. This thesis aims to investigate the locations of prominence formation through mathematical modelling. The magnetic field structures that could support prominences are investigated, typically using two models: a magnetohydrostatic model and a stability method. The distributions of prominences around the star are calculated and, where possible, compared to observations. In some cases the magnetic field of the star is prescribed to be a simple field such as a dipole or quadrupole, and in others the magnetic field is generated from observations of the surface magnetic field, with the coronal magnetic field reconstructed from this, assuming the field is potential.

This work finds that prominences can be formed both within the stellar wind of stars, and within the closed field region. With the magnetohydrostatic model, two classes of prominence are found: those close to the surface of the star that could be analogous to solar prominences, and those at very large distances from the stellar surface. Those in the second category may be ejected from the star and act as a mechanism for removing mass and angular momentum. The removal of mass and angular momentum by prominences was modelled using the stable point method, and it was found that for some stars within the sample of M-dwarfs, the prominences could be a significant angular momentum loss mechanism.

Work here shows that whilst a tilted dipolar field can typically replicate the locations of observed prominences well, using observed prominence locations to infer the tilt of the dipole is not very effective due to the degeneracy of stable point locations. Overall, prominences are likely to be important contributors to the removal of angular momentum and therefore spin down of a star at certain points in its life, whilst they are typically left out of stellar evolution models. They are likely to be very common across young stars, however they are usually only observable when they transit the stellar disc and therefore they will often be missed by observations due to geometric effects. Those that are observed are likely only being partially observed, meaning that mass predictions from observations are underestimates.

Chapter 1

Introduction

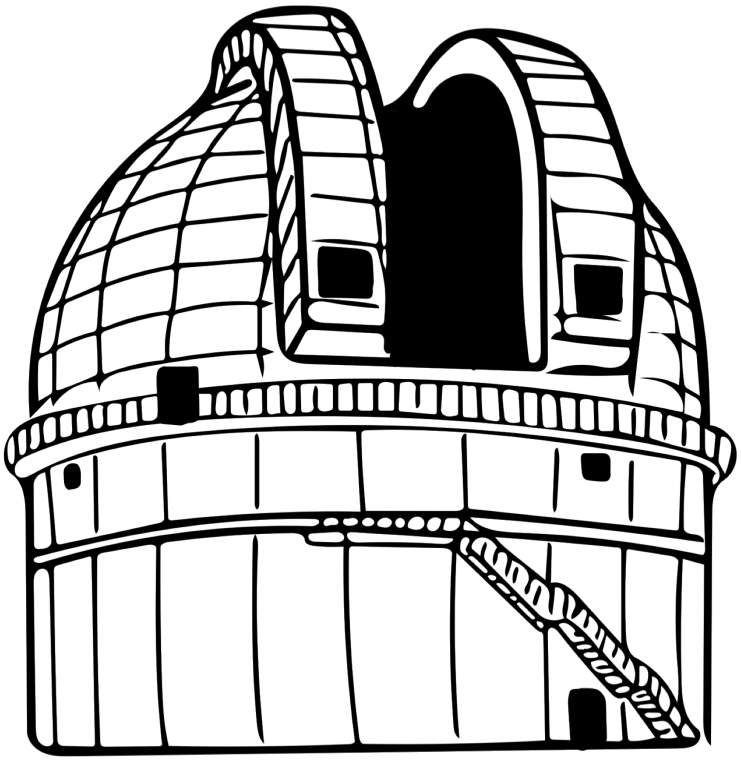

1.1 Stellar Prominences

"Prominence" is the term given to cool condensations of plasma, embedded in the hot corona of a star. Their presence is evidence for the stellar magnetic field, with closed magnetic loops being required to support the cool, condensed material above the stellar surface. The magnetic field prevents the movement of the charged coronal plasma across field lines, which can isolate regions of plasma from the rest of the corona. Thermal instabilities can cause loops to cool and without the motion of particles across field lines to reestablish thermal equilibrium, loops can cool to temperatures dramatically cooler than the rest of the corona[1]. This can lead to the condensations of neutral hydrogen termed prominences.

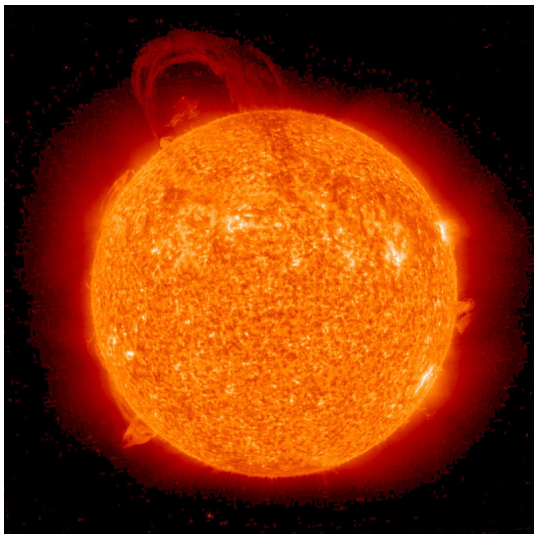

Figure 1.1: Erupting prominence, seen in extreme UV, from the 13th of April 2010. Photo Credit: STEREO, NASA

Prominences are well observed on the Sun and can be seen as filamentary structures as they cross the stellar disc or, if off disc, as loops of coronal material. Although they were first observed on the Sun, evidence of prominences has since been found on many star systems; from binary stars to single stars, and on stars of varying masses[1–3]. Prominences on young stars have been observed to be considerably more massive than solar prominences, some 10-100 times more massive[4], and are typically much larger in extent. An ejection of such a prominence, therefore, is likely to be a more dramatic event than similar ejections from the Sun. These features have consequences for the evolution of both the star and its system, since prominences are able to remove stellar mass, and angular momentum, from

the star over its lifetime. This mass may interact with orbiting planets if ejected into the planet's path. Prominences could have uses in reconstructing the star's coronal magnetic field, and providing insight into the mass loss rates from stellar winds. The work in this thesis is focused around the mathematical modelling of prominence formation sites around young, rapidly rotating stars.

1.2 Observations on binary star systems

Evidence for prominences on stars other than the Sun first arose from binary systems. Pencil beam studies, where a hot star is used to examine the atmosphere of a larger companion, provided the first hints of condensed clouds in stellar coronae. In this method, an absorption dip is observed in the spectrum before or after an eclipse has occurred (see Figure 1.2), suggesting that something other than the eclipsing star has passed in front of the companion star. In 1981 Schröder et al. observed this in the system 32 Cyg and attributed these absorption features to scattering by neutral hydrogen, which they explained by the existence of prominences[5]. From the relative velocity of the B star, the authors extracted a height for the prominence from the stellar rotation axis of $15R_{\odot}$.

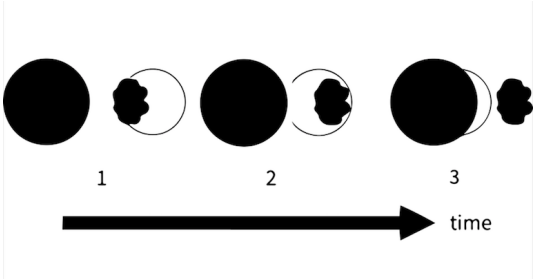

Figure 1.2: Depiction of a prominence and K primary star (black) eclipsing the B secondary star (white).

The binary system containing V471 Tauri also showed evidence of prominences. The binary, which is composed of a white dwarf and a K2 star, has an orbital period of about half a day. In a paper by Jensen et al.[6], the authors report observing the system for 28 hours and the discovery of multiple dips in soft X-ray emission. The authors found these dips to repeat on an orbital period. Four phases were found at which these absorption dips occurred, the strongest of which was seen to repeat for three orbits. Whilst some features were seen to reoccur, some were observed to weaken between rotations and others

to disappear completely. This all suggests the presence of an absorbing body in orbit that is held in place, resulting in periodic dips in the observed spectra. The authors predicted the material from one feature to be trapped at 2-3 stellar radii from the K star. Multiple explanations for the support of these clouds at such a height from the stellar surface were suggested by the authors. This included: strong magnetic loops from the corona of the K star providing support for the material, and their favoured theory: that the material could be collecting in the Lagrangian points of the binary system. However, in 2022 Zaire et al. [7] published a paper suggesting that the prominence material was forming above the Lagrange point, suggesting that the prominence is instead confined by strong magnetic field lines. The authors suggest that the mechanism supporting this prominence system would be better explained by the "slingshot prominences" discussed in the section on single star systems, rather than the Lagrange point mechanism.

Star	References	Reference in this work
II Peg	Doyle 1992, Steeghs 1996	[8, 9]
V471 Tau	Jensen 1986, Wheatley 1998, Zaire 2022	[6, 7, 10]
SS Boo	Hall&Ramsey 1992,1994,1990	[2, 11, 12]
AW Her	Hall&Ramsey 1992, 1994	[11, 12]
BV Cen	Watson 2007	[13, 14]
IP Peg	Steeghs 1996	[9]
SS Cyg	Steeghs 1996	[9]
AM Her	Gansicke 1998	[15]
Algol System	Peterson 2010	[16]
DH Leo	Barden 1986, Newmark 1990	[17, 18]
VW Cep	Newmark 1990	[19]
SZ Piscium	Cao & Gu 2012, 2019	[20, 21]
V711 Tau / HR 1099	Petit 2005	[22]
V410 Tau	Skelly 2010	[23]
AR Sco	Garnavich 2019	[24]

Table 1.1: Table of binary star systems in which potential signs of prominences have been observed.

A larger scale study was undertaken by Hall and Ramsey, as laid out in their paper from 1992[11], where the authors surveyed multiple binary systems in the search for "circumstellar clouds" or stellar prominences. Their results showed that stellar prominences may not be uncommon features, with prominences likely to be present on seven out of ten systems observed. This work came after the authors observed cool condensations on the star SS Boo in 1987 and 1988[2], when they suggested that the cool material was supported by strong magnetic fields on the stellar surface. In their study, the authors are careful to note that

the word "prominence" is taken as an analogy to the solar features we are accustomed to, but that they are different features in their own right. Table 1.1 shows the binary systems in which suspected prominences have been observed.

1.3 Observations on single star systems

1.3.1 AB Dor

Prominences on single stars were first observed by Collier Cameron and Robinson in 1989[1] on AB Doradus. AB Dor is a rapidly rotating "young Sun", with mass $0.86M_{\odot}$, a radius of $0.96R_{\odot}$ and a rotation period of 0.514 days. Collier Cameron and Robinson observed the star over multiple nights and found absorption features moving through the Hα line profile, suggesting the presence of an occulting body transiting the star. They observed these transients to reoccur on consecutive nights, sometimes for multiple nights before disappearing. These features reappeared on the stellar rotation period, i.e. they were co-rotating with the star. The authors explained these transients as "circumstellar clouds" or a stellar equivalent to prominences on the Sun. Collier Cameron and Robinson describe the clouds as cool condensations embedded in the hot and extended corona. They calculated the clouds to be typically at 3-4 stellar radii from the stellar rotation axis, and occulting up to 20% of the stellar surface area. The presence of these masses requires closed magnetic field out to these distances, and suggested that the coronae of such stars must be very extended. As the clouds pass between the star and the observer, the cloud efficiently scatters light at the Hα wavelength, causing the cloud to appear as an absorption feature. An example dynamic spectrum is shown in Figure 1.3.

The authors determined the distances of these clouds from the stellar rotation axis (ϖ) using the prominence drift rate ($\dot{v}$) which is proportional to the distance from the rotation axis:

$$\dot{v} = \Omega^2 \varpi \sin(i) \tag{1.1}$$

and thus the distances from the rotation axis can be extracted:

$$\frac{\varpi}{R_\star} = \frac{\dot{v}}{v\Omega \sin(i)}, \tag{1.2}$$

where Ω is the stellar rotation rate and i is the inclination of the stellar rotation axis to our

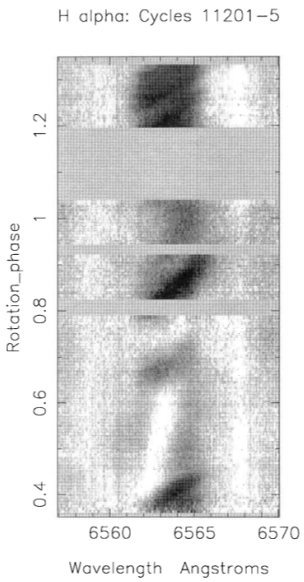

Figure 1.3: A dynamic spectrum from 1997 of AB Doradus, from the work of Collier Cameron et al.[25].

line of sight. That prominences around AB Dor preferentially appeared around 3-4 stellar radii above the stellar rotation axis suggests that these features are supported in a different manner to their solar analogues. Solar prominences are found only a few thousand kilometres above the solar surface. The prominences around AB Dor appear to congregate close to the co-rotation radius of the star (R_k), where the gravitational and centrifugal forces are balanced.

$$F_g = F_c \tag{1.3}$$

$$\frac{GM_\star}{r^2} = \Omega^2 r \sin\theta \tag{1.4}$$

$$R_k^3 \equiv \frac{GM_\star}{\Omega^2 \sin\theta} \tag{1.5}$$

From the observed hydrogen column densities (N_1) and prominence areas (A) ranging from $0.03A_\star$ to $0.38A_\star$, prominence masses of order $10^{17}g$ were calculated via

$$M_p = m_H N_1 A \tag{1.6}$$

where m_H is the mass of a hydrogen atom. These masses are 10-100 times the mass of large prominences observed on the Sun at $2 - 6 \times 10^{17}$g [26].

Since AB Doradus has a stellar inclination of about 60°, any prominences that lie at a

distance from the rotation axis that is equal to the equatorial co-rotation radius must be supported 0.5 and 2 stellar radii above this plane, in order to still transit the disc and be visible as absorption features[26].

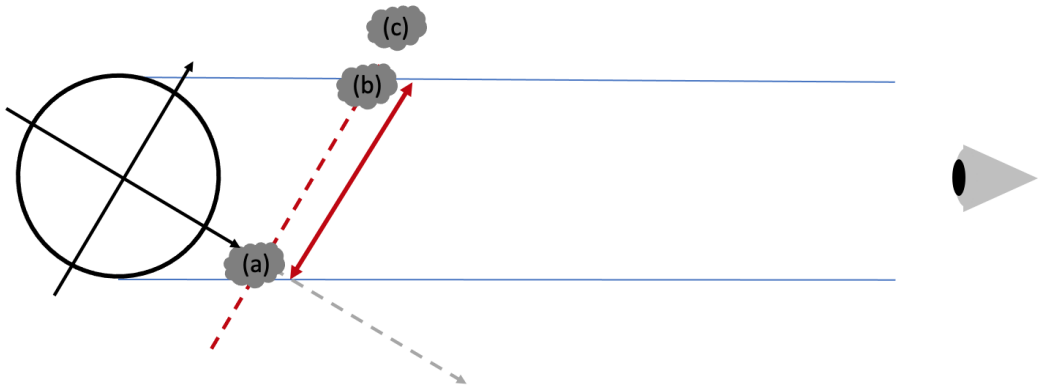

Figure 1.4: Cartoon showing three prominences at distances from the rotation axis of the equatorial co-rotation radius. AB Dor has an inclination of 60° therefore (a) and (b) would be visible as absorption features but (c) would not. The double ended red arrow shows the range of locations above and below the equatorial plane that a prominence could reside and be visible in absorption.

Since these first observations, prominences have been observed on AB Dor on many more occasions [1, 25, 27–33]. This has lead to AB Dor becoming the prototype for prominence modelling on rapidly rotating, low mass stars. Prominences have been observed at phases where there was no prominence the previous night (two stellar rotations previously). Collier Cameron [26] reported that it was common for one prominence to appear or disappear on a given observational night. Thus, with one prominence disappearing each night and about 6 or 7 clouds observed on any given night, this suggests the clouds would have a lifetime of up to about a week.

Prominences of the type seen on AB Dor are often referred to as "slingshot prominences" [26] due to the trapping of coronal material, that is being forced outwards due to the centrifugal force, within magnetic loops[34].

1.3.2 Speedy Mic

Another star on which slingshot prominences have been well observed is BO Microscopii (BO Mic), also known as Speedy Mic[1] due to its rapid rotation. Prominences were first observed on Speedy Mic in 1993 by Jeffries [35]. The clouds showed velocities that were consistent with being close to the co-rotation radius and had lifetimes of a couple of days. The author notes that this could result in prominences removing substantial angular momentum from the star. The prominence heights are given as $2.96R_\star$, $1.36R_\star$ and $1.01R_\star$.

They were later observed again, in July of 2002[36]. Dunstone et al. observed the star for three nights and collected data on 12 prominences, some of which reocurred over multiple nights. The authors quote this as 25 prominences in total (many of which are "double counts" as they reappear on consecutive nights). The prominences were observed between the radii of 1.4 and 3.6 stellar radii above the surface. The authors plotted this prominence data as a histogram, giving prominence distribution with height, and found a peak around $3R_\star$. This is beyond the co-rotation radius for this star which the authors give as about 1.8-2$R_\star$.

The authors reported that prominences were found in the same phases 5 nights after initial

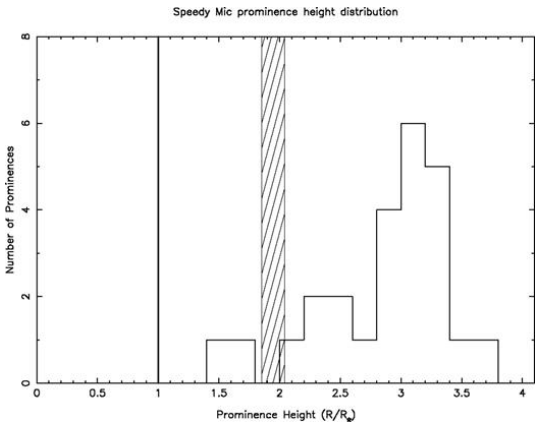

Figure 1.5: Histogram of the distribution of prominence locations on Speedy Mic in 2002, taken from Dunstone et al. 2006 [36].

observations. In other words, the prominence structures were stable over 5 nights, which is 13 stellar rotations. The individual prominences do not last for this length of time, but the structures that support them do, suggesting that prominences can be disrupted and reform in the same location.

[1]The name used throughout this thesis.

In a follow-up paper [37], Dunstone et al. compared two observations taken weeks apart so that the evolution of prominences in the system could be understood. The largest prominences in the system were observed at similar phases between the two observing runs, suggesting that the lifetime of the prominence-bearing structures was at least 2-3 weeks. Masses for the largest prominences were estimated at $0.5 - 2.3 \times 10^{14}$kg, or on the order of 10^{17}g. The prominences were seen not only as absorption features but also as features in emission once close enough to the stellar disc to scatter photons in the direction of the observer.

1.3.3 V374 Peg and the Kepler M-dwarfs

Slingshot prominences have also been seen on M dwarfs, for example the ultra fast rotator V374 Peg and a set of M dwarfs in Upper Sco.

A paper by Vida et al. [38] presented observations of a CME ejection on the star V374 Peg. A dynamic spectrum is shown in Figure 1.6. They estimated the ejected CME material to have a mass of around $10^{16}g$, which is comparable to large solar CMEs. The authors state that the rotational broadening for V374 Peg is insufficient to be able to detect transient absorption features that are characteristic of slingshot prominences. Despite this, prominence signatures can be seen in the spectra. In the published dynamic spectra, the colour table is reversed from the standard presentation, so that darker colours represent bright features in emission and light colours represent strong absorption features. This makes it somewhat harder to read the spectra if one is looking for prominence signatures. Figure 1.6 (a) and (c) show examples of the published spectra. Figures 1.6 (b) and (d) show the same plot in black and white and with an inverted colour table. With the plots in this format, absorption features transiting the stellar disc (prominences) can be more easily identified. They have also been highlighted by the red brackets.

V374 Peg is a useful star in that it has a stable magnetic topology. Its magnetic field is, globally, quite constant over a period of many years (Vida et al. [38] show it to have been stable over a 16-year period). Donati et al. [39] showed that V374 Peg has a dipolar field structure and that it rotates as a solid body. This solid-body rotation is at least in part responsible for the stability of the magnetic field since differential rotation on stars is an

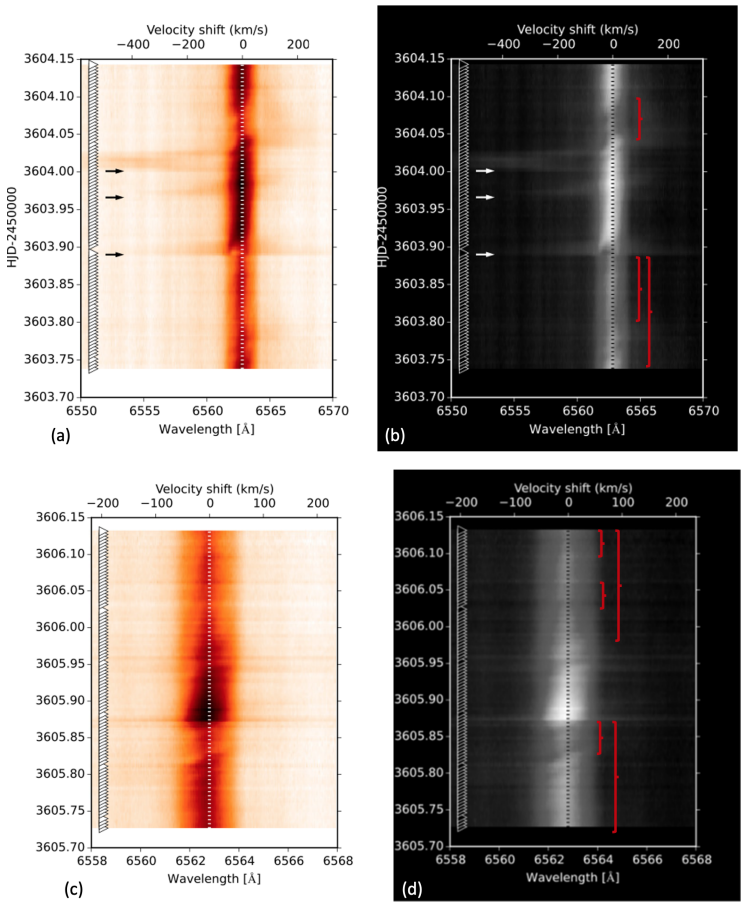

Figure 1.6: (a) A dynamic spectrum of V374 Peg as published by Vida et al. 2016 [38]. The CME ejection can be seen at large velocities and is highlighted in the image by the black arrows. (b) The same but in black and white and with an inverted colour table. (c) Another dynamic spectrum from Vida et al. [38] and (d) the black and white, colour table inverted spectrum. Red brackets highlight prominence absorption features.

important mechanism for twisting and disrupting the magnetic field.

Later, Stauffer et al. [40] found 19 M-dwarfs exhibiting prominence-like behaviour from K2 data. By observing the light curve data, variations in flux that repeated at the same phase on each rotation were attributed to cloud condensations trapped in co-rotation. This provides evidence that these features could be common across low-mass stars. The authors found that the dips in the light curves sometimes change shape and that these changes to the light curves happen over the period of one day and after a strong flare. The authors attribute these dips to slingshot prominences. Alongside these 19 stars, the authors also report a set of more slowly rotating stars with slightly different behaviour. Dips in the light curves were also seen on these stars, however, the dips were typically asymmetric and highly

variable. The authors attribute these to clouds associated with a recent collisional event or related to a closely orbiting planet.

Stauffer et al. classify their light curves into three groups: "scallop shells", "persistent flux dips" and "transient narrow dips". Scallop-shelled dips are those that appear to be very modulated and the authors report these light curves to be typically very stable. Persistent flux dips are those which are triangular in shape, narrow, and typically have longer periods than scalloped-shaped dips. Both of these may be associated with prominences. The transient narrow dips are described as triangular and narrow but very variable in depth. These dips generally have longer periods than the other dip classes. Figure 1.7 shows examples of each of the flux dip classifications.

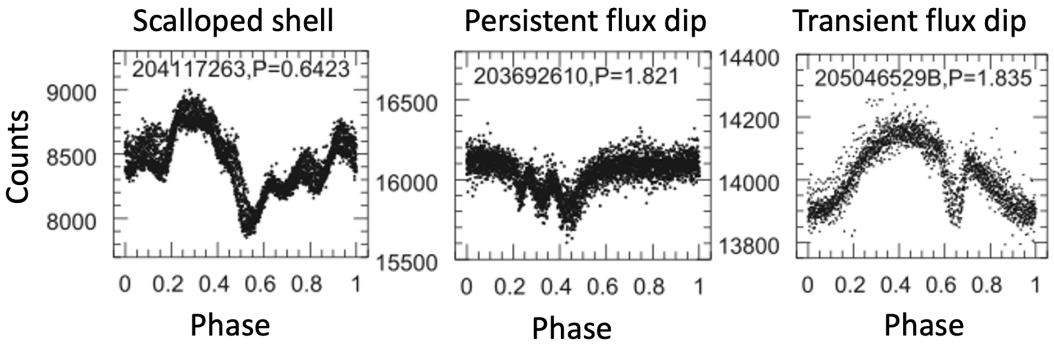

Figure 1.7: Example light curves, adapted from Stauffer et al. [40], showing the different light dip classes.

1.3.4 Other cases

Table 1.2 provides a list of stars and references of other prominence observations. Prominences on these stars have been less well observed, often only once.

In the vast majority of observations, prominences are observed on these stars as absorption features in the Hα profile, as on the star AB Dor. In the cases of LQ Lup and AP149 the prominence material was observed in emission as clumps of material around the co-rotation radius. The material is seen in emission in these cases due to the very low stellar inclinations. This low inclination means that the prominence material will be very unlikely to transit the stellar disc, but the material may be visible in the wings of the line in emission. This can happen if the material scatters enough light towards the observer such that this light is not washed out by the starlight from the disc. It is worth noting here that whilst

Star	References	Reference in this work
PZ Tel	Leitzinger 2016, Barnes 2000	[41, 42]
HK Aqr	Leitzinger 2016, van den Oord 1998, Byrne 1996, Doyle 1990	[41, 43–45]
HE373	Kolbin 2017, Cameron 1992	[46, 47]
HE520	Cameron 1992	[47]
HE622	Cameron 1992	[47]
HE699	Cameron 1992	[47]
AP225	Kolbin 2017	[46]
EY Dra/REJ1816+541	Eibe 1998	[48, 49]
RY Tau	Petrov 1990	[50]
TWA6	Skelly 2008	[51]
TWA17	Skelly 2009	[52]
LQ Lup	Donati 2000	[53]
V830 Per/RX J1508.6-4423	Donati et al. 2000	[53]
AP149	Barnes 2001	[54]
Upper Sco	Stauffer 2017	[40]
V530 Per	Cang 2020	[55]

Table 1.2: Table of single star systems in which potential signs of prominences have been observed.

the prominence material does scatter light in the direction of the observer, it scatters the light isotropically and not preferentially towards us.

Also of interest here is the selection of stars themselves. Within this list there are young G, K and M-dwarfs, suggesting that prominences could be common in young stars across a range of stellar masses.

1.3.5 Prominence ejections

As pointed out by Hussain et al.[56], AB Dor has been very intensely monitored over the years with spectroscopic time-series. Even in this case, only a handful of ejection events have been found[25, 57]. Ejection events typically last around 20 minutes[58] and observing runs last typically for three nights every year or two. Therefore, even with a star as well observed as AB Dor, observing these events is unlikely. In order to collect more data on this, a star would have to be nearly constantly observed. Due to this, there is not enough data to comment in depth on the ejections of such features but it is expected that due to their size, these events could be significant to the stellar system[59, 60].

1.3.6 Line asymmetries observed

Coronal mass ejections (CMEs) are regularly observed on the Sun (up to 6 times a day) and have velocities of about 250-500 km/s [61]. CMEs can be associated with eruptive prominences, with the prominence material, previously supported above an active region, being ejected after magnetic reconnection leading to a CME event. On other stars, similar events can be seen as asymmetries in line profiles and these could also be associated with stellar prominences. Since material is being ejected from the star, there is an associated Doppler shift that results in a blue-shifted component to the light, creating a blue-shifted wing to the line profile. The line profile is asymmetric since material is being ejected (and blue shifted) but there is not an equal amount of material falling back to the star (which would be red-shifted). Such line asymmetries have been observed on various stars, with the fastest observed event on an M dwarf being one on AD Leo, reported by Houdebine et al. [62], which had a maximum velocity of 5800km/s, over ten times the speed of those on the Sun. In a previous study of V374 Peg (see section 1.3.3) Vida et al. report a CME with a velocity of 675km/s, greater than the stellar escape speed [38]. In a large-scale study by Vida, Leitzinger et al. [63] studying over 5500 spectra, 478 were found to have line asymmetries that correspond to 25 stars. On these stars, events resulting in asymmetries occurred between 1.2-19.6 times a day. The authors report that the typical masses of these events would be 10^{15}g to 10^{18}g, however, they also note that the velocities of these events are typically lower than the stellar escape speed. Thus, these features do not represent much of the mass loss from the star. It is important to note, however, that the velocities reported by Vida et al. [63] are projected velocities. The true velocities may be far higher, depending on the projection effects and this could mean that far more material is ejected from the star than is suggested here.

A paper by Fuhrmeister et al. [64], searching for exoplanets around M dwarfs, studied 473 spectra of 28 active M dwarfs. In studying broadening and asymmetries in the Hα line, they found 41 flares and 67 broadened lines. Of those broadened lines, some were symmetric, and others had asymmetric wings. Both red and blue asymmetries were reported. The authors note that some of these events were associated with flaring, but that most were not. They ascribe the red asymmetries to be due to coronal rain or chromospheric condensations, whilst the blue asymmetries are caused by rising material. The authors suggest that the

blue shifts are connected to the up-flow of material at the flaring onset. They detect red asymmetries more often than blue, and symmetric broadening least frequently.

If slingshot prominences are destabilised, the material may be visible as line shifts [65, 66]. Because these prominences are supported beyond the co-rotation radius, their destabilisation would result in ejection from the star. Prominences like those on the Sun, however, which lie close to the star and below the co-rotation radius, would likely fall back to the stellar surface but may also be ejected depending on their velocity relative to the escape velocity. It would be impossible to tell the difference between these two situations from line asymmetries alone.

1.4 Zeeman Doppler Imaging (ZDI)

Zeeman Doppler Imaging (ZDI) is the technique used to measure the magnetic fields of stars. It uses both the Zeeman and Doppler effects to infer the stellar magnetic field from the light received by observers at Earth.

The Zeeman effect is the name for the phenomenon where a spectral line is split into multiple lines, under the influence of a magnetic field. Discovery of the phenomenon is credited to Pieter Zeeman, who published a paper on it in 1897 [67]. The presence of a magnetic field alters the atomic energy levels and therefore the transitions between them, which make up the emission and absorption spectra. This splits a single spectral line into multiple spectral lines. The change in energy, and therefore change in wavelength of light is linearly dependent on the magnetic field strength ($\Delta\lambda \propto |\mathbf{B}|$). Thus, the strength of the local magnetic field can be deduced. The direction of the magnetic field can be deduced from the polarisation of the light. This allows for a magnetic map to be generated of the stellar surface.

The Doppler effect is the phenomenon in which waves experience a shift in frequency due to the motion of the emitting object. For rapidly rotating stars, this phenomenon can be seen in the emitted light spectrum as rotational broadening. As the star rotates, the side of the disc rotating away from observer appears red shifted, whilst the side of the disc rotating towards the observer appears blue shifted. This Doppler shift occurs all across the stellar disc. Stars with faster rotations will have greater broadening effects, and therefore greater spatial resolution across the stellar disc.

ZDI, combines the Zeeman effect (splitting of spectral lines) with the Doppler effect (rotational broadening). The broadening of the line profiles makes it easier to find the fine structure of Zeeman splitting. However, this broadening of the line profile also results in it becoming shallower, and for very rapid rotators this can be a problem since determining any fine structure within this shallow profile is more difficult. ZDI as a method of inferring stellar magnetic field structures is discussed more in subsection 1.7.1.

1.5 Stellar coronae

The extent of stellar coronae is still unknown. Stellar prominences are observed multiple stellar radii above the surface of the star and this could be taken as evidence that the coronal magnetic field is closed up to this point. However, it could instead be the case that whilst the local magnetic field (confining the prominence) is closed, globally the coronal field is open at these heights. There is evidence that the coronae of these rapidly rotating stars are quite compact. By considering both the surface magnetic field and the coronal X-ray emission, multiple studies have suggested this [68–71].

Despite the compact corona, some magnetic field is likely to be closed at large distances from the star. Radio emission from the stars AB Doradus and V773 Tau A may be the result of large-scale magnetic structures such as helmet streamers, which is evidence for some closed field at great distances above the surface [72, 73]. Radio emission producing two lobes at large distances from the surface of the star (9 stellar radii) has also been found on the extremely low-mass stellar object LSR J1835+3259 [74]. This object straddles the boundary between low-mass star and brown dwarf and rotates with a period of 2.8 hours [75]. The stellar object is viewed equator-on, providing a good view of the material around the star. The lobes are stable over a period of a year and suggest a stable magnetic dipole around the star, in which the radio emitting material is trapped. This suggests that such field structures and radio emission could be common across low-mass stars.

1.6 Previous modelling

1.6.1 Closed field, Cartesian model - Jardine and Collier Cameron 1991.

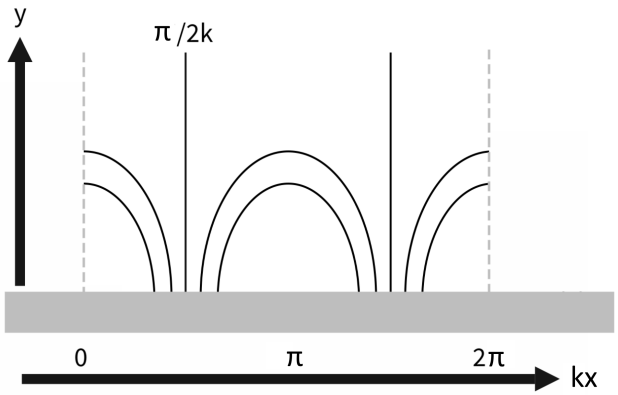

Figure 1.8: Cartoon of the magnetic field structure in this model, specifically for a dipole field ($k = 1$).

Jardine and Collier Cameron published a model in 1991 to explain the presence of these condensations at such large distances from the stellar rotation axis[76]. The two-dimensional, Cartesian model for prominence formation within the equatorial plane, shows that prominence formation can occur at large heights due to the rapid rotation of these stars.

Whilst the model is discussed here, the detailed mathematics is shown in Chapter 2, where the model is developed.

The model assumes an isothermal atmosphere, which allows for the determination of the equation of state. The fluid equation for conservation of momentum is solved along the magnetic field line to yield the pressure variation within the corona:

$$p(r) = p_0 \exp\Big(\frac{m}{K_B T} \int_{R_*}^{R} g(r) dr\Big) \tag{1.7}$$

where p_0 is the pressure at the base of the loop, g is the combined gravitational and centrifugal force and R_* is the stellar radius. The results of their calculation are shown in Figure 1.9.

The prominence bearing loop is modelled as a cooled field line, embedded within a hotter

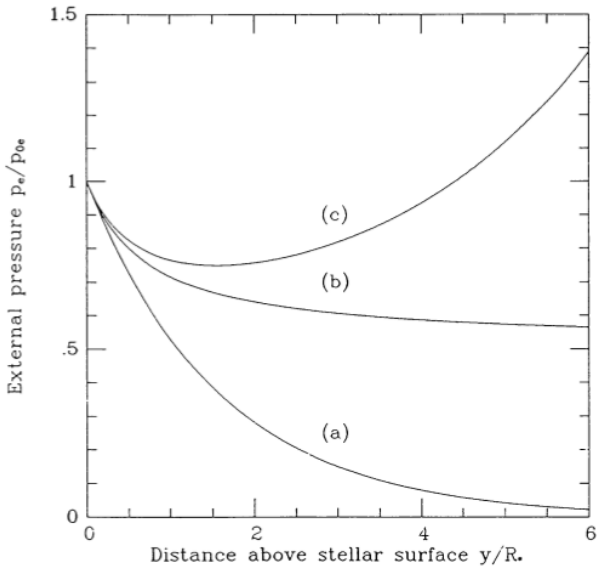

Figure 1.9: Pressure variation with height from the stellar surface for (a) gravitational force that is independent of height[3](b) a solar like star where the effects of rotation rate is small and (c) a rapidly rotating star. Plot from Jardine and Collier Cameron [76].

background magnetic field. The model does not attempt to describe how the loop cools, only that it starts with a temperature significantly cooler than the background (or external) field. The background field is set, as in Figure 1.8, and the cooled field line adjusts shape from this, according to the added mass that it supports when cooled. The background quantities, for example, the magnetic field, as denoted in the equations with a subscript "e" (external), and the cooled field with subscript "i" (internal).

The shape of the loop, X(y), is found by solving the conservation of momentum equation perpendicular to the magnetic field:

$$X'(1+(X')^2)\frac{\partial B_i^2}{\partial y} = -2X''B_i^2. \tag{1.8}$$

This can be solved analytically to give

$$X(y) = \pm\int_y^H \Big(\frac{B_i(H)^2}{B_i^2(y)-B_i^2(H)}\Big)^{1/2} dy \tag{1.9}$$

where H is the summit height. This places the constraints on the field that $B_i^2 > 0$ and

$\partial B_i^2/\partial y < 0$. Combining this second constraint with hydrostatic equilibrium leaves

$$\frac{\partial B_e^2}{\partial y} < 2\mu(\rho_e - \rho_i)g. \tag{1.10}$$

In a Cartesian geometry, the multipolar expansions of a stellar magnetic field can be defined as:

$$\mathbf{B}_e = (B_0 \cos(kx)e^{-k\bar{y}}, -B_0 \sin(kx)e^{-k\bar{y}}) = (\mathbf{B}_{ex}, \mathbf{B}_{ey}) \tag{1.11}$$

where B_0 defines the surface magnetic field strength, k defines the complexity of the magnetic field (for example k=1 is a dipole, k=2 is a quadrupole etc) and $\bar{y}$ defines the height above the stellar surface, scaled to units of stellar radius. A cartoon of the field structure is shown in Figure 1.8. Setting $B_{ex} = 0$, the x-coordinate of the loop footpoints can be found. From this it can easily be seen that $x = \pi/2k$ represents the first loop foot-point.

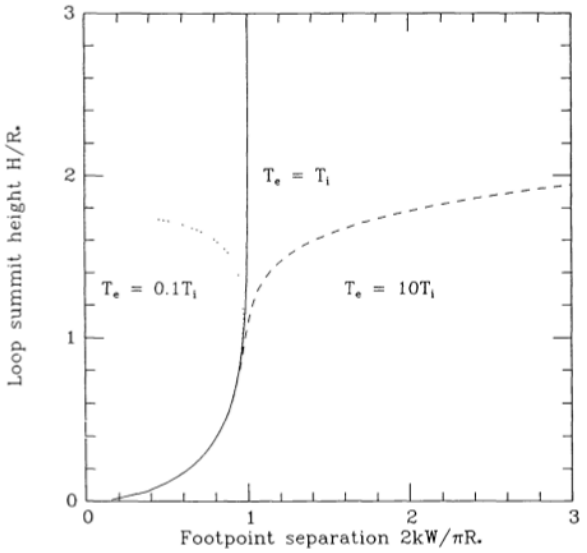

Figure 1.10: Loop summit height (H) variation with loop width (W), for loops that are under-pressured (dashed), over-pressured (dotted) and for the external field (thick). k is a constant that defines the complexity of the field. Plot taken from Jardine and Collier Cameron [76].

With everything defined, Jardine and Collier Cameron were able to solve for the shape of the "internal" or cool loops in equilibrium. The authors found a range of equilibria available for loops at various temperatures which is shown in Figure 1.10[76]. To form a prominence,

[3]This is a model often used for solar prominences as they typically form over a range of heights where g is almost constant.

the loops must be over-pressured. These cool solutions trace a path of equilibria at a range of heights above the stellar surface, including above the co-rotation radius[4] where the pressure within these loops will begin to increase with height.

The model is able to explain some important physics of these features. It can explain their formation at large radii from the rotation axis, however, it does assume that the field is closed up to this point. In order to form a prominence in this model, the coronal magnetic field must be closed. X-ray data does not support this assumption and instead suggests that the field could become open at low heights above the stellar surface[58]. This model was later built upon in 2005 by Jardine and van Ballegooijen, where the idea of an open field was incorporated. The model also has limitations in that it assumes a 2D and Cartesian geometry; ideally, a model would be three dimensional and in a spherical geometry.

1.6.2 Open field, Cartesian model - Jardine and Ballegooijen 2005.

In 2005, Jardine and Ballegooijen developed the model further[77], choosing a magnetic field configuration that included a "source surface". A "source surface" is the radius from a star at which the magnetic field becomes open. It was introduced by Altschuler and Newkirk[78] to explain the fact that during a solar eclipse the stellar magnetic field could be seen to be open at infinity. The presence of a source surface can be seen in Figure 1.11 in panel (b). The field becomes open beyond a certain radius, defined by the authors in this model by y_s.

The authors assume the "thin loop approximation"[79] in their model, such that gas pressure and density do not vary over the width of the flux tube, and also assume that the stellar atmosphere is isothermal.

The method for calculating the loop shapes is the same as for the previous model, starting with the conservation of momentum, and solving parallel and perpendicular to the field. In this model, however, the authors chose an external magnetic field structure as defined below;

$$B_{ex} + iB_{ey} = B_0\sqrt{e^{2ikz} + e^{-2ky_s}} \tag{1.12}$$

where $z = x + iy$ and $B_0 = B_0(x = 0, y = 0) = 1 + e^{-2ky_s}$ and is the magnetic field strength

[4] $1.7R_\star$ in Figure 1.10, where heights are measured from the stellar surface.

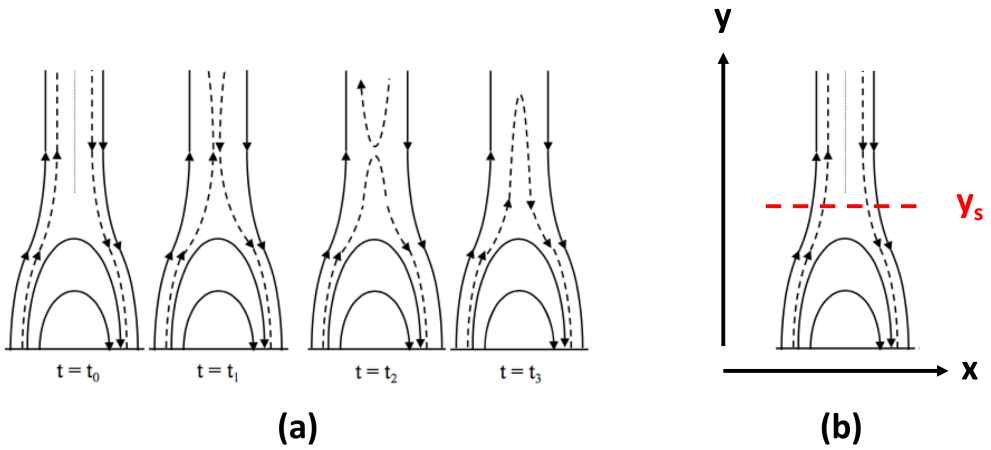

Figure 1.11: Diagram adapted from Jardine and Ballegooijen[77], showing (a) the formation of magnetic loops that can then support prominences out in the open field. Starting with a helmet streamer and the open field that surrounds it at $t = t_0$, the field evolves and reconnects, finishing at a closed pointy loop at $t = t_3$. (b) shows the source surface (y_s) and coordinate system.

at the stellar surface. k again defines the complexity of the field, i.e. $k = 1$ is the dipole configuration. Here $B_e^2 = e^{-2ky} - e^{-2ky_s}$ enforcing that the field strength drops to zero once $y = y_s$, before rising again to a constant $B_e^2 = e^{-2ky_s}$ at large values of y.

The authors solve for the shape of the loop with the same method as in the closed field model, an example of which is shown in Figure 1.12. A selection of the corresponding loop height-loop width plots are then shown in Figure 1.13. The same behaviour is found as in the previous model, with a range of possible equilibria existing for a loop of a particular temperature. Also, a loop of a given height has a range of equilibria available at various temperatures, each with a different loop width.

The authors find possible equilibria not just within the closed field region but also out within the open field. This is more realistic than the closed field model, allowing for prominence existence at multiple radii out from the rotation axis without the requirement for the coronal field to still be closed. For a source surface above the co-rotation radius, the left hand panel of Figure 1.13, many solutions are found at various heights, with whole families of equilibria being possible solutions. With the source surface placed below the co-rotation radius, as in the right hand panel of Figure 1.13, fewer solutions are found. Not all equilibria within a family are possible solutions, meaning that a loop could struggle to find a nearby

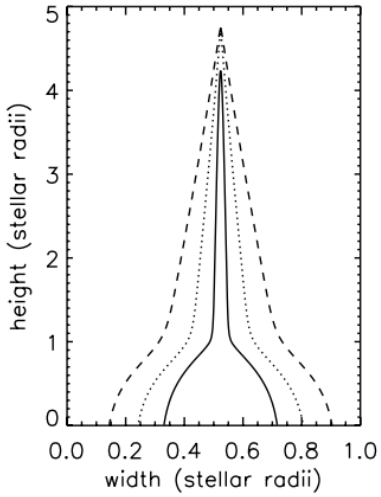

Figure 1.12: Example cool field lines; $T_i = 5 \times 10^6$K (solid), $T_i = 2 \times 10^5$K (dashed) and $T_i = 2 \times 10^4$K (dotted). The external temperature is set to $T_e = 2 \times 10^7$K and the source surface $y_s = 1R_\star$. Plot taken from Jardine and Ballegooijen's 2005 paper[77].

equilibrium to move into if more material were added to the loop.

This model is still restricted to Cartesian coordinates, however, and extension of this model to a geometry that better fits the geometry of the system might remove the unphysical behaviour seen here, namely that the loop width can be seen to extend to infinity in Figure 1.13, i.e. extends well beyond the edge of the star.

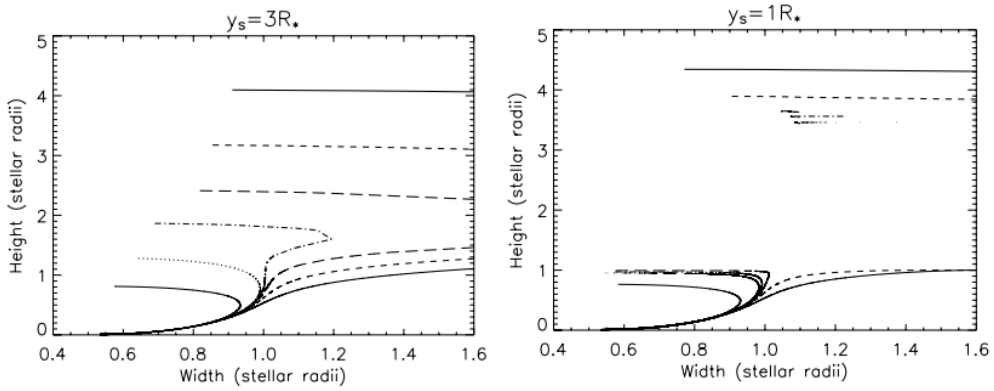

Figure 1.13: Plots taken from Jardine and Ballegooijens' 2005 paper[77]. Loop height vs loop width for loops of temperature $T_i = 2.5 \times 10^7$K (dot-dot-dot-dash); $T_i = 9.1 \times 10^6$K (dot); $T_i = 8.7 \times 10^6$K (dot-dash); $T_i = 8.3 \times 10^6$K (long dash); $T_i = 7.1 \times 10^6$K (short dash) and $T_i = 4.2 \times 10^6$K (solid). The external temperature is again $T_e = 2 \times 10^7$K and an external plasma beta of 10^{-2}. These height-width plots are for $y_s = 3R_\star$ and $y_s = 1R_\star$. The authors chose to plot this for $k = 3$, i.e. an octupolar field geometry.

1.6.3 Modelling prominences as stable points - Ferreira 2000

Whilst the previous two models solved for the equilibrium loop shapes of prominence bearing magnetic field lines, they do not determine if these equilibria would be stable. Ferreira's model specifically calculates the stable equilibrium points within a magnetic field [80]. However, this model assumes the coronal gas to be massless, because the magnetic field does not adjust its shape in order to account for the additional mass that would be supplied to the field line once it was cooled.
The model assumes that the prominence lifetime is greater than other relevant timescales so that the system is in static equilibrium.

Ferreira published work showing the stable points in a pure dipole and pure quadrupole field. They showed that for a point to be a stable equilibrium point, it must satisfy the conditions that

$$\mathbf{g}_e.\mathbf{B} = 0 \tag{1.13}$$

and

$$(\mathbf{B}.\nabla)(\mathbf{g}_e.\mathbf{B}) < 0, \tag{1.14}$$

where g_e is the effective gravity: the combined gravitational and centrifugal forces. The first condition is that the location is an equilibrium point, however, in order for this point to be stable it must satisfy the second condition. This second condition requires that as we move along the field line, in the direction of the magnetic field, the quantity $(\mathbf{g}_e.\mathbf{B})$ is always decreasing. Therefore, material collecting at the equilibrium point will remain there and thus be stable.

For a pure dipole, aligned with the rotation axis, this simplifies to

$$r > \left(\frac{2}{3}R_k\right)^{1/3} \approx 0.87R_k \tag{1.15}$$

This work provided an expression for the equilibrium points in a dipolar field, and established which were stable and which were unstable. With the dipole field structure, solutions for stable equilibria can be found below the co-rotation radius (R_k) as well as beyond it. This is shown in Figure 1.14. However, a pure dipole field will only produce stable points within the equatorial plane and not at higher latitudes, although some prominences have been observed at higher latitudes.

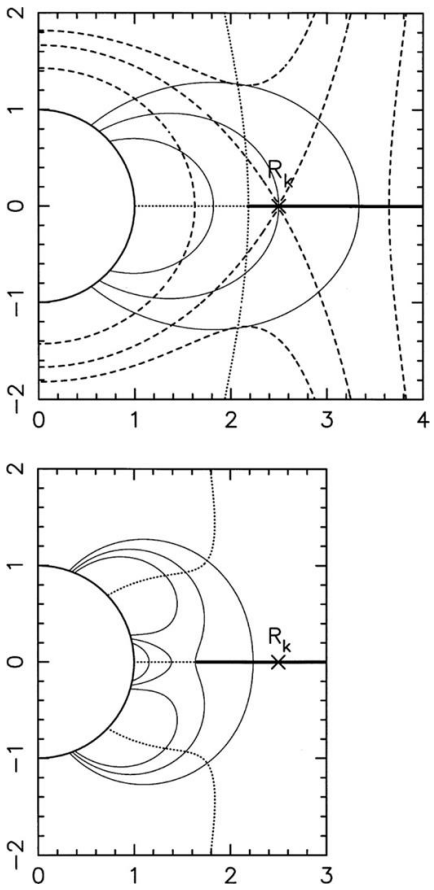

Figure 1.14: Plot from Ferreira 2000 [80], showing a dipolar field (top) and sextupole field (bottom). The field lines are shown by a solid line, the stable points by the thick lines, and the unstable equilibrium points are shown by the dotted lines. The dashed lines are equipotentials.

In order to support higher latitude prominences, a higher order field can be used, for example, a quadrupole (Figure 1.15).

1.6.4 Modelling stable points in an arbitrary field - Jardine et al. 2001

Jardine et al. [81] developed Ferreria's model to a generalised magnetic field. The authors used Zeeman Doppler Imaging (ZDI) maps of AB Dor acquired in 1995, and assumed a potential magnetic field in order to construct the coronal field. They then calculated the stable points within this field structure. The authors report that the stable point locations, shown in Figure 1.16 by the grey plane, are determined by the large scale magnetic field for which field lines have been drawn. Stable points are found both above and below co-rotation, and the outer extent of the solutions is determined by the location of the "source surface" where

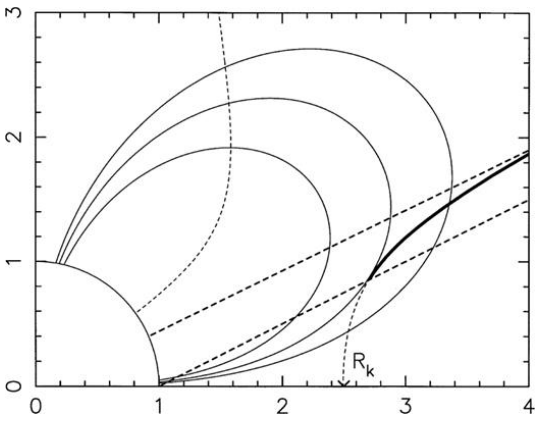

Figure 1.15: Plot from Ferreira 2000 [80], showing a quadrupolar field, the same lines are used as above.

the field becomes open. The model is unable to find solutions within the open field, since it requires closed magnetic field lines, and the field does not adjust when mass is added to a field line (as the model by Jardine and van Ballegooijen did [77]).

The authors also showed that the solutions from Ferreira's model for a dipole could not

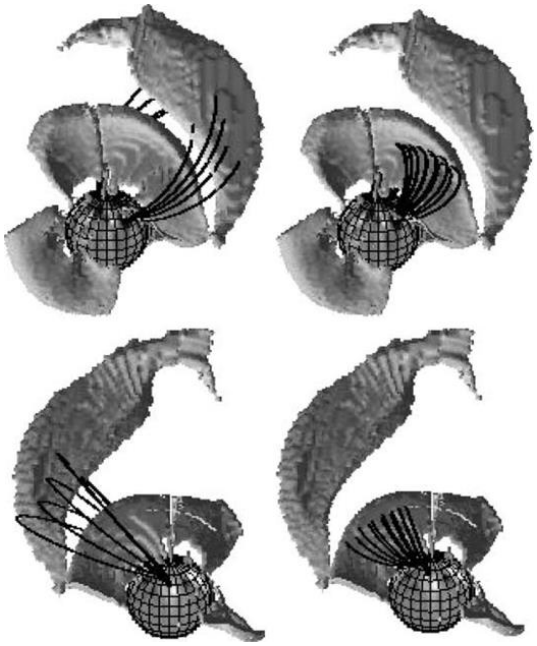

Figure 1.16: Plot from Jardine et al. 2001 [81], showing the locations of the stable points, as grey surfaces, around AB Dor for the year 1995. The left plots show the field lines above co-rotation and right hand plots below. The top plots show the view from longitude 180° and bottom plots from 0°.

explain the observations from stars such as AB Dor or PZ Tel, since with their stellar inclinations the stable points within a dipole field would never transit the stellar disc. With a

quadrupolar field, the stable points can form at higher latitudes and therefore some would transit the disc and be visible as absorption features in the dynamic spectra. They also find that stable points exist much closer to the stellar surface with the ZDI generated field structure than they do with a pure dipole. However, the ZDI generated field is not perfect since (a) very little of the southern hemisphere of the star can be seen and (b) ZDI does not work well in regions of low surface brightness, which could be the places of strongest field. The authors predict that, at the co-rotation radius of AB Doradus, the magnetic field must be more complex than an aligned dipole because this would not allow for slingshot prominences to transit the stellar disc, and yet they are observed.

1.6.5 Recent work in the field

Recently, Villarreal D'Angelo et al. published a paper categorising which low mass stars could support prominences[82]. They did so by comparing the positions of the Alfvén and co-rotation radii, a technique previously used on high mass stars [83]. The Alfvén radius is defined as the radius at which the stellar wind velocity is equal to the Alfvén velocity ($u_A = B/\sqrt{4\pi\rho}$), and is the radius beyond which the magnetic field cannot stay closed. This is because the Alfvén radius is analogous to the sonic radius, in that information cannot travel back along the field line and allow the field line to readjust shape. If the co-rotation radius lies above the Alfvén radius, all closed magnetic field lines are within co-rotation and so prominences that form will drain back to the stellar surface. The authors find that the Sun, all other solar-type stars and hot Jupiter hosts lie within this regime. They refer to these magnetospheres as "dynamical magnetospheres", a term used for the classification of high mass stars. For stars with the co-rotation radius below the Alfvén radius, closed magnetic field lines now exist beyond the co-rotation radius and slingshot prominences can now be supported. The authors refer to these as "centrifugal magnetospheres", once again in keeping with high mass stars. Young Suns and M-dwarfs are found to exist in both of these parameter ranges. In both the high mass and low mass cases, the rapidly rotating stars are those which have their co-rotation radius close enough to be inside the Alfvén radius, thus these stars are the ones likely to support prominences by the centrifugal support method, i.e. slingshot prominences.

1.7 Motivation for this work

1.7.1 Uses of prominences

Predicting magnetic field strengths

Since prominences can only be supported in closed magnetic fields, the mass of a prominence must be in part determined by the magnetic field strength of the loop. Thus the observation of prominences could help to constrain the magnetic field strength at the prominence location. Collier Cameron and Robinson in their original paper [1] estimated the field strengths of the loops supporting the observed clouds by assuming the prominences to be supported in a dipole field structure and the magnetic pressure to exceed the gas pressure. They assumed the magnetic pressure to be greater than the gas pressure as they argued that the dynamics of the fluid must be constrained by the magnetic field in order for the prominence to be contained.

Predicting magnetic field structure

Since these cool condensations are confined within magnetic loops in the stellar corona, the observed sites of these features trace out the coronal magnetic field at that particular point in time. Hence, these features could be useful for building up a picture of the evolution of the coronal field structure. The magnetic field strengths of stars are currently inferred using Zeeman-Doppler Imaging (ZDI). The technique combines Zeeman splitting of energy levels within the stellar atmosphere due to the stellar magnetic field, with the spread in photon wavelength due to the Doppler effect experienced due to the stellar rotation. However, the magnetic maps created by ZDI provide the magnetic field vectors at the stellar surface, and there is no certain way to correctly extrapolate this into the stellar corona as various forms of field can be assumed, such as potential or force-free. Models that construct the coronal field from the ZDI maps also require an upper boundary condition to define the field structure, which could be taken as the "source surface" - the radius at which the magnetic field becomes open. Determining the location of the source surface for stars can be done through stellar wind models [84], which can be used to determine the location at which the magnetic field is forced open, or estimated from the stellar rotation rate [85]. Information on prominence locations could also be a useful tool in providing greater insight into the coronal field structure, since they require closed field structures at their locations in the

corona.

As the magnetic field governs many processes within the star through the stellar dynamo, a correct picture of the magnetic field is vital to understand many aspects of the stellar behaviour.

In 2020, Jardine and Collier Cameron [86] published a model using slingshot prominences as tracers for the magnetic field structure. The model used ZDI observations of the surface magnetic field of the star AB Doradus, and the authors constructed the coronal field using different extrapolation methods: a potential field and a non-potential field[5]. The locations of prominence formation in these field structures were found, and synthetic Hα spectra were produced. These spectra were then compared to the observed Hα spectra for the corresponding observation. By comparing the model to the observations, the authors found that the potential field structure better reproduced the observed prominence trails. The authors found that both the total prominence mass and proportion of this mass that would be visible should vary with the inclination of the dipole axis. This would suggest that it may be possible to predict the orientation of the dipole axis if the total prominence mass on a star could be estimated from observations.

Figure 1.17 shows the magnetic field extrapolation with the prominence material shown

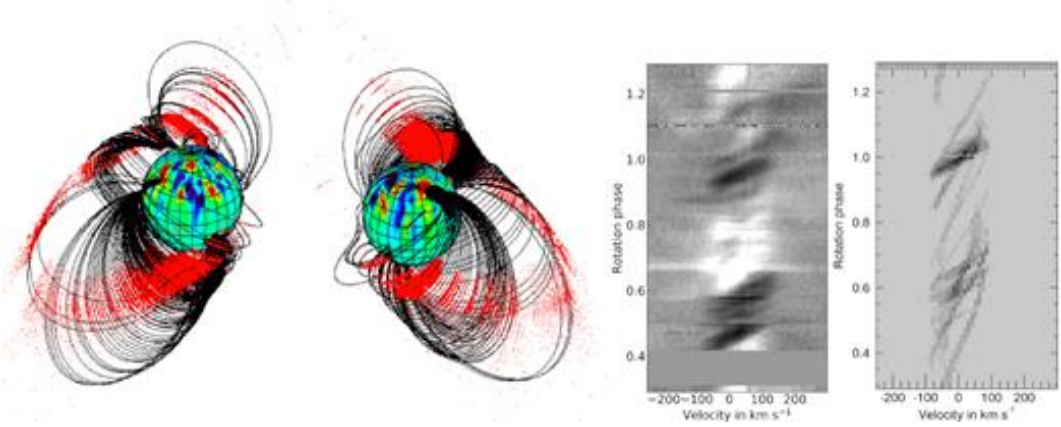

Figure 1.17: Plot from Jardine et al. 2020 [86], showing the constructed field and prominence mass (red), and the dynamic spectrum (observed on the left and synthetic on the right).

in red. The Hα spectrum shown on the left hand side is the observed spectrum, and the modelled spectrum is shown on the right. The model clearly reproduces the two dark

[5]Potential fields are those with the lowest energy state, whilst non-potential fields contain electrical currents within the stellar corona.

features of the prominences, but also shows some fainter, slower moving features that cannot be picked out of the observations. Similar examples are given for other years, with the synthetic spectra reproducing the observations well. A non-potential field did not provide such a good match to the observations.

As wind gauges

Jardine and Collier Cameron [87] showed that prominences could be used as "wind gauges" to probe the stellar wind. The winds of low mass stars are difficult to observe due to their low densities. Whilst their mass loss is relatively low, due to their low densities, the angular momentum that these winds remove can be significant [88–90]. This is due to the influence of the magnetic field. This loss of angular momentum determines how the star will evolve, determining the rate at which the star will spin down. The interplay between the stellar rotation rate and the stellar magnetic field, through the stellar dynamo, also means that the stellar wind influences the magnetic activity. Although it has been done, measuring these winds directly is challenging.

Panagia and Felli [91] presented a method in which the thermal radio emission of the wind is measured, as the wind expands with distance from the star. Whilst this produces predictions for the density of the stellar wind, typically the method produces upper-limits to the wind density since it usually produces non-detections [92–94]. Another method to produce upper limits to the wind density was suggested by Wargelin and Drake [95]. When the stellar wind, which is ionised, interacts with the neutral material in the interstellar medium, the charge exchange produces an X-ray signature.

A successful technique by Wood [96] used observations of Lyman α absorption from the edges of stellar astrospheres (or heliospheres) to calculate the wind mass loss rates. The authors found a correlation between the X-ray flux, or stellar activity, and the mass loss rate per unit surface area of the stellar wind. However, for the stars with the very largest X-ray flux, i.e. very active stars, this correlation no longer appears to hold. These stars instead show decreasing mass loss with increasing activity. The boundary between the two has been dubbed the "wind dividing line" and is of great interest since the stellar wind has such an important role in the evolution of these stars. It has also attracted attention for those with an interest in exoplanets, since the stellar wind is an important factor in the retention (or otherwise) of an exoplanetary atmosphere [97]. Despite this observation, theoretical models

of stars on either side of this boundary have not shown a difference in field geometry [98, 99]. This suggests that there should be no change in the magnetic field or the wind that drives it, at this boundary.

For stars with a white dwarf companion, their winds can be deduced by the degree of pollution found in the photosphere of the white dwarf through the impact this has on the spectrum of the white dwarf [100, 101]. The wind of the companion star strikes the white dwarf and therefore contaminates the white dwarf's surface. This material should quickly settle below the surface of the star, and therefore the quantity of pollutants that are observed can be used to place limits on the mass acretion rate onto the white dwarf. In other words, the quantity of pollutants observed can place limits on the mass loss from the stellar wind of the companion star. Multiple papers have been published on modelling stellar wind mass loss rates based on the escaping atmosphere of an orbiting planet [102–104]. A stellar wind can strip the atmosphere of a planet but the extent to which this occurs depends on the strength of the stellar wind.

Most recently, the work of Jardine and Collier Cameron 2018 [87] suggested the use of stellar prominences to deduce the wind mass loss rates. The particular advantage of their method was that it was suitable for very active stars, that lie beyond the dividing line where there are limited observations. The authors describe prominence formation as being caused by an up-flow of material from the stellar surface which has been triggered by a thermal instability at the summit of the loop. This up-flow begins in order to reestablish pressure balance, since the thermal instability leads to a drop in summit gas pressure. This is a thermal wind and therefore the same mechanism as the stellar wind itself, albeit at a different temperature. This up-flow could be modelled by a Parker wind [90], increasing in speed with distance from the surface until eventually reaching the speed of sound at the sonic radius, R_s. In their model, the authors describe three regimes in which stars with prominences could reside; hydrostatic, limit-cycle or open field. Stars forming prominences in the hydrostatic regime would support prominences that are quasi-static. This occurs for stars with the co-rotation radius below the sonic radius. Slingshot prominences, which form on very active stars, form typically around the co-rotation radius. Therefore, in stars where the co-rotation radius is below the sonic radius, the slingshot prominences could be quite stable. The up-flow from the surface will occur until the loop has reestablished pressure bal-

ance and then the up-flow will halt. Stars forming slingshot prominences in the limit-cycle regime, i.e. with co-rotation radius above the sonic radius, will not support such stable prominences. This is because the up-flow of material will continue beyond the maximum mass that the field line could support. Unlike when the sonic radius is below the co-rotation radius, here the up-flow is supersonic by the time it reaches the loop summit. This means that information can not travel back downstream to cut off the up-flow when pressure balance has been reestablished. This results in prominence formation, followed by ejection once the maximum mass is reached. Once the field line reconnects after this ejection, another prominence will form in its place and the cycle continue, hence, the name "limit-cycling". The third option is that a star forms prominences beyond the Alfven radius. In this case, the wind speed is greater than the Alfven speed at the loop summit. This means that the magnetic field can not remain closed and little material would be able to condense into a prominence. Therefore, stars can be categorised as:

$R_k < R_s < R_A$ - hydrostatic regime

$R_s < R_k < R_A$ - limit-cycle regime

$R_s < R_A < R_k$ - open field regime

For stars that lie in this limit-cycle regime, the prominences could be used as wind gauges. They trap material driven by a thermally driven up-flow (the same mechanism as the stellar wind) and gather large quantities of mass that can be visible in the Hα spectrum. In this paper, the authors use observed values of prominence masses (m_p) and lifetimes (t_p) to estimate the mass loss rate associated with the prominences ($\dot{m}_p$), and therefore the wind.

$$\dot{m}_p = \frac{m_p}{t_p} \tag{1.16}$$

In practice, however, there are a limited number of observations of these prominences that provide mass estimates. Either, more observations of prominences with derived masses, or, theoretical models of prominences around such stars, would solve this problem.

The mass loss rate of the wind ($\dot{M}_\star$) can be estimated from the mass loss rate of a prominence on these stars by

$$\dot{M}_\star = 4\pi R_\star^2 \frac{\dot{m}_p}{2A_0} \tag{1.17}$$

where A_0 is the area of a prominence loop footpoint. This equation assumes that the up-flow supplies the prominence from both footpoints. For observational estimations, this area can be calculated from flux conservation, assuming that the extent of the prominence is known.

Figure 1.18 shows a plot from Wood et al. [105] of mass loss rate per unit surface area

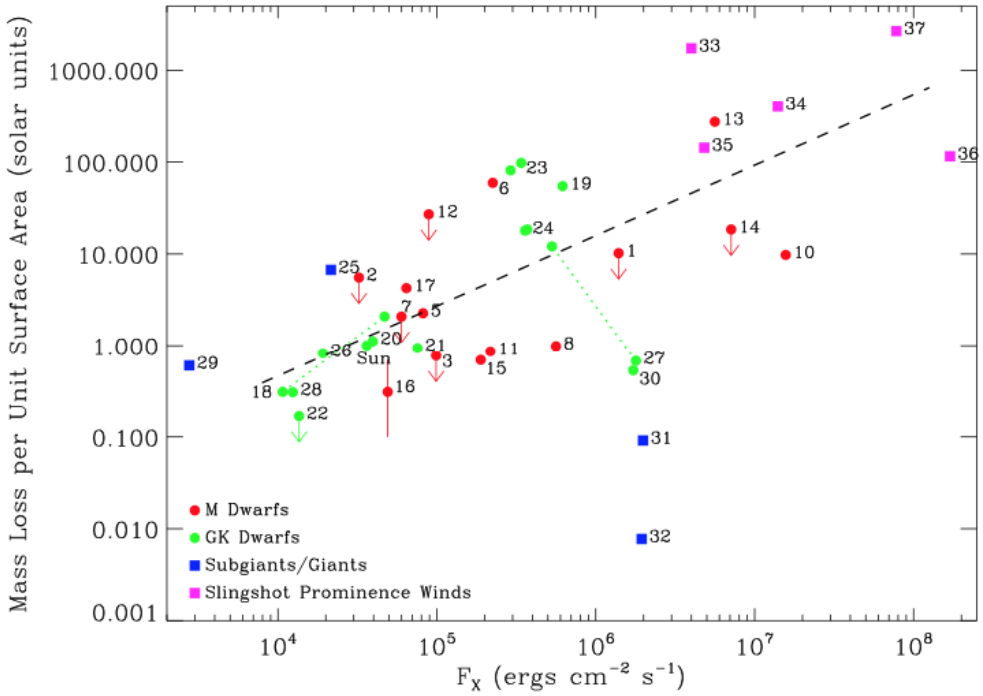

Figure 1.18: Plot from Wood et al. [105], showing the prominence mass loss alongside the wind values.

against X-ray flux. The data come from various different methods of measuring the stellar wind over a range of star types: the prominence method (pink), the exoplanetary atmosphere method and the astrosphere method. The plot shows a large degree of scatter. The prominence bearing stars follow the same trend as the less active stars and do not appear to show evidence of the wind dividing line.

Insight into the "young Sun"

The Sun, in its youth, would have been one of these rapidly rotating, low-mass stars. Whilst the Sun is the star that is the most well observed by humans, we have been observing it for an insignificant length of time in comparison to its age. In order to gather an understanding of the Sun's early evolution, we rely on observations of young solar-like stars.

Prominences on the Sun today are very different to the slingshot prominences observed on

young solar-like stars such as AB Doradus. Since these prominences have been found on many similar stars, it suggests that they could be a common feature at this point in a star's evolution. This would suggest that these prominences once existed on our Sun too. The consequences of such prominences are discussed in depth in the following section, and here they are just touched upon. The ejection of prominences could remove considerable angular momentum from the young star, influencing its spin-down rate. They could also impact orbiting planets when ejected. These raise questions about how our Solar System as we know it evolved.

1.7.2 Consequences of prominences

Habitability of exoplanets

These features, if eruptive, could play an important role in the development of any nearby planets and their ability to harbour life. Having an orbital radius in the "Goldilocks zone" or "habitable zone", the range of radii around a star where an orbiting planet can sustain liquid water on its surface, is often quoted as the requirement for a planet to harbour life. In reality, this is only one of the considerations in finding a possible host planet for life[106–109]. Other factors which should be considered include, but are not limited to: the spectral type of the star, the radius of the planet and its composition, the geological activity of the planet, and the activity of the star. Ejections of stellar prominences, and the character of these features, are intrinsically linked to this final point.

Prominences, if ejected into the orbit of the planet, could cause disruption to the planet's magnetosphere. The planetary magnetosphere can be compressed, on the side of the planet closest to the star, whilst the magnetosphere on the opposite side will be elongated[110], as shown in Figure 1.19. This distortion of the magnetic field[6] can lead to magnetic reconnection, which will release a large amount of energy and cause electrons to be channeled along the planet's magnetic field towards the poles. On Earth, this can lead to disruptions of communications, satellite damage, and damage to electrical transmission equipment, leading to power cuts[111–113].

"CME atmospheric erosion" is another possibility for exoplanets in orbit around their

[6] often referred to as a "Geomagnetic storm"[110]

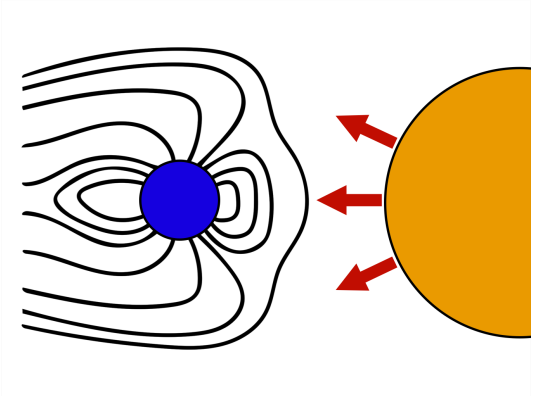

Figure 1.19: Distortion of the planetary magnetic field due to the outflow of stellar material.

host star. A CME (coronal mass ejection) is the release of stellar plasma and magnetic field and is often associated with stellar flares or prominences[114–118]. On the Sun, CMEs typically occur anywhere from 1 - 6 times a day, depending on where the Sun is in the solar cycle[118]. The solar energetic particles (SEPs) that are accelerated in the shock ahead of the CME after its ejection can cause substantial damage to a planetary atmosphere. If the atmosphere of the planet was severely stripped away, the surface of the planet would be subjected to large quantities of stellar radiation that would otherwise have been absorbed by the planetary atmosphere.

High energy radiation from host stars can be absorbed in the atmosphere of the exoplanet, causing it to heat and expand. This expansion could be extreme, causing the kinetic energy for the majority of atmospheric constituents to overcome the gravitational binding energy and escape the planet in the form of a planetary wind similar to that of a Parker wind[119–122]. This is likely detrimental to life development.

The likelihood of an impact of a CME with an orbiting planet depends on many factors. The number of prominences held in co-rotation at a given time, and their frequency of ejection, are clearly important. AB Dor. is thought to typically have around 6 prominences in orbit at once[1, 31, 33], with evidence of the ejection rate being every day or two. The proximity of the exoplanet to the star also contributes to the likelihood of impact; planets closer in to their host star will experience more, or higher intensity, impacts than planets further out, as shown in Figure 1.20. If the CME remains undiluted as it propagates through space, being closer to the host star will result in more of the orbit being in the

"danger zone" than being further out. If, however, the CME maintains the same angular size as it propagates through space, whilst the planetary distance from the star does not affect the proportion of the orbit in the danger zone, the CME will experience geometric dilution and thus the quantity of radiation that impacts the planet will decrease. The probability of impact of a CME with an orbiting planet was discussed by Khodachenko et al.[123].

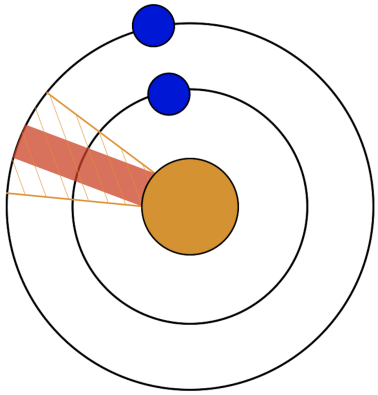

Figure 1.20: Planets (blue) orbiting a star, with ejection of prominence material (red) and prominence ejection including geometric dilution (orange).

Depending on the spectral type of the host star, the position of the habitable zone may be rather different due to the stellar luminosity. The surface temperature of the planet is related to the stellar luminosity since the radiation flux from the star provides energy to heat the planet. Assuming the planet has a set efficiency to radiate away energy as heat, the luminosity of the host star thus determines the radius at which liquid water could be present on the planet's surface. In the case of M-dwarfs, the habitable zone is very close to the star, which places the planet at a radius where it is much more likely to suffer an impact from an ejection.

Observationally, these prominences on young, rapid rotators have been found to be of considerable size, up to 20% of the stellar surface area could be occulted by them. Clearly, the larger the cloud that is ejected the more likely it is to be ejected into the path of the orbiting planet, therefore stars that host larger prominences could be poor targets in the search for life.

The more active a star is, the stronger is its magnetic field[124]. This could allow for larger prominences to be supported on active stars than on less active stars. Stars with more complex magnetic field structures could also have more condensations in co-rotation at a given time.

Stellar evolution

The evolution of a low mass star is heavily influenced by its wind [88, 125]. The winds of low mass stars are thermally driven and although typically low in mass, can remove considerable angular momentum. This is due to the influence of the magnetic field. The out-flowing gas is constrained by the magnetic field of the star. As the star rotates, a torque is exerted on the gas by the magnetic field, as it tries to enforce co-rotation. This results in angular momentum being lost from the star.

The loss of angular momentum causes the star to spin down as it ages, and this influences its activity through its magnetic field. The magnetic dynamo is the process by which a star regenerates its magnetic field, and is driven by the rotation of the star itself. In this feedback loop, the rotation rate drives the dynamo which generates magnetic field and determines the stellar wind, which removes angular momentum and causes the star to spin-down.
However, the models of stellar evolution often struggle to replicate the observed spin-down rates. In order for models to match the observations, a scaling factor is included that artificially increases the angular momentum loss or spins down the star. This ensures that the spin down rates of stars converges to the observed values [85]. Slingshot prominences could be a mechanism for angular momentum loss at early stages of the stars life.

The evolution of slingshot prominences on a solar like star was studied by Villarreal D'Angelo et al. in 2019 [126].The authors reason that whilst the Sun does not host slingshot prominences now, it did earlier in its evolution. They determined the period of the Sun's life for which slingshot prominences could have been supported, and find this could range from around 10^3Myrs to never, depending on its initial rotation rate (Figure 1.21).

A rotational evolution code was used to generate the relations between stellar rotation rate and age for fast (90th percentile), medium (50th) and slow (10th) stars. These rotational evolution models require a moment of inertia for the star and a spin-down torque.

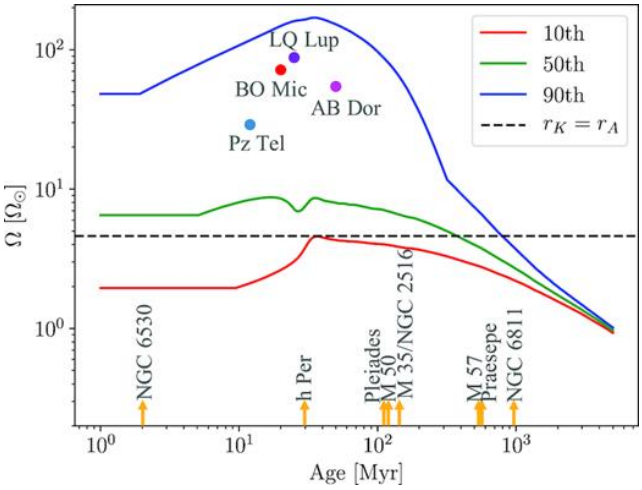

Figure 1.21: Plot taken from D'Angelo et al. 2019 [126], showing the rotation rate from their model for a fast (blue), medium (green) and slow (red) rotator, and stars on which prominences have been observed and the age is known.

This spin down torque is often taken to be the torque caused by the stellar wind, as was the case here, and there is no feedback mechanism by which these prominences can contribute to the spin-down rate. The authors showed that for around half of solar mass stars, they will support slingshot prominences into their main sequence, assuming their initial rotation rate was greater than $4.6\Omega_\odot$. For fast rotating stars, the age to which slingshot prominences could be supported was predicted to be about 800Myrs, with the prominences being most massive as the star reaches ZAMS at around 40Myrs.

The plot shows a few of the stars around which slingshot prominences have been observed, on this rotational evolution plot. All four of the stars are rapid rotators, between the 50th and 90th percentiles. The dashed line shows the age at which the stellar co-rotation radius equals the Alfven radius, and thus slingshot prominences could no longer form. They calculate this to be at $4.6\Omega_\odot$. The authors predict the prominence mass (m_p), mass loss rate ($\dot{m}_p$) and lifetime (τ_p) for both a medium and fast rotator, and compare these to the observations, the plot is shown in Figure 1.22.

Solar like stars are shown by circles and the M-dwarfs are included as squares.

The model predicted prominence masses could range from around 10^{16} to 10^{18}g, and the observations lie within this range for all stars except LQ Lup, for which the observed masses are considerably larger. The authors also predict prominence lifetimes of between 1 and 14 days, which is also consistent with observations.

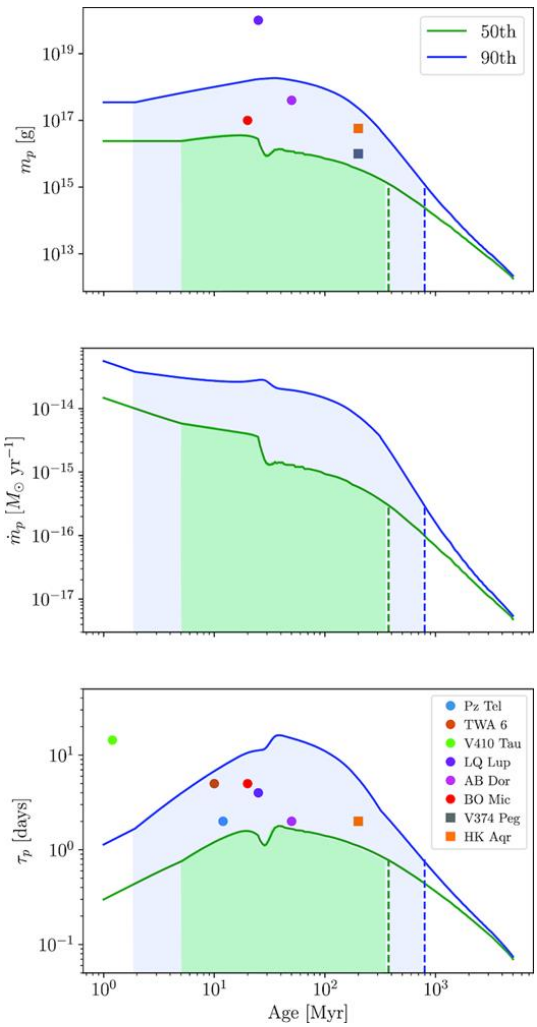

Figure 1.22: Plot taken from D'Angelo et al. 2019 [126], showing the prominence mass, mass loss rate and lifetime for a solar-like star's evolution.

1.8 This work

This thesis compiles work focused on modelling the locations of these prominences around low mass stars. Using various techniques, the locations around such stars in which prominences could be supported are found. The properties of these prominences are estimated (e.g. mass) and the consequences of the ejection of this material on the star and orbiting planets are investigated.

Chapter 2

Prominence modelling within the equatorial plane

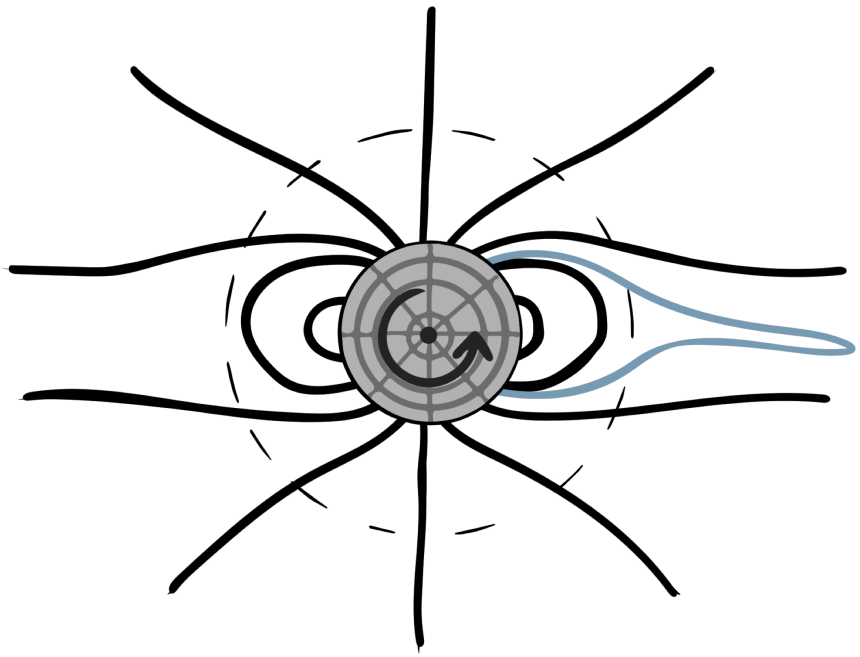

2.1 Introduction and background theory

This chapter is based on work published in Waugh et al. 2019[127].

This chapter investigates the mechanical equilibria available to magnetic loops in the coronae of rapidly rotating young stars. This model is 2-dimensional, within the equatorial plane of the star. These mechanical equilibria are found by instantaneously cooling a magnetic field line and solving for the new loop shape, assuming a hydrostatic, isothermal corona and the thin flux tube approximation. Cooled loops in mechanical equilibria are able to magnetically support dense regions of gas in the form of slingshot prominences. Three coronal (background) magnetic field structures are investigated; a dipole, a quadrupole and a dipole that becomes open field beyond a set radius. Equilibria are found in all three cases, with solutions being found in the open field (within the stellar wind) in the latter case. Equilibrium solutions can be found at all heights above the stellar surface for the closed field structures, but a gap in the distribution with height of solutions is found for a field structure that contains a source surface. In the case where the external field contains a source surface, the effect of moving the location of this surface is investigated with respect to the heights at which solutions may be found. Histograms are produced of the heights at which prominences may be formed and then compared to observations for two well-observed stars; AB Doradus and Speedy Mic. The model best reproduces the observed data when the source surface is placed above the co-rotation radius.

2.1.1 Previous models

This model aims to expand the model by Jardine and van Ballegooijen [77] into polar coordinates. Their model, discussed in the introduction, modelled the mechanical equilibria for cooled loops. These loops were set in a background field that was dipolar, but with a source surface (i.e. becoming open field at a set radius). The model used Cartesian coordinates, since the surface of the star was assumed to be flat. On a local level this is of course true, however, globally the surface of a star would be best represented as spherical (or circular in 2 dimensions). In this section, the model by Jardine and Van Ballegooijen is developed in polar coordinates, still within the equatorial plane of the star, such that the stellar surface is circular. The same overall behaviour is found here as in their model.

2.1.2 Momentum equation

Force balance on a fluid, for example plasma within a stellar corona, can be defined by the momentum equation:

$$\rho\left(\frac{\partial \mathbf{u}}{\partial t} + (\mathbf{u}.\nabla)\mathbf{u}\right) = -\nabla p + \mathbf{F}_{ext} \tag{2.1}$$

where $\mathbf{F}_{ext}$ is the summation of the external forces and p is the plasma pressure. In the case of a plasma in the presence of gravity it takes the form:

$$\rho\left(\frac{\partial \mathbf{u}}{\partial t} + (\mathbf{u}.\nabla)\mathbf{u}\right) = -\nabla p + (\mathbf{j} \times \mathbf{B}) + \rho\mathbf{g} \tag{2.2}$$

where $\mathbf{j}$ is the current density and $\mathbf{B}$ is the magnetic field. In hydrostatic equilibrium, the case of steady state with no flows, the left hand side of this equation is equal to zero.

$$\mathbf{0} = -\nabla p + (\mathbf{j} \times \mathbf{B}) + \rho\mathbf{g} \tag{2.3}$$

This is the form of the equation used throughout the project.

2.1.3 Equation of state

Alongside the momentum equation, an equation of state is required to define how the state of matter (in this case the coronal plasma) varies with conditions such as pressure, temperature of volume.

Here the ideal gas law is used, as the corona is assumed to be isothermal and hot. Whilst the classic form of the equation is

$$pV = NK_BT, \tag{2.4}$$

with p and V being gas pressure and volume, respectively. N is the number of molecules, K_B the Boltzmann constant and T the temperature. This can be rewritten into the form:

$$p = \frac{K_BT}{m}\rho \tag{2.5}$$

where m is the mean particle mass and ρ the density.

2.1.4 Effective gravity

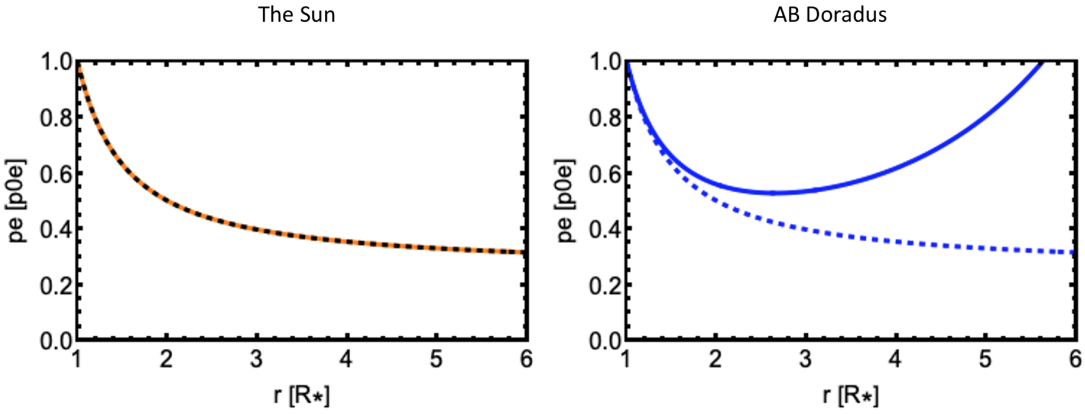

Figure 2.1: Plots showing the pressure variation with height for the Sun (orange) and AB Doradus (a rapidly rotating star) (blue). The lines where the centrifugal term is neglected are shown by dashed lines (shown in black for the Sun) and the line where the centrifugal term is included are shown as solid lines. Figure adapted from Waugh [128].

The observations of prominences on rapidly rotating stars suggest that these features co-rotate with the star, i.e. stay above the same point on the stellar surface as the star rotates. Therefore, when modelling these condensations, it makes sense to do so within the co-rotating frame. Within the equations, this can be encapsulated by defining the "effective

gravity", which encompasses the gravitational, Coriolis and centrifugal forces.

This first model developed in this thesis is restricted to the equatorial plane of the star, with no gas flows. This simplifies the centrifugal term and removes the Coriolis term. Thus, in this model the effective gravity is defined by:

$$\mathbf{g}_{rot} = -\frac{GM}{r^2}\hat{\mathbf{r}} + \omega^2 r\hat{\mathbf{r}} \tag{2.6}$$

Where M is the mass of the star, r is the radial distance from the star, ω is the stellar rotation rate and G is the gravitational constant. The full expression for the effective gravity can be found in Appendix A[129].

By analysis of Equation 2.6, it can be seen that there is a critical radius below which the effective gravitational force acts inwards, and beyond which it acts outwards. The critical point at which the gravitational and centrifugal forces balance is referred to as the "co-rotation radius":

$$r_k = \left(\frac{GM}{\omega^2}\right)^{1/3}. \tag{2.7}$$

On slow rotators like the Sun, which has a co-rotation radius of $37R_\odot$, the rotational term of the effective gravity can be neglected. The difference between rapid and slow rotators can be easily seen in Figure 2.1 showing the gas pressure with radius from the centre of the star. There is no need to account for the rotation on slow rotators like the Sun, whilst the effect of rotation on rapid rotators should not be neglected.

2.1.5 Magnetic topologies

Within this model, a background magnetic field must be prescribed in order to find the shapes of cooled loops that could support prominences. In this chapter, there are three field topologies that are used; a dipolar field, a quadrupolar field and a dipolar field with a source surface. All of these are embedded within the equatorial plane of the star in this model.

The simplest case used here is the dipolar field and can be described mathematically by

$$B_e^2 = B_{0e}^2\left(\left(\frac{2\cos\phi}{r^3}\right)^2 + \left(\frac{\sin\phi}{r^3}\right)^2\right). \tag{2.8}$$

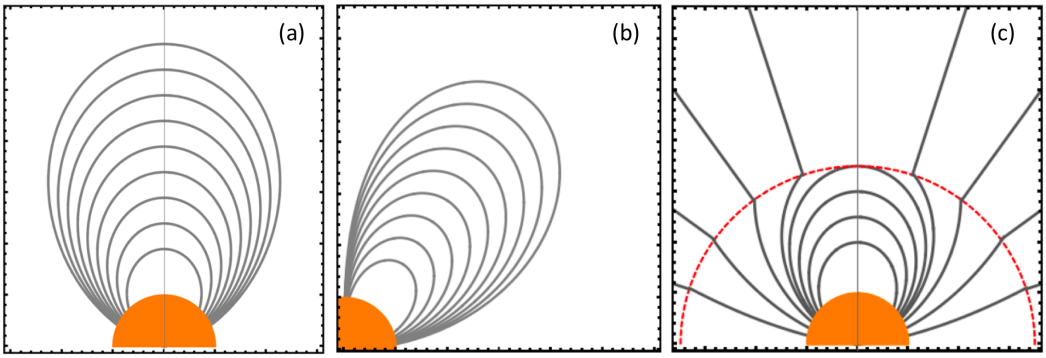

Figure 2.2: (a) Dipole field (b) quadrupolar field and (c) dipolar field with source surface, shown by the red dashed line.

The quadrupole field structure is defined by

$$B_e^2 = B_{0e}^2\left(\left(\frac{3(3\cos^2\phi - 1)}{2r^4}\right)^2 + \left(\frac{3\cos\phi\sin\phi}{r^4}\right)^2\right) \tag{2.9}$$

and the most complicated field used here is a dipolar field with a source surface, i.e. a dipolar field that becomes open beyond a critical radius, r_s:

$$B_e^2 = \begin{cases} B_{0e}^2\left(\left(\left(\frac{2\cos\phi}{r^3}\right)\left(\frac{r^3+2r_s^3}{1^3+2r_s^3}\right)\right)^2 + \left(\left(\frac{\sin\phi}{r^3}\right)\left(\frac{-2r^3+2r_s^3}{1^3+2r_s^3}\right)\right)^2\right) & \text{if } r < r_s \\ B_{0e}^2\left(\left(\left(\frac{2\cos\phi}{r^3}\right)\left(\frac{r^3+2r_s^3}{1^3+2r_s^3}\right)\right)^2\left(\frac{r_s}{r}\right)^4\right) & \text{if } r > r_s. \end{cases}$$

Here r and ϕ represent the polar coordinates, radius and longitude, B_{0e} is the (external) field strength at the base of the loop and these field structures are depicted in Figure 2.2.

2.1.6 The thin flux tube approximation

Flux tubes can be thought of as a tubular region in which the "walls" of the tube are always parallel to the magnetic field. Flux is conserved along the flux tube, thus the area of the tube varies throughout space according to the local field strength. The magnetic flux tubes here are assumed to be 'thin' and isothermal. Thin loops are those in which internal quantities, like pressure, do not vary across the flux tube width. This approximation therefore assumes that the flux tube area is much smaller than the pressure scale height squared. It is also assumed that the tube does not disturb the background coronal field [79, 130].

Flux tubes must be in pressure balance with their environment, i.e.

$$B_i^2 = B_e^2 + 2\mu(p_e - p_i) \tag{2.10}$$

where μ represents the permeability of free space, B is the magnetic field strength and p the gas pressure. The internal and external quantities are denoted with the subscripts i and e, respectively.

This equation can also be written in the form where it has been scaled to the external field strength at the loop base;

$$\frac{B_i^2}{B_{0e}^2} = \frac{B_e^2}{B_{0e}^2} + \frac{2\mu p_{0e}}{B_{0e}^2}(\frac{p_e}{p_{0e}} - \frac{p_i}{p_{0e}}) \tag{2.11}$$

$$\bar{B_i}^2 = \bar{B_e}^2 + \frac{2\mu p_{0e}}{B_{0e}^2}(\bar{p_e} - \bar{p_i}) \tag{2.12}$$

where $\bar{B_i}^2 \equiv B_i^2/B_{0e}^2$, $\bar{p_e} \equiv p_e/p_{0e}$ and $\bar{p_i} \equiv p_i/p_{0e}$.

The expression $2\mu p_{0e}/B_{0e}^2$ is the "plasma beta" for the external field at the base of the field line. The plasma beta is a ratio of the gas pressure to the magnetic pressure:

$$\beta_{0e} \equiv \frac{p_{0e}}{B_{0e}^2/2\mu}, \tag{2.13}$$

with a large plasma beta requiring that the gas pressure dominates over the magnetic pressure, and a small plasma beta requiring a stronger magnetic pressure than gas pressure.

In other words, the expression for pressure balance across a thin flux tube may be written as

$$\bar{B_i}^2 = \bar{B_e}^2 + \beta_{0e}(\bar{p_e} - \bar{p_i}), \tag{2.14}$$

throughout the remainder of this chapter the plasma beta β_{0e} is simply denoted by β.

2.1.7 Mechanical equilibria

Mechanical equilibrium is a state in which all forces present on an object are balanced and therefore the net force is zero. This has been introduced mathematically in Equation 2.3

and this subsection introduces in more detail the forces present.

The first term in the momentum equation ($\mathbf{0} = -\nabla p + (\mathbf{j} \times \mathbf{B}) + \rho\mathbf{g}$) is the gradient of the gas pressure. The gas pressure decreases with height from the stellar surface reaching a minimum at the co-rotation radius, before increasing again due to the centrifugal force. This was shown in Figure 2.1. In other words this force acts towards the surface at heights below co-rotation, and away from the surface at heights above co-rotation.

The second term in this equation is the Lorentz force, which can be decomposed into the magnetic tension and magnetic pressure forces.

$$(\mathbf{j} \times \mathbf{B}) = (\mathbf{B}.\nabla)\frac{\mathbf{B}}{\mu} - \nabla\Big(\frac{B^2}{2\mu}\Big). \tag{2.15}$$

The magnetic tension force $(\mathbf{B}.\nabla)\mathbf{B}/\mu$ always acts to straighten out field lines, acting inwards from the loop summit.

The magnetic pressure force $-\nabla\Big(B^2/(2\mu)\Big)$ acts to smooth out gradients in the magnetic field, just as a gradient of gas pressure does with mass. The magnetic pressure force acts from locations of high field strength to locations of low field strength. The direction of this force is more difficult to imagine, but in general, it will act outwards since field strength drops away with distance from the star.

The final force is the buoyancy force, $\rho\mathbf{g}$. The buoyancy force depends on both the local density and effective gravity. For a cool loop embedded in a hotter corona, it will be over-dense (i.e. $\rho_i - \rho_e > 0$) whilst hot loops embedded in a cooler corona will be under-dense ($\rho_i - \rho_e < 0$).
The effective gravity acts inwards below co-rotation and outwards above co-rotation, meaning that for cool loops the buoyancy force also acts inwards below co-rotation and outwards above co-rotation. For hot loops, the opposite would be true, with buoyancy acting outwards below co-rotation and inwards above co-rotation. Here however we only consider cool loops.

2.2 Setting up the equations: Force balance

In order to solve for the loop shapes, we first decompose the momentum equation into components along ($\hat{s}$) and perpendicular ($\hat{n}$) to the magnetic field line, using the same method as Jardine, Ballegoojien and Collier Cameron[76, 77].

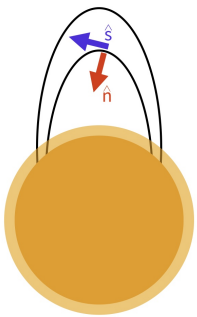

Figure 2.3: Splitting up the field line into components parallel (blue) and perpendicular (red) to the field line.

The line element along the field line in cylindrical coordinates is

$$ds\hat{s} = dr\hat{r} + rd\phi\hat{\phi} \tag{2.16}$$

where $ds = \sqrt{dr^2 + r^2 d\phi^2} = d\phi\sqrt{r^2 + (r')^2}$. The unit vectors can be defined as:

$$\hat{s} = \frac{1}{\sqrt{r^2 + (r')^2}}(r', r) \tag{2.17}$$

$$\hat{n} = \frac{1}{\sqrt{r^2 + (r')^2}}(-r, r'). \tag{2.18}$$

The pressure variation with height can be found by taking the component of the momentum equation along the field, and assuming the base pressure is independent of ϕ. This yields:

$$0 = -\nabla p.\hat{s} + (\mathbf{j} \times \mathbf{B}).\hat{s} + \rho\mathbf{g}.\hat{s} \tag{2.19}$$

but $(\mathbf{j} \times \mathbf{B}).\hat{s} = 0$ since $\mathbf{B} = B\hat{s}$ and thus $(\mathbf{j} \times \mathbf{B}).\hat{s} = B(\mathbf{j} \times \hat{s}).\hat{s} = 0$.

Thus, Equation 2.19 simplifies to:

$$0 = -\nabla p.\hat{s} + \rho \mathbf{g}.\hat{s}. \tag{2.20}$$

Evaluating:

$$(\frac{dp}{dr}\hat{r} + \frac{dp}{rd\phi}\hat{\phi}).(r'\hat{r} + r\hat{\phi})\frac{1}{\sqrt{r^2 + (r')^2}} = \rho\Big((-\frac{GM}{r^2} + \omega^2 r)\hat{r} + 0\hat{\phi}).(r'\hat{r} + r\hat{\phi})\frac{1}{\sqrt{r^2 + (r')^2}}\Big), \tag{2.21}$$

which simplifies to

$$\frac{dp}{dr} = g\rho. \tag{2.22}$$

Solving this for the gas pressure leaves:

$$\int_{p_0}^{p(r)} \frac{dp}{p} = \int_{R_*}^{\bar{r}R_*} \frac{m}{K_B T} g(r) dr \tag{2.23}$$

and so,

$$p = p_0 \exp\Big(\frac{m}{K_B T} \int_{R_*}^{\bar{r}R_*} g(r) dr\Big), \tag{2.24}$$

with p_0 being the pressure at the base of the loop, $p_0 \equiv p(R_*)$. Defining

$$H(r) \equiv \frac{m}{K_B T_e} \int_{R_*}^{\bar{r}R_*} \Big(-\frac{GM_*}{r^2} + \omega^2 r\Big) dr \tag{2.25}$$

simplifies this expression for the gas pressure into a more manageable equation:

$$p_e = p_{0e} \exp(H(r)). \tag{2.26}$$

The full expression for the pressure variation can be shown to be

$$p = p_0 \exp(\frac{m}{K_B T}\Big(\frac{GM(1-\bar{r})}{\bar{r}R_*} + \frac{\omega^2 R_*^2(\bar{r}^2 - 1)}{2}\Big), \tag{2.27}$$

where $\bar{r}$ is the radial distance from the stellar centre in units of stellar radii. In the work below, $\bar{r}$ is replaced with r to make the equations easier to read.

Normal to the magnetic field, the momentum equation is:

$$0 = -\nabla p.\hat{n} + \Big((\mathbf{B}.\nabla)\frac{\mathbf{B}}{\mu} - \nabla\Big(\frac{B^2}{2\mu}\Big)\Big).\hat{n} + \rho \mathbf{g}.\hat{n} \tag{2.28}$$

Using $\mathbf{B} \equiv B\hat{s}$ and noting that $\hat{s}.\hat{n} = 0$ leaves;

$$0 = -\nabla p.\hat{n} + \frac{B^2}{\mu}\Big((\hat{s}.\nabla)\hat{s}\Big).\hat{n} - \nabla\Big(\frac{B^2}{2\mu}\Big).\hat{n} + \rho \mathbf{g}.\hat{n}. \tag{2.29}$$

Noting that:

$$\hat{\mathbf{n}}.\nabla = \frac{1}{\sqrt{r^2 + (r')^2}}\Big(- r\frac{\partial}{\partial r} + r'\frac{\partial}{\partial \theta}\Big) \tag{2.30}$$

and

$$\frac{\partial \hat{s}}{\partial s} = (\hat{s}.\nabla)\hat{s} = \frac{\hat{n}}{R_c} \tag{2.31}$$

where R_c is the radius of curvature. This is a standard result, where the expression for the radius of curvature is given by

$$R_c = \frac{(r^2 + (r')^2)^{3/2}}{(rr'' - r^2 - 2(r')^2)}. \tag{2.32}$$

A full derivation for equation 2.32 is given in Appendix B. Ultimately, equation 2.29 simplifies to:

$$\frac{2B_i^2 r(r^2 + 2(r')^2 - rr'')}{(r^2 + (r')^2)} = \Big(-r^2\frac{\partial}{\partial \theta} + r'\frac{\partial}{\partial r}\Big)B_i^2 \tag{2.33}$$

which is the differential equation that must be solved to find the new, cooled magnetic loop shapes, $r(\phi)$.

2.3 Pressure variation with height

As mentioned in the introduction to this section, the pressure variation with height is defined by Equation 2.27.

$$p = p_0 \exp\Big(\frac{m}{K_B T}\Big(\frac{GM(1-r)}{rR_*} + \frac{\omega^2 R_*^2(r^2-1)}{2}\Big)\Big), \tag{2.34}$$

This term describes the external and internal pressures, although the base pressure and temperature may vary between the two. Therefore the pressure variation shows the same behaviour internally and externally, decreasing above the surface to the co-rotation radius

and then increasing beyond this[1], although the rate at which the pressure varies is steeper for the cooled internal loops than the background corona.

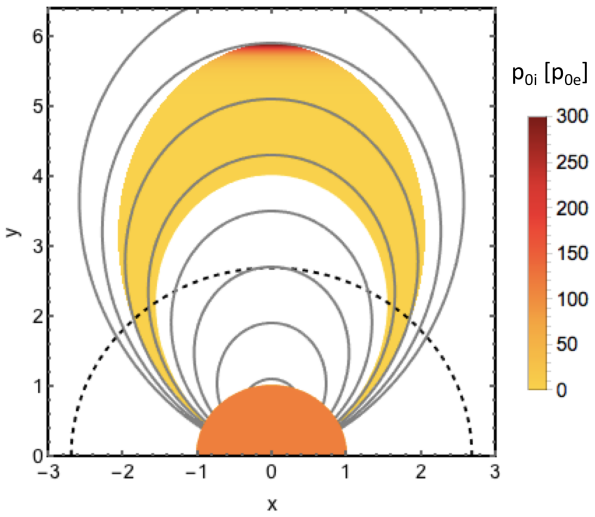

Figure 2.4: Example of the pressure variation within a cooled flux tube.

Figure 3.3 shows an example of the pressure variation with height assuming AB Doradus stellar parameters. It becomes apparent that on rapidly rotating stars such as this, the gas is driven into the tops of magnetic loops a few stellar radii above the surface.

Whilst the internal and external gas pressures do not depend on each other, the internal pressure is constrained by the pressure in the corona. The expression for the internal magnetic field,

$$B_i^2 = B_e^2 + 2\mu(p_e - p_i) \tag{2.35}$$

places constraints on the internal gas pressure. B_i^2 must always be greater than or equal to 0, i.e.

$$p_i \geq B_e^2/(2\mu) + p_e. \tag{2.36}$$

This places constraints on the maximum loop height, since at some height this constraint will likely not be met. This is discussed in more detail in Section 2.5.

[1] As was seen in the right hand panel of Figure 2.1.

2.4 Loop Shapes

By solving the differential equation (Equation 2.33 in Section 2.2), the shape of the cooled loops can be found and plotted. For most external loops within the background field, there is an available equilibrium for the loop to take if it were cooled to a chosen temperature. This yields a family of solutions, i.e. equilibria for loops of all heights. Equilibria are parameterised by their "heights" and "widths". The height of a loop is measured from the surface to the loop summit, and the width is measured from the loop footpoint to the centre of the loop (this is depicted in Figure 2.5 for clarity). Width here is measured as an angle.

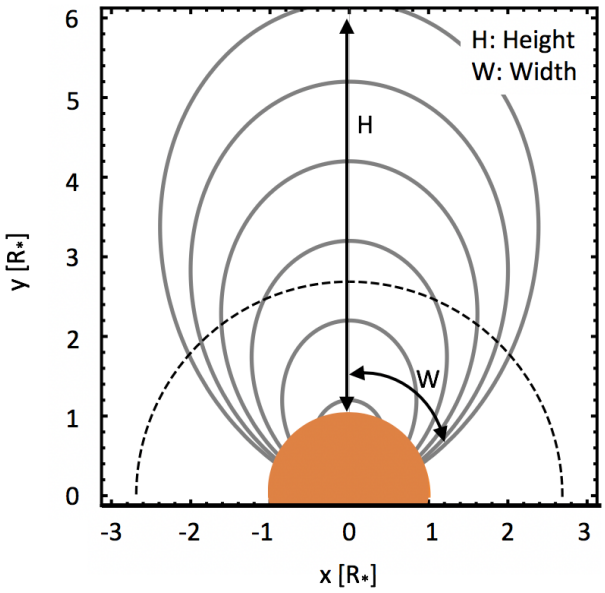

Figure 2.5: Cartoon to define loop "height" and "width" used here.

2.4.1 Pure Multipoles

Equation 2.33 can be solved once the chosen external field structures are combined with pressure balance, and the following parameters specified: internal and external temperatures; base pressures and the plasma beta. Figures 2.6 and 2.7 show the loop shapes and height-width curves for an external field of a pure dipole and pure quadrupole, respectively[2]. It is worth highlighting here that these solutions do not all exist within the corona at once (evidenced by the blue field lines that cross each other in the left hand panel of Figure 2.6) but that they have all been shown here as a "family". The field strength in these calculations

[2]Recall that here "Width" refers to the half-width of the loop, i.e. measured from the loop summit to one of the footpoints.

is scaled to the external field strength at the stellar surface. The external loops are shown in grey with the cooled solutions shown in blue. The presence of the cooled plasma does not alter the loop shape at low heights but distorts the loops with a summit at large distances from the stellar surface. This distortion is caused by the increasing pressure with height beyond the co-rotation radius. The height-width curves show the entire family of solutions and the cooled family follow the external field very closely at low heights. At large heights the distortion can be seen in the height-width plots by the sudden veering off of the curve from the external field track and towards the vertical axis. With the parameters used here, the distortion of loops occurs very suddenly, with a small change in loop height causing a drastic change in loop width (and therefore shape). The height-width curve does not track fully back to the vertical axis, because the final solutions become increasingly more difficult to find with summit height. This occurs due to the sudden changes in loop shape at this point on the curve, with a very small change in height resulting in a large change in loop shape. This makes resolving the last solutions tricky since large resolution is required to sample the final heights.

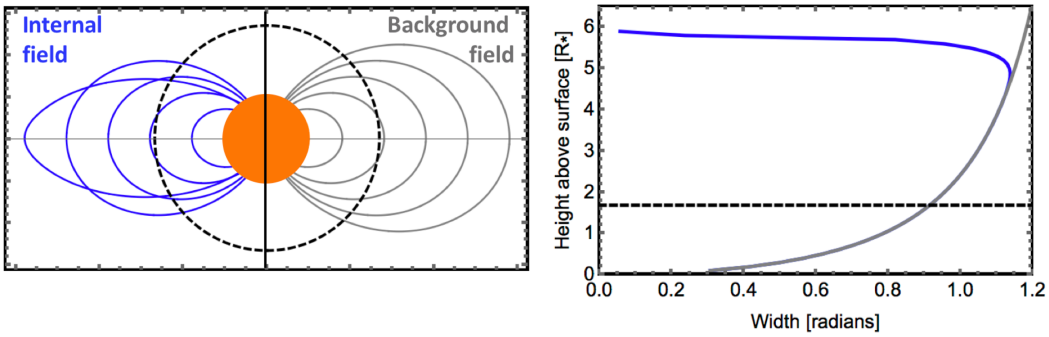

Figure 2.6: Loop shapes and height-width curves for a pure dipolar external field with parameters; $T_e = 10^7 K$, $T_i = T_e/10$, $p_{0i} = 2p_{0e}$ and $\beta = 10^{-7}$. The black dashed line represents the co-rotation radius.

For a pure quadrupolar external field the same behaviour is seen as for the dipolar case, with the cooled solutions matching the external field at low heights and adjusting shape at large heights to account for the large gas pressure compared to the local field strength. However, the loops cover a significantly smaller angular extent, constrained now to $\pi/4$ rather than $\pi/2$.

The lowest order multipoles examined here show slight variations in the maximum loop

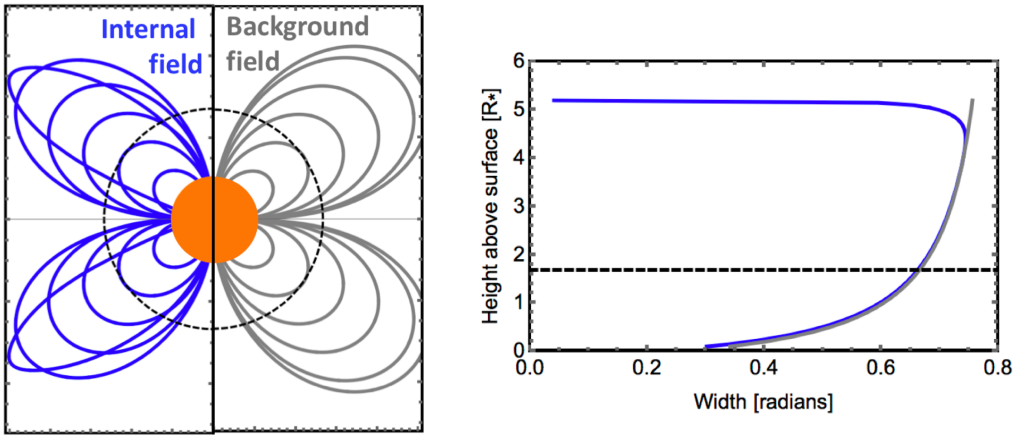

Figure 2.7: Loop shapes and height-width curves for a pure quadrupolar external field with parameters; $T_e = 10^7 K$, $T_i = T_e/10$, $p_{0i} = 2p_{0e}$ and $\beta = 10^{-7}$. The black dashed line represents the co-rotation radius.

heights, with $r = 5.98R_*$ and $r = 5.34R_*$ for the dipolar and quadrupole respectively. This maximum height mentioned here is determined by the height at which the loop becomes infinitely thin, i.e. the height-width curve reaches a width of 0 radians. This can be found by extrapolating the height-width curve to the vertical axis, or analytically, as discussed in section 2.5. Since the quadrupolar field dies off more quickly with height than the dipole, a lower maximum height for a quadrupole is to be expected. This difference in height is so small that this model predicts it to be unlikely that observations of prominence height alone would be able to determine the topology of the loop. It is important to note that this maximum height is very dependent on the input parameters of the model, which can not be obtained from observational data such as; p_{0e}, p_{0i}, β. The loops become infinitely thin in width once the magnetic field is no longer strong enough to support the increasing pressure being driven up into the loop summits.

2.4.2 Inclusion Of A Source Surface To A Pure Dipole

Prominences have been observed on AB Dor at heights of 8 stellar radii from the stellar rotation axis. The coronal magnetic field may not be closed at such large heights above the stellar surface. It may be more realistic to prescribe a background field that becomes open at a chosen radius.

Figures 2.8 and 2.9 show results for this field structure, with the source surface depicted by the red dashed lines. Results are shown for a source surface placed above the co-rotation

radius and below the co-rotation radius. Prescribing this background field yields ultimately similar behaviour to the pure dipolar field, with the family of cooled solutions following the external family at low heights and deviating from them at larger heights above the surface. Note that here the values for the plasma beta and base pressures have been changed from the plots shown in the multipole section, in which the plasma beta was set to a very small value to exaggerate the results for the purposes of illustration. Here the value chosen for the plasma beta is likely a more realistic value, since the higher value of β reflects a lower field strength.

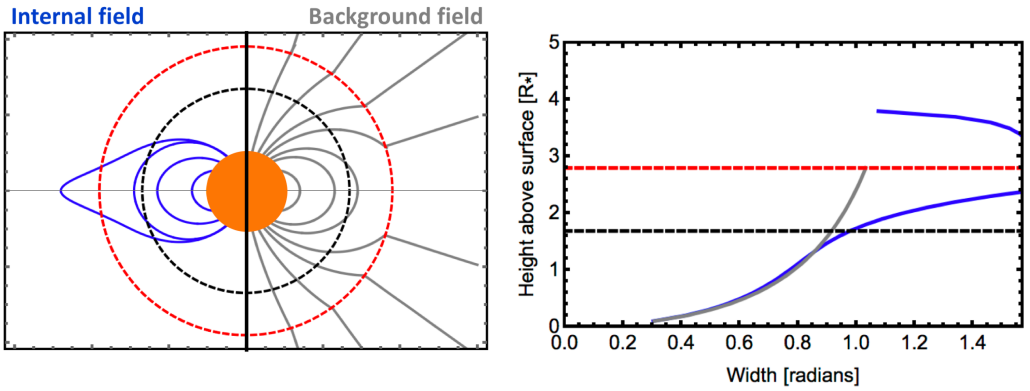

Figure 2.8: Loop shapes and height-width curves for a dipolar external field with source surface at $r_s = 3.8R_*$ with parameters; $T_e = 10^7 K$, $T_i = T_e/10$, $p_{0i} = 11 p_{0e}$ and $\beta = 10^{-3}$. The black dashed and red dashed lines represents the co-rotation radius and source surface, respectively.

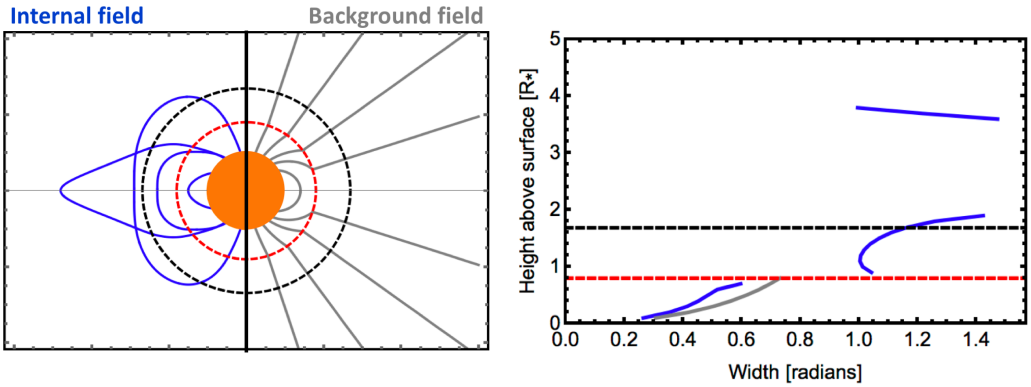

Figure 2.9: Loop shapes and height-width curves for a dipolar external field with source surface at $r_s = 1.8R_*$ with parameters; $T_e = 10^7 K$, $T_i = T_e/10$, $p_{0i} = 11 p_{0e}$ and $\beta = 10^{-3}$. The black dashed and red dashed lines represents the co-rotation radius and source surface, respectively.

With the source surface above the co-rotation radius, the height-width curve of the cooled solutions follows the external field closely at low heights before extending beyond the external arcade in order to maintain force balance at the co-rotation radius. Solutions can be found beyond width = $\pi/2$ radians, but they have been discounted on the grounds that they are unphysical. Any loop with footpoints that are more than π radians (width of $\pi/2$ radians) apart have footpoints that have crossed over to the other side of the star and over the poles. This results in a gap in the solutions around the source surface (red dashed line in the plots) where the loops can not expand enough to allow the tension force to balance the other forces present, thus no mechanical equilibrium may be reached for these heights. Beyond the source surface, solutions are found that represent solutions within the stellar wind. Here the external field is open, but there are mechanical equilibria available for closed cooled loops. This result was also found in the Cartesian geometry by Jardine and van Ballegooijen [77]. Once again, it is very mathematically challenging to find solutions that extend the height-width curves all the way back to the vertical axis. Here a very small change in height will result in a large change in width, due to the steep gradients in pressure relative to the magnetic support available.

With the source surface below the co-rotation radius as shown in Figure 2.9, solutions are more difficult to find. Once again, the cooled solutions match the external field well at low heights, but their shape deviates from the background field much sooner than the case with the source surface above the co-rotation radius. There are now three branches of solutions; (1) solutions at low heights within the closed field, (2) solutions above the source surface and within the wind, where the loops are still expanding with height and (3) solutions well above the co-rotation radius where loops are becoming thinner with height. The overall behaviour is similar to the previous cases shown in this chapter, though the solutions are much more broken up and more distinct from the background field.

2.4.3 Combining Multipoles

The cases of a pure dipole (B_d) or quadrupole (B_q) can be combined to create a more realistic stellar field:

$$B_e^2 = \left(B_d^2 + B_q^2 \right) \tag{2.37}$$

$$B_d^2 = \left(B_{0d}^2 \left[\left(\frac{2\cos(\phi)}{r^3} \right)^2 + \left(\frac{\sin(\phi)}{r^3} \right)^2 \right] + B_{0q}^2 \left[\left(\frac{3(3\cos^2(\phi)-1)}{2r^4} \right)^2 + \left(\frac{3\cos(\phi)\sin(\phi)}{r^4} \right)^2 \right] \right)$$

$$B_q^2 = B_{0e}^2 \left[\left(\frac{2\cos(\phi)}{r^3} \right)^2 + \left(\frac{\sin(\phi)}{r^3} \right)^2 + \left(\frac{3(3\cos^2(\phi)-1)}{2r^4} \right)^2 + \left(\frac{3\cos(\phi)\sin(\phi)}{r^4} \right)^2 \right]. \quad (2.38)$$

Here, for simplicity, the components are combined so that the dipole and quadrupole are equal in strength at the stellar surface (i.e. $B_{0d}^2 = B_{0q}^2 \equiv B_{0e}^2$).

Figure 2.10 shows example loop shapes and height-width curves for this combined field structure (blue) compared to a pure dipole (grey). Most variation in loop shape is seen at low heights since the quadrupolar term dies off more quickly than the dipolar term and leaves loops at large heights more similar to a pure dipole.

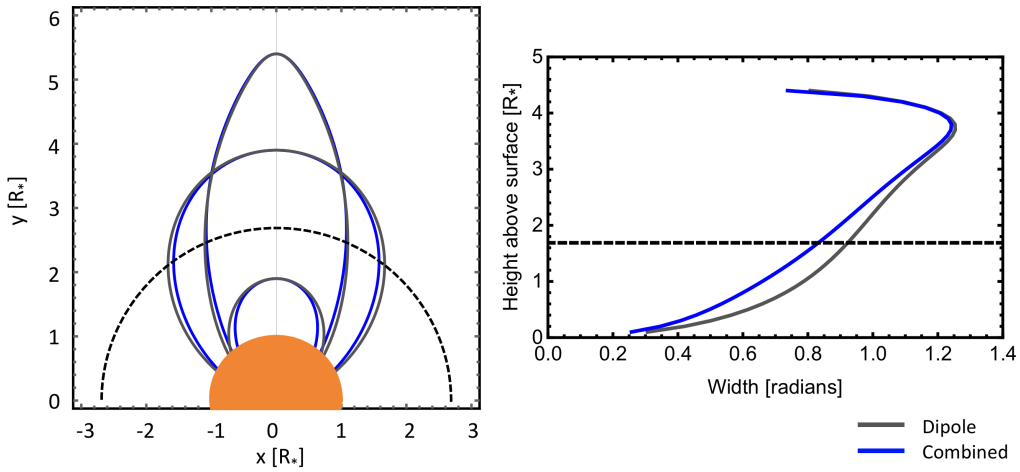

Figure 2.10: Loop shapes and height-width curve for a combined dipolar and quadrupolar external field, with parameters; $T_e = 10^7 K$, $T_i = T_e/10$, $p_{0i} = 3p_{0e}$ and $\beta = 10^{-4}$, shown in blue. A pure dipole at the same parameters is shown in grey for comparison. The black dashed line represents the co-rotation radius.

2.5 Maximum Loop Height

The maximum height of the cooled loops can be calculated starting from the condition that

$$B_i^2 \geq 0 \tag{2.39}$$

and considering the case where the internal field strength drops to zero. The internal magnetic field strength squared can not be negative and still be physical. Using the expression for pressure balance;

$$\bar{B_e}^2 + \beta(\bar{p_e} - \bar{p_i}) = 0 \tag{2.40}$$

and expanding out the terms gives

$$\frac{B_e^2}{B_{0e}^2} + \beta\Big(e^{(H(r))} - \frac{p_{0i}}{p_{0e}} e^{(H(r)\frac{T_e}{T_i})}\Big) = 0. \tag{2.41}$$

Solving this expression for r with the prescribed external field gives the maximum loop height for which the cool magnetic field gives a physical result.

2.5.1 Dipole

Prescribing a dipole external field and considering the summit of each loop ($\phi = \pi/2$) where the loop has its maximum radial value, gives the condition:

$$\frac{4(\cos\pi/2)^2 + (\sin\pi/2)^2}{r^6} + \beta\Big(e^{(H(r))} - \frac{p_{0i}}{p_{0e}} e^{(H(r)\frac{T_e}{T_i})}\Big) = 0 \tag{2.42}$$

which simplifies to

$$\frac{1}{r^6} + \beta\Big(e^{(H(r))} - \frac{p_{0i}}{p_{0e}} e^{(H(r)\frac{T_e}{T_i})}\Big) = 0, \tag{2.43}$$

and therefore, r_{max} is a function of p_{0i}/p_{0e}, T_i/T_e, β, M_*, R_* and ω.

2.5.2 Quadrupole

Prescribing a quadrupole external field and considering the summit of each loop ($\phi = cos^{-1}(1/\sqrt{3})$) [131] gives the condition:

$$\frac{9(3((1/\sqrt{3})^2 - 1)^2}{4r^8} + \frac{9(1/\sqrt{3})^2(\sin(\arccos(1/\sqrt{3})))^2}{r^8} + \beta\Big(e^{(H(r))} - \frac{p_{0i}}{p_{0e}} e^{(H(r)\frac{T_e}{T_i})}\Big) = 0 \tag{2.44}$$

which simplifies to

$$\frac{12}{4r^8} + \frac{2}{r^8} + \beta\Big(e^{(H(r))} - \frac{p_{0i}}{p_{0e}} e^{(H(r)\frac{T_e}{T_i})}\Big) = 0 \tag{2.45}$$

leaving

$$\frac{5}{r^8} + \beta\Big(e^{(H(r))} - \frac{p_{0i}}{p_{0e}} e^{(H(r)\frac{T_e}{T_i})}\Big) = 0. \tag{2.46}$$

2.5.3 Dipole With Source Surface

As for the pure dipole and quadrupole cases, with the inclusion of a source surface there will be a maximum height beyond which there are no possible solutions. Again, this corresponds to the point at which B_i^2 goes to zero. Recall that the expression for this field structure can be written as;

$$\frac{B_e^2}{B_{0e}^2} = \begin{cases} \left(\left(\frac{2\cos\phi}{r^3}\right)\left(\frac{r^3+2r_s^3}{1^3+2r_s^3}\right)\right)^2 + \left(\left(\frac{\sin\phi}{r^3}\right)\left(\frac{-2r^3+2r_s^3}{1^3+2r_s^3}\right)\right)^2 & \text{if } r < r_s \\ \left(\left(\frac{2\cos\phi}{r^3}\right)\left(\frac{r^3+2r_s^3}{1^3+2r_s^3}\right)\right)^2 \left(\frac{r_s}{r}\right)^4 & \text{if } r > r_s. \end{cases}$$

where the equation has been scaled to the base value.

If we wish to find the maximum loop height that can be found, and using the knowledge that loops could be found out in the open field region, the field structure outside of the source surface is the term of importance i.e.

$$\frac{B_e^2}{B_{0e}^2} = \left(\left(\frac{2\cos\phi}{r^3}\right)\left(\frac{r^3+2r_s^3}{1^3+2r_s^3}\right)\right)^2 \left(\frac{r_s}{r}\right)^4 \tag{2.47}$$

Once again, $Bi^2 = 0$ gives the maximum height of the cooled solutions, which is evaluated at $\phi = \pi/2$, i.e. the loop summit:

$$\frac{B_i^2(\phi = \pi/2)}{B_{0e}^2} = 0. \tag{2.48}$$

Noting that $B_e^2(\phi = \pi/2) = 0$, since $cos(\pi/2) = 0$, leaves

$$\frac{B_i^2}{B_{0e}^2} = \beta\Big(\frac{p_e}{p_{0e}} - \frac{p_i}{p_{0e}}\Big) \geq 0. \tag{2.49}$$

This shows that the maximum loop height in such a case is independent of the position

of the source surface. In full, the equation can be written as

$$e^{\left(H(r)\right)} - \frac{p_{0i}}{p_{0e}} e^{\left(H(r)T_e/T_i\right)} = 0, \tag{2.50}$$

and it can be seen that this depends on the stellar parameters, through the function $H(r)$, and the ratio of gas base pressures. Since the internal temperature is only a scaling factor on the exponential, it doesn't determine the root of the function $(p_e - p_i)$. It is also independent of β.

2.5.4 The effect of varying the coronal parameters

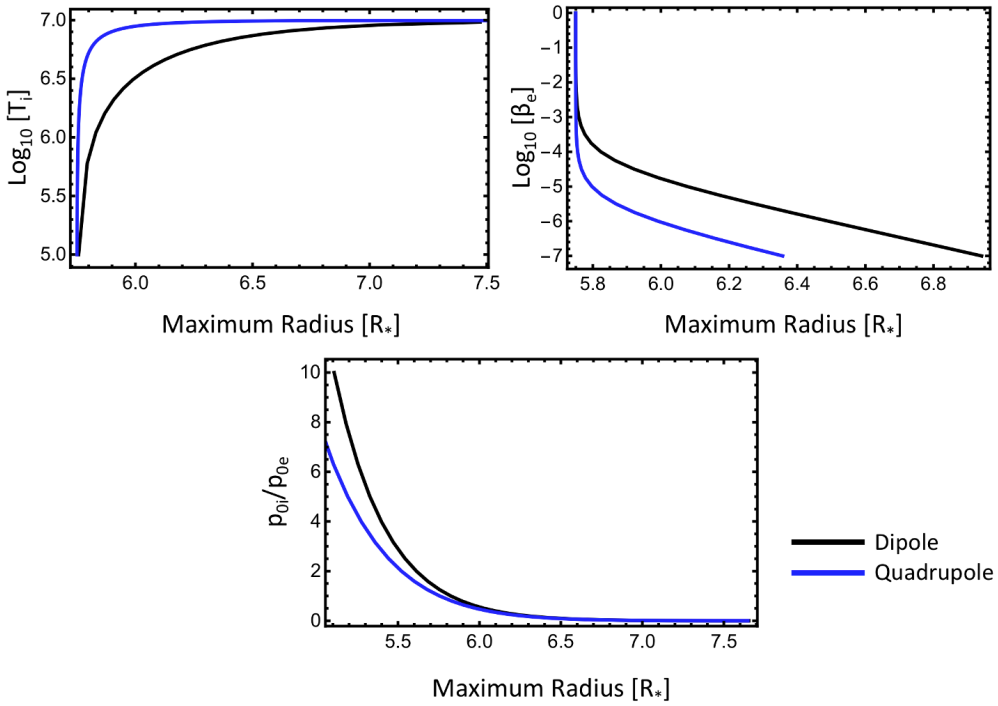

Figure 2.11: Maximum height for cool loops with various parameters; internal base pressure (scaled to external base pressure), internal temperature and external plasma beta. The parameters chosen here were $T_i = T_e/10 = 10^6 K$, $\beta = 10^{-4}$ and $p_{0i} = p_{0e}$, before each was varied whilst keeping the other two fixed. The blue curves show the quadrupolar field and black show the dipolar field.

Here the effect of coronal parameters is investigated on the maximum heights of prominence bearing loops, for a pure dipolar or quadrupolar external field structure. Solving Equations 2.43 and 2.46 for r, yields the maximum loop height for a given star (i.e. for a given stellar mass, radius and rotation rate, all of which are hidden within $H(r)$) and for given values of the input parameters β, p_{0i}/p_{0e} and T_e/T_i. Figure 2.11 shows the maximum

radius of solutions for the star AB Doradus over a set of coronal parameters[3]. In all cases, the maximum attainable height is lower for the quadrupolar external field (blue) than for the dipolar external field (black). As the quadrupole field falls off with height considerably quicker than the dipole field, this is to be expected.

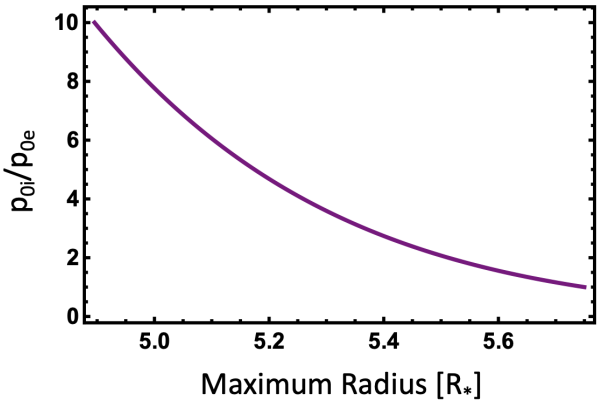

Figure 2.12: Maximum height for cool loops for a source surface field structure with varying internal base pressure (scaled to external base pressure).

In the case where the external field is a dipole with a source surface, the maximum height is independent of the plasma beta or temperature ratio (see Equation 2.50). The coronal parameter that influences the maximum prominence height is the ratio of gas pressures. This is shown in Figure 2.12. The equation for the maximum height also shows that the maximum height is independent of the location of the source surface.

2.6 Prominence Distributions

From this model, a distribution of prominence locations can be calculated and compared to the observations. The blue and green histograms in Figures 2.13 and 2.14 show the observed distribution of prominence heights on the stars AB Dor.[1, 25, 31, 33] and Speedy Mic.[36] respectively. The co-rotation radius is also shown on these plots by the black dashed line, and the source surface locations by the red dashed lines. Histogram data produced by the model are shown overlain in grey. These are generated by sampling the height-width curve in intervals of $0.2R_*$ in width. The stellar parameters used are; $M_* = 0.87M_\odot$, $R_* = 0.96R_\odot$

[3]Where radius = height + 1 $R_\star$.

and a period of 0.52 days for AB Dor. [132–134] and for Speedy Mic.; $M_* = 0.82M_\odot$, $R_* = 1.06R_\odot$ and a period of 0.380 days[36].

2.6.1 Placing the source surface above the co-rotation radius

Figure 2.13 shows the buoyancy force and height-width plots, for both AB Dor and Speedy Mic, in the top panels. The dashed line shows the results for the hotter temperature of $T_i = 1 \times 10^6$K and the thick line shows $T_i = 0.67 \times 10^6$K.

The buoyancy force on Speedy Mic changes more quickly with height than on AB Dor. This is due to the faster rotation rate of Speedy Mic. The buoyancy force is important for supporting the slingshot prominences, at large heights from the stellar surface and thus the difference in buoyancy between the two stars is reflected in the prominence height distributions. In order for a solution to be available, all forces on the loop must balance. At large heights above the surface and in the open field region especially, the magnetic pressure term is small. The magnetic tension and buoyancy forces must counteract each other for an equilibrium to be available. The height-width plots are much tighter for Speedy Mic than AB Dor, due to this difference in buoyancy.
A cooler loop temperature also causes steeper changes in buoyancy, which can be seen in the difference between the solid and dashed lines of this figure, and thus alters the shape of the height-width plots. Despite temperature playing a role in the height-width curve shape, the stellar parameters play a much more significant role as can be seen by the difference between the two stars.

For both stars, the histograms generated from this model show a similar shape with both temperatures shown here. Whilst the exact values on the histogram don't match the observations, the overall trends show similar behaviour. The model generates a peak in the histogram above co-rotation but below the source surface, and a secondary peak beyond the source surface. The model histograms also show a peak below co-rotation and close to the stellar surface. These would represent solar-like prominences, and do not appear in the observations. It could be that they are not present on these stars, or that they did not show up in the observations due to their low masses and therefore low absorption. Alternatively,

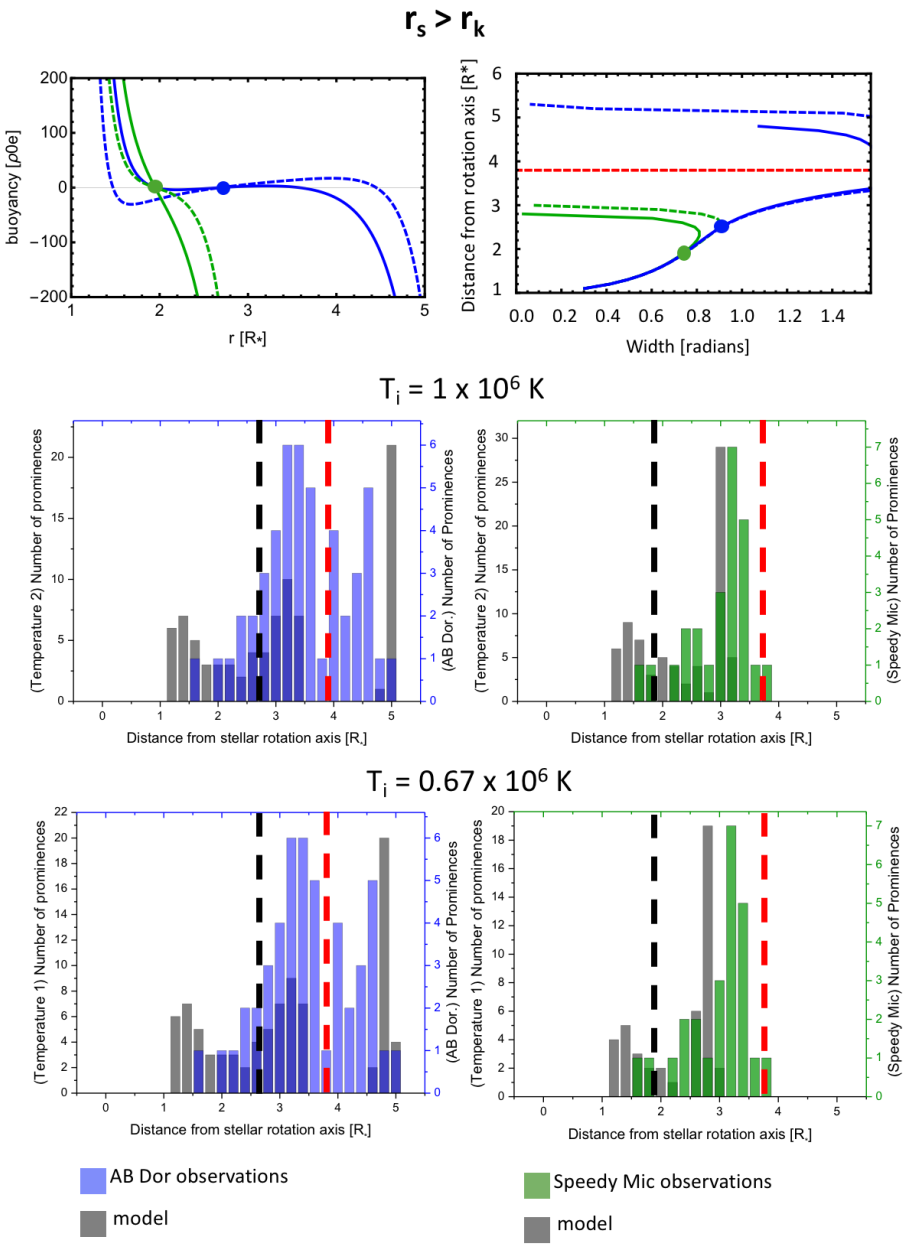

Figure 2.13: Prominence distributions for $r_s > r_k$ at $T_i = T_e/10$ and $r_s > r_k$ at $T_i = T_e/15$ for AB Dor and Speedy Mic. Grey shows the distributions calculated from this model whilst blue and green show the observed distributions for AB Dor and Speedy Mic, respectively. The black dashed lines show the co-rotation radius and the red dashed lines show the radius of the source surface.

they may have been difficult to distinguish from variations on the stellar surface, such as star spots or darker regions.

The trends of the modelled histograms match the observations for AB Dor slightly better

for the lower of the two temperatures, where the height-width curve is less flat above the source surface. This creates a smoother peak in the histogram. However, the temperatures otherwise yield similar histogram shapes. For Speedy Mic, neither of the modelled histograms appears to fit too well to the observations, but the hotter of the two temperatures appears to give the better distribution. This choice of source surface location allows for prominences to form in the wind of AB Dor. For Speedy Mic this is not the case, as the stellar parameters mean the buoyancy force quickly becomes too large to be supported by the magnetic tension and pressure forces. This means that the maximum height of prominence formation is below this choice for the source surface, making equilibria in the wind an impossibility. With a different choice of parameters, it should be possible to find solutions in the wind for Speedy Mic too. However, this is not found here with these parameter choices.

2.6.2 Placing the source surface below the co-rotation radius

Figure 2.14 shows the buoyancy force and height-width plots, for both AB Dor and Speedy Mic, in the top panels for a cooled temperature of $T_i = 0.67 \times 10^6$K. The height-width plots for both AB Dor and Speedy Mic are much more limited than with the source surface placed above co-rotation. At low heights, the curves are almost identical for the two stars, where the magnetic field is strong and the difference in rotation is not yet felt. The top branch in the case of AB Dor is very similar to with $r_s > r_k$, but for Speedy Mic the top branch no longer exists. Finding solutions at these heights, just beyond the source surface is difficult once below co-rotation. Around co-rotation there is little to no buoyancy force, since the effective gravity is close to zero. When this occurs within the open field, there is very little magnetic pressure force to provide support because the field has become suddenly radial. This leaves nothing to balance the magnetic tension force and so finding equilibria is difficult to impossible. It is possible that with a different choice of parameters solutions within this region might be easier to find. However, in all of the parameters that I have searched, these solutions have been hard to find.

The histograms generated in this case do not match the observed histograms as well as the previous case. The peak that occurs at very low heights, which is not present in the observations, is much larger than before. The model generates a peak beyond co-rotation, however, for AB Doradus it appears to be too close to the co-rotation radius when compared

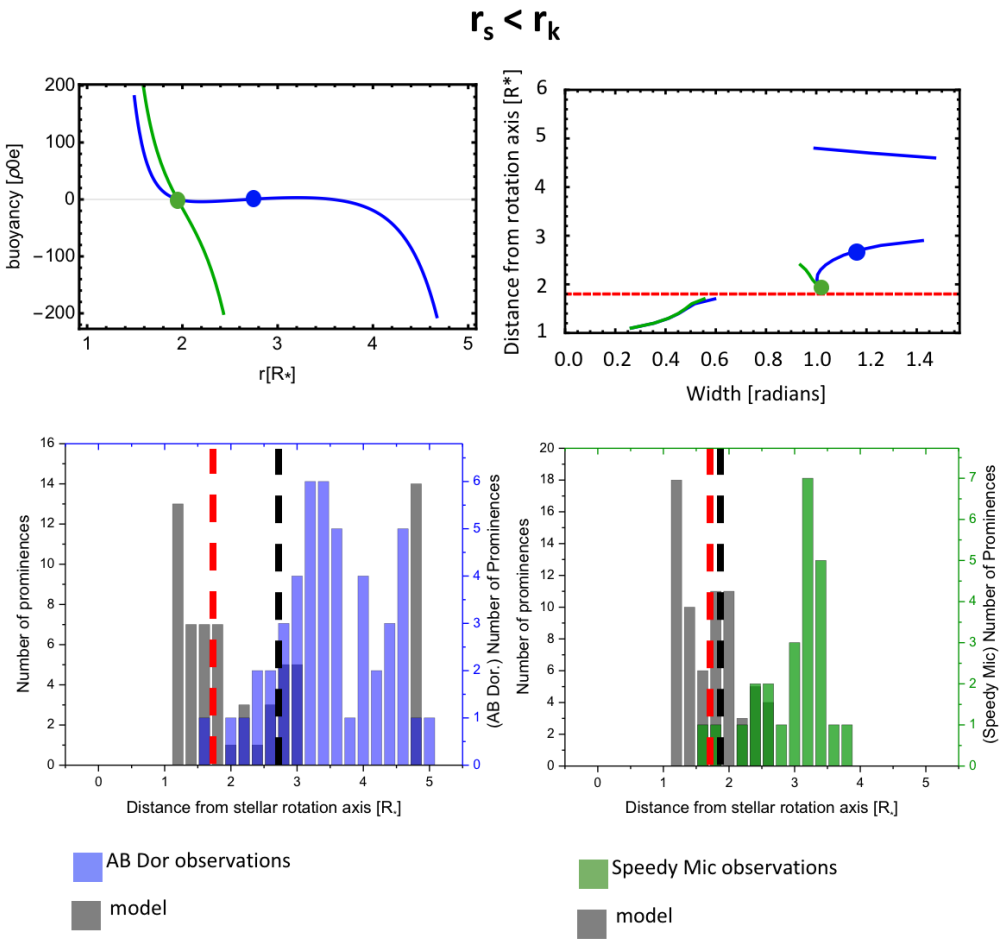

Figure 2.14: Prominence distributions for $r_s < r_k$ at $T_i = T_e/10$ for AB Dor and Speedy Mic. Grey shows the distributions calculated from this model whilst blue and green show the observed distributions for AB Dor and Speedy Mic, respectively. Black dashed lines show the co-rotation radius and red dashed lines show the radius of the source surface.

to the observations. The peak at very large heights is much more sudden than in the observations. For Speedy Mic, the peak at low heights is again much larger than previously. A peak does appear at $2.5R_\star$ which matches the observations, but there is also a peak directly after co-rotation that is not present in observations. The peak observed at larger heights does not occur in this model.

2.6.3 Comparison to observations for AB Dor.

Of the modelled histograms presented here, the field structure with $r_s > r_k$ and temperature $T_i = 0.67 \times 10^6$K appears the most similar to the observations. With this said, the histogram

given here for the observed data has been collated from many years worth of observations. The magnetic field structure for AB Doradus has not been constant over this time. The modelled histograms have assumed all solutions are at the same temperature and magnetic field strength, but there is no requirement for this to be true in the stellar corona. This is examined briefly in section 2.6.5.

The observed distribution shows a trend of two peaks. The first peak slowly increases to a maximum at around $3.2R_\star$ and drops away suddenly by $4R_\star$. The second peak begins around here and appears to peak just after $4.5R\star$.

2.6.4 Comparison to observations for Speedy Mic.

The observational data for the prominences on Speedy Mic are all taken from one observing run, over which the background magnetic field structure will have been constant. The parameters of $r_{ss} > r_k$ and $T_i = 1 \times 10^6$K appear to generate a distribution that fits the observations better than the other parameters used here. The observational distribution shows two peaks, one just beyond the co-rotation radius and one at larger heights and centred around $3.3R_\star$ from the centre of the star. Unlike for AB Doradus, this secondary peak appears to be much larger than the first.

2.6.5 A more complex corona

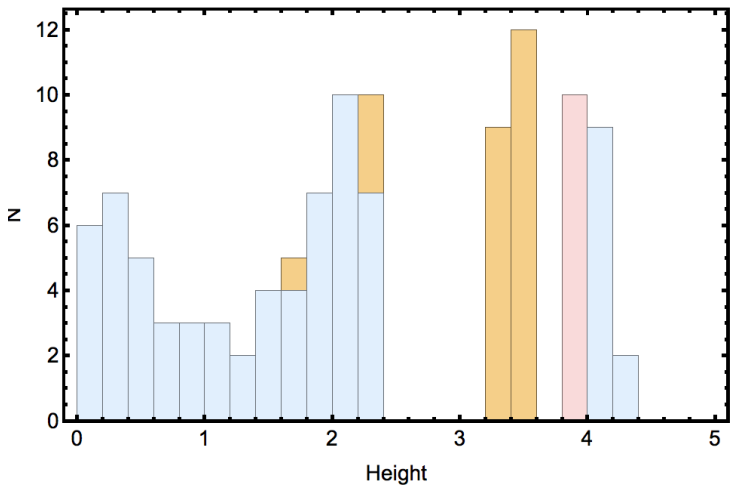

Figure 2.15: Histogram of prominence distributions from $p_{0i} = 20p_{0e}$ and $T_i = T_e/10$ (orange), $T_i = T_e/15$ (blue) and $T_i = T_e/20$ (pink), again for AB Dor stellar parameters.

All histograms shown in Figure 2.13 and 2.14 are for a single temperature. The reality

is that it is a simplification that all prominence loops would be at exactly the same temperature, it is much more likely that there would be a range of temperatures. Changing the loop temperature alters the shape of the height-width plot, as seen in the top right panel of Figure 2.13. Thus, changing the cooled loop temperature causes the peak of the distribution to shift, with a decrease in this temperature leading to the distribution moving inwards. Combining a range of internal temperatures into one histogram yields Figure 2.15. It can be seen that the gap in the modelled data seen above the source surface can be reduced in this case. An observed histogram would likely be composed of multiple temperatures.

It is important to note that whilst the histogram of prominence heights for Speedy Mic is taken from one observing run, the observed histogram for AB Dor is composed of observations over a ten-year period. Over this time period, the magnetic field (derived from ZDI) strength has varied by a factor of 10, and thus the plasma beta (the proxy parameter for field strength in this model) has varied by a factor of 0.01. This is not a small variation. Figure 2.16 shows three histograms plotted at $\beta = 10^{-3}$, $\beta = 10^{-4}$ and $\beta = 10^{-5}$. This lowest value of β was chosen by assuming an average field strength on AB Dor of 10G (from ZDI maps) and then using $\beta = 2\mu p/B^2$ with $p = \kappa B^2 = 10^{-5.5}B^2$ (for B in Gauss). This yields $\beta = 2 \times 4\pi \times 10^{-7} \times 10^{-5.5} \times 10^2/10^{-6} = 10^{-3.5}$. As the observations suggest that β may have varied by 10^{-2} over the time period considered, we then choose to consider the impact this would make on the histograms.

There is a large gap in the histograms for $\beta = 10^{-2}$ and $\beta = 10^{-3}$. This gap is not visible for $\beta = 10^{-4}$ and $\beta = 10^{-5}$. All cases show a peak at very low heights and a second peak at larger heights. For $\beta = 10^{-3}$ and $\beta = 10^{-4}$ this comes not far after co-rotation (at a height of $1.8R_\star$), as is seen in the observations of AB Dor. For $\beta = 10^{-2}$ this secondary peak is below the co-rotation radius and for $\beta = 10^{-5}$ it is further out. A third peak is present for $\beta = 10^{-2}$, $\beta = 10^{-3}$ and $\beta = 10^{-4}$ but is not clear in $\beta = 10^{-5}$. As with the temperature, it is likely that prominence bearing loops in a stellar corona could have a range of magnetic field strengths. This would also complicate the observed histograms from the simple model presented in Figures 2.13 and 2.14.

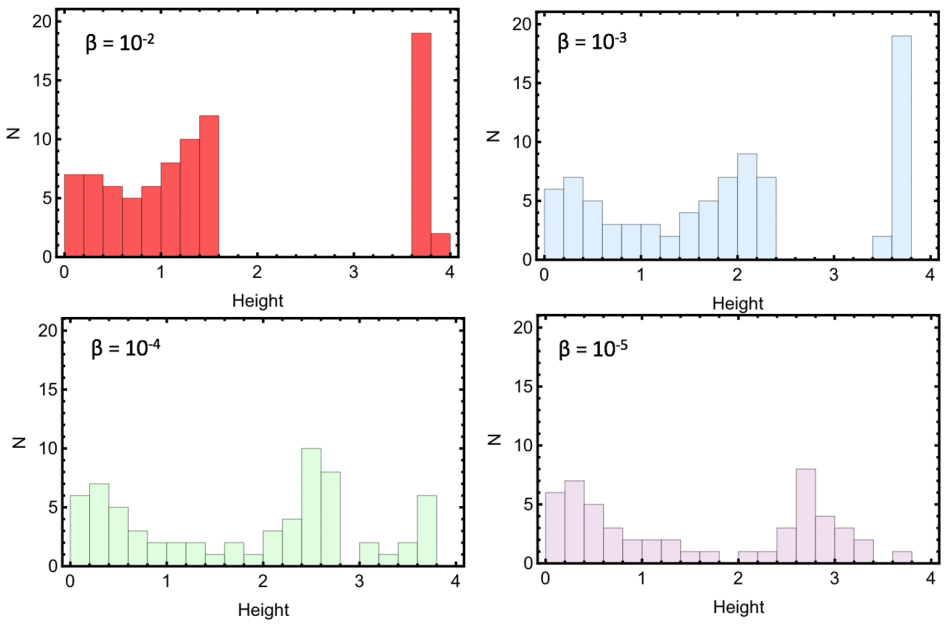

Figure 2.16: Histogram of prominence distributions from $p_{0i} = 11p_{0e}$ and $T_i = T_e/10$ with $\beta = 10^{-2}$ (red), $\beta = 10^{-3}$ (blue), $\beta = 10^{-4}$ (purple) and $\beta = 10^{-5}$ (green).

2.6.6 Further work and conclusions

This chapter has covered the expansion of Jardine and van Ballegooijen's model of prominence formation within the equatorial plane of a rapidly rotating star from Cartesian and into polar coordinates. The same general behaviour is found here as within their work. The height-width plots of the cooled solutions show the same characteristic shape, with loop width increasing with height but then decreasing beyond the co-rotation radius. The coronal field structures that have been considered here are; a pure dipole, a pure quadrupole and a dipole with a source surface. The chapter has also touched very briefly on a combined dipole and quadrupole field.

The cooled family of solutions formed by applying a purely dipolar or purely quadrupolar coronal field are very similar. Although, for a given set of input parameters, the maximum height of solutions is lower in the case of a quadrupolar field compared to the dipolar field, the height-width plots otherwise look very similar in shape. Quadrupolar fields always result in loop widths being smaller than for a dipolar field, as restricted by the geometry. The difference in maximum height is caused by the steeper drop off with height of the quadrupolar field strength when compared to a dipole.

The field can be adapted to include a source surface, beyond which the field is open. Here

a source surface has been included to a dipole field structure, and placed both above and below the co-rotation radius. Cooled solutions have been found out in the wind for both of these cases, although with the source surface placed below the co-rotation radius it is hard to find equilibria around the co-rotation radius. This is particularly noticeable from

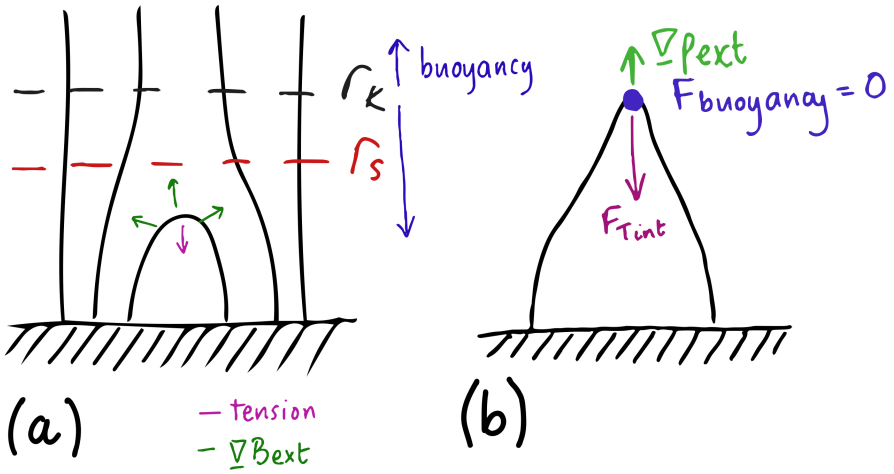

Figure 2.17: Cartoon showing (a) the forces acting on loops in Cartesian geometry and (b) the forces acting on a loop with the summit at the co-rotation radius. The red dashed line shows the source surface and the black dashed line shows the co-rotation radius.

the distributions just beyond co-rotation. It is not fully clear from this preliminary work if this is always the case, or if it is a result of the input parameters used. If it is the case that this is universally true, then observations of stars that show many prominences just beyond co-rotation would imply that the magnetic field is closed to this height. It may be the case that these solutions are always difficult to find in a Cartesian geometry because above the source surface, there is no gradient in the external field. This is shown in Figure 2.17. Looking at the region between the source surface and co-rotation, the magnetic tension and buoyancy forces act down (because solutions are below co-rotation). There is no gradient in the external field here, which would act upwards, and therefore there is no force to balance the other two and produce an equilibrium. For a polar case (rather than Cartesian) it appears that this gradient does exist but that it is very small. Future work to determine when this field would be strong enough to support solutions (e.g. source surface

location, co-rotation radius location, field strength, and temperature) would be valuable in determining how difficult these solutions are to support - or if there are situations in which these solutions are common.

This work also raises the question of how exactly the location of the source surface influences the distribution of solutions. Further work on this could be beneficial in determining the potential source surface location of stars: if certain source surface locations provide certain distribution shapes then observations of prominences from a star might help constrain the source surface radius.
As proof of concept, it has been shown here that multipoles may be used as external fields in order to produce a more general background field structure. The example shown here combines a dipole and quadrupole of the same field strength at the stellar surface. This combined field resulted, as one might expect, in a height-width plot that deviated from the dipolar height-width plot at low heights but matched it at large distances from the surface where the quadrupolar term had significantly died off.

The internal temperature of a prominence bearing loop, the external plasma beta (proxy for external base field strength) and the ratio of internal and external base gas pressures all alter the maximum height at which cooled solutions can be found. A cooler loop, weaker coronal magnetic field or higher internal base pressure will all yield a lower maximum height. Cooler or higher pressure loops will have larger buoyancy forces and thus make it more difficult to support their large masses at large heights above the surface. A weaker external field will not be able to provide as much of an inward force to support loops at large heights as the mass increases. This is increasingly the case for a quadrupolar field since the field strength decreases with height faster than a dipole, and would become increasingly more difficult for higher order multipoles.

Different stars could be in different regimes even if they have the same magnetic field strength, if they have different effective gravity. This leads to potentially very different buoyancy forces and thus different regimes. Histograms of prominence distributions have been shown here for two stars, AB Doradus and Speedy Mic, and for a dipole field structure with the source surface both above and below co-rotation. For AB Doradus, placing the source surface above co-rotation and the cooler of the temperatures investigated here

produced the best results when compared to observations. For Speedy Mic, the hotter temperature but same field structure appears closer to the observations. None of the examples presented here match the observations perfectly. This could be partly due to the fact that observations cover many years for the star AB Doradus, as well as the simplification here that all field lines are at the same temperature.

In the next chapter, this model is developed further using a more realistic field structure. Within this chapter the model is restricted to the equatorial plane, which simplifies the effects of the stellar rotation. In the next chapter, the model remains two dimensional but is instead perpendicular to the equatorial plane.

Chapter 3

Prominence modelling with an aligned dipole

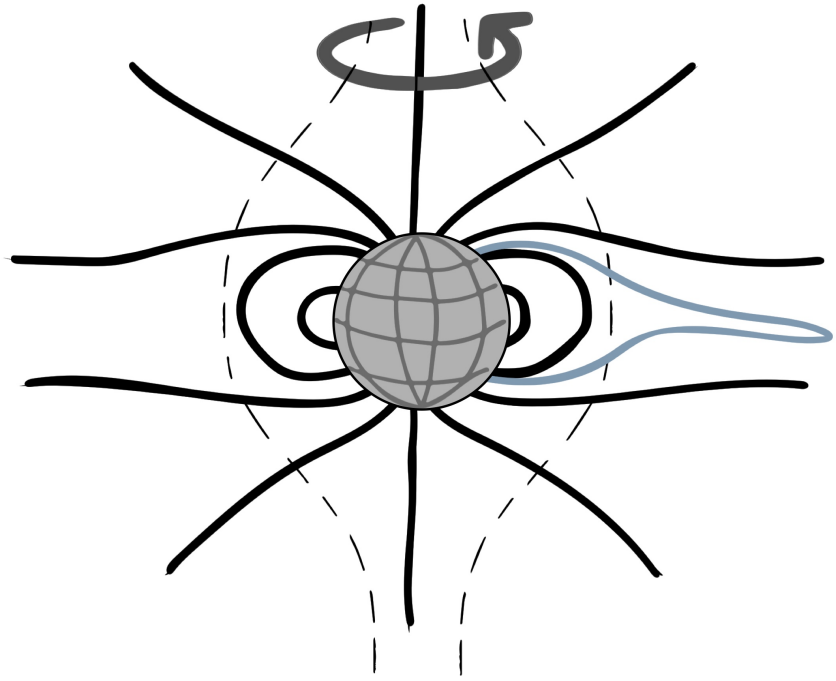

3.1 Development on the previous model

This chapter is based on work published in Waugh et al. 2022[135].

This chapter develops the model introduced in the previous chapter, which is limited by its restriction to the equatorial plane. Within the work presented here, the plane perpendicular to this is investigated. In other words, the magnetic field is now orientated to be aligned with the rotation axis, as shown in Figure3.1.

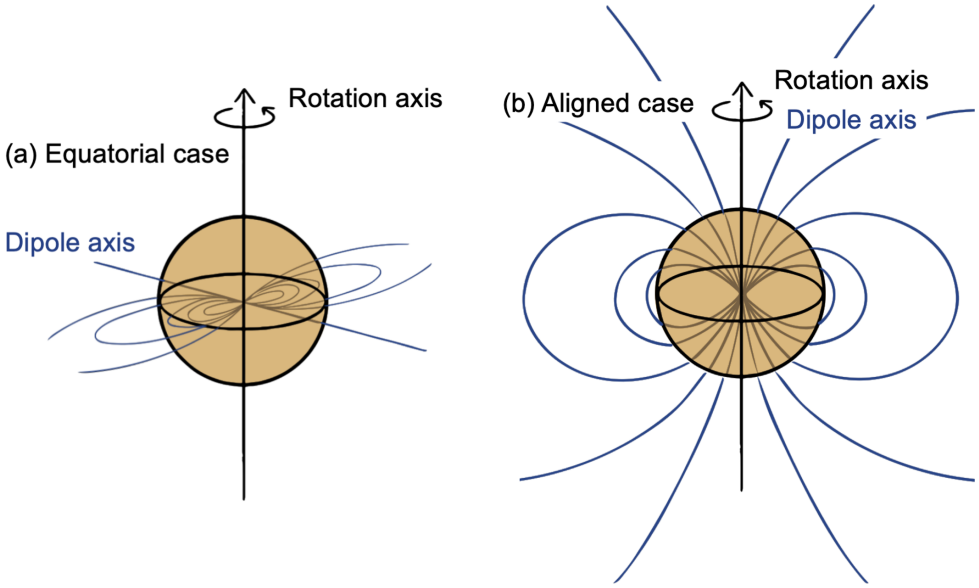

Figure 3.1: (a) A dipole field embedded within the equatorial plane. The field and dipole axis is shown in blue. (b) A dipole field with dipole axis that is aligned with the rotation axis.

The aligned case allows for a more realistic magnetic field, and also a fuller investigation into the centrifugal effects. The centrifugal term in the effective gravity equation is largest within the equatorial plane and drops to zero at the rotational poles of the star.

Within this work, a dipolar magnetic field is applied as the external, coronal field structure. A dipolar field with a source surface is also applied.

The magnetic field structure for the dipole is defined by:

$$B_e = B_0\left(\left(\frac{2\cos\theta}{r^3}\right)\hat{r}+\left(\frac{\sin\theta}{r^3}\right)\hat{\theta}\right). \tag{3.1}$$

The expression for a dipole field with a source surface is given by:

$$B_e = B_0\bigg(\bigg(\frac{2\cos\theta}{r^3}\bigg)\bigg(\frac{r^3+2r_s^3}{R_\star^3+2rs^3}\bigg)\hat{r}+\bigg(\frac{\sin\theta}{r^3}\bigg)\bigg(\frac{-2r^3+2r_s^3}{R_\star^3+2r_s^3}\bigg)\hat{\theta}\bigg), \tag{3.2}$$

the radius of the star is denoted by $R_\star$, the field strength at the stellar surface by B_0 and the subscript "e" signifies that this is the "external" field i.e. coronal field. The derivation for this is shown in Appendix C.

As in the previous chapter, the isothermal equation of state is used to relate pressure, density and temperature, and we assume that the "thin flux tube approximation" holds.

3.2 Mathematical Framework

3.2.1 Determining the loop shapes

Starting again from the equation of motion,

$$\mathbf{0} = -\nabla p + (\mathbf{j}\times\mathbf{B}) + \rho\mathbf{g}, \tag{3.3}$$

and splitting the Lorentz term into magnetic tension and magnetic pressure forces we obtain:

$$\mathbf{0} = -\nabla p + (\mathbf{B}.\nabla)\frac{\mathbf{B}}{\mu} - \nabla\Big(\frac{B^2}{2\mu}\Big) + \rho\mathbf{g}. \tag{3.4}$$

The equations are formulated in the co-rotating frame, meaning that the gravitational force is replaced by an "effective gravity". As before, this combines the gravitational and centrifugal forces:

$$\mathbf{g}_e = \Big(-\frac{GM_\star}{r^2} + \omega^2 r\sin^2\theta\Big)\hat{r} + \Big(\omega^2 r\sin\theta\cos\theta\Big)\hat{\theta} \tag{3.5}$$

where ω represents the stellar rotation rate, $M_\star$ is the stellar mass and G is the gravitational constant.

As in Chapter 1, this equation can be decomposed into two unit vectors, one perpendic-

ular ($\hat{n}$) and one parallel ($\hat{s}$) to the magnetic field.

$$\hat{s} = \frac{1}{\sqrt{r^2 + (r')^2}}(r', r) \tag{3.6}$$

and

$$\hat{n} = \frac{1}{\sqrt{r^2 + (r')^2}}(-r, r'). \tag{3.7}$$

Where r' represents the derivative of r with respect to θ: $dr/d\theta$.

Parallel to the field line, the momentum equation simplifies to

$$0 = -\nabla p.\hat{s} + \rho \mathbf{g}_e.\hat{s}, \tag{3.8}$$

which when evaluated leaves

$$\frac{dp}{ds} = \frac{mp}{K_B T}\left[\left(- \frac{GM_\star}{r^2} + \omega^2 r \sin^2\theta\right)\frac{r'}{\sqrt{(r')^2 + r^2}} + \frac{\omega^2 r \sin\theta\cos\theta r}{\sqrt{(r')^2 + r^2}}\right]. \tag{3.9}$$

This can be simplified, since $ds = \sqrt{(r')^2 + r^2}d\theta$, to

$$\frac{dp}{d\theta} = \frac{mp}{K_B T}\left[\left(- \frac{GM_\star}{r^2} + \omega^2 r \sin^2\theta\right)r' + \omega^2 r^2 \sin\theta\cos\theta\right]. \tag{3.10}$$

Integrating this equation gives the expression for the pressure distribution throughout the corona:

$$\int_{p_\star}^{p(r,\theta)} \frac{1}{p}dp = \frac{m}{K_B T}\left[\int_{R_\star}^{rR_\star}\left(- \frac{GM_\star}{r^2} + \omega^2 r \sin^2\theta\right)\frac{dr}{d\theta}d\theta + \int_0^{2\pi} \omega^2 r^2 \sin\theta\cos\theta d\theta\right], \tag{3.11}$$

$$p = p_0 \exp\left[\frac{m}{K_B T}\left(GM_\star\frac{(1-r)}{rR_\star} + \omega^2 R_\star^2 \sin^2\theta\frac{(r^2-1)}{2}\right)\right]. \tag{3.12}$$

Here p_0 denotes the base pressure and r has been scaled to units of the stellar radius. This expression for the gas pressure can be used to solve for both inside and outside of the cooled field line.

The momentum equation perpendicular to the field line takes the form

$$0 = -\nabla p.\hat{n} + \Big(B^2 \frac{\partial \hat{s}}{\partial s}\Big).\hat{n} - \nabla\Big(\frac{B^2}{2\mu}\Big).\hat{n} + \rho \mathbf{g}_e.\hat{n}. \tag{3.13}$$

The first term on the right hand side of this equation can be expanded to give

$$-\nabla p.\hat{n} = \frac{1}{\sqrt{r^2 + (r')^2}}\left(\frac{\partial p}{\partial r} r - \frac{r'}{r}\frac{\partial p}{\partial \theta}\right) \tag{3.14}$$

and the second and third expressions to

$$(\mathbf{j} \times \mathbf{B}).\hat{n} = \frac{B^2\big(rr'' - r^2 - 2(r')^2\big)}{\mu(r^2 + (r')^2)^{3/2}} + \frac{1}{2\mu\sqrt{r^2 + (r')^2}}\left(r\frac{\partial B^2}{\partial r} - \frac{r'}{r}\frac{\partial B^2}{\partial \theta}\right). \tag{3.15}$$

The final expression when evaluated gives

$$\rho \mathbf{g}_e.\hat{n} = \frac{\rho}{\sqrt{r^2 + (r')^2}}\left(\frac{GM_\star}{r} - \omega^2 r^2 \sin^2\theta + \omega^2 r r' \sin\theta\cos\theta\right). \tag{3.16}$$

Simplifying these, the equation of motion perpendicular to the field lines is

$$\begin{aligned}\frac{2rB^2\big(r^2 + 2(r')^2 - rr''\big)}{(r^2 + (r')^2)} = &-\left(r^2\frac{\partial B^2}{\partial r} - r'\frac{\partial B^2}{\partial \theta}\right) + \left(\frac{\partial p}{\partial r}r^2 - r'\frac{\partial p}{\partial \theta}\right) \\ &+ 2\mu r\rho\left(\frac{GM_\star}{r} - \omega^2 r^2 \sin^2\theta + \omega^2 r r' \sin\theta\cos\theta\right).\end{aligned} \tag{3.17}$$

This differential equation can be solved to give the shape of the field line $r(\theta)$, when combined with the expression for the pressure variation (Equation 3.12) and the equation of state to relate ρ and p.

3.2.2 Determining flux tube masses

Solutions of Equation 3.17 give the shape of magnetic field lines and in order to calculate a loop mass associated with a given field line, a flux tube must be constructed. Here, this is done using flux conservation,

$$B_\star A_\star = B(r)A(r), \tag{3.18}$$

so that an area around the field line can be calculated. $A_\star$ is the area of the flux tube at the stellar surface (base of the loop), as shown in Figure 3.2. This was chosen to be 1% of

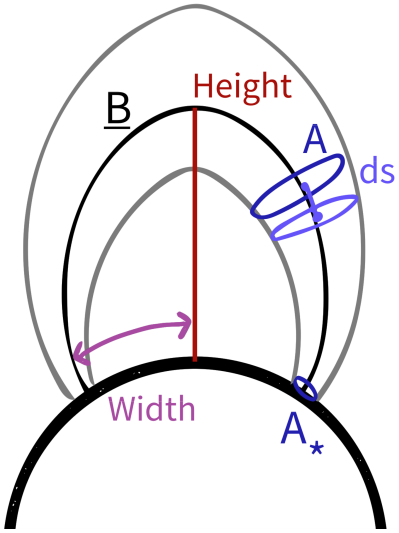

Figure 3.2: Cartoon showing a field line (black) and the surrounding flux tube (grey). The area of the flux tube (A) and length of tube elements (ds) are shown, alongside definitions of loop height and width.

the surface of the star for all flux tubes in this work, to match work by Jardine et al [87]. With this variable fixed, the area at each point along the field line can be calculated. The mass at a given segment of the flux tube was calculated by multiplying the density at that location on the field line by the volume of that flux tube element ($A \times ds$). The flux tube mass is the sum of the multiple flux tube elements.

3.2.3 Generating Hα spectra for these loops

In this section, Hα trails are generated so that they can be compared to observations, in the hope of generating similar dynamic spectra to those observed and in order to determine if certain kinds of loop generate certain trails within the observations. With the field line shapes determined, ten lines are selected at random from the height-width plots and randomly assigned a longitude value (ϕ). Hα spectra are generated by assuming that these loops co-rotate with the star AB Doradus, with the following stellar parameters; $M_\star = 0.87 M_\odot$, $R_\star = 0.96 R_\odot$, $P = 0.5148$ days [136] and a stellar inclination of 60°. As the material on these field lines co-rotate with the star, their velocities can be calculated from

$$v = \Omega_\star r_{FT} \sin\theta_{FT} \sin(\phi_{FT} - \phi_0). \tag{3.19}$$

r_{FT} denotes the radius of a given flux tube element, θ_{FT} its colatitude and ϕ_{FT} its longitude. The longitude of the observer is denoted by ϕ_0.

To account for the inclination of the star, the line of sight velocity is required and simply calculated by

$$v_{los} = v \sin i. \tag{3.20}$$

This must be calculated for each loop segment, over multiple stellar rotations and for all selected loops, in order to generate a Hα spectrum. In order to assign a colour to each area of the Hα spectrum, the absorption (or emission) intensity must be calculated.

The intensity of absorption (I_a) is calculated from

$$I_a = e^{\int_0^s -\kappa\rho ds}. \tag{3.21}$$

which sums the product of the local density (ρ) and local flux tube diameter (ds), in the observers line of sight. κ represents an absorption coefficient which is chosen to ensure that the loop intensities are visible within the spectra.

In the line wings, the intensity in emission (I_e) is found using the simple relation

$$I_e = \Sigma_i \left(r_{FTi}^2 / (4\pi r_i^2) \right) \tag{3.22}$$

where for a flux tube segment (i), the flux tube radius is denoted by r_{FTi} and the radial distance from the stellar centre by r_i. The star is treated as a point source, with light emitted from the star into 4π steradians and the the that reaches the prominence material depending on its distance from the centre of the star (r_i). The light scattered from the prominence material depends on the size of this material, i.e. r_{FTi}^2.

3.3 The gas pressure distribution

Figure 3.3 shows the pressure variation for both the equatorial case investigated in the previous chapter (a) and for the aligned case presented here (b). In the previous model, the gas pressure at any fixed distance from the stellar surface is constant in phase (ϕ). The

pressure is high close to the stellar surface, and again at large heights beyond co-rotation. The co-rotation radius, shown by the black dashed line, is the pressure minimum.

Now, out of the equatorial plane the pressure distribution is more complex. Here, due to the rotation of the star, gas is driven out beyond co-rotation and into the equator. The co-rotation radius is again shown by the black dashed line but is no longer circular, reaching the same value in the equatorial plane as previously but tending to infinity above the rotational poles, where the centrifugal force is zero. The pressure distribution along the line of the equatorial plane is identical to that shown in (a) of Figure 3.3.

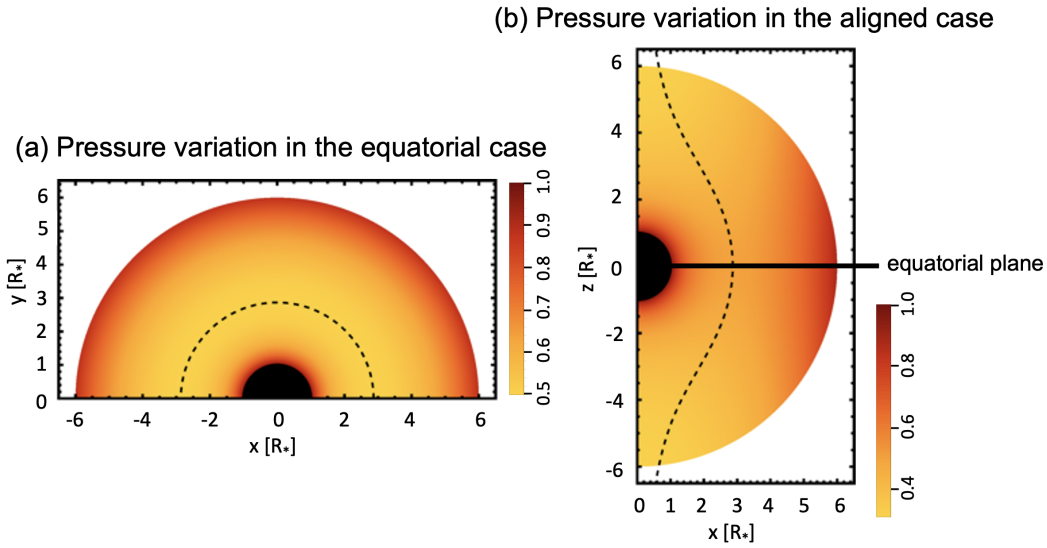

Figure 3.3: Plots showing how the gas pressure varies between (a) a dipole embedded within the equatorial plane and (b) the aligned dipole and rotation axis. The colour scale is in units of the base pressure in both cases. The black dashed line represents the co-rotation radius of the star and the star itself by the black circle. The rotation axis of the star lies along the z-axis.

3.4 Loop shapes

3.4.1 The aligned dipole compared to the equatorial dipole

Figure 3.4 shows example loop shapes and height-width plots for the equatorial case and the aligned case. The overall behaviour is the same in the two cases, showing the classic height-width curves seen in previous studies [76, 77]. At low heights from the stellar surface, the equatorial and aligned cases show identical height-width curves. Here the magnetic field is strong and dominates over the gas pressure and therefore the difference in pressure

distributions between the two cases does not alter the loop shapes significantly. At very large heights, where the loops become increasingly tall and thin, the two cases again show similar behaviour. This is because the maximum loop height is determined by the stellar parameters [77]. Since loop widths shrink so drastically over a short height, there is little variation between the two cases. The difference in loop shapes is apparent in the middle section of the height-width curves. Here, the aligned dipole shows a wider loop for a given height when compared to the equatorial dipole. This qualitative difference is due to the difference in the pressure distribution within the corona of these two cases (as shown in Figure 3.3). In the equatorial case, the pressure is constant in ϕ for a fixed radius whereas out of the equatorial plane this is no longer the case. This means that a loop with summit at radius r must take a smaller width (or smaller radius of curvature) in order to support the same mass as the aligned case and remain in equilibrium.

3.4.2 Including a source surface

Rather than a pure dipole field, a dipole with a source surface can be applied as the external field. An example is shown in Figure 3.5. The external field is closed until the source surface, shown by the red-dashed line in the figure, after which it would become purely radial. In this example the co-rotation radius is shown by the black-dashed line and placed below the source surface. This allows for a region of closed field between the co-rotation radius and the source surface.

As in the equatorial case, presented in the previous chapter, cooled solutions can be found both within the closed field region and out in the wind. The height-width plot in (b) of the figure shows both the external (grey) and cooled solutions (blue). At very low heights where the magnetic field is strongest, the cooled solutions follow the external field. For these input parameters, the cooled solutions deviate from the external field just below the equatorial co-rotation radius, becoming wider than the external field. These loops have empty summits since the gas pressure decreases to a minimum at co-rotation. Loops continue to widen between the co-rotation radius and source surface since the buoyancy term is still small and therefore the radius of curvature of the field must be large in order to maintain equilibrium. The top branch of the height-width curve represents the solutions within the wind.

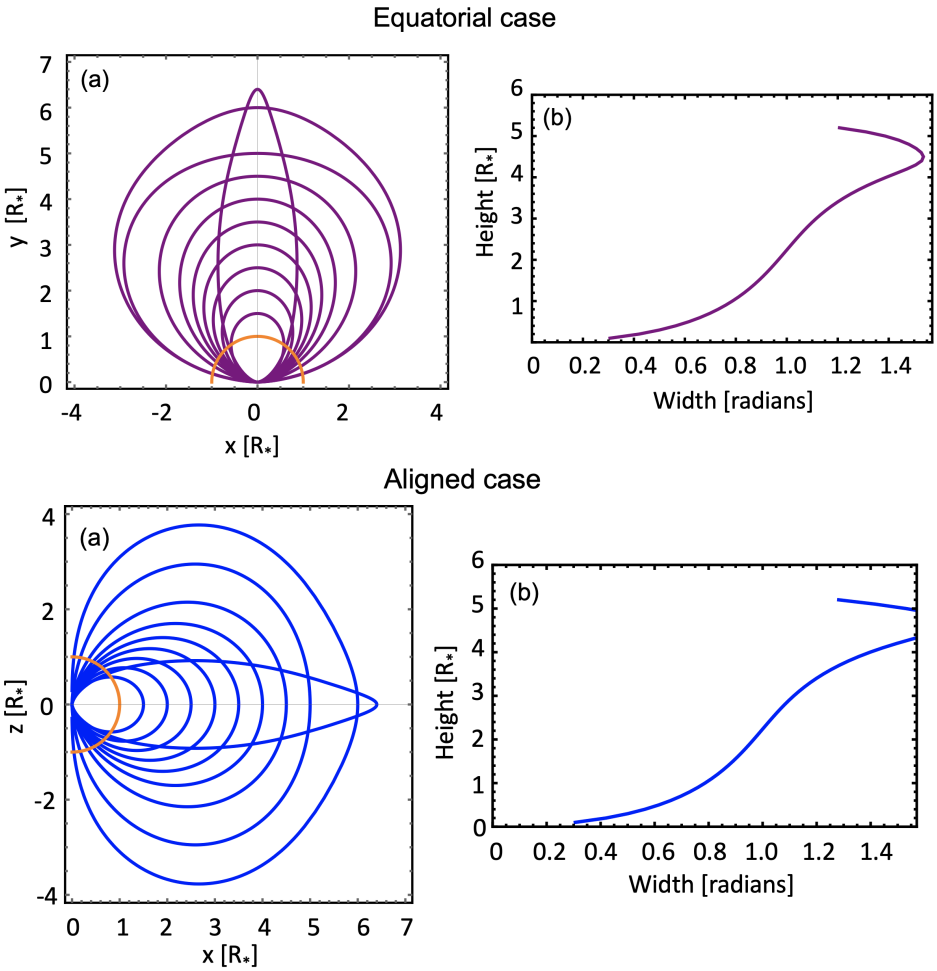

Figure 3.4: (a) Example loop shapes for cool loops embedded within a dipole external field. The stellar surface is shown in orange. (b) The height-width curve for these families of solutions. The parameters used to generate this example are; $p_{0i} = 1$, $p_{0e} = 1$, $T_e = 8.57 \times 10^6$K, $T_i = T_e/10$ and $\beta = 10^{-4}$, and for AB Dor stellar parameters.

3.5 Flux tube mass distributions

The solutions calculated from Equation 3.17 give the shapes of cooled magnetic field lines. In order to estimate the mass associated with a prominence supported by such a field line, a flux tube must be determined. As mentioned in section 3.2.2 flux tubes are constructed around the field line. Figure 3.6 shows the masses associated with these flux tubes for one family of solutions. This family of solutions are shown by the blue curve on the height-width plot in the middle panel, with the external, pure dipole, field shown in grey. The left hand panel is a histogram showing the distribution of loops with height. This is generated by binning along the height-width curve in steps of 0.01 radians in width. The third panel of this plot, the flux tube mass, is scaled to units of 10^{17}g. This is the order of magnitude of

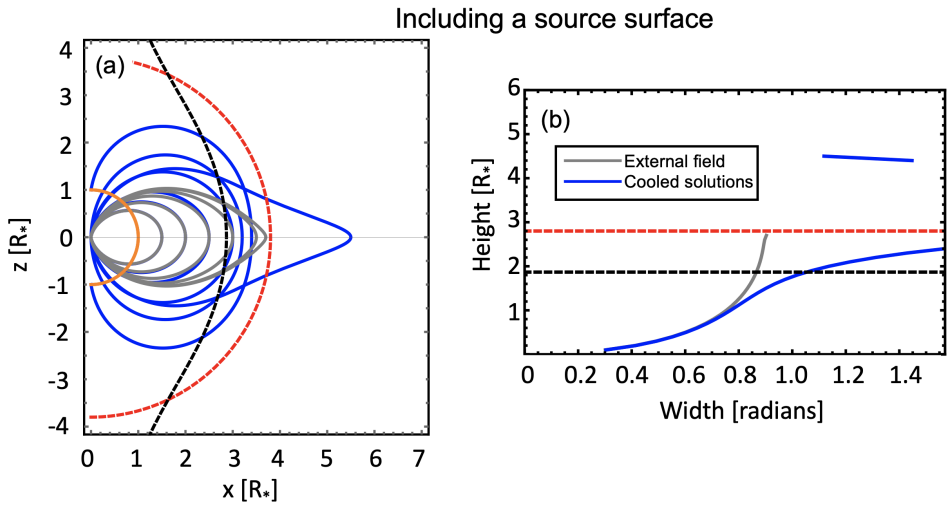

Figure 3.5: (a) Example loop shapes for the cooled solutions (blue) and external field (grey) (b) The height-width curve for these families of solutions. The parameters used to generate this example are; $p_{0i} = 11$, $p_{0e} = 1$, $T_e = 8.57 \times 10^6$K, $T_i = T_e/10$ and $\beta = 10^{-3}$, and for AB Dor stellar parameters (as mentioned previously). The co-rotation radius and source surface are shown by the black and red dashed lines, respectively. Note that in (b) the black dashed line is specifically for the equatorial co-rotation radius.

observed prominence masses on the star AB Doradus [1].

The grey points in this plot show the total mass of the flux tube, and the black points show the mass of the top 80% of the flux tube (i.e. everything above 0.8 times the maxmimum loop summit, $0.8r_{max}$). Flux tubes at all heights are found to have total masses in keeping with the observations. Prominences at very low heights have a total mass around 1×10^{17}g and the total flux tube mass decreases as height increases to the co-rotation radius. On the top branch of the height-width curve, flux tube masses decrease from a maximum of around 2.7×10^{17}g as the total volume of flux tubes drastically decreases with summit height. Here the grey and black points are very similar, whilst for lower heights there is a large deviation between the total mass and the top 80%.

The field lines highlighted by the two blue points on the middle panel of Figure 3.6 have the same loop widths. Despite the same widths, these loops have drastically different heights, with one lying below the co-rotation radius and one well above. These field lines are shown in Figure 3.7, coloured by the local flux tube mass. The black dashed line in these plots represents the co-rotation radius. Panel (a) shows the low-lying loop, which carries most mass in its footpoints with a relatively empty summit. Panel (b) shows the tall loop, which is summit heavy. The mass is carried almost exclusively at the loop summit in this case,

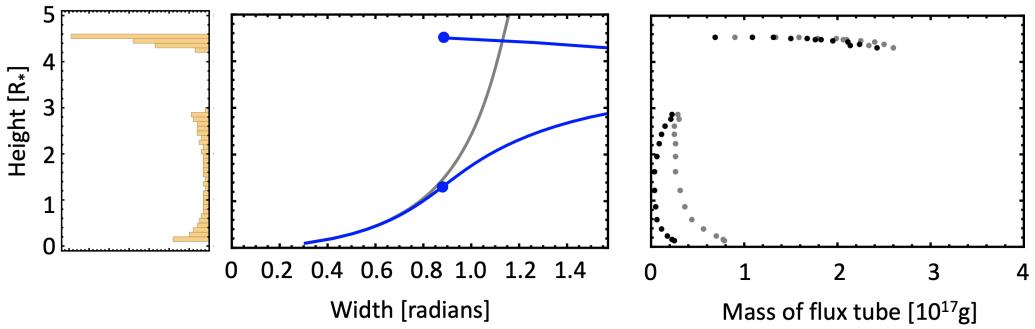

Figure 3.6: Left panel: histogram showing the distribution of the number loops with height. Middle panel: height width plot for the cooled solutions (blue) and external pure dipole field (grey). The two blue dots represent two cooled solutions with the same loop width but different heights. Right panel: Flux tube mass against loop height, shown in units of a typical AB Doradus prominence (as determined by observations). The input parameters used to generate this example are; $p_{0i} = 11$, $p_{0e} = 1$, $T_e = 8.57 \times 10^6$K and $T_i = T_e/10$, $\beta = 10^{-3}$.

and whilst the loop footpoints also carry mass, this is significantly less than the summit.

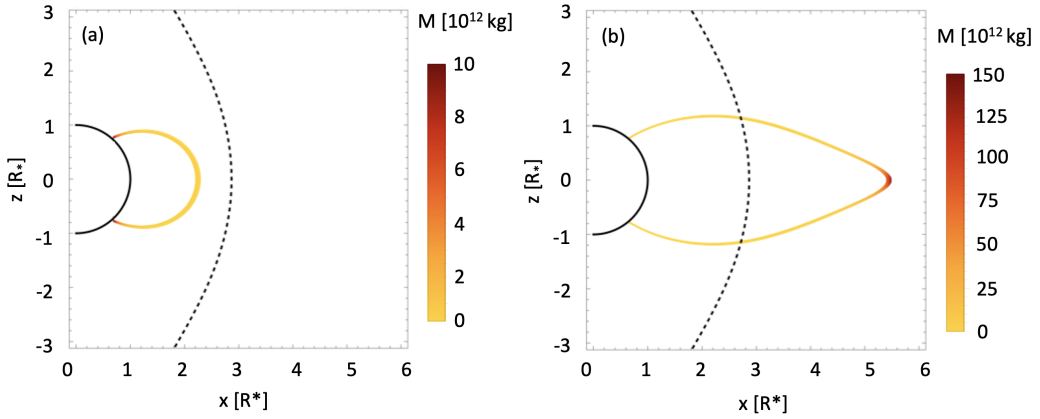

Figure 3.7: Example loops of the same width (1.76 radians) but different heights. The colour represents the flux tube mass.

3.6 Generating synthetic Hα spectra

3.6.1 The equatorial dipole

Figure 3.8 show the magnetic field structures (a) and associated Hα trails (b) for an equatorial dipole at two different stellar inclinations. The magnetic field structures are generated by selecting 10 of the solutions from the height-width curve shown in Figure 3.4. To ensure

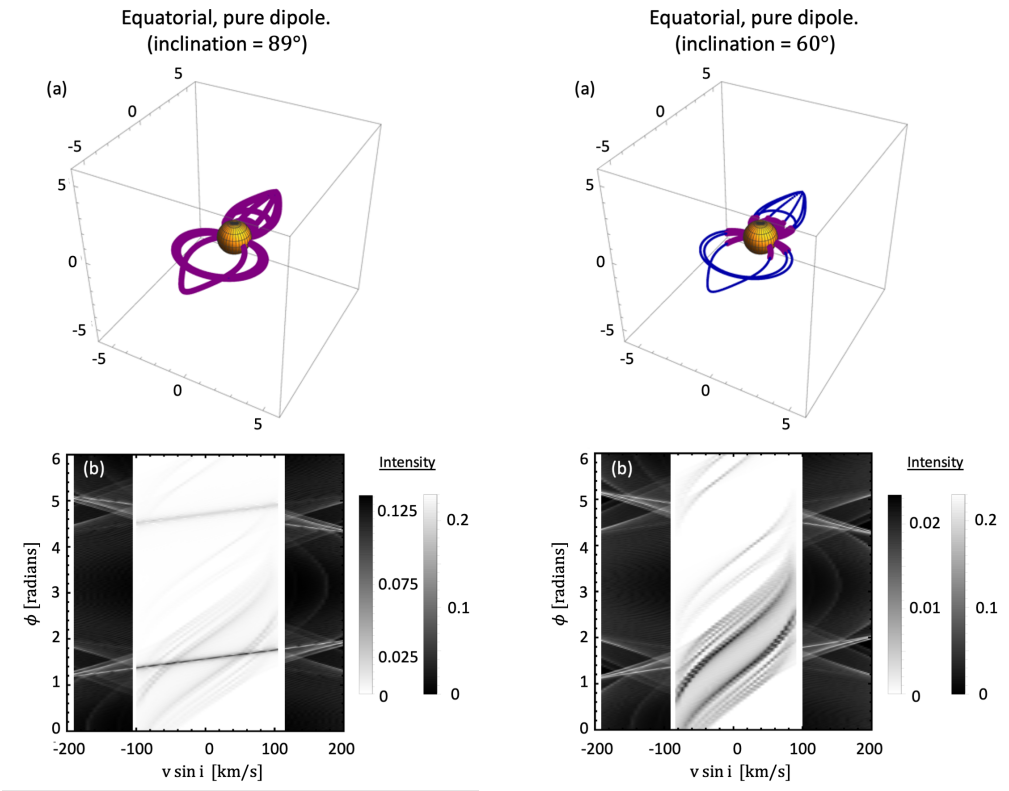

Figure 3.8: (a) Example field lines and (b) the associated Hα spectrum, for the aligned case. The field lines are shown in blue, with sections of the field line that contribute to absorption shown in purple. Left: stellar inclination of 85° and right: stellar inclination of 60°.

a dipole field structure, these field lines must all have loop summits at one of two ϕ values, creating two lobes. The sections of the field lines that transit the stellar disc, and thus are present as absorption features, are shown in purple. The remainder of the field lines are shown in blue.

With an inclination of close to 90°, i.e. viewing into the equatorial plane of the star, all of the field lines will transit the disc over one stellar rotation. Within the Hα trails, features can be found about the two ϕ values of the lobe summits ($\pi/2$ and $3\pi/2$).

For each lobe, there is a fast travelling dark line which is caused by the dense summits of the tallest field lines. These features can also be seen travelling quickly through the emission profile. Centred on the same phase but with a different gradient are other, fainter features. These features are symmetric, lying on both sides of the dark central line. These fainter

features are the footpoints of the loops and are symmetric in the spectrum due to the loop symmetry. Some of these features relate to the tall loops but others are caused by the lower lying loops. One of these lower lying loops can be seen faintly in the emission profile in the red shifted velocity between $\phi = 0$ and $\phi = \pi/2$, and then again in the blue shifted velocity between $\phi = \pi/2$ and $\phi = 3\pi/2$. This feature is fainter than the loop summits of taller loops, despite being closer to the star, due to the area of this flux tube being much smaller than for the taller loops.

The lobe centred on $\phi = 3\pi/2$ is much fainter than the lobe centred about $\pi/2$. This lobe corresponds to the lobe on the left hand side of Figure 3.6.1(a). There are fewer loops in this lobe than the other one, and two of the three field lines are very extended. These "bloated" loops are those above the co-rotation radius and typically carry little mass in their summits. They have very wide footpoints, meaning that the two footpoint trails in the spectrum are separated by a large ϕ.

Figure 3.6.1 shows the same field structure with a stellar inclination of 60°. With this inclination, chosen to be close to the inclination of AB Doradus, very few sections of the field lines now transit the disc. Only sections of the field line legs close to the surface are seen in absorption. The Hα trails are very similar to the previous case, but without the dark, fast travelling features associated with the dense summits of the tall loops.

With an equatorial dipole, an individual loop can create two or three features depending on its height. The tallest loops with dense summits can show up to three features: the dense loop summit and the two footpoints, whilst lower loops only add features from the two footpoints to the spectrum. The inclination of the star will determine if the loop summits of tall loops, i.e. the prominence itself, is visible in absorption.

A feature of this model is that flux tube footpoints may stack on top of each other. This is particularly true for this field geometry where summits of loops are restricted to two phases. These stacked flux tubes all contribute mass to the absorption, and thus darken features where this couldn't be the case physically.

3.6.2 The aligned dipole

With an aligned dipole, field lines can be assigned to any longitude. This creates Hα trails with features spread throughout the spectrum in phase, and not restricted to two values. An example is shown in Figure 3.9. There are a range of loop shapes, which can be seen in (a), and now typically only one field line leg transits the stellar disc. Again, loop summits typically do not transit the disc as they themselves are still within the equatorial plane. For very low-lying loops, however, the loop summits are visible in absorption. For the bloated loops, the section of the loop that transits the disc does not include the summit or either footpoint.

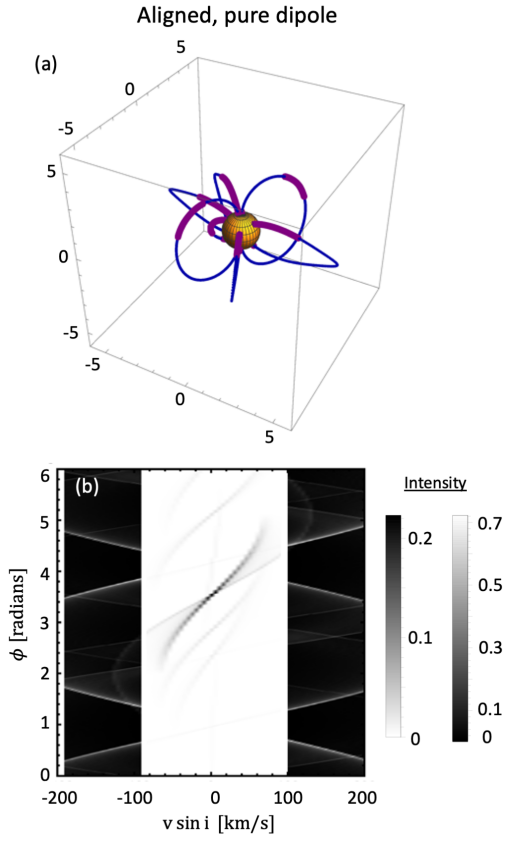

Figure 3.9: (a) Example field lines and (b) the associated Hα spectrum, for the aligned case and stellar inclination of 60°. The field lines are shown in blue, with sections of the field line that contribute to absorption shown in purple.

With this field structure, there are two tall, thin field lines, that are roughly $\phi = \pi$ radians apart. Although the summits of these loops do not transit the disc, they are visible

in emission as the two fast travelling and bright lines.

The darkest feature in the absorption profile corresponds to a low-lying loop. The footpoint of this loop contributes the darkest and slowest moving portion of this feature whilst its summit contributes the fainter, fast-moving portion. The summit of this loop can also be seen faintly in emission. The footpoint carries more mass than the summit of this loop, thus causes more absorption.

Other features on this example spectrum are relatively faint. These are either a footpoint of the tallest loops or the less dense legs of the bloated loops. These features are almost invisible in the spectrum since the density, and therefore mass, of these legs is so low at these heights of the corona.

3.6.3 The aligned dipole with a source surface

The overall behaviour found here is similar to the pure, aligned dipole. Since this field structure is an adapted dipole, this is to be expected. The field structures presented in (a) of Figures 3.6.3 and 3.6.3 appear different to the pure dipole in Figures 3.9(a), but once encoded into the Hα trails the differences in the absorption features are more difficult to spot.

The loops, as previously, are selected at random from the height-width plots. The height-width plot for the pure dipole was shown in Figure 3.6, although the top branch was interpolated to the minimum loop width of 0 radians before being sampled here. The height-width plots for the field structures presented here are shown in Figure 3.11. The maximum height, and top branch, for all three cases are very similar however the lower branch is very different. This is especially true for the source surface placed below the co-rotation radius, where the lower branch is very small and also deviates in shape from the other two cases. Whilst for the pure dipole, or dipole with $r_{ss} > r_k$ have a wider variety of loop shapes, loops for $r_{ss} < r_k$ must be either very low lying or very tall. Because the height-width curves are sampled at random, loops that are very tall *and* wide are more likely in the case of $r_{ss} < r_k$ than the other two cases.

The low lying loops in (a) of Figure 3.10 correspond to the features centred around $\phi = 4.5$ and $\phi = 5.5$ radians. The feature at $\phi = 2.5$ radians corresponds to a loop with its summit around the co-rotation radius, with a dark footpoint and relatively empty summit.

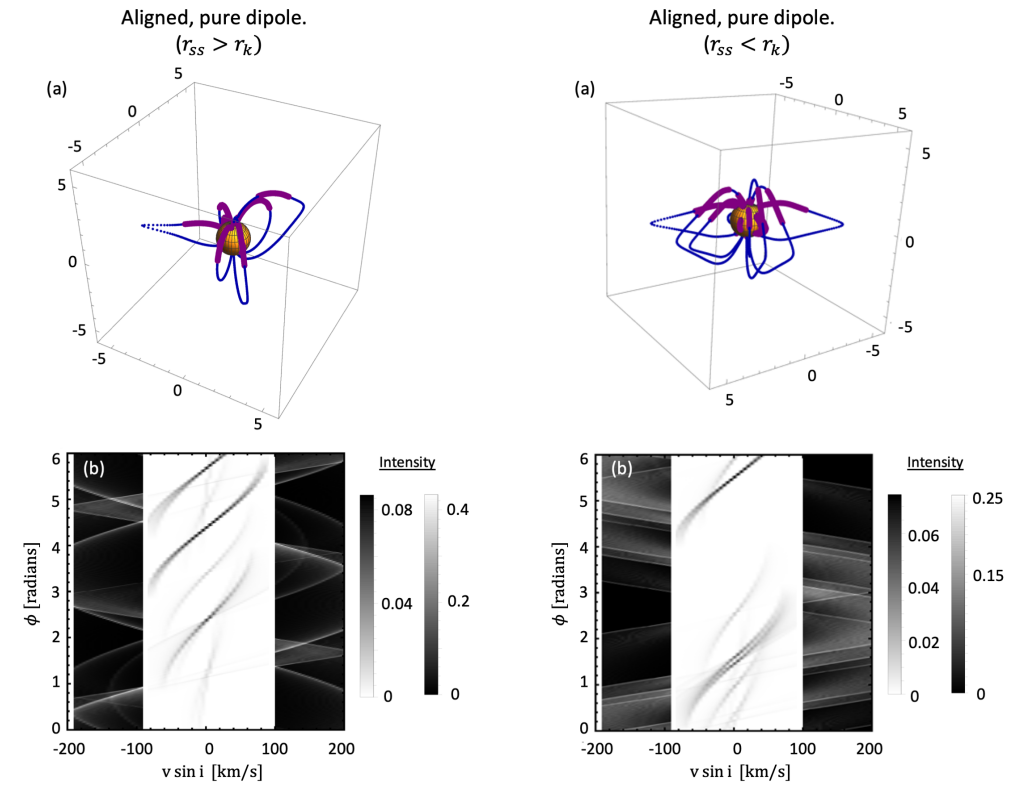

Figure 3.10: (a) Example field lines and (b) the associated Hα spectrum, for and aligned dipole with: $r_{ss} = 3.8R_\star$, $r_k = 2.8R_\star$. The field lines are shown in blue, with sections of the field line that contribute to absorption shown in purple. Both have a stellar inclination of 60°.

The summit of this loop can be seen very faintly in absorption, and crosses into emission. The features around $\phi = 1$ and $\phi = 5$ are faint and transit very slowly through the absorption profile i.e. have a steep slope. They keep very close to the centre of the spectrum, since the footpoints are at high latitudes and do not have much of the disc to transit. These correspond to the tall, wide loops. The tall and thinnest loop in this example corresponds to the absorption feature centred around $\phi = 3.5$ radians, which is caused by the loop footpoint. This feature looks similar, albeit fainter, to the low-lying loops and without the field structure would look indistinguishable.

The Hα trail for the field structure with $r_{ss} < r_k$ is the most distinct. As previously mentioned, field lines in this sample are either very low-lying loops or very tall loops. The low-lying loops are very close to the stellar surface, and create the absorption features centred at $\phi = 1.5$ and $\phi = 5.5$ radians. The tall loops can either be wide or thin. The thin

loops have a footpoint that transits the disc, whilst for wide loops only a middle section of the leg transits. This wide loops are responsible for the absorption features at $\phi = 0.1$, 0.5, 1 and 1.2 radians. Whilst the thin loops are present at $\phi = 1$, 2.5 and 6 radians. All tall loops have dense summits and whilst they are not visible in absorption, they are very clearly seen in emission. There are more tall loops with this field structure due to the shape of the height-width curve, and this creates a busier emission spectrum than in the other cases presented here.

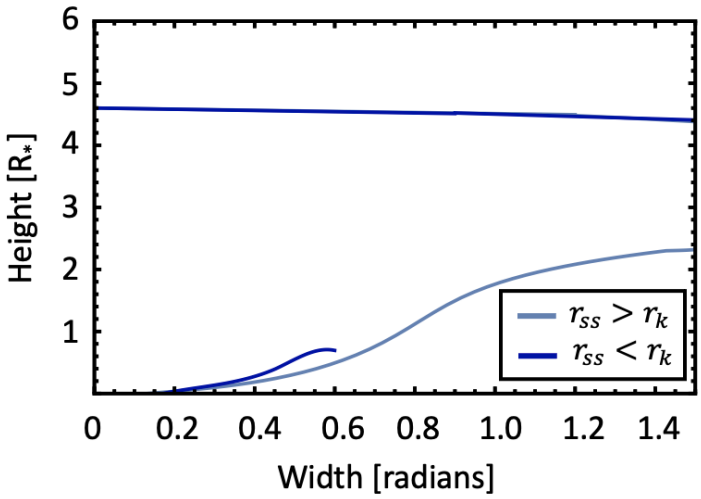

Figure 3.11: Height-width curves showing the family of solutions for the source surface above and below co-rotation.

3.6.4 Distinguishing between field structures from the Hα spectra

Whilst there are distinctions between the absorption features made by different types of loop, and some distinctions in the full Hα spectra generated by the field structures applied here, these distinctions are not always obvious. There are four types of field line in the structures presented here: low-lying loops, loops with summits near co-rotation, tall and wide loops and, finally, tall but thin loops. The full absorption trails generated by these loop types are distinct. Low-lying loops generate dark, slow travelling features that have a similar intensity across them as the density is relatively similar along the loop. Loops with their summits close to the co-rotation radius show dark features corresponding to their footpoints, but have empty summits due to the pressure minimum at co-rotation. Thus, their summits do not contribute to the absorption features. Tall, wide loops produce absorption features with footpoints that transit near the poles and thus appear close to line centre.

These loops also have dense summits and thus add a dark, fast-travelling section to the full feature. Tall, thin loops produce similar absorption spectra to the tall, wide loops, but with tighter footpoints that are further from the pole of the star, the footpoint features create longer $v \sin i$ trails.

Whilst low-lying loops can produce two features and tall loops can produce three features in a spectrum, the stellar inclination and orientation of the dipole can limit this. With a non-equatorial view of the star, summits of tall loops that support the slingshot prominence material will rarely transit the disc. Due to this, the Hα trails from the tall loops resemble the trails from the lower lying loops. Despite the potential differences in the features from various loop geometries, once stellar inclination is accounted for it may not be a straight forward task to pick them out of the spectra.

The orientation of the magnetic field plays a more noticeable role in the spectra generated. Whilst for an aligned dipole there is typically one feature per loop, and these may occur at any phase, this is not the case for the equatorial dipole. The constraint on the lobes being $\phi = \pi$ radians apart is partly responsible for this. In the example shown here, the two lobes are very apparent in the Hα spectra, especially with the inclination = 89° case presented. However, one can imagine that if the loop shapes selected were different then this may be less immediately obvious. Because the footpoints of loops can take a wide range of values, features from the footpoints of bloated loops can appear at phases far from the central phase (i.e. of the loop summit). In Figure 3.8 an example of this occurs for the lobe centred on $\phi = 3\pi/2$. The two, symmetric stripes here could be mistaken for independent structures had the magnetic field structure not been available to compare to.

The emission spectra in the equatorial case is important for differentiating between this field structure and the others investigated here. The symmetry in the trails is valuable information, and the emission trails all join the absorption part of the spectrum at the same phase. This is caused by the loops all stacking on top of each other. This behaviour is not present in the other spectra. The emission from the aligned dipole with source surface below co-rotation is also particularly different, caused by many more tall loops in this field structure than in the others.

Here, Hα trails have been generated from specified magnetic field structures. However, looking at the Hα spectra alone it is difficult to say that, by eye, much information on the field structure can be inferred. The model here allows for a simple way to populate

a stellar corona with potential prominence bearing loops. From this, one could generate many synthetic Hα spectra using a given field structure, by randomly selecting the loop shape and phase. With a great many Hα spectra, they could be used as a training set for AI to investigate more fully the relationship between magnetic field structure and the possible Hα trails.

3.7 The light curves

As a prominence crosses the stellar disc, it appears in the Hα spectrum as an absorption feature. These dynamic spectra plot the line of sight velocity against rotation phase, and when multiple features are present it can be difficult to determine the structure caused by a given feature. The advantage of models of these features is that the individual trails can be separated from the combined spectrum, so that the trail caused by any given feature can be examined, as well as examining the combined spectrum that would be observed.

As well as dynamic spectra, the light curves generated by a feature can be generated. These light curves plot the intensity against phase, a show the dip in intensity that would be observed as the prominence transits the disc. An example of a light curve can be seen in (c) of Figure 3.12.

3.7.1 The equatorial dipole

Inclination = 90°

First, an equatorial dipole and a stellar inclination of 90°, such that we observe into the stellar equator, is considered.

A selection of the field lines shown in (a) of Figure 3.8 are considered below. The first example shows a low lying field line (a), the associated absorption feature (b), and the light curve (c). The absorption feature shows dark footpoints at the edges of the feature with absorption intensity decreasing towards the centre, representing the loop summit. The light curve is a wide v shape. The dark line of a footpoint absorption feature is not symmetric in ϕ: looking at the first footpoint that comes onto the disc (the dark feature that begins at the earliest phase), it can be seen that the feature darkens with increasing phase. In other

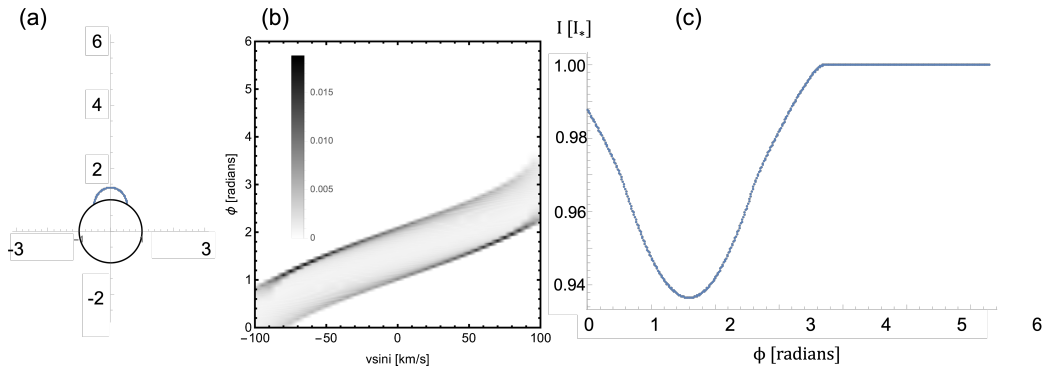

Figure 3.12: (a) the field line shape (b) the associated Hα trail and (c) the light curve for a low lying loop.

words, the first footpoint to enter the disc appears to absorb more as it exits the disc than when it enters. This is not actually caused by the footpoint itself, but by the additional material along the loop that occults it (see Figure 3.13). The same occurs for the other footpoint, however in the opposite order. This leads to asymmetries in the light curves, although in this case it is difficult to spot by eye.

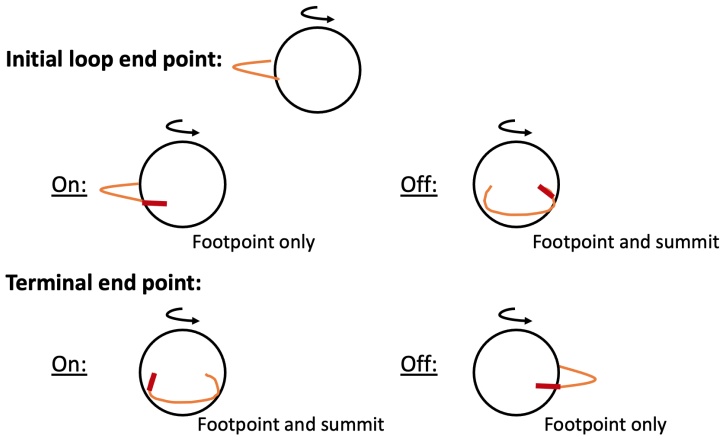

Figure 3.13: Top: a field line about to cross the stellar disc. Middle: The leading leg (red) is seen alone as it comes onto the disc and through the loop as it leaves. Bottom: The trailing leg (red) is seen through the loop as it comes on to the disc and alone as it leaves.

The second loop has a summit around the co-rotation radius, and is much wider than the previous example. The absorption feature shows this, with the two dark footpoints being further separated in ϕ than was the case in Figure 3.12. The summit (centre of the absorption feature) is much lighter than previously, since the loop summit is empty at co-rotation. The light curve is faintly scallop-shaped, showing three lobes. The first lobe is caused by

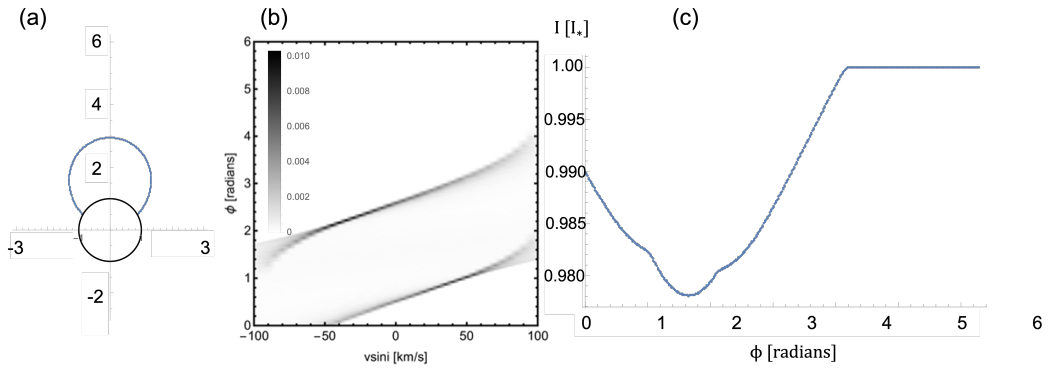

Figure 3.14: (a) the field line shape (b) the associated Hα trail and (c) the light curve for a loop with summit at co-rotation.

the leading footpoint, the central lobe is present when both legs of the loop are transiting the disc, and the third lobe is caused by the trailing footpoint.

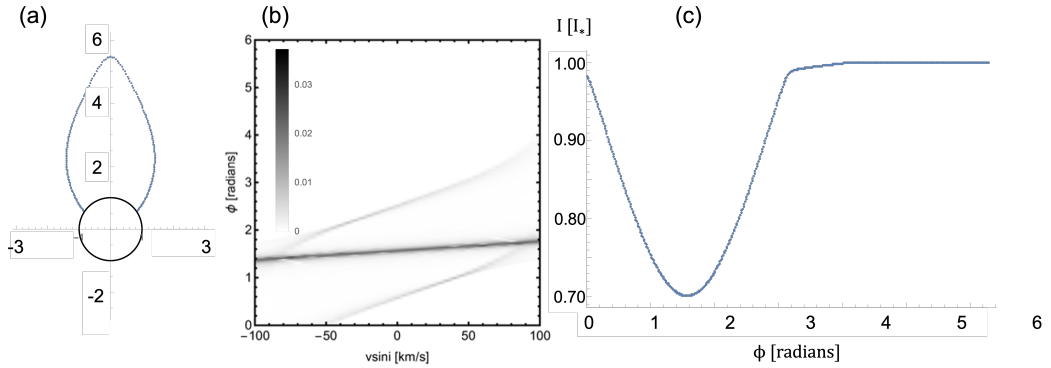

Figure 3.15: (a) the field line shape (b) the associated Hα trail and (c) the light curve for a tall, wide.

The third loop example is tall, but a similar width to the second loop. The absorption features look similar, however in this case the dark central line of the loop summit is a far stronger absorption feature, washing out the footpoint absorption. The light curve is a deep u, dominated by the loop summit.

The fourth loop is only slightly taller than the third, however is considerably thinner. This is caused by the extra mass supported in the loop summit. The absorption feature caused by the footpoints looks similar to Figure 3.12, however a dark and very fast travelling feature associated with the loop summit dominates the absorption. The light curve is again a deep u, dominated by dense summit.

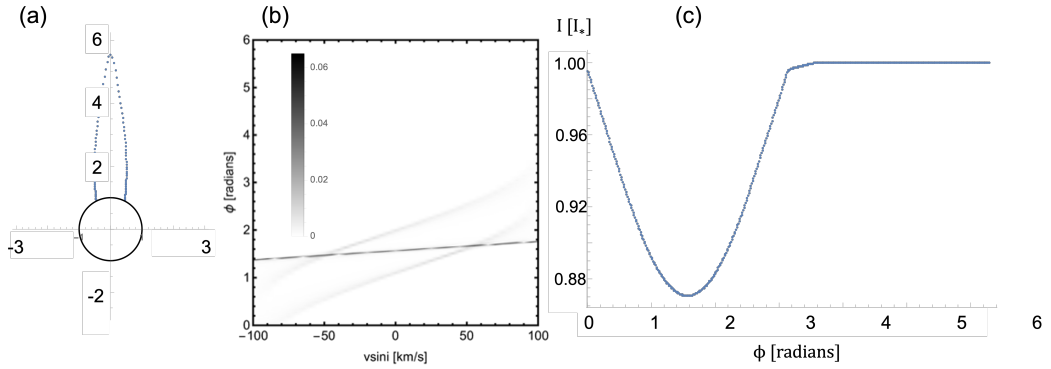

Figure 3.16: (a) the field line shape (b) the associated Hα trail and (c) the light curve for a tall, thin loop.

Inclination = 60°

A selection of the field lines shown in (a) of Figures 3.6.1 is considered below. The first ex-

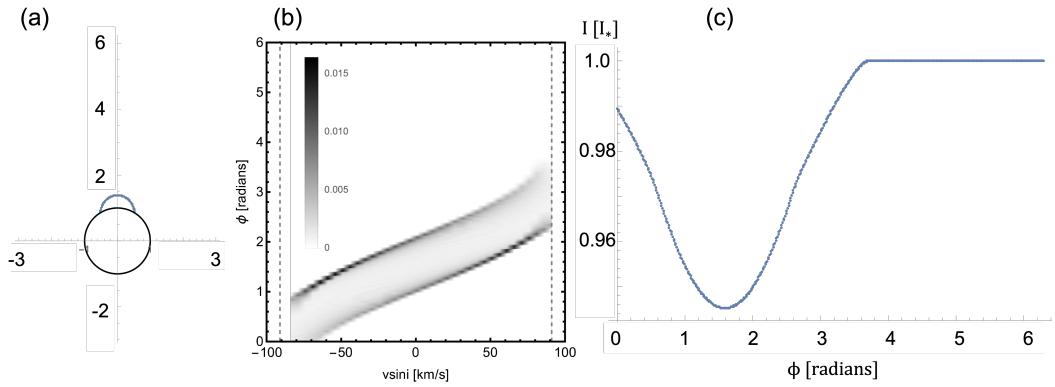

Figure 3.17: (a) the field line shape (b) the associated Hα trail and (c) the light curve for a low lying loop.

ample shows the same loop as in Figure 3.12. The absorption feature shows dark footpoints at the edges of the feature with absorption intensity decreasing towards the centre, representing the loop summit, and very similar to the previous case. The change in inclination has very little effect on this loop, since it lies so close to the stellar surface, The light curve is again a wide u shape.

The second loop has a summit around the co-rotation radius, and is the same loop shown in Figure 3.14. The absorption feature shows the two dark footpoints with an empty summit. The light curve is again scalloped shaped, with the three lobes being more apparent than in Figure 3.14. The asymmetry in the absorption is more apparent than previously.

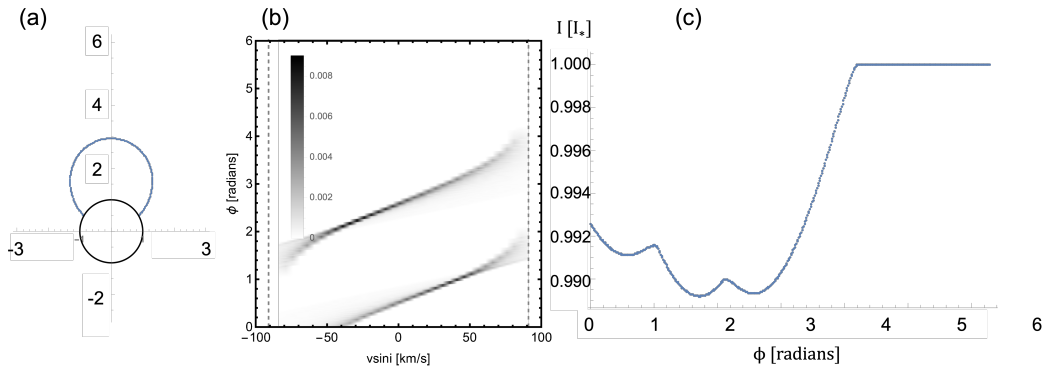

Figure 3.18: (a) the field line shape (b) the associated Hα trail and (c) the light curve for a loop with summit at the co-rotation radius.

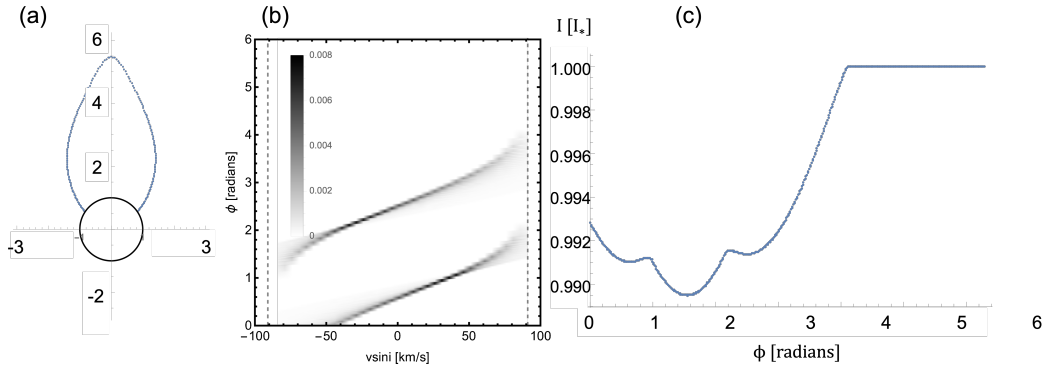

Figure 3.19: (a) the field line shape (b) the associated Hα trail and (c) the light curve for a tall wide loop.

The tall but wide loop now shows an absorption feature that looks virtually identical to the previous one (Figure 3.18). Since the loop summit is not visible in this inclined case, there is no way to tell the difference between these two absorption features by eye. The light curve is also scalloped, and also looks similar to the previous case, albeit more symmetric.

The tall but thin loop now produces an absorption feature and light curve that appears very similar to the low lying loop (Figure 3.17). The light curve has slightly flatter wings than the low lying loop, but the dip does not reach such large absorption intensities as the low lying loop.

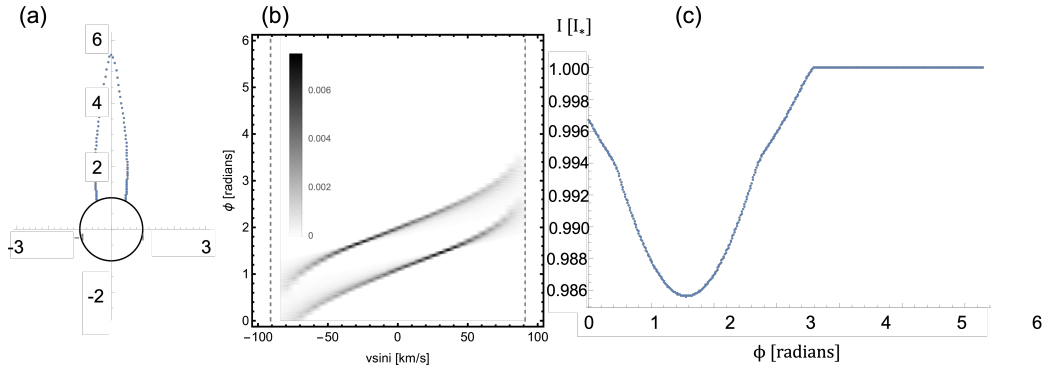

Figure 3.20: (a) the field line shape (b) the associated Hα trail and (c) the light curve for a tall, thin loop.

3.7.2 The aligned dipole

The light curves and Hα trails for individual loops are again considered, this time for an aligned dipole with a source surface. The inclination is still set to 60°.

Case 1: $R_{ss} > R_k$

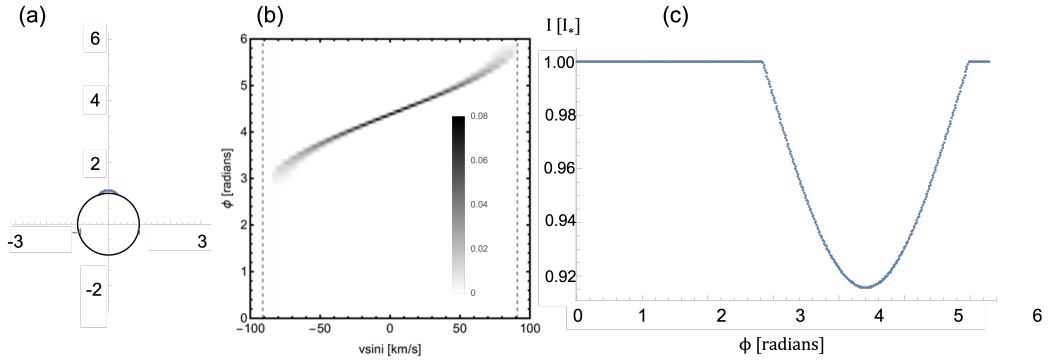

Figure 3.21: (a) the field line shape (b) the associated Hα trail and (c) the light curve for a low lying loop.

Figure 3.21 shows a very low lying loop. Whilst the entire loop transits the disc, the Hα spectrum is a very thin line, due to the proximity of the loop footpoints. The light curve shows a smooth u shape.

The loop with summit around the co-rotation radius, is shown in Figure 3.22. The detail in the density distribution along the loop can be seen here when the Hα trail is plotted for this loop alone. The footpoint that transits the disc can be seen by the dark line, closest to line centre, that passes slowly across the disc. The material closer to the summit of the

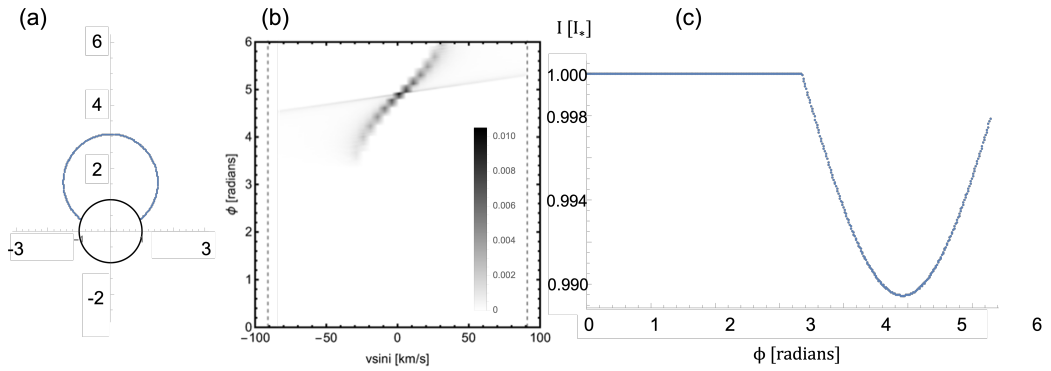

Figure 3.22: (a) the field line shape (b) the associated Hα trail and (c) the light curve for a loop with its summit at co-rotation.

loop, at the maximum height that is visible, can be seen by the fast travelling, faint line. The light curve again shows a smooth u shape, since there is only one footpoint to transit the disc so the scalloped shell appearance is not replicated.

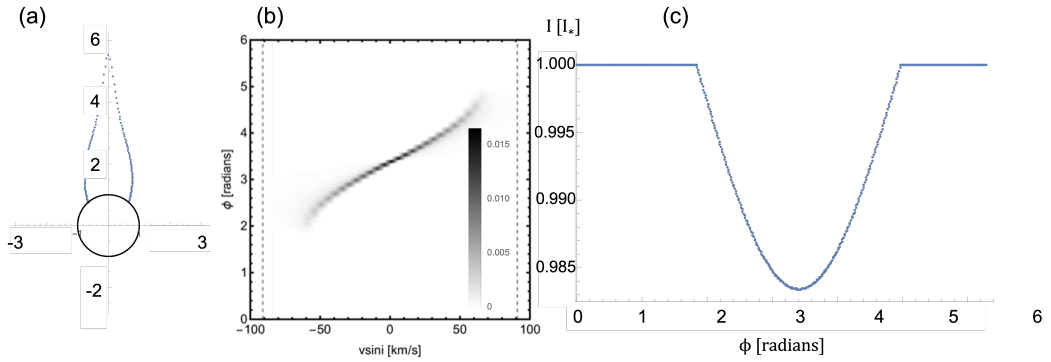

Figure 3.23: (a) the field line shape (b) the associated Hα trail and (c) the light curve for a tall, thin loop.

The tall, thin loop is shown above. The Hα trail again shows a similar behaviour, with only one footpoint present. The loop summit never transits the disc due to the inclination. Since the prominence footpoints are closer together than in Figure 3.22 above, the footpoint feature takes longer to transit the disc because the footpoint is at a lower latitude. The Hα trail again looks similar to the very low lying loop (Figure 3.21). The light curve again shows a smooth, and symmetric u.

The tall but wide loop shown below again produces a Hα trail similar to the shorter but wide loop (Figure 3.22). Again, the loop summit does not transit the disc. The light curve

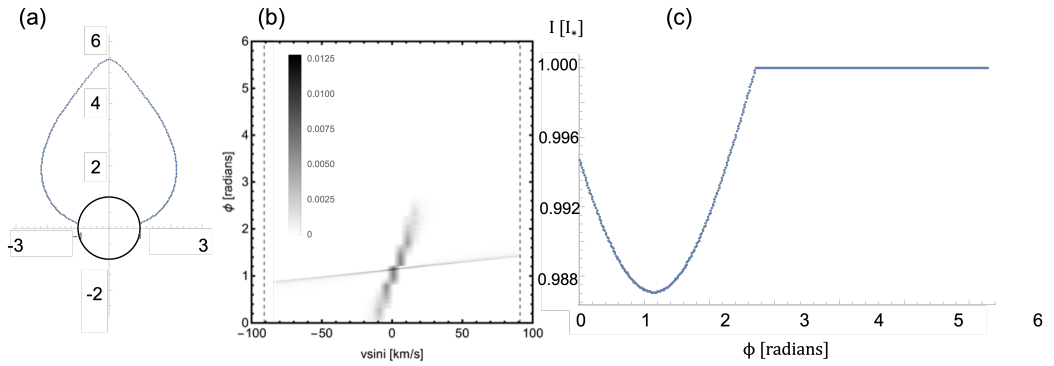

Figure 3.24: (a) the field line shape (b) the associated Hα trail and (c) the light curve for a tall, wide loop.

is once again a smooth u shape.

Case 2: $R_{ss} < R_k$

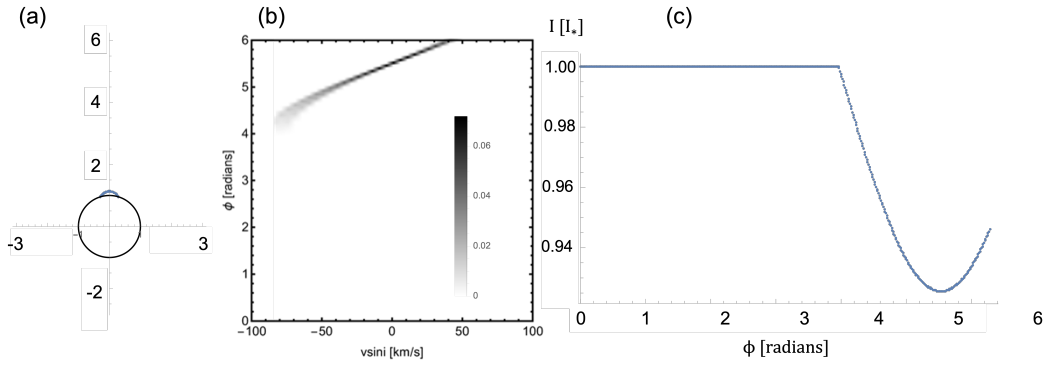

Figure 3.25: (a) the field line shape (b) the associated Hα trail and (c) the light curve for a low lying loop.

Figure 3.25 shows a low lying loop and the observable Hα trail and light curve. The trail is very similar to the source surface placed above co-rotation (Figure 3.21). Whilst the trail differs from the equatorial dipole, the light curves are very similar (Figure 3.17).

Figure 3.26 shows a taller loop, closer to the co-rotation radius, although still below it. Finding solutions at co-rotation is very difficult in this regime. The trail appears very similar to the very low lying loop above (Figure 3.25), although there is more variation in absorption across the trail. The light curve is similar in shape to other small loops.

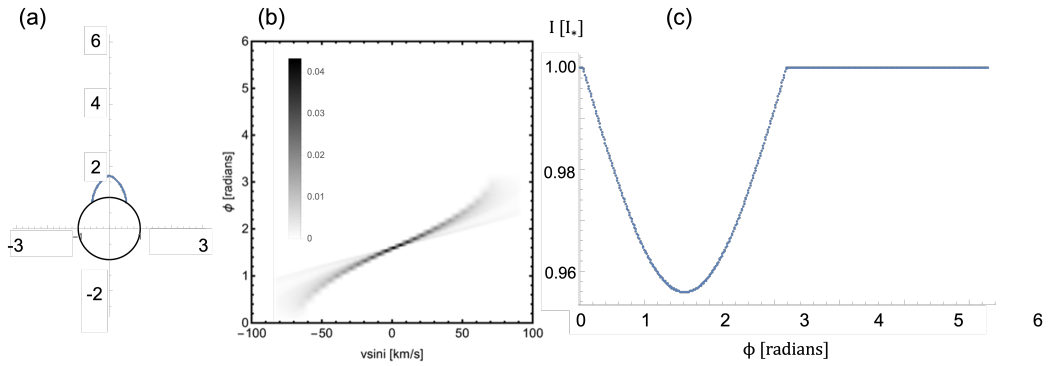

Figure 3.26: (a) the field line shape (b) the associated Hα trail and (c) the light curve for a loop with its summit at co-rotation.

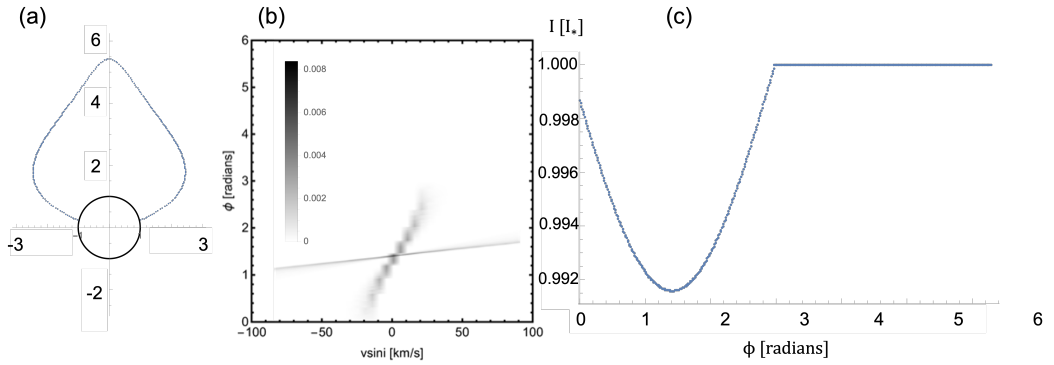

Figure 3.27: (a) the field line shape (b) the associated Hα trail and (c) the light curve for a tall, wide loop.

The tall, wide loop in Figure 3.27 shows a Hα trail with two features: a slow moving footpoint and a faster moving feature relating to material at larger heights. The light curve again is u shaped.

The tall, thin loop in Figure 3.28 shows a similar Hα trail to the case with source surface placed above co-rotation (Figure 3.23). The light curve again looks like a smooth u.

3.7.3 Comparison

Most light curves produce a smooth u shaped dip. Scallop shell like light curves can be produced with an equatorial dipole and an inclination here of 60°. This allows for the multiple dips within the absorption feature as the two features associated with the loop footpoints can each contribute to a small dip, and a combined dip in the centre where both footpoints are infront of the disc at the same time (eg Figure 3.18 or Figure 3.19). If the footpoints

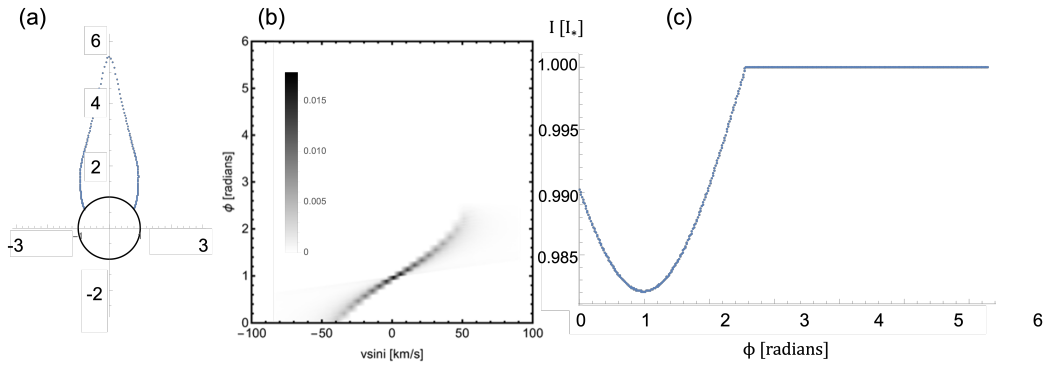

Figure 3.28: (a) the field line shape (b) the associated Hα trail and (c) the light curve for a tall, thin loop.

are very close together, as with a solar-like prominence bearing loop such as Figure 3.17, then the multiple dips cannot be seen as the overlap over too large a range of ϕ so that they combine into one dip. Off to the wings, the gradient of the curve can be seen to have altered although it is slight. The same occurs for tall loops such as Figure 3.20.

With a too large an inclination, such as here with 90°, the scallop shelled behaviour can be completely washed out. The light curves for thin loops appears very similar to when the inclination is higher, but the scalloped behaviour seen in wider loops is not always present. In this case, the summit of the loops transits the disc, and this can be a considerably dense feature and dominate over the footpoints for tall loops (Figure 3.15). For loops at co-rotation however where the summit is empty the behaviour is still present, albeit fainter.

3.8 Conclusions

The results presented in this chapter prove the previous, simplified model to be robust, despite being restricted to the equatorial plane. The overall behaviour of the loop shapes does not alter when translated to a more realistic field geometry that accounts for the full centrifugal force. Allowing for the full effects of rotation does alter results quantitatively, however.

This model produces closed, cooled field lines at a range of heights above the stellar surface, including within the range of the observed slingshot prominences of AB Dor. These cooled solutions at heights of around 4-5 $R_\star$ above the surface (or 5-6 $R_\star$ from the centre of

the star) can be found for a range of field structures; an equatorial dipole, aligned dipole, a dipole with source surface above, or below, the co-rotation radius. The model also produces prominence masses that are comparable to the observations for AB Dor, on the order of 10^{17}g. With these field lines, a stellar corona can be simply modelled to contain a selection of these prominence bearing field lines, which can then be used to generate Hα spectra.

Hα trails can vary with the field structure, but whilst it may be possible to distinguish between the equatorial and aligned dipole, it may be difficult to pick out any other intricacies. The stellar inclination plays an important role in determining if loop summits transit the disc and appear in absorption. With an inclination of 60°, similar to that of AB Doradus, none of the tall loop summits transit the disc. The loop summits are always within the equatorial plane here, regardless of the field geometry, but if the loop summits were above the equatorial plane then it would make it more probable that a transit would occur. This would involve either using a tilted dipole or a more complex field structure such as a quadrupole. This would generate loop summits out of the equatorial plane, though would not alter the pressure distribution. The loop summits would not be pressure maxima, and it is not immediately clear what shape the cooled loops would take. However, the loop summits would be more easily transit the stellar disc and the Hα trails generated would make an interesting comparison to the work presented here. This is also of interest because prominences are observed in Hα trails for AB Doradus at distances of up to 8 stellar radii from the rotation axis, with a similar stellar inclination.

Chapter 4

Modelling prominence formation sites on M-dwarfs

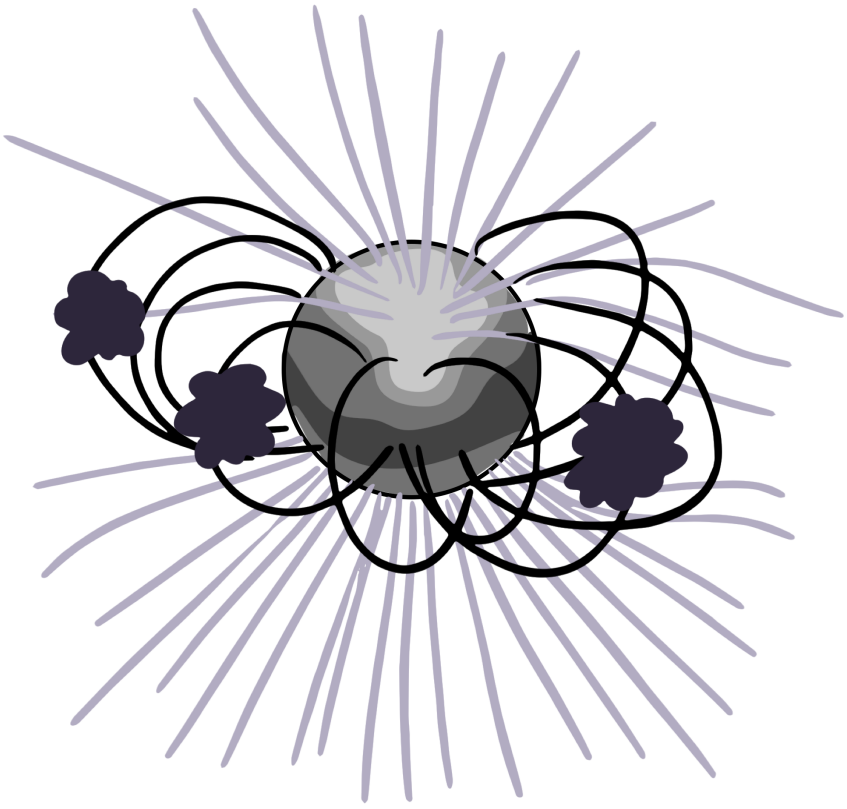

4.1 Introduction

This chapter contains work published in Waugh et al. 2021[137].

Rather than prescribing a field for the star, as in the previous chapter, this chapter uses observed maps of the stellar magnetic field to predict where prominences would have been located around a set of M-dwarfs.

4.1.1 Zeeman Doppler Imaging

Prominence formation on a selection of M-dwarfs is investigated using the observed Zeeman-Doppler Imaging (ZDI) maps available for these stars. ZDI maps provide the magnetic field vector at the surface of the star. With this information, the full coronal magnetic field structure of stars can be generated. Typically this involves assuming the magnetic field to be potential[1] and requires one other boundary condition which can be provided by the location of the source surface.

The Zeeman effect describes the behaviours of atoms and molecules in the presence of a magnetic field, and therefore is a useful tool throughout astronomy as a way of measuring magnetic fields[138]. Consider an isolated atom within the presence of a magnetic field, $\mathbf{B}$. The magnetic field will influence the electrons within the atom, such that the spin (intrinsic angular momentum) of the electron will align either parallel or anti-parallel with the field. This results in a splitting of energy levels and thus a range of possible transitions that would yield different spectral lines than a non-magnetic case. This is shown in Figure 4.1. The change in energy experienced by a split energy level is proportional to the strength of the magnetic field applied[138]. This makes the magnetic field strength quantifiable to observers of the stellar spectral lines. The Zeeman effect results in a splitting or sometimes unresolved broadening of the line profile.

Since stars rotate, all light that is emitted from them is subjected to the Doppler effect. Light that is emitted from the star in the direction that is rotating towards us will be blue shifted from the original wavelength. Light from the side of the star that is rotating away from us will instead be red shifted. This also broadens the spectral line over a range of

[1] A potential field is one with zero volume currents i.e. $\nabla \times \mathbf{B} = \mathbf{0}$.

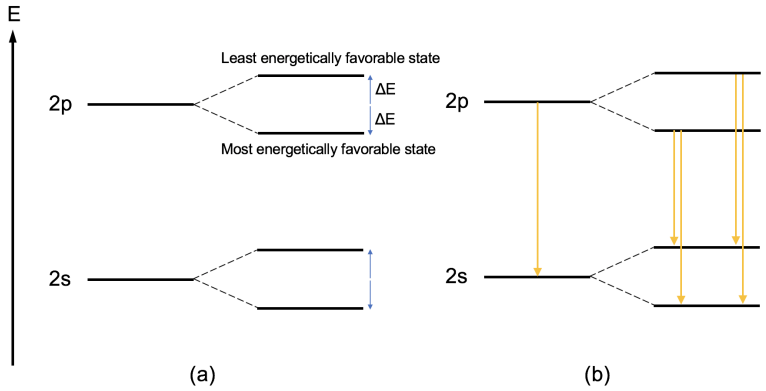

Figure 4.1: (a) shows the splitting in energy levels caused by the magnetic field, whilst (b) shows the change in number, and energy, of the transitions (yellow arrows).

wavelengths, depending on the stellar rotation rate. There is also a shift in wavelength that is associated with the overall motion of the star, since the star will likely be moving towards or away from us. This moves the entire broadened spectral line.

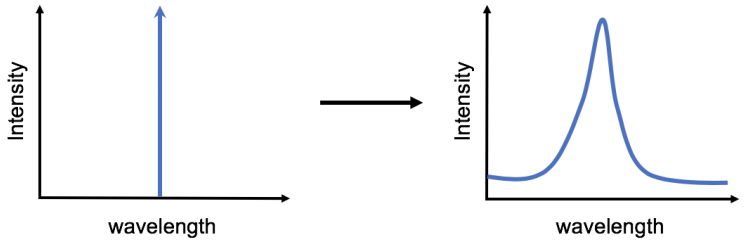

Figure 4.2: Typically, for a given spectral line, we would expect to see a delta function in wavelength. This line is broadened by the Zeeman-Doppler effect.

The combination of these effects is used in determining the magnetic field strength at the stellar surface. ZDI is a useful technique for measuring the surface magnetic field of stars. However, whilst ZDI is useful for measuring large scale fields, it can not resolve finer details from small scale fields. ZDI produces a map showing the net field in each resolution element, so if within a resolution element there is some small scale field with a net field of zero, it can not be distinguished from there being no field in this region.

4.1.2 The stellar sample

The ZDI maps here are observations from the stars in Table 4.1. All stars used here are M-dwarfs, with a range of masses, radii, rotation rates and stellar inclinations, as shown in the table. In some cases, there are maps for multiple years of the same star. The sample used here is from a large survey by the BCool Collaboration [139–141] of M-dwarfs which investigated their magnetic fields. The stars used here were selected from this survey based on their small co-rotation radii. A small co-rotation radius is needed in order to support slingshot prominences in this modelling method.

Maps	M [$M_\odot$]	R [$R_\odot$]	P [days]	i [deg]	R_k [$R_\star$]
V374 Peg (2006)	0.30	0.35	0.45	70	4.77
EQ Peg B (2006)	0.25	0.25	0.40	60	5.80
GJ1156 (2007/08/09)	0.14	0.16	0.33	40	6.57
EQ Peg A (2006)	0.39	0.35	1.06	60	9.21
GJ1111 (2007/08)	0.10	0.11	0.46	60	10.67
GJ1245b (2006/07/08)	0.12	0.14	0.71	40	11.90
GJ182 (2007)	0.75	0.82	4.35	60	12.53
GJ494 (2007/08)	0.59	0.53	2.85	60	13.50
AD Leo (2007/08)	0.42	0.38	2.24	20	14.31
GJ9520 (2008)	0.55	0.49	3.40	45	16.04

Table 4.1: Table of parameters for the stars, and years of observation, used here. Symbols here are for the stellar parameters; M for mass, R for radius, P for period and i for inclination [139–141].

4.1.3 Constructing the coronal field from ZDI maps

The observed ZDI maps are used to construct the coronal field, giving the field vector at the stellar surface. In order to extrapolate into the corona, it is assumed that the field is potential, i.e. $\nabla \times \underline{B} = \underline{0}$ and since it is a requirement that $\nabla.\underline{B} = 0$, they combine to give Laplace's equation $\nabla^2\Psi = \underline{0}$, where Ψ is the flux function. This expression is solved in spherical polar coordinates (R,θ,ϕ) using separation of variables. This gives a solution of spherical harmonics:

$$\Psi = \sum_{l=1}^{N} \sum_{m=-l}^{l} [a_{lm}R^l + b_{lm}R^{-(l+1)}]P_{lm}(\theta)e^{im\phi}. \tag{4.1}$$

Here P_{lm} are the associated Legrendre polynomials. The magnetic components are then given by;

$$B_R = -\sum_{l=1}^{N} \sum_{m=-l}^{l} [la_{lm}R^{l-1} - (l+1)b_{lm}R^{-(l+2)}]P_{lm}(\theta)e^{im\phi} \tag{4.2}$$

$$B_\theta = -\sum_{l=1}^{N}\sum_{m=-l}^{l}[a_{lm}R^{l-1} + b_{lm}R^{-(l+2)}]\frac{d}{d\theta}\Big(P_{lm}(\theta)e^{im\phi}\Big), \tag{4.3}$$

$$B_\phi = -\sum_{l=1}^{N}\sum_{m=-l}^{l}[a_{lm}r^{l-1} + b_{lm}R^{-(l+2)}]\frac{P_{lm}(\theta)}{\sin\theta}ime^{im\phi}. \tag{4.4}$$

a_{lm} and b_{lm} are coefficients that are determined by the boundary conditions.

Considering the radial component of the field, the value at the stellar surface is a known quantity from the ZDI maps. Another boundary condition can be set by assuming that the magnetic field becomes purely radial at some fixed height from the surface. This radius is called the "source surface" and denoted here by R_{ss}. Since it becomes purely radial, it can be described by $B_\theta(R_{ss}) = B_\phi(R_{ss}) = 0$. In the work shown in this chapter, the source surface was set to $R_{ss} = 18R_\star$ for all maps. In order to form prominences in this method at and beyond the co-rotation radius, the magnetic field must be closed to heights beyond co-rotation. Many slingshot prominences are found around or beyond the co-rotation radius and these are the types of prominence that this work models. Thus, this value for the source surface was chosen to ensure that the field would be closed to large enough heights for all stars in this sample.
The full magnetic field structure is then constructed using a code initially developed by Van Ballegooijen, Cartledge & Priest in 1998 for studying filament formation on the Sun [142].

The prominence formation sites here are stable mechanical equilibrium points. These mechanical equilibrium points are those in which the forces acting upon the field line are balanced.

$$\underline{0} = -\nabla p + (\boldsymbol{B}.\nabla)\frac{\boldsymbol{B}}{\mu} - \nabla\Big(\frac{B^2}{2\mu}\Big) + \rho\boldsymbol{g}. \tag{4.5}$$

As earlier in this thesis, p represents the gas pressure, $\boldsymbol{B}$ the magnetic field, μ the permeability of free space, ρ the gas density and $\boldsymbol{g}$ represents the effective gravity. As in the previous chapter, the effective gravity here includes a θ component since this model is not confined to the equatorial plane.

$$\boldsymbol{g} = \Big(-\frac{GM_\star}{R^2} + \Omega^2 R\sin\theta\Big)\hat{R} + \Big(\Omega^2 R\sin\theta\cos\theta\Big)\hat{\theta}, \tag{4.6}$$

In order for a point to be in mechanical equilibrium it must satisfy the condition $\underline{g}.\underline{B} = 0$ as shown by [80]. For these points to *also* be stable, the component of effective gravity along the field line must be decreasing. This ensures that the point is a potential minimum. This condition can be written as

$$(\boldsymbol{B}.\nabla)(\boldsymbol{g}.\boldsymbol{B}) < 0. \tag{4.7}$$

In the following work, it is assumed that where ever there is a stable point, a prominence forms i.e. all stable points are filled with prominence material. The sites are also assumed to be filled to the maximum mass that they can support. This maximum mass is determined by the density through $\rho g = B^2/\mu R_c$ where R_c is the radius of curvature of the field about the stable point [82]. The lifetime of the prominence is then the time taken to supply this material from the surface to the stable point by a thermal wind.

4.1.4 The visibility of prominences

Whether a prominence will be visible to an observer on Earth depends on the stellar inclination. Visible locations around a star are defined as those that transit the stellar disc, this is because prominence observations are typically seen as absorption features in the Hα dynamic spectra.

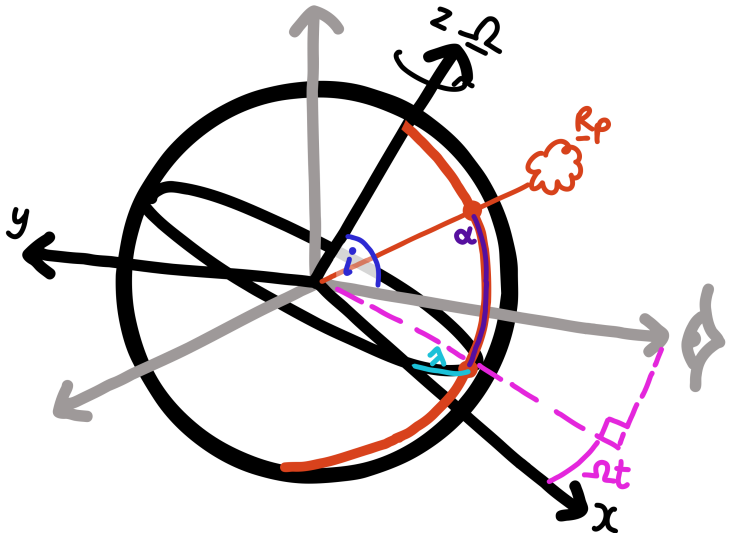

Figure 4.3: Cartoon of the set-up for checking the visibility.

The stable point, or prominence formation site, can be written in Cartesian coordinates

as $\boldsymbol{R}_p = (x_p, y_p, z_p)$, which by coordinate transformation becomes:

$$\boldsymbol{R}_p = |\boldsymbol{R}_p|(\cos(\lambda)\cos(\alpha), \sin(\lambda)\cos(\alpha), \sin(\alpha)). \tag{4.8}$$

Here λ is the prominence phase at time t = 0 and α is its latitude.

The line of sight vector is defined by

$$\hat{\boldsymbol{d}} = (d_x, d_y, d_z) \tag{4.9}$$

which can be written in terms of the stellar inclination (i) and rotation phase (Ωt) as

$$\hat{\boldsymbol{d}} = (\cos(-\Omega t)\sin(i), \sin(-\Omega t)\sin(i), \cos(i)). \tag{4.10}$$

The locations around the star that would transit the stellar disc are found by considering the distance cosine:

$$\cos(\phi) = \frac{\boldsymbol{R}_p.\hat{\boldsymbol{d}}}{|\boldsymbol{R}_p|}, \tag{4.11}$$

which, when expanded, becomes

$$\cos(\phi) = \cos(\lambda)\cos(\alpha)\cos(\Omega t)\sin(i) - \sin(\lambda)\cos(\alpha)\sin(\Omega t)\sin(i) + \sin(\alpha)\cos(i). \tag{4.12}$$

It is a requirement for it to enter the disc that

$$R_* = |\boldsymbol{R}_p|\sin(\phi) = R_p\sqrt{1 - \cos^2(\phi)} \tag{4.13}$$

i.e. $\cos(\phi) = \sqrt{1 - (R_*/R_p)^2}$ which can be combined with Equation 4.12 to give:

$$\cos(\Omega t + \lambda) = \frac{\sqrt{1 - (R_*/R_p)^2} - \sin(\alpha)\cos(i)}{\cos(\alpha)\sin(i)}. \tag{4.14}$$

Equation 4.14 must be ≤ 1 for a transit to occur, i.e. for a prominence to be visible. The visible locations around a star can be found in terms of latitude (α) and distance from the rotation axis (R_p). These plots are referred to here as "visibility plots". Prominence locations are then over-plotted on these visibility plots (see, for example, Figure 4.11).

4.1.5 Prominences as wind gauges

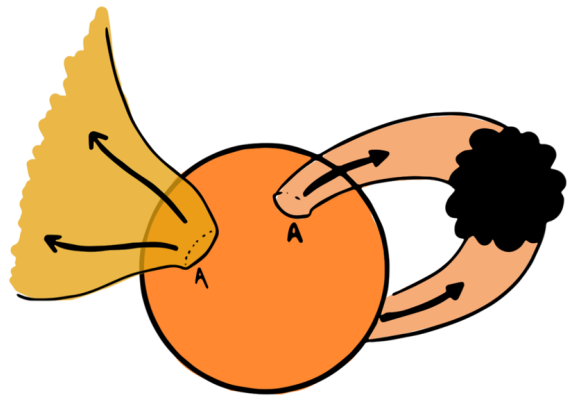

Figure 4.4: Cartoon showing the stellar wind (left) and prominence (right).

Mass loss rates associated from the prominences can be calculated from the flow of material along closed prominence-bearing loops. Prominences are formed in this model by an up-flow of material from the stellar surface, as an isothermal wind, at the temperature of the stellar corona.

The up-flow material is supplied until the mass at the stable point reaches the maximum mass that can be supported there. The time taken to supply this maximum mass is defined here as the prominence lifetime. The lifetime for a prominence can be calculated from the mass loss rate and the maximum mass.

The M-dwarfs in this sample all lie within the "limit-cycle regime" [87]. Because the co-rotation radius of these stars is above the sonic point for the prominence up-flows, the up-flow will keep supplying mass to the stable point, even after the maximum mass is reached. This means that stable points will continually fill up to their maximum mass before being ejected from the star, and then re-filling. Thus, the mass loss rate can be calculated from

$$\dot{M}_{\rm prom} = \rho_p u_p A_p \tag{4.15}$$

since the time-averaged mass loss rate will be equal to the mass flow rate from the surface. Here ρ_p denotes the prominence density, u_p the up-flow velocity of the material and A_p the area of the flux tube that is contributing to the prominence.

Using mass conservation this could be evaluated from any radius above the star, here it is evaluated from the stellar surface i.e.

$$\dot{M}_{\rm prom} = \rho_\star u_\star A_\star. \tag{4.16}$$

The isothermal up-flow of the prominence material ($u_\star$) is set to the coronal temperature, which is here set to $T = 8.57 \times 10^6 K$.[2] The density ($\rho_\star$) is related to the plasma pressure by the isothermal equation of state. The plasma pressure is estimated using $p = \kappa B^2$, where $\kappa = 10^{-5}$ [143], which relates the scaling of the gas and magnetic pressures at the stellar surface. Prominence temperatures were given by Collier Cameron et al.[28] for prominences on AB Doradus as $T_p = 8500K$. This temperature is used here to calculate prominence masses, which are calculated by summing the mass at increments along the field lines, depending on local flux tube volume and local density.

Angular momentum loss rates can also be calculated once the mass loss rates are known:

$$\dot{J}_{\rm prom} = \Omega (R_p \sin\theta)^2 \dot{M}_{\rm prom}. \tag{4.17}$$

Ω is the stellar rotation rate, R_p the stable point spherical radius coordinate and θ the stable point co-latitude. This estimate represents a lower limit to the angular momentum loss rates since it neglects magnetic stresses applied to the outflowing material by the magnetic field.

[2] The coronal temperature of AB Dor.

4.2 Prominence modelling

4.2.1 Where are the prominence formation sites?

Plots showing histograms of the locations of the prominence formation sites are shown in Figures 4.5, 4.6, 4.7, 4.8 and 4.9.

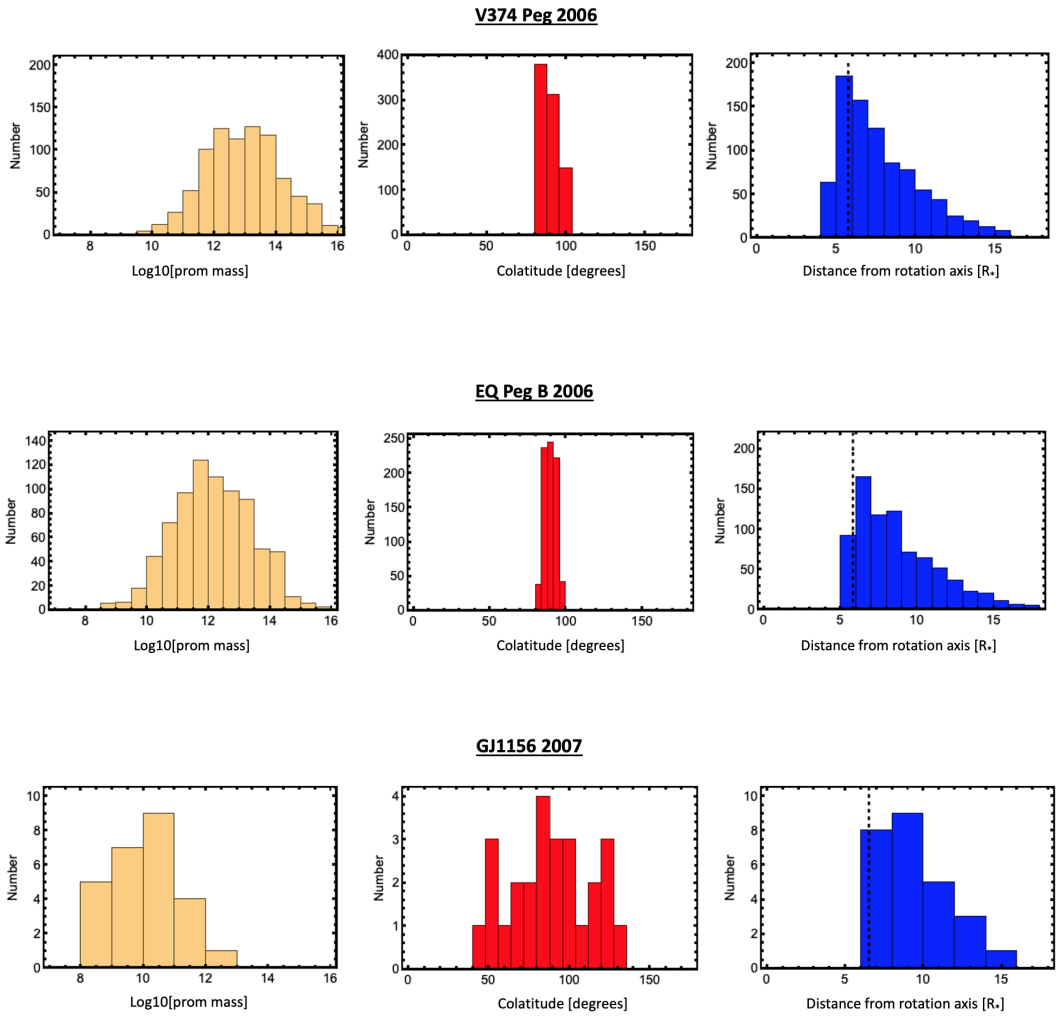

Figure 4.5: Histograms showing the number of stable points with; left: prominence mass, middle: co-latitude and right: distance from rotation axis (cylindrical radius). The equatorial co-rotation radius is shown in the right hand plots as a black line.

Plots typically show a range in masses, with a peak in mass around the central value. This is more apparent in some maps than others, for example EQ Peg A, GJ1111 (2007) and AD Leo (2007). These maps have many stable points, which creates a much smoother histogram than say GJ494 (2008) for which there was only a single stable point found.

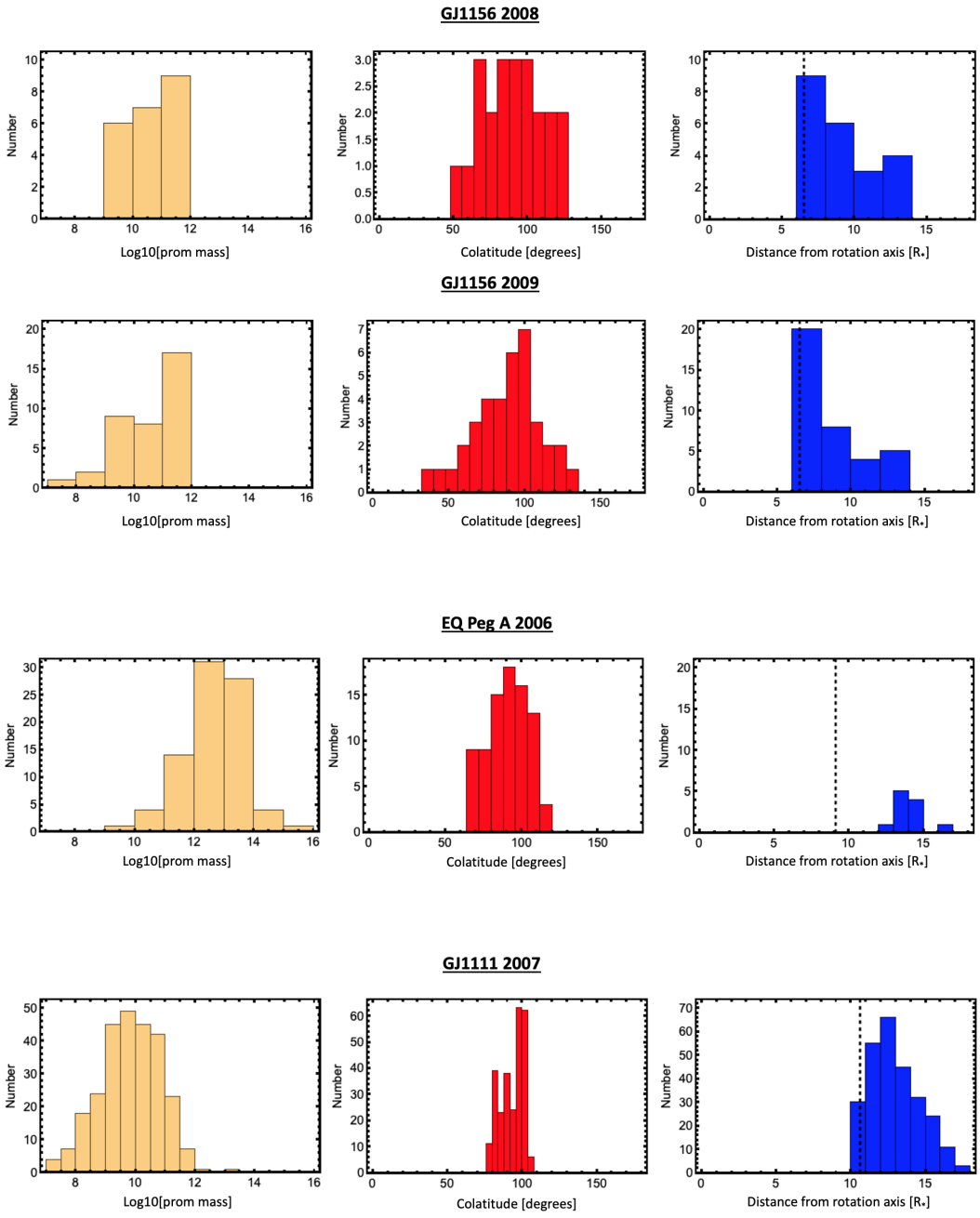

Figure 4.6: Histograms showing the number of stable points with; left: prominence mass, middle: co-latitude and right: distance from rotation axis (cylindrical radius). The equatorial co-rotation radius is shown in the right hand plots as a black line.

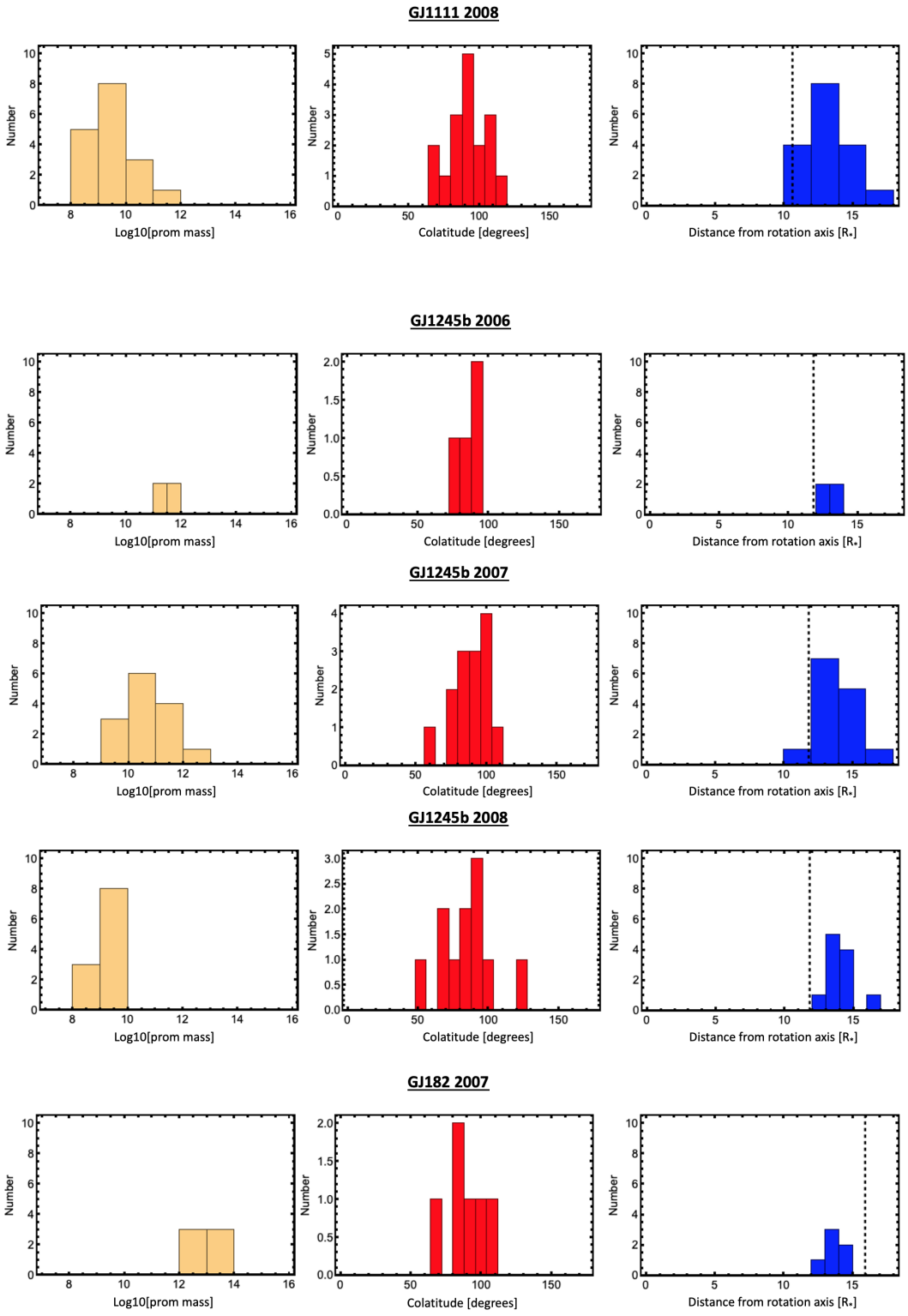

Figure 4.7: Histograms showing the number of stable points with; left: prominence mass, middle: co-latitude and right: distance from rotation axis (cylindrical radius). The equatorial co-rotation radius is shown in the right hand plots as a black line.

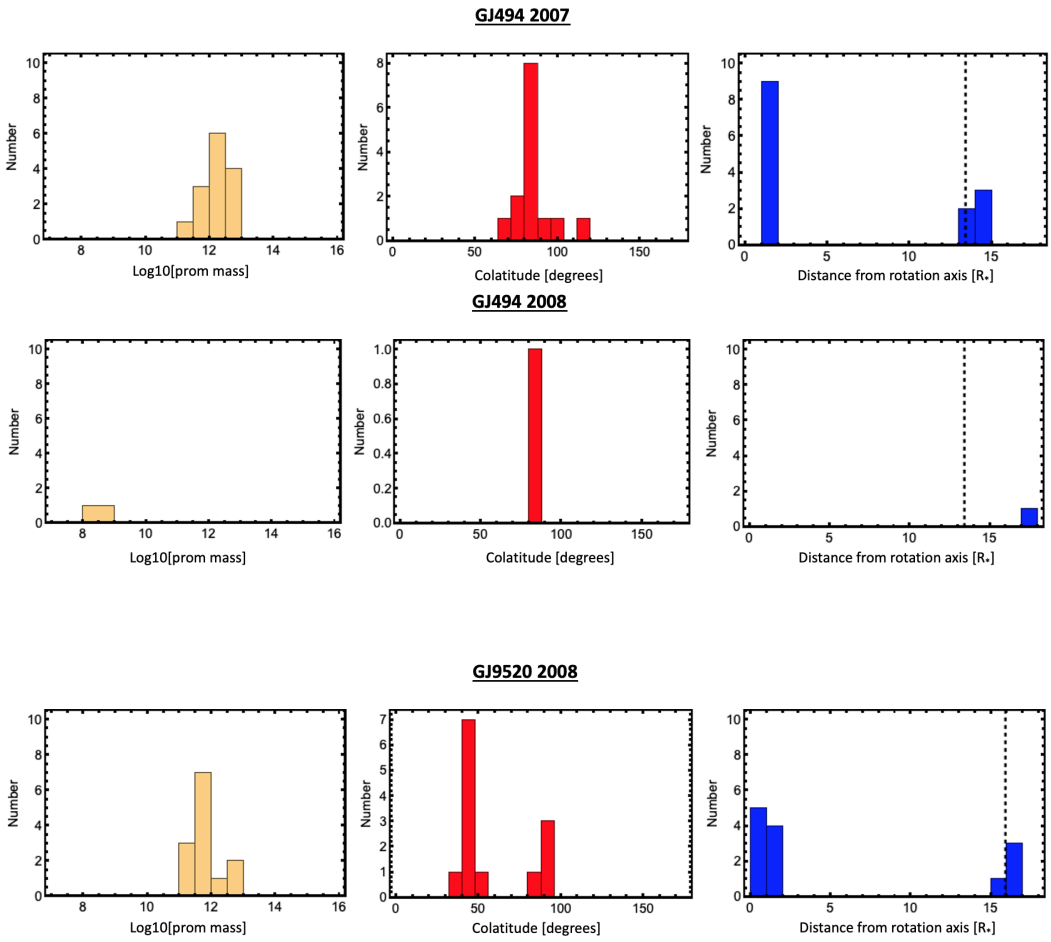

Figure 4.8: Histograms showing the number of stable points with; left: prominence mass, middle: co-latitude and right: distance from rotation axis (cylindrical radius). The equatorial co-rotation radius is shown in the right hand plots as a black line.

Looking at the middle panels of Figures 4.5, 4.6, 4.7, 4.8 and 4.9, the stable points tend to peak about the equatorial plane i.e. a co-latitude of 90 degrees. Again, this is especially apparent for maps that support a large number of stable points. There are a few maps of particular note from these plots. Firstly, GJ494 (2008) with only one stable point, leading to a trivial histogram. GJ9520 (2008) may also stand out as atypical, showing two peaks in the histogram with a gap between. This map supports only a few prominences, which from these histograms can be seen to be low in mass, often at higher latitudes and typically close to the rotation axis. These are likely to be more solar-like prominences rather than the slingshot prominences that this work hopes to model, and therefore little time is spent examining this map in detail throughout this chapter.

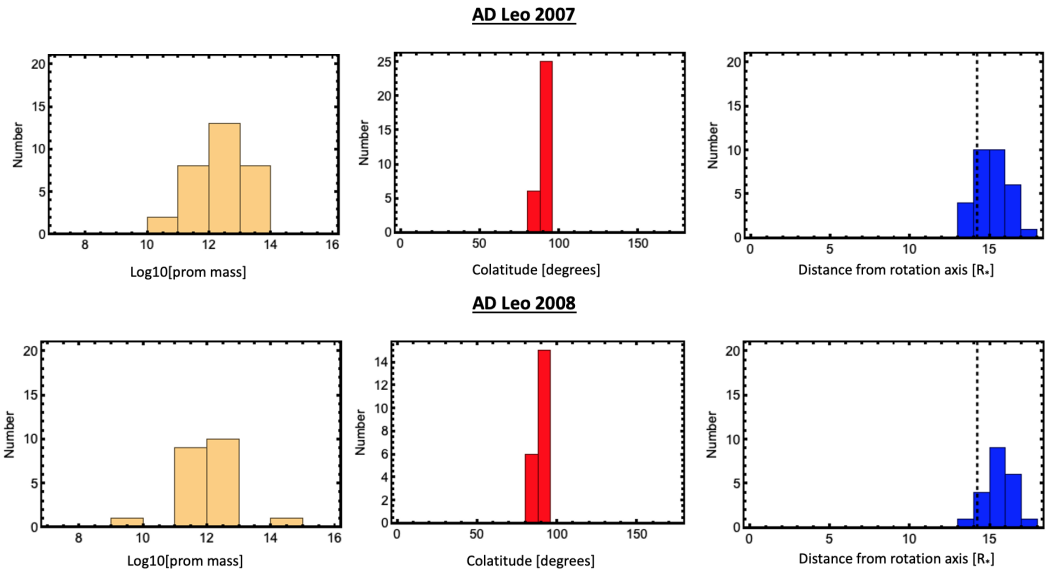

Figure 4.9: Histograms showing the number of stable points with; left: prominence mass, middle: co-latitude and right: distance from rotation axis (cylindrical radius). The equatorial co-rotation radius is shown in the right hand plots as a black line.

GJ1111 (2007) and GJ1156 (2007) both show a large number of stable points in their field structures. The histograms of co-latitude show, in both cases, a central peak around the equatorial plane and also two peaks at higher latitudes.

The right hand panel of these figures shows the distance from the rotation axis of the stable points. This is a cylindrical radius, i.e. $R_p \cos\theta$. The black line on these plots represents the location of the equatorial co-rotation radius. Typically the trend is for the distribution to peak just beyond this radius, though this is not always clear in the maps with few stable points. GJ9520 (2008) again shows a split distribution, with multiple stable points very close to the rotation axis, and a smaller number beyond the co-rotation radius. GJ494 (2007) shows similar behaviour. GJ182 (2007) also has few stable points, and all of these are supported close to the rotation axis.

Prominences around all maps are most likely to form about the equator of the star. Here the effective gravity is largest, which helps support these slingshot prominences at large distances from the stellar surface. The most massive prominences are typically found about the equatorial plane. Distributions of prominence mass with stable point co-latitude is shown in Figures 4.10 and 4.11. The red line in these figures shows the equatorial plane, i.e. a co-latitude of 90 degrees. In many cases, the stable points can be seen to take a large

range of co-latitudes when low in mass, but that high mass prominences are typically found very close to the equatorial plane. EQ Peg B, EQ Peg A and GJ1111 (2007) show this particularly well, since they support a great number of stable points, although the behaviour can be seen in many other maps too.

As before, GJ9520 (2008) shows behaviour very different to the other maps in this sample. There is a clump of stable points at a high latitude, around 45 degrees. These stable points support low mass prominences.

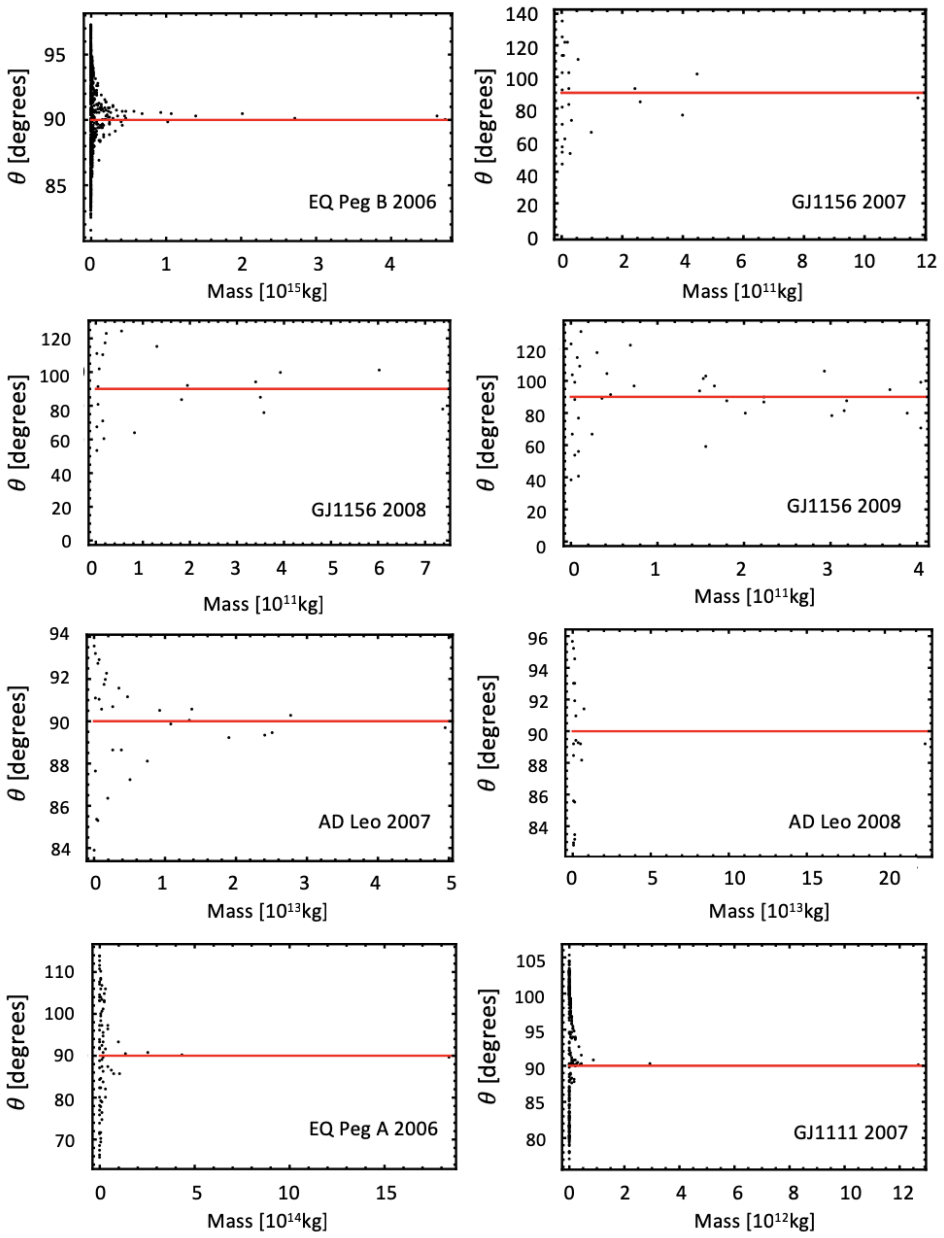

Figure 4.10: Plots showing the co-latitude of and mass supported by each stable point found on each map. The red line shows the equatorial plane.

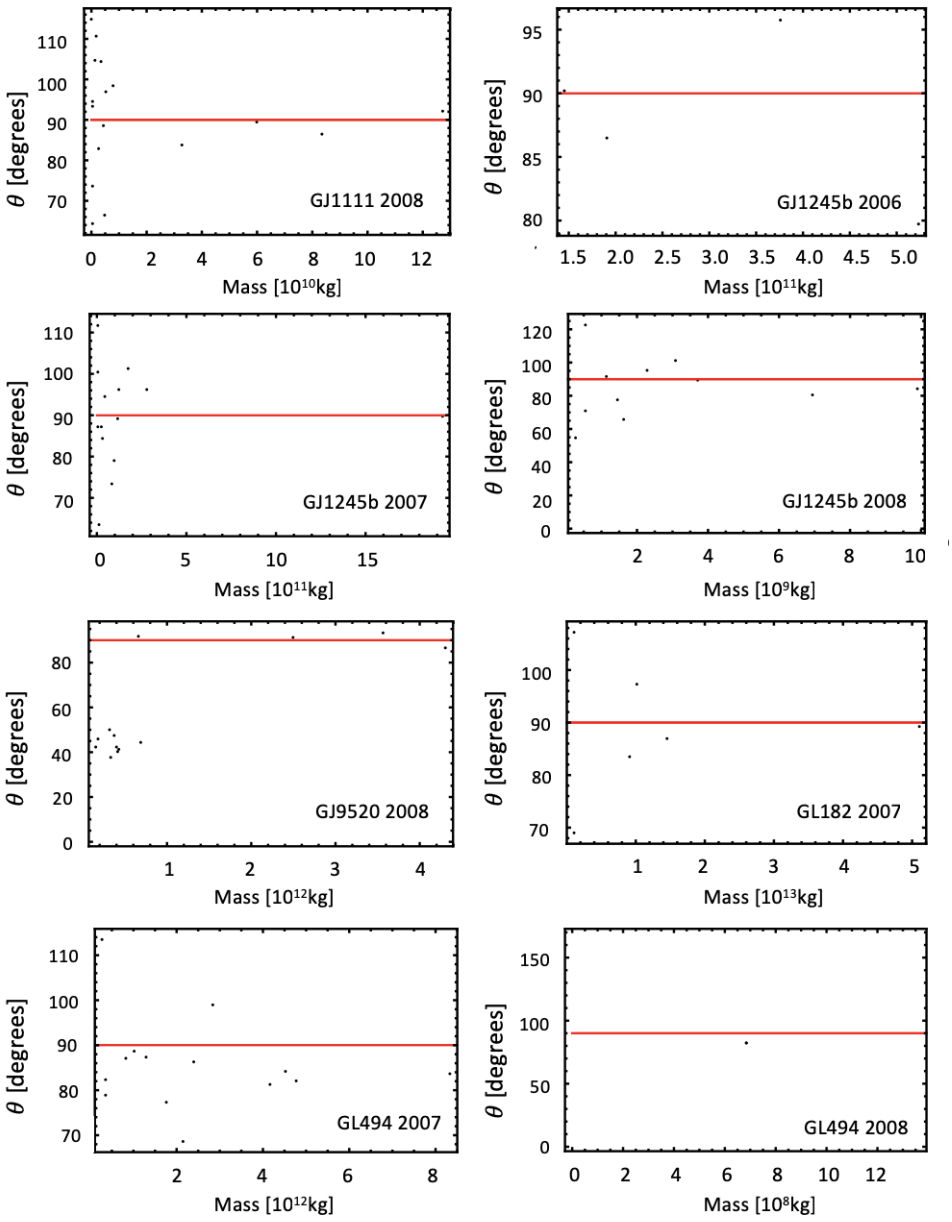

Figure 4.11: Plots showing the co-latitude of and mass supported by each stable point found on each map. The red line shows the equatorial plane.

4.2.2 Are these prominences geometrically visible?

Whilst most maps investigated here support many stable points, these may not be visible to observers. Prominences are typically only visible if they transit the stellar disc, creating absorption features in the Hα dynamic spectrum. There are exceptions where the star is viewed pole on and prominence material may be seen in emission. However, these observations are less common than those present as absorption features. Therefore throughout this chapter, a visible prominence is one which would transit the stellar disc from our vantage point on Earth.

Figures 4.12 and 4.13 show plots of the locations around each map in terms of the radial coordinate (R_p) and latitude ($\pi/2$ - θ). The grey regions are those locations around the star that never transit the stellar disc, thus these locations would never be visible. The middle, white section show the locations that would transit the stellar disc. The co-rotation radius for each map is shown by the purple dashed line. The co-rotation radius varies with stellar latitude, with a minimum value in the equatorial plane and reaches an asymptote at the rotational pole, where the centrifugal term goes to zero.

Prominences that form closer to the stellar surface are more likely to be visible, since they can take a large range of latitudes and still transit the stellar disc. As prominences form at larger heights above the surface, the range of latitudes they can take and still be visible decreases sharply. The "ideal" prominence latitude is $(90 - i)$, which would ensure that a prominence would be visible at all radii above the stellar surface.
The prominences are shown on these plots and are coloured based on their mass, with red being the most massive prominence supported on that map.

Prominences can be seen to form typically around the equatorial plane. There are some cases that show a larger spread of latitudes for example GJ1156 (2007, 2008, 2009), GJ1111 (2008) and GJ1245b (2007), although this spread still appears to centre on the equatorial plane.

The largest mass prominences on all maps, shown in red, form around the equatorial co-rotation radius. In almost all maps this makes them impossible to observe as absorption features, since this region around the star rarely lands in a visible region around the star.

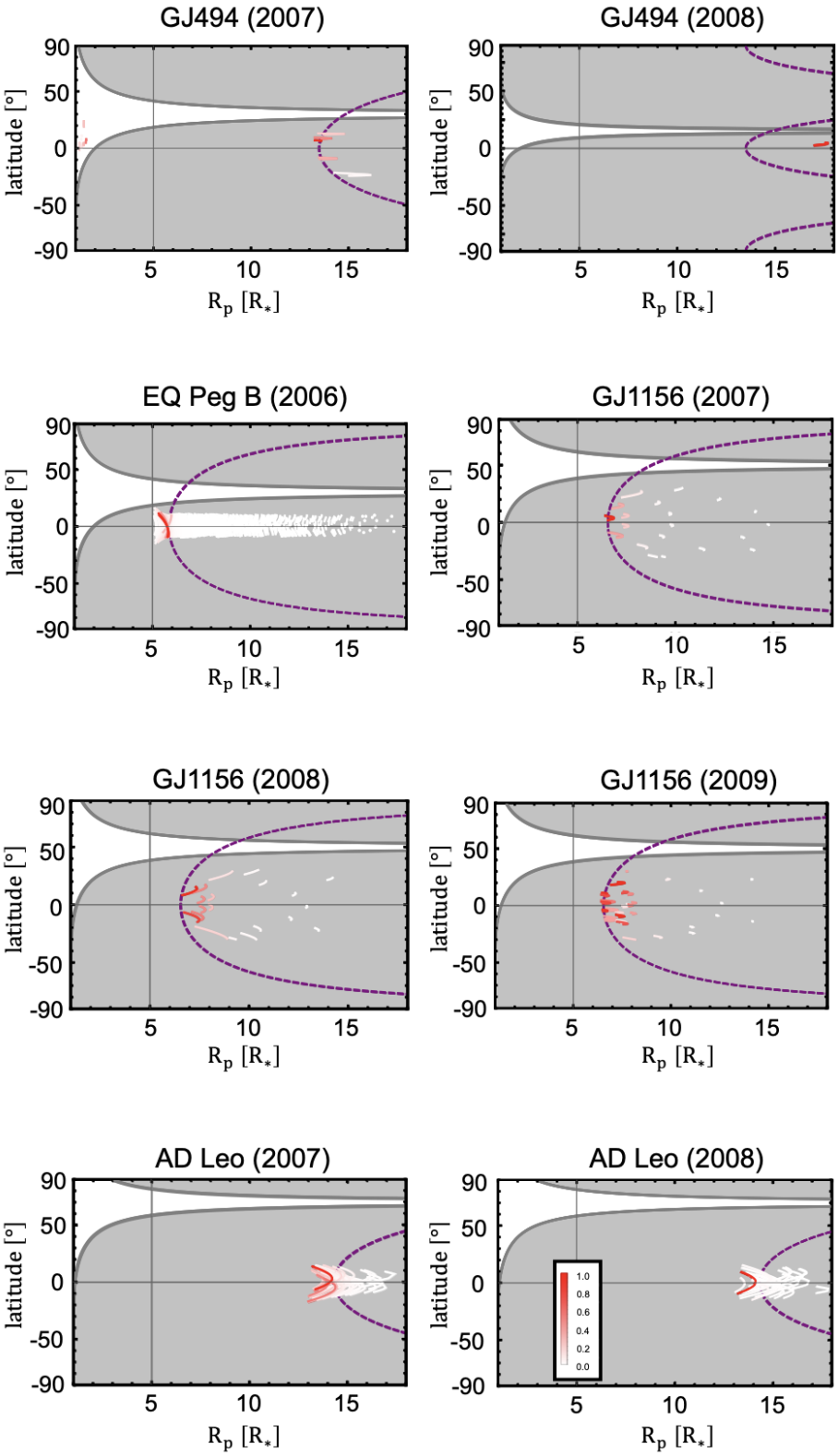

Figure 4.12: Plots showing the visible regions around a star (white) and "invisible" (grey). Prominences are shown, scaled to the maximum mass on each map. The co-rotation radius is shown by the purple dashed line.

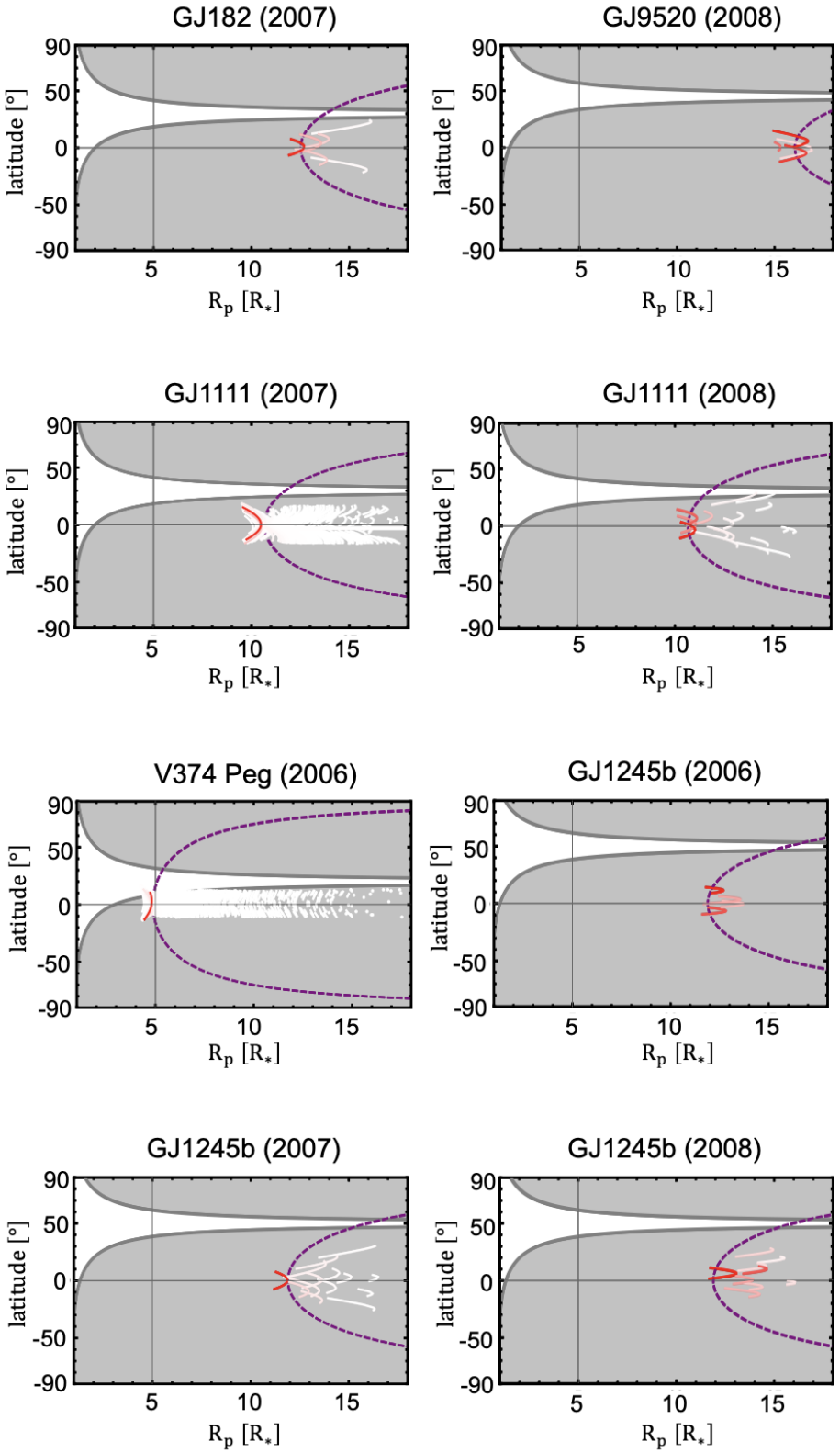

Figure 4.13: As in Figure 4.12.

In addition, the formation of prominences around the equatorial plane makes them difficult to observe through ZDI methods. The inclination of stars that can be reasonably observed using ZDI methods are restricted. Stars with very high inclinations (i.e. viewed directly into the equator) produce inaccurate field maps, because it is unclear which hemisphere light was emitted from. This makes distinguishing between the two hemispheres almost impossible.

The maps in this sample have a range of dipole tilts, from aligned with the rotation axis to perpendicular. This concept was depicted in the cartoon Figure 3.1 from Chapter 2. The dipole tilt determines where prominences can form since it alters the locations at which $g.B = 0$ and $(B.\nabla)(g.B) < 0$, which are the requirements for a location to be a stable equilibrium. Aligned dipoles generate prominences tightly bound to the equatorial plane, for example AD Leo (2007, 2008), EQ Peg B and V374 Peg. Tilted dipoles, such as GJ1156 (2007, 2009) and GJ1245b (2008), allow for the formation of prominences at higher latitudes. Hence, the tilt of the dipole axis is responsible for the locations at which prominences can be supported on a given star. This influences whether prominences are visible around a star.

The stellar inclination also determines the visibility of prominences. The inclination determines which locations around a star are visible, for example V374 Peg allows for prominences around the equatorial co-rotation radius to be partly seen, however AD Leo and GJ1245b have very high inclinations, making the equator (where prominences typically form) invisible to observers.

The stellar inclination for a star is fixed, however the dipole tilt will change with changing large scale field structure. Thus, prominences may not be visible on a star one year but be visible at a later date.

4.2.3 How does the prominence mass distribute?

Figure 4.14 shows the distribution of mass over latitude for the maps in this sample. Maps are organised by their dipole tilt. Aligned dipoles are on the right hand side of this figure, with latitudes of the dipole axis close to 90 degrees. Very misaligned dipoles are on the furthest left of this figure, with low dipole axis latitudes. The colour represents the prominence mass, binned into 1° latitude bands. These masses are normalised individually for

each map, scaled to the maximum binned mass. These maximum masses are shown in the second column of Table 4.2.

Map	Max prom. mass in 1° latitude band [kg]	Total prom. mass supported [kg]	% mass visible
EQ Peg B 2006	2.6×10^{16}	3.7×10^{16}	0
GJ1156 2007	1.2×10^{12}	2.9×10^{12}	0.1
GJ1156 2008	7.4×10^{11}	3.5×10^{12}	0
GJ1156 2009	5.9×10^{11}	4.8×10^{12}	0.2
AD Leo 2007	1.3×10^{14}	2.3×10^{14}	0
AD Leo 2008	2.4×10^{14}	2.6×10^{14}	0
EQ Peg A 2006	1.9×10^{15}	3.6×10^{15}	0.1
GJ1111 2007	2.0×10^{13}	2.6×10^{13}	0
GJ1111 2008	1.3×10^{11}	3.4×10^{11}	0.7
GJ1245b 2006	5.2×10^{11}	1.2×10^{12}	0
GJ1245b 2007	2.0×10^{12}	2.9×10^{12}	0
GJ1245b 2008	9.9×10^{9}	3.1×10^{10}	0
GJ9520 2008	4.3×10^{12}	1.4×10^{13}	22.9
GJ182 2007	5.1×10^{13}	8.7×10^{13}	0
GJ494 2007	8.3×10^{12}	3.5×10^{13}	50.4
GJ494 2008	6.8×10^{8}	6.8×10^{8}	0
V374 Peg 2006	6.5×10^{17}	5.1×10^{17}	12.9

Table 4.2: Values of the maximum prominence mass supported in any 1° latitude band, the total mass supported in each star and the percentage that is visible.

Aligned dipoles show material that is confined close to the equatorial plane, with a smooth distribution. Tilted dipoles on the other hand have stable points spread over a wide range of latitudes, and thus an extended distribution in latitude. These tilted fields support high latitude prominences, which support little mass. These distributions are clumpy, compared to the smooth distributions seen around aligned dipoles. The largest masses are found within the equatorial plane, regardless of field geometry. The centrifugal term in the effective gravity is largest here, and this does not depend on field structure.

The "bistable stars" are on the left hand side of Figure 4.14. These are the very low mass M-dwarfs with weak but complex field structures. These two factors result in lower mass prominences on these stars when compared to others in the sample, and finding stable points in these fields is difficult. This creates the clumpy distribution.

The total mass supported on these maps ranges from 6.8×10^{8}kg on GJ494 (2008) to 5.1×10^{17}kg on V374 Peg. For most stars, the total mass is on the order of 10^{12}-10^{14}kg.

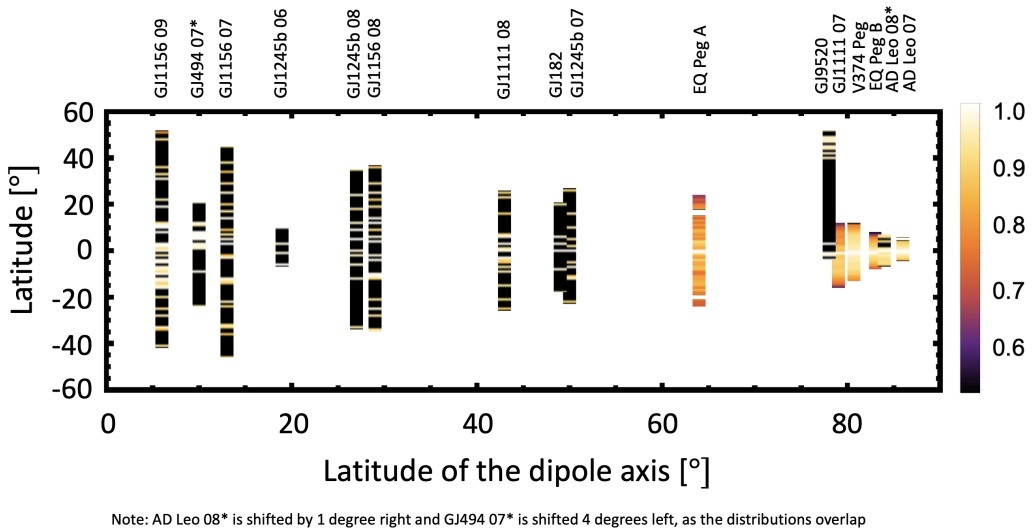

Figure 4.14: The range of latitudes where stable points are supported on each map, against latitude of the dipole axis. The prominence mass supported on each map is shown by the colour, and is scaled to each map. Equatorial dipoles are those on the furthest left hand side and a fully aligned dipole would be situated at the furthest right.

However, the visible mass is much smaller than this total value. GJ494 (2007) shows the largest fraction of mass visible at 50.4%, then GJ9520 (2008) at 22.9%. In both cases, these prominences all lie very close to the stellar surface and are likely to be closer to solar prominences than slingshot ones. V374 Peg shows the next largest percentage mass visible, about 13%. These prominences are about the equatorial co-rotation radius and slingshot prominences. However, for the remaining maps, the percentage of total mass that is visible lies below 1%.

4.2.4 Which stars would make good candidates for observing prominences?

This research has established that while prominence support is likely a very common occurrence on these stars, the visibility of these prominences is far from guaranteed. In order to establish which kinds of star would make good candidates for observing these prominences, the follow points are reiterated:

- stars with small co-rotation radii allow for prominence formation at lower heights than stars with large co-rotation radii. These prominences are also likely to be the most massive.

- A high stellar inclination is preferable, as it allows the observer to view into the equatorial plane and see the highest mass prominences.
- Alternatively, if viewing a star with a low stellar inclination, it should have a dipole tilt with a low latitude i.e. highly misaligned. This allows for the support of high latitude prominences around the star, which whilst less massive could still transit the stellar disc. Those prominences in the equatorial plane of such a star would never transit the disc.

Whilst the inclination of a star can not be changed, the dipole tilt will not be a constant. For the stars in this sample where maps from multiple years were available, it is clear that the dipole tilt has changed with time. Our Sun has a magnetic cycle of 22 years, and other solar like stars have also been observed to show some sort of cycle. Jeffers [144] found a stellar cycle on the star Tau Boo of 120 days, whilst Boro Saikia [145] showed a cycle length of 14 years for 61 Cyg A. M-dwarfs such as those used here can have magnetic fields that are stable for long periods of time (Morin 2008 [140] and Vida 2016 [146]). However, even a small change in the large scale field structure could change the latitude of the dipole axis, and likely alter the locations of prominence formation. The star AD Leo, which is in this sample, was found to have magnetic field variability over a long time period [147], and others in this sample may have similar behaviour.
A stellar cycle, or some variability in the field structure, would cause a star to move across the plot (Figure 4.14) over time. Hence, its prominence distribution may at times be smooth and confined close to the equatorial plane, and at other times be dispersed and clumpy. This also means that it may be possible to observe prominences on a star some years, but not others, regardless of the stellar inclination. Equally, observing a star but seeing no evidence for prominences does not mean that they are not present. There is no way to distinguish between a star with no prominences and a star where prominences are not visible due to geometric effects.

Looking specifically at the stars in this sample, the maps GJ1156 (2007/2009), EQ Peg A (2006), GJ1111 (2008), GJ9520 (2008), GJ 494 (2007), V374 Peg (2006) showed visible prominences. The visible prominences found on GJ9520 are very close to the stellar surface and are likely to be more similar to solar-like prominences than the slingshot prominences investigated here. They are also unlikely to be visible in observations, due to their low

masses and heights. Thus they are not investigated in depth here. In most cases where prominence material could be visible, less than 1% of the total mass is visible. V374 Peg is notable star in the sample as there are observations of prominences on this star to compare to. These do not exist for others in this sample. This work suggests only 13% of the total prominence mass to be visible, and this prediction is an upper limit. The masses predicted here assume that, at a given time, all prominence formation sites are filled when in reality not all sites will be filled at once. Thus, some of the stable points will not be filled at the time of an observation, making the total mass visible less than this 13%. This suggests that the observed predictions for prominence masses on V374 Peg is far lower than the true value. This also extends to other stars in which prominences have been observed. Therefore, of these stars the best candidates for prominence observing are V374 Peg, GJ1111, EQ Peg A and GJ1156. The stars GJ494 and GJ9520 are also potential candidates although their prominences are likely to be very close to the stellar surface.

4.2.5 What are the prominence mass loss rates?

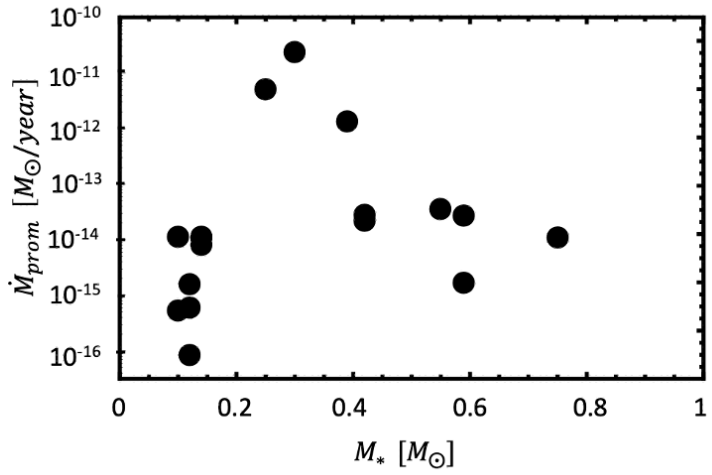

Figure 4.15: Prominence mass loss rate (in solar masses per year) against stellar mass (in solar masses).

Plotting the mass loss rate of prominences against the stellar mass shows the presence of two groups of stars (Figure 4.15). The higher mass star group shows an increase in mass loss rate as stellar mass decreases. On the other hand, the group of stars with very low mass, the bistable stars, show a decrease in mass loss rate with a decrease in stellar mass.

As previously mentioned, these bistable stars have weak and complex field structures that prohibit them from forming massive or many prominences. This leads to low prominence mass loss rates. Due to the complex field structures of these stars, the prominences that do form are often found at higher latitudes, where less mass can be supported due to the weaker effective gravity term that must balance the magnetic tension. For the other group of stars, however, a decrease in stellar mass leads to an increase in prominence mass loss rate due to the increased magnetic field strength. Total prominence mass will scale with the magnetic field strength squared [82], and generally this increases with decreasing stellar mass. The largest mass loss rates in this sample are for the stars V374 Peg, EQ Peg A and EQ Peg B. These stars have strong magnetic fields and aligned dipole axes, making them great candidates for supporting large prominence masses. They also all have small co-rotation radii, which also helps to drive up prominence masses and mass loss rates. This is because large prominences typically form around, but not at, the equatorial co-rotation radius. Since field strength decreases with height, stars for which large prominences can be supported at lower heights can be supported by larger field strengths.

Figure 4.16 shows relates the prominence mass loss rate to the observed X-ray flux, and the data is also given in Table 4.4. The stellar values for the X-ray flux were found through Vizier [148] and Simbad [149] and can be found in the following references; [150–152]. The vertical axis of the plot is the prominence mass loss rate per unit surface area that contributes to the prominence. The values from this work are shown in (a) of this figure as black points. There is a lot of scatter on this plot, that is present even for stars in which there are multiple maps. The blue dashed line gives the line of best fit for this data, which is $\dot{M} \propto F_X^{1.32}$. This value is close to the observationally derived values for the wind, as given in Table 4.3. It is worth noting that the scatter in this plot is also seen in the data for the wind values. That the scatter seen in this work is present even for stars with multiple maps, implies that the scatter is intrinsic. This is due to variation in the field and therefore could be linked to stellar cycles.

The relation from the line of best fit is close to the wind derived value, specifically from Wood [96]. This provides further evidence that prominences could indeed be good proxies for measuring wind mass loss rates, as in the model by Jardine and Collier Cameron, 2019 [87]. An important consideration, however, is that once this plot is made with only the

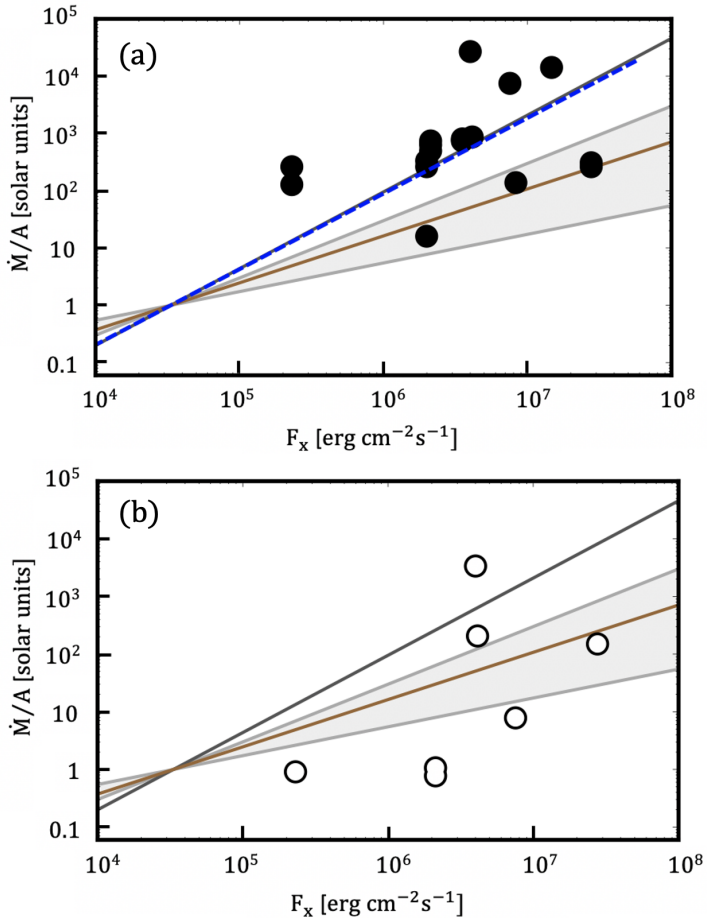

Figure 4.16: (a) Plot showing the prominence mass loss rate per unit area against observed X-ray flux. The black points show the values from this work and the blue dashed line is the line of best fit. Other lines represent literature values for the wind mass loss rates, as given in Table 4.3. (b) Plot showing the visible fraction of the mass loss.

visible prominences, the results no longer match the wind values well. This is shown in Figure 4.16 (b). This figure shows the mass loss rate per unit area that would have been visible, based on the geometrically visible prominences. These values are much lower, and for some stars there is no visible prominence mass loss at all. The exact values of the visible $\dot{M}/A$, plotted in Figure 4.16(b), are given in the final column of Table 4.4.

V374 Peg is again especially interesting, as it can be directly compared to the work of Jardine and Collier Cameron [87] from the observed values. The authors predicted a mass loss rate per unit area of 2×10^4 solar units and the value here is 10 times their predicted value. This is actually consistent with the authors, since this work has predicted only around 10% of the mass to be visible.

Relation $\dot{M}/A \propto F_X^a$	Reference	colour in Figure 4.16
$a = 1.34$	[96]	dark grey
$a = 0.82$	[153]	brown
$a = 0.5$ to 1	[154]	light grey
$a = 1.32$	the prominence model in this work	blue

Table 4.3: Table of relations between $\dot{M}/A$ and F_X.

Map (year)	F_X [10^6 ergcm^{-2}s^{-1}]	Prominence $\dot{M}/A$ [$10^{-14}A_\odot$]	Surface area contributing to prominences [%]	Visible $\dot{M}/A$ [$10^{-14}A_\odot$]
EQ Peg B 2006	6.51	14103	4.67	0.0
GJ1156 2007	0.46	759	0.48	0.8
GJ1156 2008	0.02	624	0.42	0.0
GJ1156 2009	0.02	514	0.68	1.0
AD Leo 2007	3.52	752	0.21	0.0
AD Leo 2008	3.85	816	0.15	0.0
EQ Peg A 2006	5.09	7643	1.15	7.6
GJ1111 2007	0.06	265	2.85	0.0
GJ1111 2008	0.02	128	0.28	0.9
GJ1245b 2006	0.95	327	0.07	0.0
GJ1245b 2007	0.20	267	0.25	0.0
GJ1245b 2008	4.27	17	0.21	0.0
GJ9520 2008	3.87	890	0.13	203.7
GJ182 2007	1.20	135	0.10	0.0
GJ494 2007	0.34	298	0.26	150.2
GJ494 2008	0.01	253	0.02	0.0
V374 Peg 2006	54.93	25857	6.48	3335.6

Table 4.4: Table of values for Figure 4.16. X-ray fluxes are calculated from the X-ray fluxes observed at Earth and the distance to each star.

The percentage of the stellar surface that supplies the prominences are given in column 4 of Table 4.4. This value is typically below 1%, with a few maps with higher percentages. V374 Peg has the highest surface area contributing to prominences at around 6%, and EQ Peg B is also notably larger than the rest at around 5%. These maps have strong fields and aligned dipoles, so these relatively large percentages are sensible. However, most maps show a very small percentage of the stellar surface contributing to prominence mass loss. In the work of Jardine and Collier Cameron [87], the authors assumed a prominence contributing surface area of 1% of the stellar surface. This work is consistent with that being a good "ball park" figure.

Overall, this work suggests that using prominences as wind gauges is a reasonable method of gathering data on the mass loss rates of low mass stars. However, it is apparent that these observational predictions will underestimate the true value, the extent to which will depend on the proportion of prominence mass visible to observers. Observational values will always underestimate the mass loss, often greatly so. This should be kept in mind when such predictions are made.

It is worth commenting that Woods et al. [96] plot mass loss rate per unit surface area against X-ray flux in order to remove the relationship of the radius of the star, and that these are X-ray fluxes at the stellar surface. It would also be interesting to plot this against X-ray luminosity.

4.2.6 What are the prominence angular momentum loss rates?

Plotting the angular momentum loss rate against stellar mass gives Figure 4.17, and shows two groups of stars and the same behaviour as the mass loss rates. This is not surprising given the linear relationship between mass loss rate and angular momentum loss rate. Again, the "bistable" stars can be seen at the bottom left of the plot.

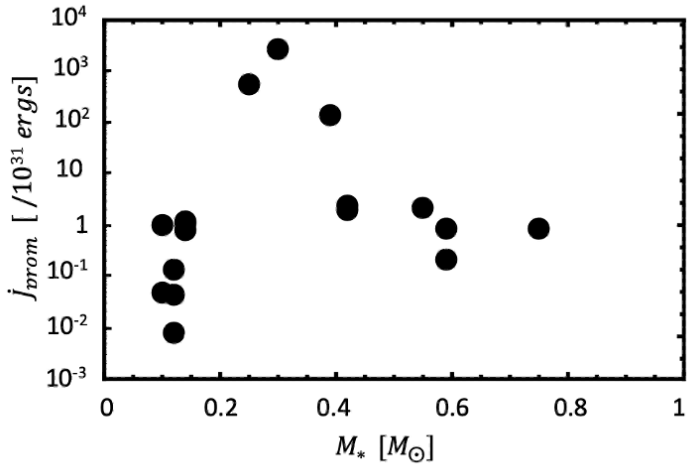

Figure 4.17: Angular momentum loss rate against stellar mass.

The spin-down timescales are calculated from this angular momentum loss rate as $\tau = J_\star/\dot{J}_p$. These timescales are given in Table 4.5, where there are a wide range of values from 0.1Gyr for V374 Peg to 588.2Gyr for GJ494 (2008). These values are lower limits on the true

Map	$\dot{M}_{\rm prom}$ [$M_\odot$/year]	$\dot{J}_{\rm prom}$ [ergs]	Prominence spin-down timescale [Gyr]
EQ Peg B 2006	5.2×10^{-12}	5.8×10^{33}	0.2
GJ1156 2007	1.2×10^{-14}	1.2×10^{31}	20.0
GJ1156 2008	8.4×10^{-15}	8.1×10^{30}	29.4
GJ1156 2009	1.1×10^{-14}	1.1×10^{31}	21.4
AD Leo 2007	2.8×10^{-14}	2.4×10^{31}	24.2
AD Leo 2008	2.2×10^{-14}	2.0×10^{31}	29.4
EQ Peg A 2006	1.4×10^{-12}	1.4×10^{33}	0.7
GJ1111 2007	1.1×10^{-14}	1.0×10^{31}	5.5
GJ1111 2008	5.4×10^{-16}	4.9×10^{29}	116.7
GJ1245b 2006	6.2×10^{-16}	4.5×10^{29}	159.3
GJ1245b 2007	1.6×10^{-15}	1.4×10^{30}	52.6
GJ1245b 2008	8.5×10^{-17}	8.1×10^{28}	894.8
GJ9520 2008	3.6×10^{-14}	2.2×10^{31}	38.2
GJ182 2007	1.1×10^{-14}	8.9×10^{30}	285.6
GJ494 2007	2.8×10^{-14}	8.8×10^{30}	114.2
GJ494 2008	1.7×10^{-15}	2.2×10^{30}	588.2
V374 Peg 2006	2.4×10^{-11}	2.8×10^{34}	0.1

Table 4.5: Table of mass and angular momentum loss rates. Also shown are the spin down timescales associated with the prominence angular momentum loss rates.

value of the angular momentum loss rate as this work has assumed that there is no magnetic stressing, and this means that the spin down timescales are upper limits. The faster rotating stars in the sample lose more angular momentum from this prominence ejection than the slower rotators, which means that the prominences act as a regulation mechanism which results in the rotation rates of stars converging as they age. The range of angular momentum loss rates for this sample of maps spans about 5 to 6 orders of magnitude. A large range was also seen in the mass loss rates in Figure 4.15. This huge range occurs over a very small variation in stellar mass - only about a factor of 4 in this sample from $0.1M_\odot$ to $0.8M_\odot$. Despite the very similar mass for stars in this sample, there is no one value of mass loss or angular momentum loss rates that would have been a suitable choice to represent these stars. This huge range of values is due to the total prominence mass supported on stars having multiple factors which includes; field strength, latitude of the dipole axis, stellar rotation rate and co-rotation radius. It is also important to keep in mind that these prominences will not be present for all of a stars lifetime and thus will only contribute to the angular momentum at certain points in its evolution.

4.2.7 Impact on orbiting exoplanets

The ejection of prominences clearly has consequences for the star itself, however perhaps less obvious is the impact on orbiting planets. Planets orbiting a star will experience the stellar wind and the intermittent wind. But planets orbiting a star with these slingshot prominences, routinely ejected into the stellar system have the potential to orbit into the path of ejected prominence material, will also experience intermittent prominence ejection. It is assumed here that this theoretical planet orbits the star within the stellar equatorial plane, since this would be the most common orientation for planetary orbit.

Figure 4.18 shows (a) the maximum percentage of the orbit that this planet would experience prominence ejecta material for the stars in this sample. The horizontal axis shows the latitude of the dipole axis, with the right hand side showing an aligned dipole and left hand side showing a fully misaligned dipole. As well as the assumption that the planet resides in the equatorial plane, it has also been assumed that if the ejected material could collide with the orbiting planet, then it does. This is why the percentage of the orbit intercepted (the vertical axis of Figure 4.18) is a maximal value.

This percentage was calculated by first selecting the range of latitudes that could collide with the planet, i.e. the angular extent of the planet (see Figure 4.19). The longitude of the prominence stable points within this range of latitudes are then used as points from which the material is ejected into space. The angular extent of the orbit encompassed by prominence ejecta is then found, as depicted in Figure 4.18(b). In this way, we calculate the maximum percentage of the planetary orbit that could be affected.

For the maps GJ494 2007, GJ494 2008, GJ1156 2007, GJ1156 2008, GJ9580, GJ1245b 2008 and AD Leo 2008, no prominence material would be intercepted by the planet, thus they are not shown on the plot. For the remaining maps, the maximum percentage of an orbit for which a planet would intercept prominence material is around 20%. For the majority of maps however, the value is below 2%.
If the host star has a large latitude of dipole axis (i.e. is on the far right of Figure 4.18(a)), the planet is more likely to *frequently* be impacted by ejected prominence material. These are also the stars for which it is most likely that *large quantities* of prominence material

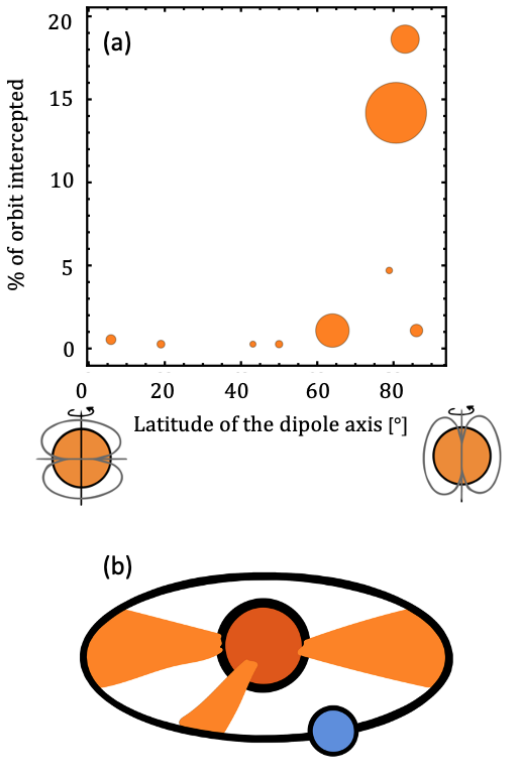

Figure 4.18: (a) The percentage of the orbit intercepted by prominences against stellar dipole tilt. The point size represents the maximum $\dot{M}_{\rm prom}$ intercepted over the orbit. (b) A cartoon of the system showing example locations where the orbit could be intercepted.

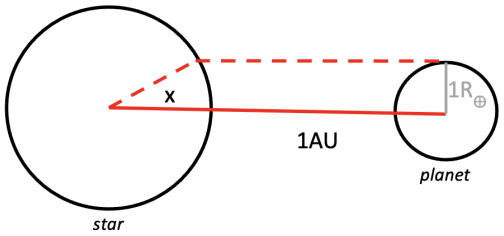

Figure 4.19: Cartoon of the planet orbiting 1AU from the host star, in the equatorial plane. x shows the range of latitudes that a prominence could take and interact with the planet.

could be experienced by the planet. In other words, the largest values of $\dot{M}_p$. This is because these maps hold more material in their equatorial plane than the maps with low dipole axis latitudes, although all maps support most of their material in the equatorial plane. Thus, planets around stars on the right hand side of this plot experience more frequent *and* more intensive prominence ejecta collisions. Planets that orbit outwith of the equatorial plane, which are less common, will escape much of this prominence material because their orbit will only take them into the equatorial plane in two points.

4.3 Conclusion

This chapter has investigated the locations of prominence formation (mechanical stable points) around a set of M-dwarfs, given the observed magnetic surface maps and an assumed potential field reconstruction.

This work finds that prominence locations depend on the alignment of the rotation and magnetic dipole axes. To form prominences at high latitudes, a large misalignment between these two axes is required, and these prominences typically do not support much mass. Large prominence masses are typically supported around stars with little tilt between these two axes, as this allows for the support of large masses close to the equatorial plane of the star. Whilst the tilt between these two axes influences the latitudes of prominence formation and the total mass, in all cases the largest prominences on a given map were found at low latitudes.

Whilst the inclination of a star is fixed, the alignment (or misalignment) between the rotation and dipole axes is not fixed. It likely varies over time, relating to a stellar cycle or even just changes to the large scale field. This change will alter whether prominences could be visible to observers of the system. This is notable as the work presented in this chapter predicts that the prominences likely exist around almost all of these type of stars (as all maps here have shown prominence support) but that in many cases the material would never be visible as it wouldn't transit the stellar disc. Even for those maps investigated here where prominence material was visible, it was only a small fraction of the total material present.

The work encompassed by this chapter suggests that good stellar candidates for observing prominences must:

- allow us to observe into, or close to, the equatorial plane. This would result in the most massive prominences transiting the stellar disc and being present in the Hα trails as absorption transients. This would translate to the stellar rotation axis having a high inclination to the line of sight of the observer.

- If this is not the case and the stellar rotation axis is at a low inclination relative to the observers line of sight, such that the equatorial plane is not visible, then prominences may still be observed if they can form at high latitudes. This requires that the magnetic dipole axis is highly tilted compared to the stellar rotation axis.

- These stars should also have a low co-rotation radius. Stars with small co-rotation radii will form their most massive prominences closer to the stellar surface than those stars with large co-rotation radii. This makes the most massive prominences easier to observe as they are more likely to transit the stellar disc, regardless of the stellar inclination. This can be seen from the visibility plots, where the visible locations around the star decreases quickly with height above the stellar surface.

Specifically from this work, the stars in this sample that would make possible candidates for prominence observations using current techniques are; V374 Peg, EQ Peg A, EQ Peg B, GJ1156, GJ1111, GJ1245b and GJ494. As these are the stars around which this work has predicted the prominence material to transit the stellar disc.
It is of note that all calculations here on visibility of prominence material has required the material to transit the stellar disc. In the vast majority of cases, prominences are observed in absorption as they transit the stellar disc, and thus this constraint is reasonable. However, there have been cases such as LQ Lup [48] and V830 Per [53] where prominences have been seen in absorption when the star is viewed pole on.

When plotting the mass loss or angular momentum loss rates with stellar mass, two categories are found, the higher mass stars following one relation and the very low mass "bistable" stars which do not follow this relation. This is caused by the very weak and complex fields of the bistable stars, which does not allow them to support much prominence material in their corona.

In the higher mass regime, an increase in stellar mass is linked to lower prominence mass loss and angular momentum loss rates. These stars have lower field strengths than their lower mass counterparts, and leads to less material being supported.
The bistable stars seem to show an increase in mass/angular momentum loss rates with increasing stellar mass.
Spin down timescales as contributed by prominence ejections are calculated. They are inversely proportional to the prominence angular momentum loss rates. Thus, stars with larger $\dot{J}$ have smaller spin down timescales. These are the lower mass stars in the higher mass regime (ie the lowest stellar masses but not the bistable stars). These spin down timescales range from 0.1-588.2 Gyrs. These timescales are dependent on the prominence mass loss rates, through the angular momentum rate. These mass loss rates are an upper limit, having assumed that all prominence sites are filled at any given time, and this means that the spin down timescales are a lower limit. Also, this calculation has assumed that the prominence mass loss rate has not varied, which is likely not the case. As the field structure changes, so too will the tilt of the dipole axis and therefore the prominence mass supported. As suggested here already, it is likely that the large scale field structure of these stars should change over time.

In plotting $\dot{M}/A$, this work has found that the prominences around these young stars could be comparable to the wind mass loss rates. The relation for this mass loss rate per unit area as contributed by the prominences is very similar to the relation found for the observationally derived wind values. This is especially the case for the relation by Wood [96]. The study here found there to be a large amount of scatter in the prominence $\dot{M}/A$ values, which is also consistent with the wind observations. As there are a few stars in this sample for which there are multiple ZDI maps, it can be seen from this work that there can be variation also for a given star when viewed over multiple years.
This work is consistent then with Jardine et al. [87] that showed prominences could be used to measure the winds of these stars. However, this work suggests that care should be taken when doing so, as observations can greatly underestimate the quantity of prominence material present in a system. This would then lead to incorrect calculations of the mass loss rates. V374 Peg is a good example of this, which is in this stellar sample and has also been used by Jardine 2019 [87] to estimate the mass loss rates. This work found a value a factor of 10 greater than Jardine and Collier Cameron, and also found that likely only

about 10% of the material would be visible. Thus, whilst this work is consistent with that work, it also shows that the value gathered from observation is considerably less than the true value could be.

The consequences of prominence ejection extends beyond the star and also to orbiting planets. Prominence mass loss rate could typically intercept less than 2% of the planets orbit. For some maps the percentage is much higher, 18% for EQ Peg B. Maps with more aligned dipole axes show larger percentages of the orbit that could be intercepted by ejected prominence material. These maps support more prominence material in the equator and thus this makes sense.

Overall, the alignment of the stellar magnetic axis to rotation axis, and the magnetic field strength both influence the quantity of prominence material that could be supported around a star. The visibility of this prominence material then depends on the stellar inclination, i.e. the angle into which the observer sees the star.
Using prominences as wind gauges should come with the warning that the proportion of prominence material observed could be far less than the true value and this should be carefully considered when making estimates based on the observations alone.

Chapter 5

Comparison of the modelled wind and prominences

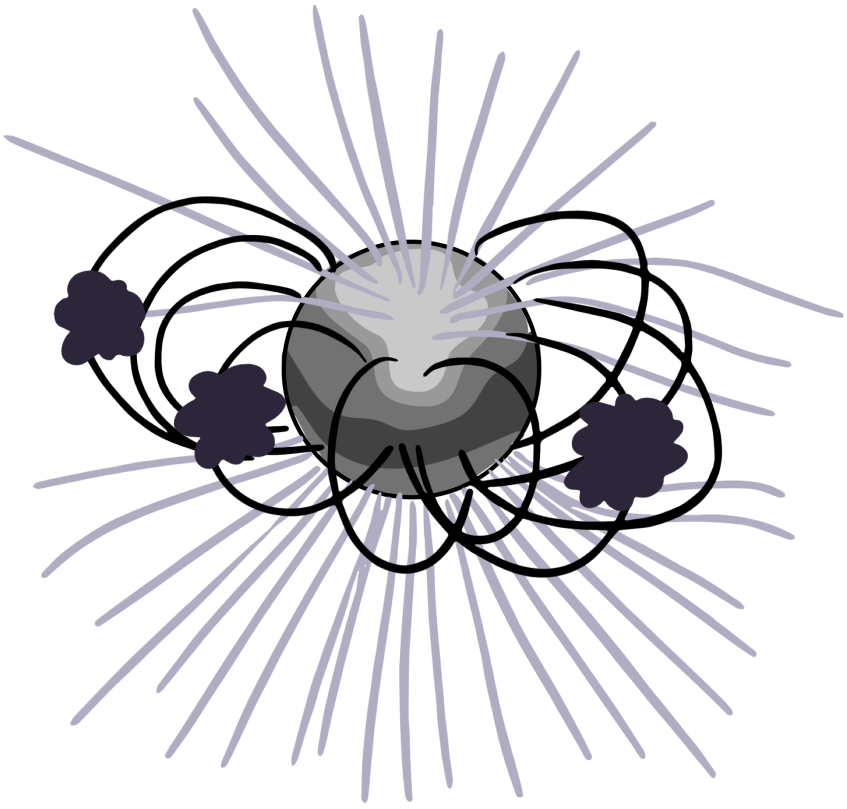

5.1 Introduction

This chapter is work that follows from the previous chapter, but was never published.

In the previous chapter, the modelled prominence mass loss rates were compared to the observed values for the stellar wind. In this short chapter, the prominences are compared to a modelled wind. This modelled wind is consistent with the modelled prominences, since the same field structure that was reconstructed from the ZDI maps is used to calculate the open regions on the maps and estimate the wind mass loss.

5.1.1 Comparison to the previous chapter

The coronal magnetic field structure is constructed from the ZDI maps as in the previous chapter. Here the difference is that the open field lines i.e. the wind bearing fields lines are evaluated for their mass and angular momentum loss rates and compared to the modelled prominences. In the previous chapter, this modelled wind was not considered. This comparison of the modelled wind to the modelled prominences makes this work fully self consistent.

As discussed in more detail in 5.2.3, the placing of the source surface has consequences for the mass and angular momentum loss rates calculated by this wind model. The value chosen here likely underestimates the wind mass loss, and for this reason in the previous chapter the prominences were compared to the observationally derived relations for wind mass loss rate. Comparison of the prominence mass loss rates to the wind observations provides insight into how the prominences mass loss rates may compare to the wind values. For clarity, this chapter where the *modelled* wind is considered was separated from the previous chapter where the observed wind was considered.

The modelled wind and prominence mass loss rates (and angular momentum loss rates) are interconnected and negatively correlated, since the model can only generate open or closed field lines. More open field automatically results in less closed field, and therefore likely fewer prominence bearing loops, and vice versa. Thus, this self consistent model is useful for understanding potential trends, and whilst the modelled wind may underestimate the mass and angular momentum loss rates, including the prominences would then overestimate them.

5.1.2 Calculating the mass loss and angular momentum loss rates

The mass loss and angular momentum loss rates of the stellar winds are found using Equations 5.1 and 5.2.

$$\dot{M}_{wind} = \rho_w u_w A_w. \tag{5.1}$$

Given that this is a conserved quantity, this can be evaluated at any point along the field lines, with the easiest point being at the stellar surface. Here A_w is the area of the surface contributing to the open field and u_w is the wind speed at the stellar surface. The wind field lines have a distribution of velocities and therefore temperatures. The velocity on a field line is calculated using a Wang-Sheeley-Arge (WSA) wind model, which provides the wind velocity at a distance of 1AU from the stellar surface. The corresponding isothermal Parker solution that matches this velocity at large distances is then used to calculate the temperature and hence surface velocity of this field line. The density at the stellar surface, ρ_w, is determined from the plasma pressure. This is estimated by scaling the surface gas and magnetic pressures through the relation $p = \kappa B^2$ with a value that fits the solar wind of $\kappa = 10^{-2.6}$ [70]. The angular momentum loss rates of the stellar wind can then be found:

$$\dot{J}_{wind} = \Omega r_A^2 \dot{M}_{wind}, \tag{5.2}$$

where r_A denotes the Alfvén radius.

5.2 Wind modelling

5.2.1 Wind mass loss rates

The mass and angular momentum loss rates for the modelled prominences and wind can be compared, and are shown in Figure 5.1. The dashed lines in the plots depict where the modelled prominences and wind values would be equal. It is interesting to note that whilst the wind is often taken to be the mass loss mechanism for stars, the prominence contribution in this sample is often larger than the modelled wind contribution, and the general trend is for the prominence mass loss rates to increase linearly with wind mass loss rates. The notable exception to this is GJ1245b, a very low mass star, that lies in the bistable region of the mass-rotation period parameter plane [155]. This shows the wind to dominate over the prominences in two years out of the three shown here. The mass loss rate for the stellar

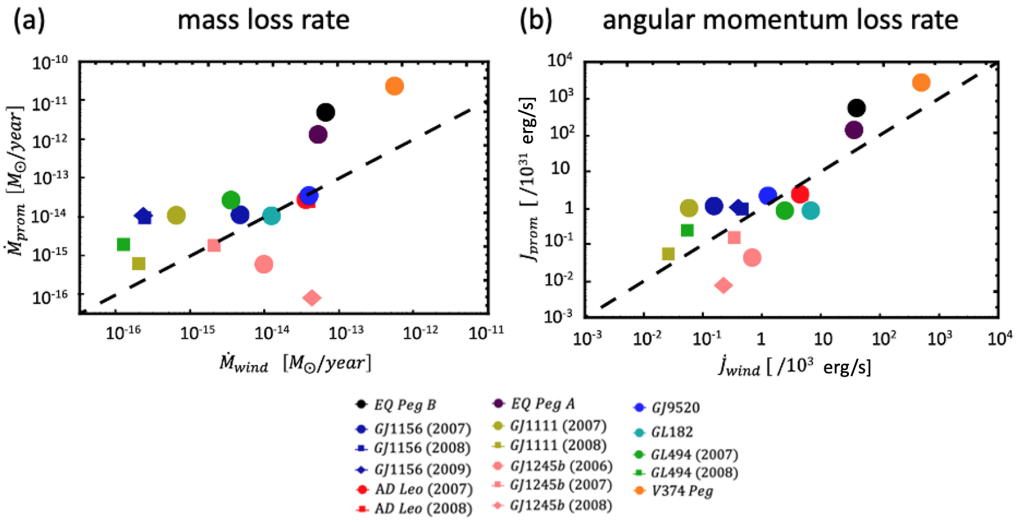

Figure 5.1: Mass loss rates (a) and angular momentum loss rates (b) for the prominences and the wind, scaled to solar values. The dashed line on both plots shows where the wind and prominence values are equal.

wind is calculated by summing the quantity $\rho u_* A$ for each wind bearing field line. Thus, it is not a straightforward task to unpick exactly what causes a map to yield a specific value of $\dot{M}$, since this mass loss rate of a field line depends on the field strength, wind temperature and surface area, which all vary across field lines. The distribution of wind temperatures for the maps GJ1245b (2006) and GJ1245b (2008) is higher than most other maps, and this - which plays into both the density and wind velocity terms in the $\dot{M}$ equation - is the main cause of the high wind mass loss rates when compared to the trend.

5.2.2 Angular momentum loss rates

The angular momentum loss rates reflect a similar pattern to the mass loss, which is unsurprising as these quantities scale linearly for both the prominences and in the 1D wind model. Again, the prominence angular momentum loss rates are comparable to the wind. For many maps the prominences remove more angular momentum that the wind, exceptions being GJ1245b, GJ494, AD Leo and GJ182. Prominences are released from the stable point locations, but the wind is released from the Alfvén radius.

5.2.3 Discussion on limitations of this model

The assumption within this work of placing the source surface radius at $R_{ss} = 18R_\star$ was a requirement for ensuring the possibility of forming prominences on all maps. In this model,

prominences can only form in closed field regions and therefore, to have the chance of finding stable points around these stars, the field must be closed to large heights. $18R_\star$ is very far from the stellar surface, and may not be realistic that all field lines must be closed to this height. This is especially true as the model has a spherical source surface radius, rather than one that may vary with latitude. This has consequences for the wind model, which can only occur on open field lines. With an source surface radius that is larger than it "should" be, the modelled wind mass loss rates will be lower than in reality, as the model will under-predict the number of open field lines by forcing more of the field lines to be closed than is accurate. This means that the modelled wind values here are likely to be underestimates or lower limits. However, it is still of interest to consider the wind values here as they are self-consistent with the modelled prominences. Again, whilst the wind will remove angular momentum throughout a stars life, the prominences will only contribute for part of it.

Map	Spin-down timescale (wind) [Gyr]	Spin-down timescale (wind + prom) [Gyr]
Eq Peg B 2006	2.1	0.2
GJ1156 2007	156.5	17.8
GJ1156 2008	50.7	18.6
GJ1156 2009	59.9	15.8
AD Leo 2007	13.5	8.7
AD Leo 2008	12.3	8.7
EQ Peg A 2006	2.7	0.5
GJ1111 2007	98.4	5.2
GJ1111 2008	216.5	75.8
GJ1245b 2006	10.6	10.0
GJ1245b 2007	21.4	15.2
GJ1245b 2008	32.2	31.1
GJ9520 2008	67.7	24.4
GL182 2007	38.0	33.5
GL494 2007	52.3	38.4
GL494 2008	2325.0	469.5
V374 Peg 2006	0.3	0.1

Table 5.1: Table of spin down timescales as calculated by the wind angular momentum loss rates and the combined wind + prominence loss rates.

5.2.4 The combined prominence and wind spin-down timescales

The spin-down timescales as calculated from the wind contributions alone range from 0.3Gyrs for V374 Peg to 2325Gyrs for GJ494 in 2008, with most maps yielding a spin-

down timescale of around 10-60Gyrs. These are shown in Table 5.1.

Including the prominences in the angular momentum loss rates results in a spin-down timescale that is slightly lower, in some cases an order of magnitude lower (shown in column 3 of Table 5.1). The maps for GJ1245b (2007 and 2009) yield very similar spin-down timescales in both cases, with the timescale calculated from the combined wind and prominence angular momentum loss rates being around 95% that calculate from the wind alone. However, many maps show this percentage to be much lower. For EQ Peg B and GJ1111 (2007) it is about 5% and in 10 of the maps it is below 50%. This would suggest the prominences could be having a noticeable impact on the spin-down of these young stars.

5.3 Comparison of prominence and wind mass loss rates from this model

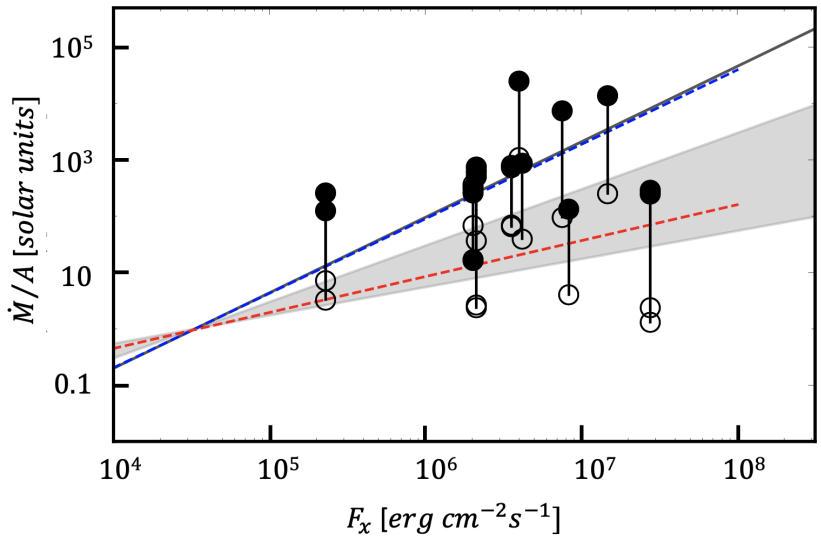

Figure 5.2: The predicted mass loss rates per unit area for both the wind (hollow points) and prominences (filled points). The lines of best fit are shown by the dashed lines with the wind in red and prominences in blue. The grey shaded region shows the predicted range predicted by Ahuir 2020 and dark grey line shows the observationally-based result from Wood [96]. Table 5.3 shows the corresponding equations for these fits, alongside a few others.

The mass loss rates per unit area for the wind and prominences are compared in Figure 5.2. Again, this quantity is plotted against stellar X-ray flux, with the prominences shown by the filled points and the wind by the hollow points. The data is tabulated in Table 5.2. The observed wind relations are shown on the plot by the various grey lines, with the

relations given in Table 5.3. The blue dashed line is the line of best fit for the prominence points and the red dashed line is the line of best fit for the modelled wind points. These are found to be $\dot{M}/A \propto F_X^{1.32}$ for the prominences and $\dot{M}/A \propto F_X^{0.64}$ for the wind. As discussed in the previous chapter, the prominence fit is close to the observationally derived wind relations. Here it can be seen that whilst the prominence relation is close to the upper end or these literature values, the modelled wind fit is at the lower end, within the limits predicted by Ahuir 2020 [154].

Map (year)	F_X $[10^6 ergcm^{-2}s^{-1}]$	Wind $\dot{M}_\odot/A$ $[10^{-14}A_\odot]$	Prominence $\dot{M}_\odot/A$ $[10^{-14}A_\odot]$	Area contributing to the wind [%]	Area contributing to prominences [%]
EQ Peg B 2006	6.51	4007	14103	3.28	4.67
GJ1156 2007	0.46	1146	759	3.81	0.48
GJ1156 2008	0.02	104	624	2.75	0.42
GJ1156 2009	0.02	92	514	2.98	0.68
AD Leo 2007	3.52	449	752	2.96	0.21
AD Leo 2008	3.85	488	816	2.98	0.15
EQ Peg A 2006	5.09	775	7643	3.44	1.15
GJ1111 2007	0.06	587	265	5.83	2.85
GJ1111 2008	0.02	270	128	3.95	0.28
GJ1245b 2006	0.95	3486	327	5.59	0.07
GJ1245b 2007	0.20	856	267	4.89	0.25
GJ1245b 2008	4.27	18471	17	4.73	0.21
GJ9520 2008	3.87	164	890	3.22	0.13
GJ182 2007	1.20	6	135	3.52	0.10
GJ494 2007	0.34	8	298	4.04	0.26
GJ494 2008	0.01	5	253	0.27	0.02
V374 Peg 2006	54.93	7361	25857	3.43	6.48

Table 5.2: Table to support the Woods plot in Figure 5.2

The larger magnetic field strengths and temperatures in the prominence regions when compared to the wind, lead to larger $\dot{M}/A$ values than the modelled wind, since $\dot{M}/A = \rho u$ and density and up-flow speed increase as field strength and temperature increase.

In Table 5.2, the surface area contributions for the wind and prominences are listed. The prominences were discussed in the previous chapter so here the wind is focused on. The wind area contributions are larger than the prominences, though still relatively low, typically taking up 3-5% of the stellar surface. This values may actually be slightly larger in reality and had the source surface been placed closer to the stellar surface, the open field region would have increased as closed field would not have been forced to such a large height

Relation $\dot{M}/A \propto F_X^a$	Reference
$a = 1.34$	Wood 2005 [96]
$a = 0.82$	Suzuki 2013 [153]
$a = 0.5$ to 1	Ahuir 2020 [154]
$a = 0.64$	the wind model in this work
$a = 1.32$	the prominence model in this work

Table 5.3: Table of relations between $\dot{M}/A$ and F_X

above the surface. However, in moving the source surface in from $18R_*$ to $9R_*$ for the map of V374 Peg, the area of closed field decreases to 95% of the original value and for the open field increases by 2% (from 3.4% to 5.4%). For such a large decrease in the radius of the source surface, this is not a large change to the field contributions.

5.4 Impact on orbiting planets

The impact of mass loss on orbiting planets is again revisited. Figure 5.3 shows the stellar mass loss at the source surface, which is the maximum radius in our modelled field. Beyond this the field is purely radial and thus, had the mass loss rates been plotted at any radius beyond this, they would have reproduced the same pattern albeit with a different value of $\dot{M}/A$ in each grid point. The top panels of these figures show surface maps (at the source surface), with the wind mass loss in purple and prominences in red.

Panel (a) of this figure examines the map of EQ Peg A (2006) which has an aligned dipole axis relative to the rotation axis. This map therefore shows high wind mass loss rates near the rotational pole and low values around the equator. The prominence mass loss rates, however, congregate around the equator of the star. Ejection of the prominence material would result in the mass loss appearing from the formation sites. As examined in the previous chapter, the prominence formation sites around this star are confined to very low latitudes, due to the highly aligned dipole axis. In the bottom panel of Figure 5.3(a), a slice is taken through the equatorial plane, to plot what an orbiting planet would experience. Whilst the wind mass loss here is very low (again shown in purple), the limited number of prominences (again, shown in red) exactly around the equator ($\pm 0.5°$) show mass loss rates 10^4-10^5 times that of the wind. The angular extent over which a prominence is

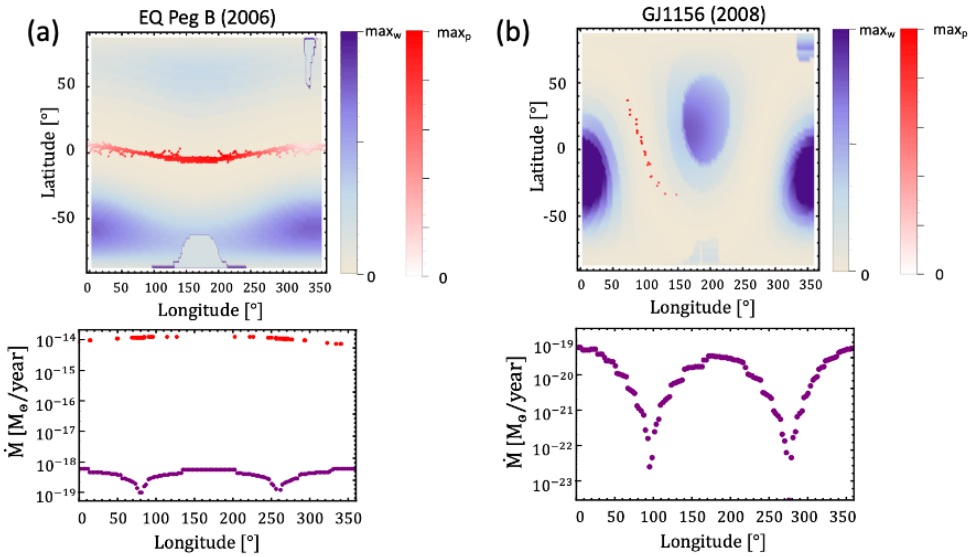

Figure 5.3: (a) Mass loss rates as seen from the source surface. The wind is shown in purple and the prominences in red. (b) A slice through the equatorial plane ($\pm 0.5^o$) of the mass loss rates, showing the mass loss rates that would be experienced by an orbiting planet. Shown for EQ Peg B (left) and GJ1156, 2008 (right).

likely to impact on the planet ($\pm 0.5°$) is calculated by considering the angular extent the planet takes up, assuming an Earth size planet at 1AU from the host star.

On the other hand, GJ1156 in (b) of Figure 5.3 has a dipole axis that is highly tilted from the rotation axis. Therefore, it shows high wind mass loss rates around the rotational equator. The prominence formation sites, and thus mass loss rates, however, are not in the equatorial plane in this case. The latitude range at which prominences can form is much greater as the topology of the closed field region differs significantly to the previous case. An orbiting planet will not pass through the firing line of any of these prominences, though would experience a variation in the wind mass loss throughout its orbit. The wind experienced by such a planet around GJ1156 in 2008 would be much weaker than experienced by a planet around EQ Peg B in 2006.

The colour tables in the plots within Figure 5.3 are scaled to their maximum values. These maximum values are $\max_w = 5.5 \times 10^{-18}$ $M_\odot$/year and $\max_p = 1.1 \times 10^{-14}$ $M_\odot$/year for EQ Peg B and $\max_w = 7.1 \times 10^{-20}$ $M_\odot$/year and $\max_p = 4.6 \times 10^{-16}$ $M_\odot$/year for GJ1156 (2008).

5.5 Conclusions

For many maps in this work, the prominences provide a larger, or at least comparable, mass loss mechanism to the modelled stellar wind. This could vary as the star progresses through its cycle, as maps with more inclined fields typically support less mass than aligned ones. There is limited data from this work to say much more, however as most stars in this sample have only one ZDI map. The larger mass loss rate from the prominences when compared to the wind is due to the fact that the prominences are rooted in hotter, higher-field regions than the wind-bearing field lines. The prominence area contribution for these maps is generally $< 1\%$ and for the wind is often around 3% (ranging from 0.3-5.83)%. The mass loss rates are likely maximum limits for the prominences, as they assume that all of the predicted prominence support sites are filled, as discussed in the previous chapter. On the other hand, the mass loss rates from the wind are probably underestimates, with the area contributing to the wind likely to be larger than found here where we have forced the coronal field to be closed to very large heights above the surface.

Here, the modelled wind $\dot{M}/A$ is plotted against X-ray flux and line of best fit produced, as was done for the prominences in the previous chapter. This yielded a relation of $\dot{M}/A \propto F_X^{0.64}$. It is similar to the lower limits of the relations produced from the observations. As the results here are a lower limit on the mass loss rates, this is still encouraging.

The spin down timescales can be estimated from $\dot{J}_{wind}$ alone or from the combined modelled wind and prominences ($\dot{J}_{wind+prom}$). The prominences alone were previously investigated. Values for spin down rates as caused by this modelled wind, range between 0.3-2325 Gyrs. For the combined wind and prominences, the spin-down timescales range between 0.1 and 470 Gyrs. This would imply that the prominences could have large effects on the spin-down of some stars, causing them to spin-down at a much faster rate than the wind alone.

The wind angular momentum loss rate is a lower limit, meaning that the spin-down timescale for the wind is an upper limit (since it is inversely proportional to the timescale). The prominence angular momentum losses are upper limits, and therefore their timescales are lower limits.

Typically $\dot{J}_{wind}$ is around 2.7 times the timescale from $\dot{J}_{wind+prom}$, and for some maps the

timescale calculated from the wind alone is a factor of 10 larger than when the prominences are included, for example EQ Peg B.

Overall, this work suggests that prominences could have a considerable contribution to the stellar spin-down and should not be discounted at this point in a stars life cycle. Whilst this work has likely overestimated the contribution of prominences, their contribution is very noticeable in the spin-down timescales and mass loss rates and more investigation is needed to quantify this. This is particularly interesting because models of stellar evolution, which use the wind as the only mechanism for angular momentum loss and therefore stellar spin down, require an additional torque which is added to the model in order to produce rotation rates that match observations [156]. The physics behind this additional torque is unknown and might be related to the uncertainties in the observations for stellar mass loss rates, or there could be another mechanism at play such as the ejection of prominences.

Chapter 6

Finding stable points in a tilted dipole

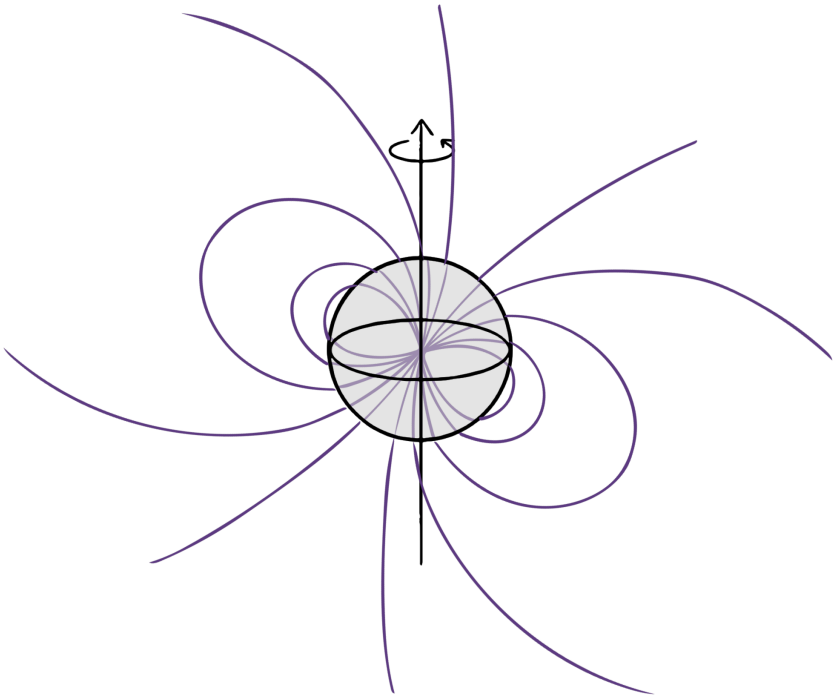

6.1 Introduction

The work within this chapter has yet to be published.

This chapter investigates the locations of stable points around tilted dipolar and quadrupolar fields. These are locations of stable mechanical equilibria. The stable points occur when, if we move along the magnetic field, the component of the effective gravity along this magnetic field decreases. This means that material pools at this location and can not escape the potential well. The dipole is of most interest, since it is expected that at large heights above the stellar surface, where slingshot prominences are found, the dipole would be the dominating term. It has, however, been found that the quadrupolar component may also be of significance, for example at certain points in a stellar cycle [157]. These stable points allow for the support of material within the stellar corona which may result in prominence formation.

6.1.1 Observed velocity plots

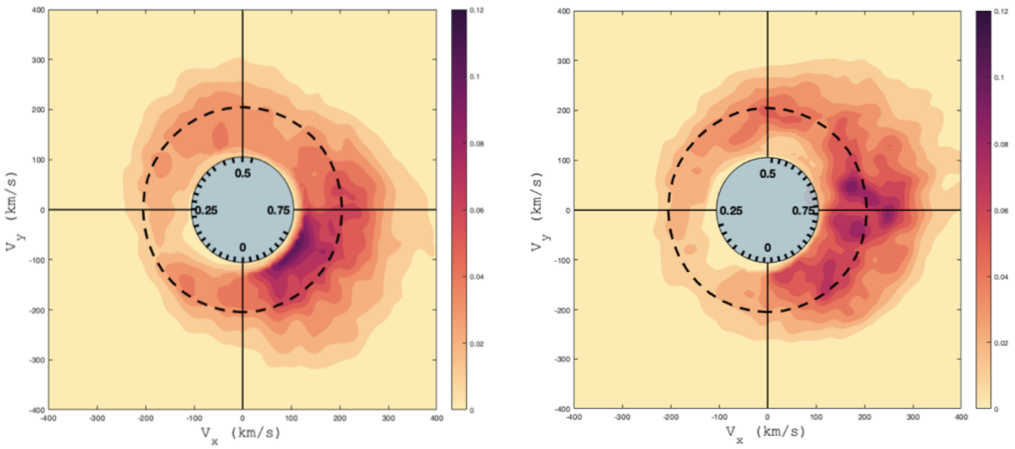

Figure 6.1: Velocity plots for observed prominences around the star V530 Per, as published by Cang et. al [55]. The blue circle shows the stellar disc, the black dashed line is the equatorial co-rotation radius, and the colour table shows the local Hα equivalent width.

Observations of slingshot prominences are typically shown as dynamic spectra, where the prominences can be seen as absorption features or trails in the Hα line. There are a couple of examples in the literature where the observed data has been shown in the form of velocity plots [53, 55]. A recent example from Cang et. al [55] is shown in Figure 6.1. These plots

have the benefit that they allow the reader to better understand the spacial distribution of the prominence material around the star. The velocity plots show the projections of the x and y velocities of orbiting material onto the equatorial plane of the star. The colour of the material represents the absorption intensity in Hα, which relates to the density of the material at that point. This was also done for the star RX J1508.6±4423 by Donati et. al [53], using a model developed by Marsh and Horne in 1988 [158] for imaging accretion discs. The main use of these kinds of plot is to be able to locate around the star the condensed material of prominences. Multiple observations of such plots make it very easy to see the evolution of such material around the star, and they can be far quicker to read than dynamic spectra if the location of prominence material is of most interest.

The observations in Figure 6.1 shows two large blobs on the right hand side of the velocity plots. As well as the particularly large clump in each plot, there is also material all around the equatorial co-rotation radius. Between the two plots (late November to early December) there has been some sort of evolution of the material such that the blob appears to have moved, whilst still congregating around the co-rotation radius. This may be the same feature as in the first observation, or it may be another feature that formed between these two observations after the breakup of the blob in the November observation.

The observations by Donati et al [53] show a different distribution. On the 6th of May 1998 for the star RX J1508.6±4423, there appears to be only one dark blob, towards the top left of the image. The ring around co-rotation is still present and there is the suggestion of the beginnings of a blob forming on the right hand side at $v_y = 0$. By May 10th, there are 3 dark blobs in the plot and the blob from the previous plot has moved or disappeared.

RX J1508.6±4423 and V530 Per are particularly interesting stars, as they are viewed almost pole on (35° [53] and 30° [54, 55], respectively). Because of this, the prominence material is seen in emission and not absorption as the ring of prominence material around the star is illuminated by the starlight. It also means that almost all of prominence material in this hemisphere of the star is visible.

6.1.2 A tilted dipole

A tilted dipole can be described by the following equation [159]:

$$\underline{B} = \Big(B_r, B_\theta, B_\phi \Big) \tag{6.1}$$

where

$$B_r = \frac{m}{r^3}\Big(2\cos\beta\cos\theta + 2\sin\beta\sin\theta\cos\phi \Big), \tag{6.2}$$

$$B_\theta = \frac{m}{r^3}\Big(\cos\beta\sin\theta - \sin\beta\cos\theta\cos\phi \Big) \tag{6.3}$$

and

$$B_\phi = \frac{m}{r^3}\Big(\sin\beta\sin\phi \Big). \tag{6.4}$$

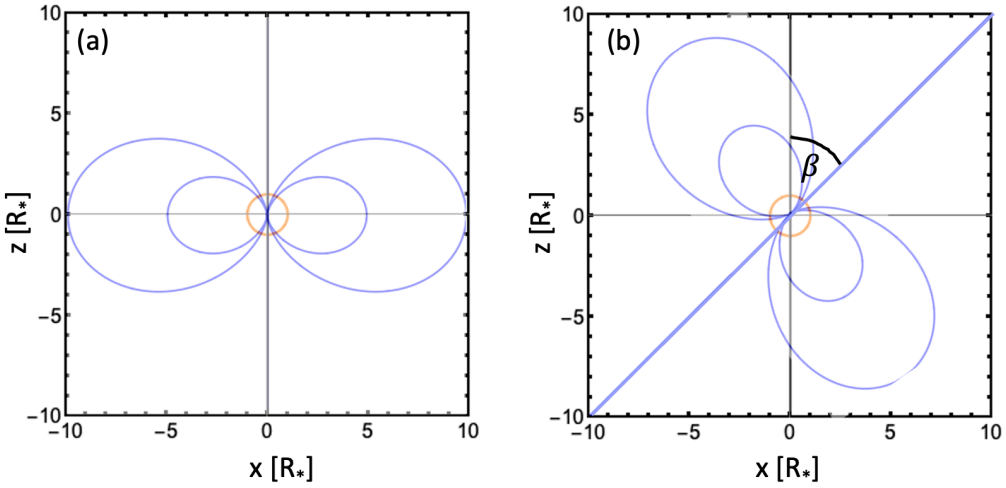

Figure 6.2: A diagram showing, for a star with its rotation axis along the z-axis, (a) a dipole aligned with the rotation axis and (b) a dipole tilted by β.

This is given in spherical polar coordinates, such that r is the radial coordinate, θ is the co-latitude and ϕ is the longitude. β is the angle between the rotational axis and the dipole axis. $\underline{m}$ is the dipole moment, which is this work has been set to one for simplicity.

The expressions above for the tilted dipole (Equations 6.2, 6.3 and 6.4) can be found by taking the expression for a dipole field in spherical coordinates, converting it to Cartesian coordinates and then rotating the dipole around the y-axis using a rotation matrix. This expression can then be converted back into spherical coordinates, giving the general expression for a tilted dipole as above. This method can be used for any magnetic field and is

later used to tilt a quadrupole and octupole field. Appendix F gives more detail on tilting the dipole field.

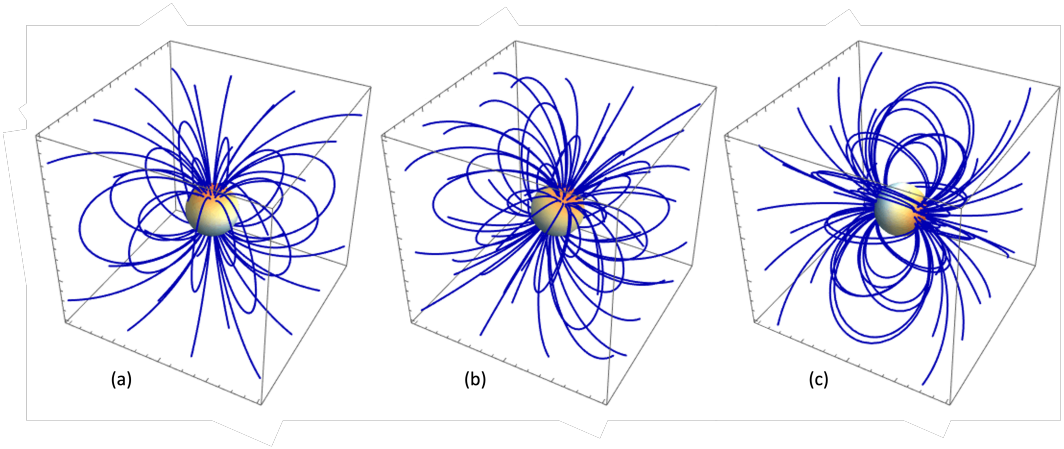

Figure 6.3: An illustration showing an (a) fully aligned dipole (b) dipole tilted by 0.5 radians and (c) fully misaligned dipole.

Other multipoles

Following the method given in Appendix F, the following expression can be found for a tilted quadrupole field:

$$B_r = \frac{3((1+3\cos 2\beta)(1+3\cos 2\theta)+12\cos 2\phi \sin^2\beta \sin^2\theta + 12\cos\phi \sin 2\beta \sin 2\theta))}{16r^4}, \quad (6.5)$$

$$B_\theta = \frac{3(-4\cos 2\theta \cos\phi \sin 2\beta + \sin 2\theta(\cos 2\beta(3+\cos 2\phi)+2\sin^2\phi)))}{8r^4}, \quad (6.6)$$

and

$$B_\phi = \frac{(3\sin\beta(\cos\beta\cos\theta + \cos\phi\sin\beta\sin\theta)\sin\phi)}{r^4}, \quad (6.7)$$

where the quadrupolar moment has been normalised from the expression.

6.2 Finding the stable points

As discussed in Section 4.1.3, for a location to be a stable point it must satisfy $\underline{g}_e.\underline{B} = 0$ and $(\underline{B}.\nabla)(\underline{g}_e.\underline{B}) \leq 0$. The stable points within a tilted dipolar field are found using these

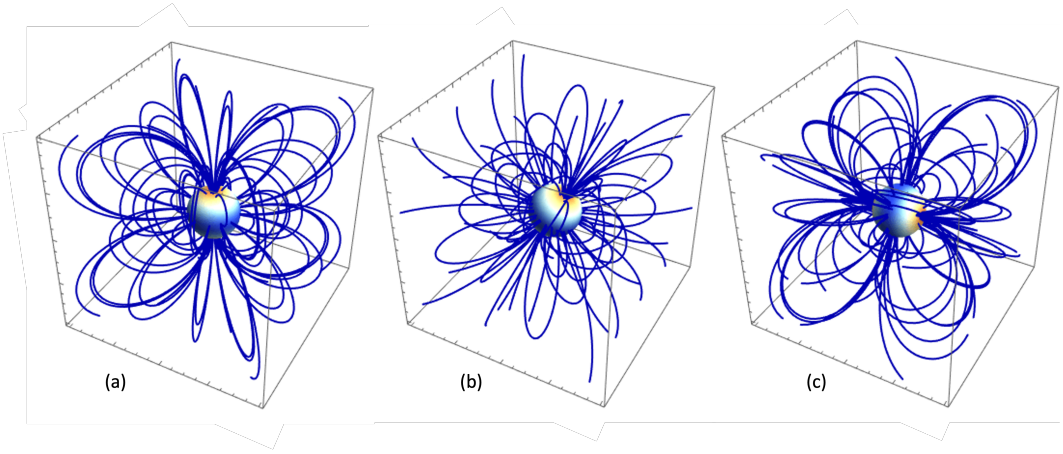

Figure 6.4: An illustration showing an (a) fully aligned quadrupole (b) quadrupole tilted by 0.5 radians and (c) fully misaligned quadrupole.

two constraints. These are evaluated using the expression for the effective gravity:

$$\underline{g}_e = \Big(-\frac{GM_\star}{r^2} + \Omega^2 r \sin\theta \Big)\hat{r} + \Big(\Omega^2 r \sin\theta \cos\theta \Big)\hat{\theta}, \tag{6.8}$$

and the expression for the magnetic field, given in section 6.1.2.

The first condition yields:

$$\underline{g}_e . \underline{B} = 0 \tag{6.9}$$

$$\begin{aligned} &\Big(\Big(-\frac{GM_\star}{r^2} + \Omega^2 r \sin\theta \Big) . \frac{2}{r^3} \Big(\cos\beta\cos\theta + \sin\beta\sin\theta\cos\phi \Big) \Big) \\ &+ \Big(\Big(\Omega^2 r \sin\theta\cos\theta \Big) . \frac{1}{r^3} \Big(\cos\beta\sin\theta - \sin\beta\cos\theta\cos\phi \Big) \Big) + \Big(0 . \frac{1}{r^3} \Big(\sin\beta\sin\phi \Big) \Big) = 0 \end{aligned} \tag{6.10}$$

$$\begin{aligned} 2\Big(\Big(-\frac{GM_\star}{r^2} + \Omega^2 r \sin\theta \Big) . \Big(\cos\beta\cos\theta + \sin\beta\sin\theta\cos\phi \Big) \Big) \\ + \Big(\Big(\Omega^2 r \sin\theta\cos\theta \Big) . \Big(\cos\beta\sin\theta - \sin\beta\cos\theta\cos\phi \Big) \Big) = 0 \end{aligned} \tag{6.11}$$

which can be simplified and rearranged to

$$r^3 = \frac{-2GM_\star(\cos\beta\cos\theta + \cos\phi\sin\beta\sin\theta)}{\Omega^2\sin\theta(\cos\theta^2\cos\phi\sin\beta - 3\cos\beta\cos\theta\sin\theta - 2\cos\theta\sin\beta\sin\theta^2)}, \tag{6.12}$$

$$r = \left(\frac{-2GM_\star(\cos\beta\cos\theta + \cos\phi\sin\beta\sin\theta)}{\Omega^2\sin\theta(\cos\theta^2\cos\phi\sin\beta - 3\cos\beta\cos\theta\sin\theta - 2\cos\theta\sin\beta\sin\theta^2)} \right)^{1/3}. \tag{6.13}$$

The locations of the stable points can then be found by combining Equation 6.13 with the second condition, $(\underline{B}.\nabla)(\underline{g}_e.\underline{B}) \leq 0$. This gives the stable points (r, θ, ϕ), for a given dipole tilt, β. This was evaluated in Mathematica and the full working has been omitted here.

This can equally be evaluated for a quadrupole, or any magnetic field that can be written analytically, by replacing the expression for the dipole magnetic field with the new magnetic field expression.

6.3 Analysing the stable points

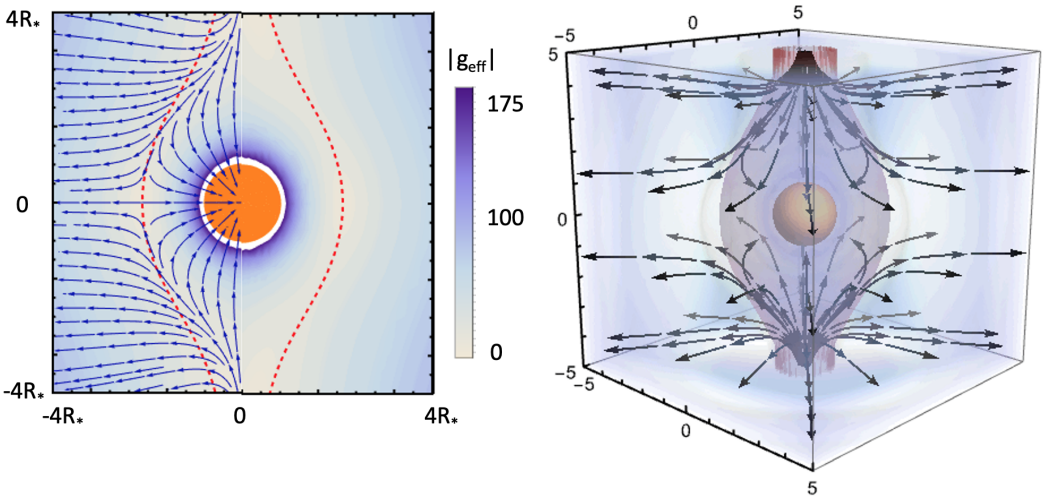

Figure 6.5: Left: the effective gravity (arrows show the direction and colour shows the magnitude) and the co-rotation radius (red dashed line). Right: the same but in 3 dimensions. The rotation axis is along the vertical axis in both cases.

Stable points occur when the equilibrium point meets the condition that

$$(B.\nabla)(g.B) < 0. \tag{6.14}$$

The effective gravity changes sign at the co-rotation radius (shown by the red dashed

line, and red amphora-shaped surface in Figure 6.5). The magnitude varies with latitude, due to the centrifugal term, and these two things will partly determine the locations of stable points. Figure 6.5 is shown here to help visualise the variation of the effective gravity about the rotating star.

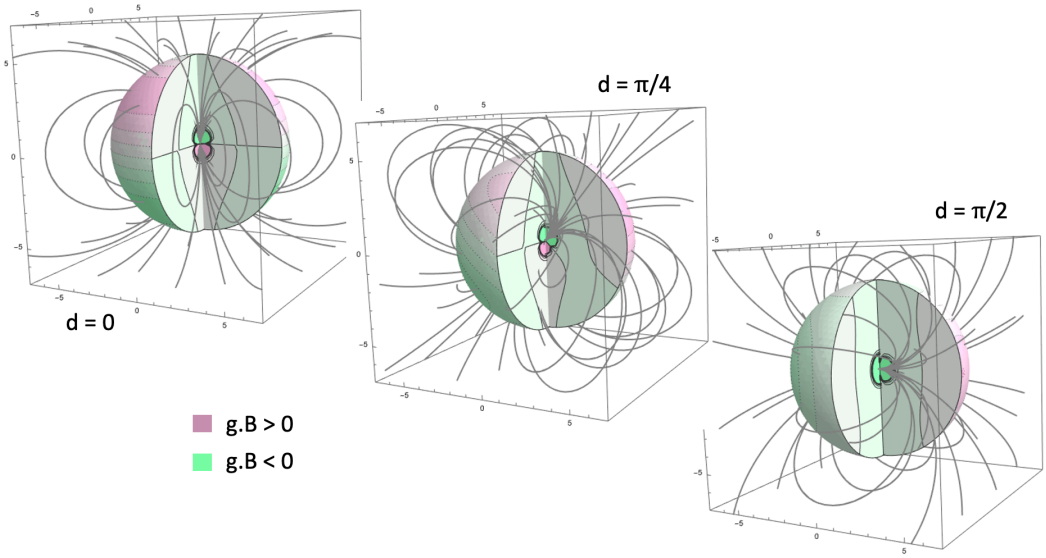

Figure 6.6: Dipolar fields with different dipole tilts (d [radians]) and the quantity (g.B) shown as contour surfaces. Pink shows when g.B > 0 and green when g.B < 0.

The direction of the magnetic field relative to the effective gravity is of importance when determining the locations of stable points. The quantity ($\underline{g}.\underline{B}$) must decrease as we walk along the direction of the magnetic field line. In other words, ($\underline{g}.\underline{B}$) must get more negative/less positive. Figures 6.6 and 6.7 show the quantity (g.B) and field structure for a range of tilted dipoles and quadrupoles, respectively.

Stable points will form at equilibrium points where the field line passes from pink to green on the plots in Figures 6.6 and 6.7, or when the field line passes from a green section to a more vibrant green section, or from a vibrant pink section to a paler pink section.

6.4 A young solar-like star

In most of this work, a young solar-like star is investigated, with the stellar parameters of AB Dor being used; $M = 0.87 M_{\odot}$, $R = 0.96 R_{\odot}$ and $P = 0.515$ days.

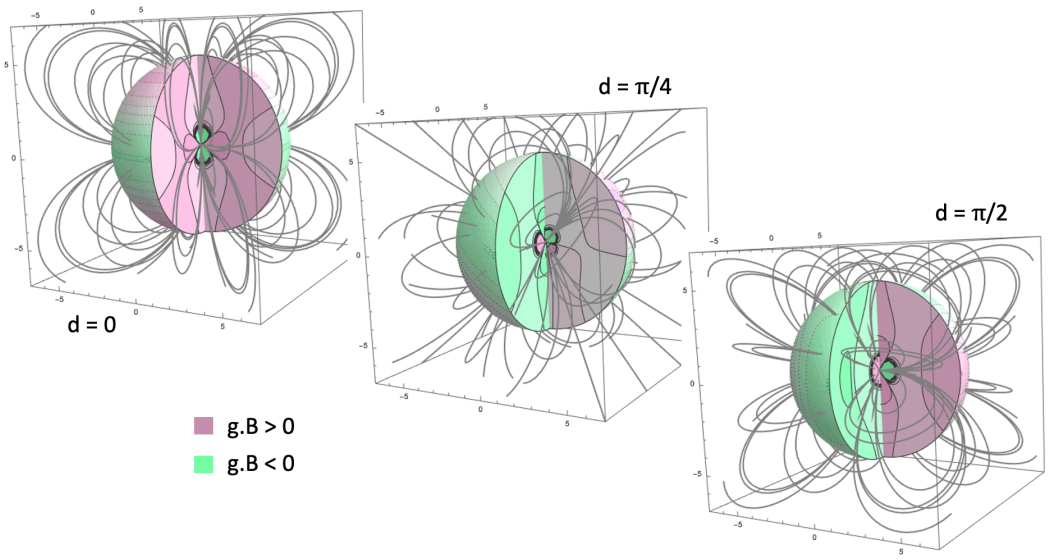

Figure 6.7: As in Figure 6.6 but for a quadrupole.

6.4.1 The stable points in 2 dimensions

Initially a longitude of 0 is selected so that the stable point expression be evaluated with two variables. Figure 6.8 shows a selection of dipole tilts relative to the stellar rotation axis, and the equilibrium points and critical radii for stability. The critical radius for stability (the pink lines) show the minimum radius at which the condition $(\underline{B}.\nabla)(\underline{g}_e.\underline{B}) \leq 0$ is met. In other words, any black equilibrium points that lie above the critical radius will be stable equilibrium points.

An aligned dipole

The aligned dipole, seen in the left panel of Figure 6.8, yields the same results as Ferreira 2000 [80]. The equilibrium points that lie within the pink lines of the critical radius are unstable and thus only the points within the equatorial plane are stable. Thus, the equilibrium points that follow the shape of the co-rotation radius, but at lower heights, are unstable. The stable points lie within the equatorial plane, on the summits of field lines and extend slightly within the co-rotation radius of the star to $0.87R_k$, which was shown by Ferreira 2000 [80].

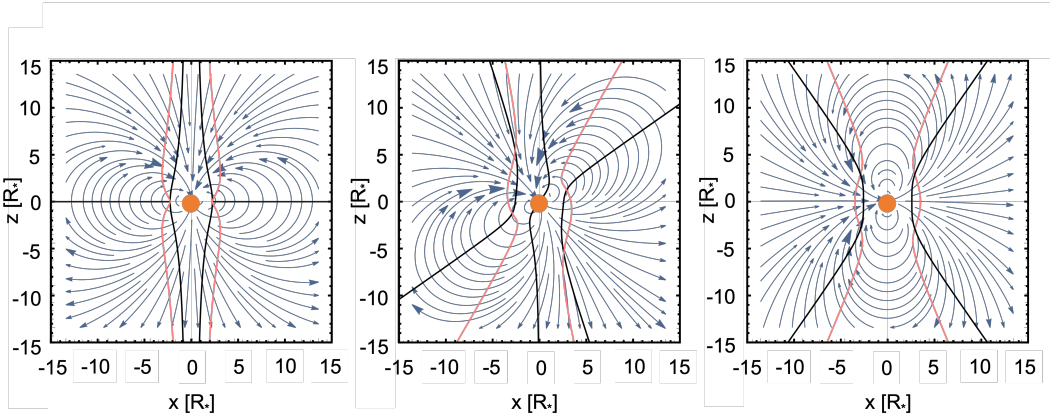

Figure 6.8: The locations of the equilibrium points (black lines) and the critical radius (pink lines) beyond which these equilibrium points are stable. The star is again shown by the orange circle and the magnetic field is shown in blue.

A dipole tilted at $\pi/5$ radians

When the dipolar field is tilted, as in the middle panel of Figure 6.8, the locations of the equilibria also move. Equilibrium points can now be found at very high latitudes and close to the star, which lie within the pink curves and are thus unstable. There are also solutions for stable equilibrium points. These curves still lie close to the summits of the dipole field lines.

A misaligned dipole

For a fully misaligned dipole, i.e. a dipole tilt of $\pi/2$ radians, the equilibrium points are shown in the right hand panel of Figure 6.8. Here the stable points form in a cone and can no longer form close to the summits of the loops, as these lie along the rotational poles.

6.5 3D locations of the stable points

6.5.1 A dipole tilted at $\pi/5$ radians from the rotation axis

Here, the stable points are found in 3-dimensions for a dipole tilted by $\pi/5$ radians, as in section 6.4.1. Figure 6.9 shows the locations of the stable points on polar plots.

A polar plot marks the radial position of the stable points with one of the angles, co-latitude (θ) or longitude (ϕ). These plots are not a projection of the points onto an x-y plane. Instead, they can be thought of with the following analogy: if each stable point in a

3D volume is an ink drop and a piece of paper is placed in a meridional plane and spun about the z-axis through 360 degrees, the ink drops will mark the paper and produce the polar plot.

Figure 6.9 (a) shows a polar plot in θ (co-latitude), where the star is shown by the orange circle and the rotation axis is shown by the black line. A 2-dimensional plot of the dipolar field is overlaid in grey. Figure 6.9 (b) shows a polar plot in ϕ (longitude), with the star again shown by the orange circle and the rotational pole now seen as a black dot.

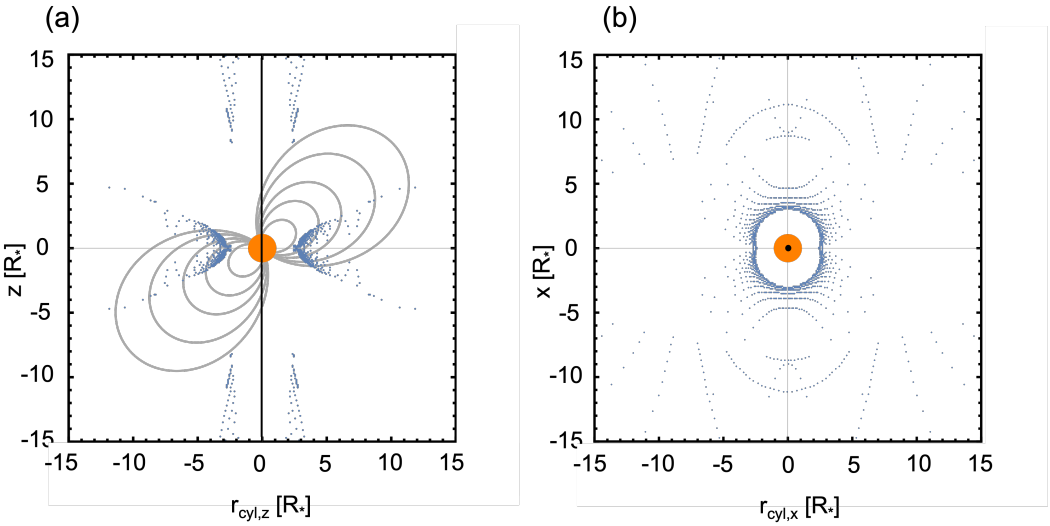

Figure 6.9: Polar plots of the locations of the stable points (blue) for a dipole tilted by $pi/5$ radians from the rotation axis. The star is shown in orange and rotation axis in black. The field is shown in grey in (a).

The stable points can be seen to form in two groups: around the equatorial plane at a range of latitudes that increases with distance from the star, and a group at very high latitudes about the axis of rotation. These high latitude stable points are unlikely to support as much mass as the lower latitude prominences.

Figure 6.10 shows the distribution of the stable points around this tilted dipole. Figure 6.10 (a) shows a "wine glass" plot, the distribution of stable points in latitude and radial distance from the star. Figure 6.10 (b) shows a 3D distribution of the stable points, shown here for completeness. The stable points typically form in a plane around the star with some spread in latitude, seen most clearly in Figure 6.10 (a), with some stable points also found at very high latitudes around the rotational axis. The plane of stable points lies very close to, but not on, the magnetic equator.

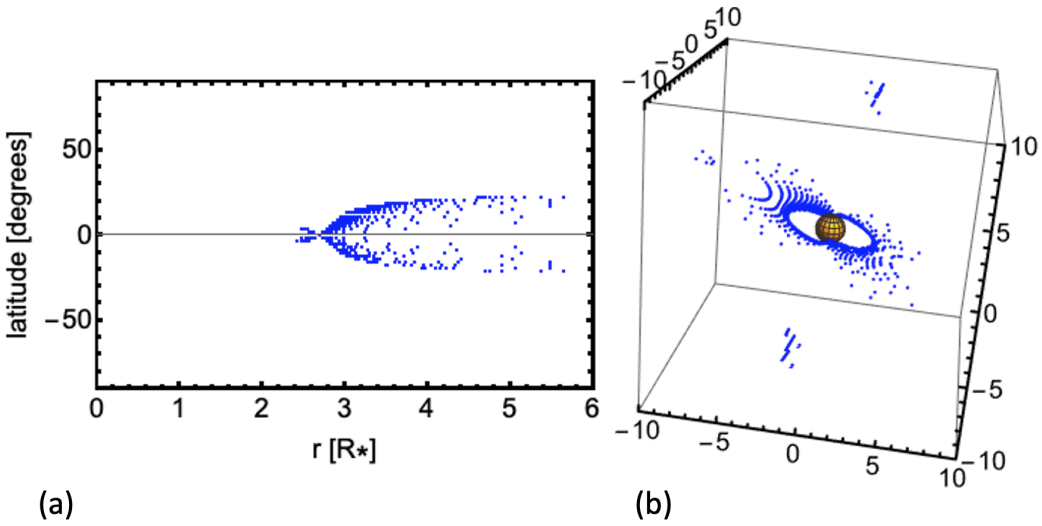

Figure 6.10: (a) The distribution of stable points in latitude and radial distance from the star. (b) The 3D distribution of stable points.

6.5.2 Wine glass plots

Figure 6.11 shows the radial positions and latitudes of the stable points produced, for a range of dipole tilts. For a fully aligned dipole, (a) in Figure 6.11, the stable points form a straight line in the equatorial plane. With a tilted dipole of $\pi/8$ radians ((b) in Figure 6.11), the stable points begin to spread in latitude. There are still solutions below the equatorial co-rotation radius, and these form in two lobes that form a heart shape. As the tilt increases, this wine glass shaped distribution spreads in widens in latitude, until at a dipole tilt of $\pi/2$ radians (a fully misaligned dipole) only two lines of stable points remain. For some highly tilted dipoles, for example (d) in Figure 6.11 which corresponds to $3\pi/8$ radians, there are some very high latitude stable points that form on branches off the main distribution. These correspond to the solutions in the plot for a misaligned dipole. These very high latitude stable points would likely not support much material because of these high latitudes.

Stable points can be found within the equatorial co-rotation radius for all tilts except a fully misaligned dipole. As would be expected, tilting the dipole compared to the rotation axis allows for stable points to form at latitudes above the equatorial plane. Not all latitudes can support a stable point for a given dipole tilt, and thus the latitude of a stable point could be used to constrain the value of the dipole tilt.

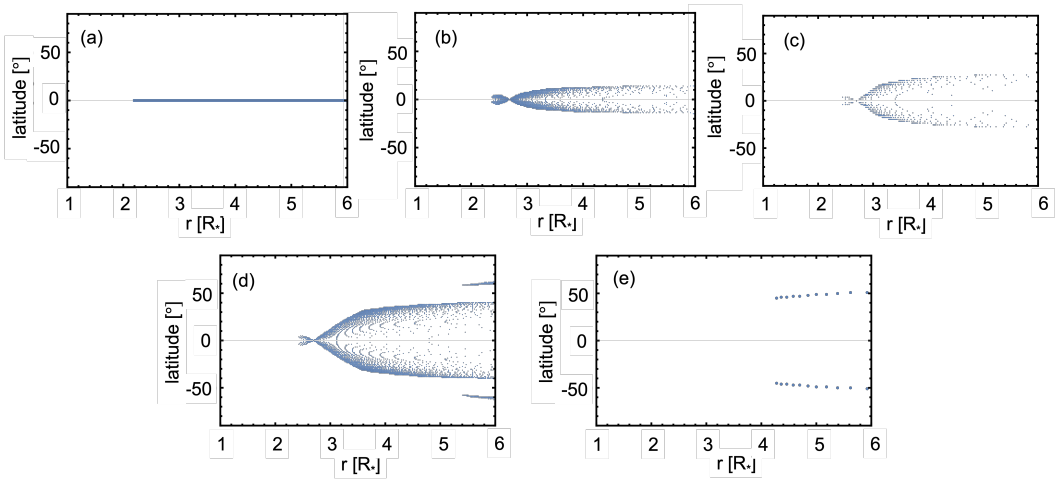

Figure 6.11: Latitude and radial positions of stable points or "wine glass plots". These are given for a range of dipole tilts: (a) 0, (b) $\pi/8$, (c) $\pi/4$, (d) $3\pi/8$ and (e) $\pi/2$ radians.

6.6 Stable point distribution

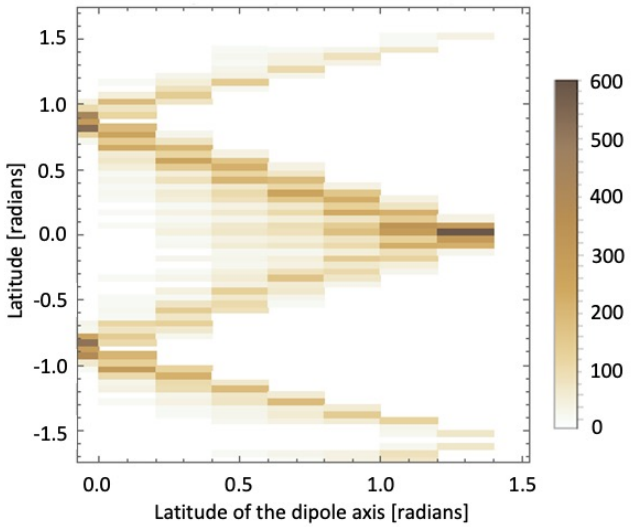

Figure 6.12: The latitudes of stable points against latitude of the dipole axis. The colour shows the number density of stable points, with dark showing regions of high density.

Figure 6.12 shows a plot of the distribution of stable point number with dipole tilt. Whilst the exact number of stable points does not have physical meaning, as it depends on the grid sampling, the distribution does. Locations of high density are regions where stable points can easily be found and thus prominence formation would be very likely, whilst regions of low stable point density will be more difficult to support prominences in. In the

figure, the left hand side of the horizontal axis is a fully misaligned dipole, with dipole axis within the equatorial plane. A fully aligned dipole, with a latitude of the dipole axis being at 1.5 radians, lies at the right hand side of the horizontal axis. The vertical axis shows the latitude around the star, i.e. 0 representing the equatorial plane and ± 1.5 radians representing the poles. For a fully aligned dipole on the right hand side of the plot, stable points can be very easily formed within the equatorial plane but not at other latitudes. As the dipole axis tilts over towards the equatorial plane, moving from right to left across the plot, stable points can then be found at higher latitudes. Due to the symmetry of the magnetic field, the distribution is symmetric about the horizontal axis and creates a W shape. There are two branches of the distribution; a line at lower latitudes (from 0 to 1 radians) and a fainter line at higher latitudes (from 1 to 1.5 radians). This higher branch would support less mass than the lower branch, not only due to the difference in the number of stable points but also because supporting mass at higher latitudes becomes increasingly difficult due to the centrifugal force acting.

This plot suggests that stars of different dipole tilts will support different distributions of prominences and is in keeping with previous work [86, 135, 137]. As the magnetic field of a star changes over it's cycle, an individual star would migrate across this plot with time. Previous work has shown that prominences in the equatorial plane will support the most mass [135, 137]. Therefore, whilst observationally it would be easier to find prominences around stars in the equatorial plane, this might not be possible due to the inclination of the system. This plot is in keeping with previous work in suggesting that for stars where the inclination is not ideal for prominence observation, it may still be possible to observe prominences in these systems at certain points in their stellar cycle.

6.7 Dynamic spectra

Figure 6.13 shows the synthetic dynamic Hα spectra for three different dipole tilts and two stellar inclinations. Plots in the left-hand column show the spectra with a stellar inclination of 65° and the right-hand column shows 80°. The rows show results for a dipole tilt of 0.4, 0.8 and 1.2 radian tilt, respectively, from top to bottom of the figure. Intensities have been normalised to each individual plot so that the structure of the spectra can be easily seen.

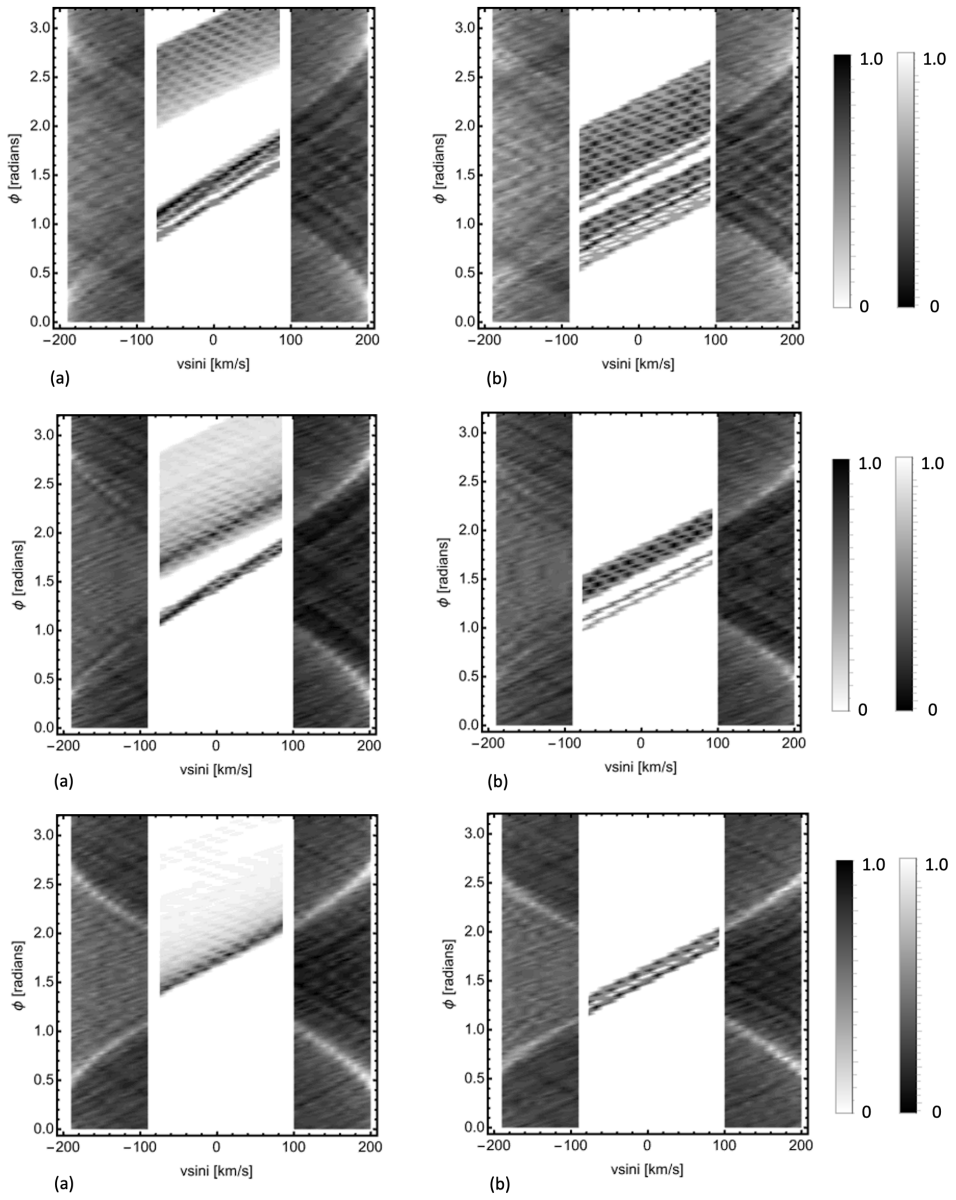

Figure 6.13: Dynamic Hα spectra for a tilted dipole of 0.4, 0.8 and 1.2 radians for the rows, respectively from top to bottom. The left hand plots show an inclination of 65° and right show 80°.

In absorption, only the stable points in front of the star contribute to the intensity and therefore there is only one line passing from left to right across the plot. In emission, the stable points on both sides of the star, π radians apart, both contribute to the intensity and this leads to two matching curves that are π radians out of phase.
In emission the results are very similar regardless of inclination because, in both cases, all of the stable points contribute to emission. In absorption this is not the case, since the inclination determines which stable points transit the stellar disc. There is some variation with dipole tilt, with more inclined dipoles showing much brighter, thick lines in emission, whereas the less inclined case shows more of a spread of these emission curves in phase. For an aligned dipole and viewing into the equator, stable points would form at all phases and thus the emission spectra would be filled with emission curves. As the dipole is tilted over, and therefore the plane of stable points is tilted too, the stable points now lie at phases that are closer together to two particular values. This leads to sharpening of two curves in the emission profile.

Plots on the right, with an inclination of 80° show more of the high mass prominences, since stable points close to the equatorial plane are visible in absorption. With an inclination of 65° this is true less often.

The top row of Figure 6.13 shows dynamic spectra for a dipole tilt of 0.4 radians. Much of the material seen with an inclination of 80° is not visible with a tilt of 65°. Lower mass stable points can now be seen around $\phi = 2.5$ radians because of the normalised colour table. In reality it would not be easy to observe this material as the densities of the features are low, which would make the features very faint in the absorption spectrum, but here the opacities have been selected so that the structure of the features can be seen and are emphasised. The dark region around $\phi = 1.5$ radians has shrunk in phase as the inclination drops from 80° to 65°. For a tilt of 0.8 radians, the middle row of Figure 6.13, the dark band at 1.5 radians can sill be seen. Again, this feature shrinks in phase as the inclination is lowered. With the lower inclination, lower density stable points can also be seen in a feature from about 1.5 to 3 radians, whose intensity varies across this phase band. With a dipole tilt of 1.2 radians, the final row in the figure, the dark band at $\phi = 1.5$ radians is present with an inclination of 80° but not when the inclination is 65°.

In some spectra, it is noticeable that the dark feature in absorption does not line up with the brightest feature in emission. This is because the features seen in absorption are a subset of those present in emission. Those in absorption need not be centred on the same phase as the most intense emission feature, and they do not necessarily have the same gradient as this is dependent on the location of the stable point. The brightest feature in emission may not be visible in absorption as this cluster of stable points might not cross the stellar disc. Or, a small part of this cluster might cross the disc and thus be present in absorption without the features aligning. With a high inclination, the absorption and emission features are more likely to align. This is because far more of the stable points transit the disc and, lying in the equatorial plane, they can support higher densities.

6.8 Velocity plots

There have been two publications in which the observations of prominences have been shown on velocity plots [53, 55]. Here a pure dipole is used in order to generate synthetic observations of these velocity plots, using various dipole tilts and inclinations.

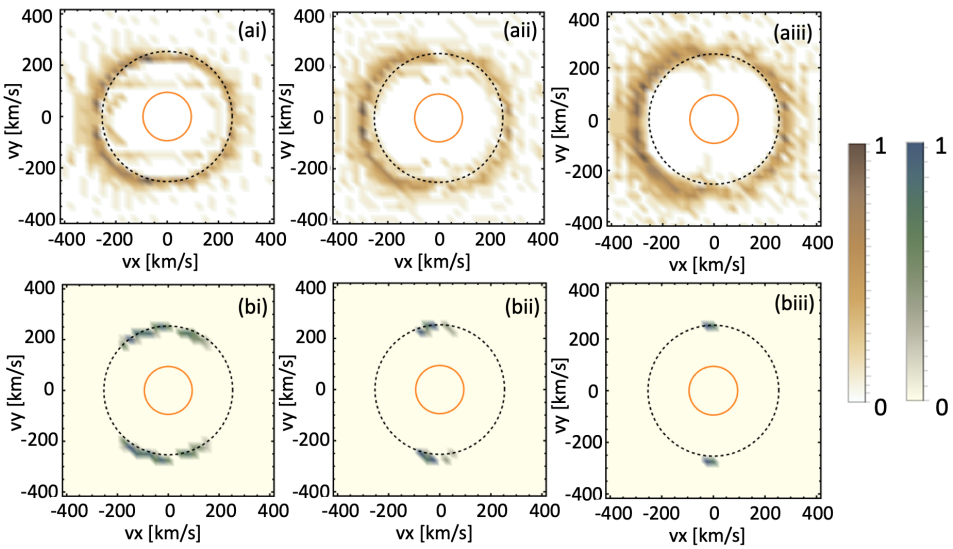

Figure 6.14: Top row (panels (ai-aiii)): velocity plots showing the density of stable points for a dipole tilted by (i) 0.4 radians (ii) 0.8 radians and (iii) 1.2 radians. Bottom row (panels (bi-biii)): velocity plots showing the absorption intensity for the material with tilts as above. The colour tables have been normalised, orange circles show the stellar surface and black dashed lines show the co-rotation radius.

Figure 6.14 shows the stable point number density (i.e. the number of stable points in a cell on the $v_x - v_y$ grid) on the top row, for dipole tilts of 0.4, 0.8 and 1.2 radians respectively. The bottom row of the figure shows the absorption intensity for the material supported at the stable points, for the same dipole tilts. The orange circles represent the stellar surface and the black dashed line shows the equatorial co-rotation radius.

With a dipole tilt of 0.4 radians (left column), the stable points congregate around the equatorial co-rotation radius as well as forming an inner ring within co-rotation. When the opacity is plotted, only two blobs, π radians apart in phase and at co-rotation, remain (Figure 6.14 (bi)).

With a dipole tilt of 0.8 radians (middle column), the outer ring of stable points around co-rotation remains but bulges outwards slightly when compared to a tilt of 0.4 radians. The inner ring has also changed shape. The two blobs at co-rotation are still present in the opacity plot, however, they have shrunk in size.

Once tilted to 1.2 radians (right column) the ring of stable points at co-rotation has widened further and in the opacity, the two blobs have shrunk further.

Since not all stable points can support the same mass, they do not all contribute equally to the opacity plots. Thus, despite the many points on plots (ai) - (aiii) of Figure 6.14, the structure of plots (bi) - (biii) can be quite different. Those stable points in the equatorial plane that can support the most mass dominate the opacity plots. The fine structure seen below co-rotation in plots (ai) and (aii) is no longer visible in (bi) and (bii) due to the very low masses that these stable points support. These plots show all of the stable points present around these tilted dipolar fields, the reality is that not all of these stable points will transit the stellar disc, a condition usually required to be considered visible. In the following paragraphs, the visible proportion of these stable points is considered and compared to the total material.

6.8.1 Inclining the star at 80°

With an inclination of the rotation axis to the observer of 80°, most of the stable points around the equatorial plane are visible. This can be seen from the 3-dimensional plot and "wine glass" plots in Figure 6.15 where the visible stable points are highlighted in red. Within this figure, the velocity plots are shown for all of the stable points in the field (top

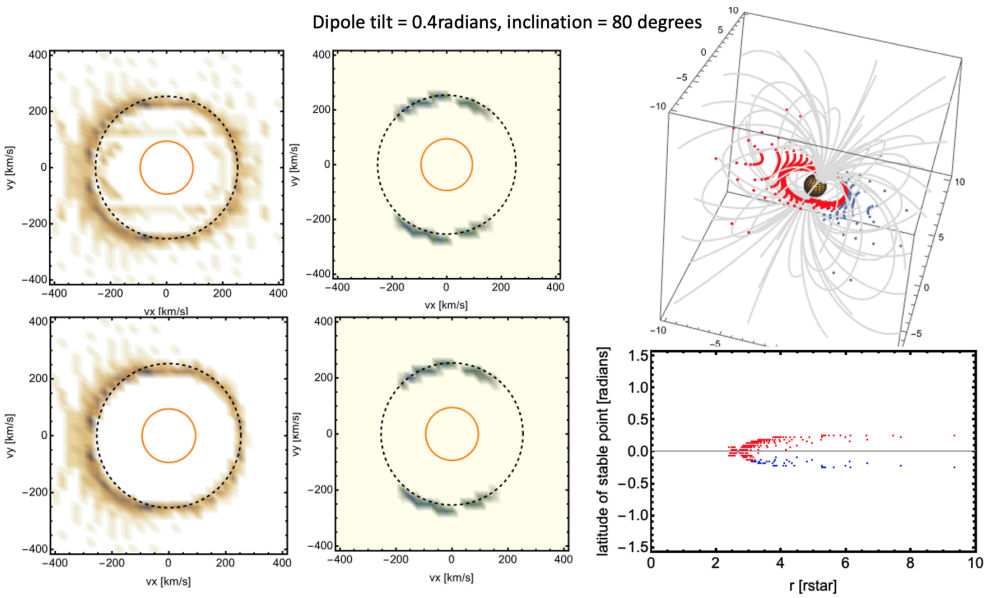

Figure 6.15: Velocity plots for a dipole tilted by 0.4 radians and an inclination of 80° for the total material (top row) and visible material (bottom row). Orange plots show the density of visible stable points and green show the visible material. On the far right: 3D plot of the visible stable points (red) and remaining stable points (blue) and below, the associated wine glass plot.

panels) and for only the visible ones (bottom panels). The orange plots show the density of stable points whereas the green plots show the absorption intensity, which relates to the density of the material present. The latter is a synthetic observation in that it is similar to the plots published by Cang and others [55]. These plots are normalised, i.e. scaled to their own maximum value. In some cases, very little material is visible and therefore if the visible plots were scaled to the same value as the total material plots, it may be difficult or impossible to discern any details. Therefore, in order to analyse the shapes of the plots produced, the colours of all plots are individually normalised. The stellar surface is shown by the orange circle and the black dashed line shows the equatorial co-rotation radius. Whilst stable points can be found at all longitudes, the highest densities congregate around the co-rotation radius, and the material produces two blobs around co-rotation in the synthetic observation. Once the inclination is accounted for, the synthetic observation appears almost identical. Whilst some stable points are not visible, those that are support most of the mass, and thus the shape of the synthetic observation is unaltered.

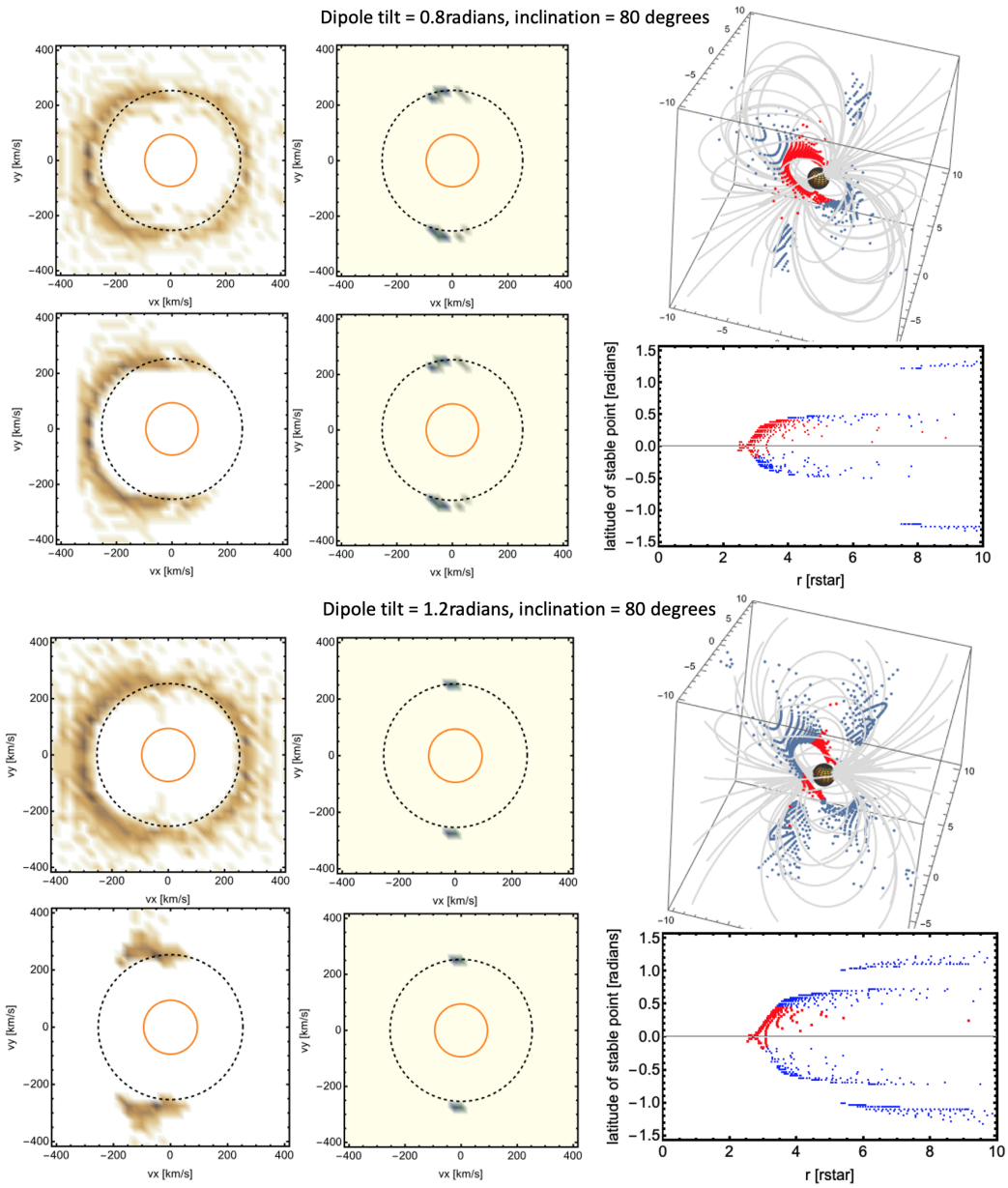

Figure 6.16: As in Figure 6.15 but for a dipole tilt of 0.8 radians and 1.2 radians.

With a dipole tilt of 0.8 radians, fewer stable points are visible. The highest mass stable points, at the equatorial co-rotation radius, are still just visible although the synthetic velocity observations now show two much smaller blobs than in the case of a 0.4 radian dipole tilt. Despite the half ring of stable points that is visible in the stable point velocity plot, those around the equatorial co-rotation radius (that forms the stem of the wine glass in the "wine glass" plots) are those that support the highest densities. All other stable points are washed out in the velocity plot since far less material can be supported at these points.

If the dipole is tilted further, to 1.2 radians, fewer still stable points are visible and the blobs in the velocity plots grow smaller still. The stable points that are visible no longer encompass one full side of the star and now also form two clumps.

6.8.2 Inclining the star at 65°

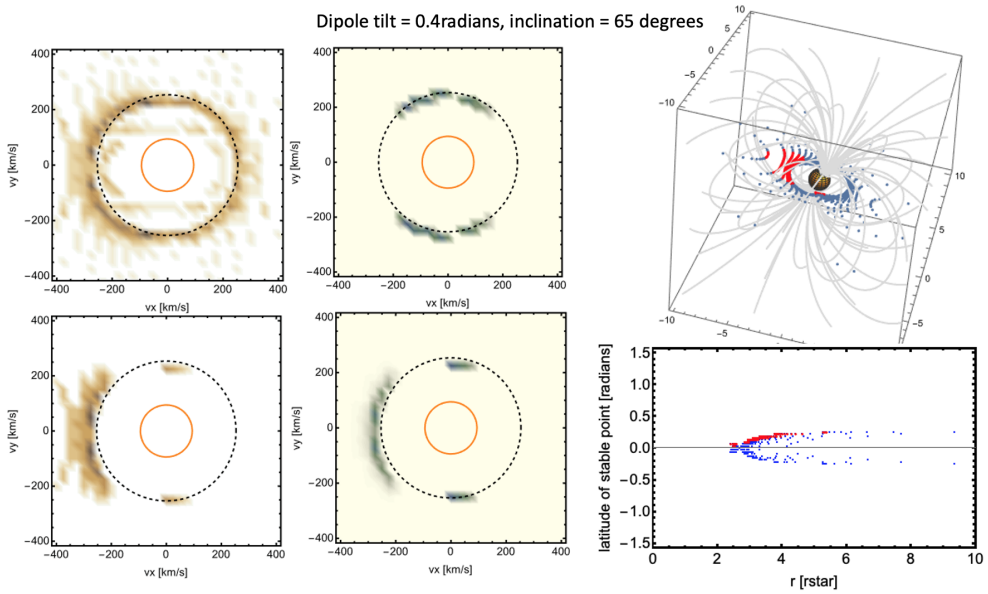

Figure 6.17: As in Figure 6.15 but for an inclination of 65°.

With an inclination of 65°, the observer sees far less of the equatorial plane. Figure 6.17 again shows, from left to right, the velocity plots in terms of stable point density and absorption intensity, and the stable point distribution in 3-dimensions (top) and as a wine glass plot. Rather than the full ring of stable points that was visible with an inclination of 80°, now only half of the ring is visible. This alters the absorption intensity velocity plot which now shows three blobs rather than the previous two. The third blob that is now present on the left-hand side of the velocity plot can be seen since the masses of the other two blobs are now smaller and therefore they no longer dominate the intensity.

With a dipole tilt of 0.8 radians, the intensity velocity plot now shows a half ring with two very small blobs, corresponding to the stable point regions that lie closest to the equatorial co-rotation radius. This again differs from the two blobs present in the other case with a higher inclination.

If the dipole is tilted further to 1.2 radians, the two blobs from stable points corresponding to the equatorial co-rotation radius are now not at all visible and thus a half ring is all that remains in the velocity plot. For the absorption intensity plot, the half ring shows two darker regions, which correspond to the stable points closest to the equatorial co-rotation radius.

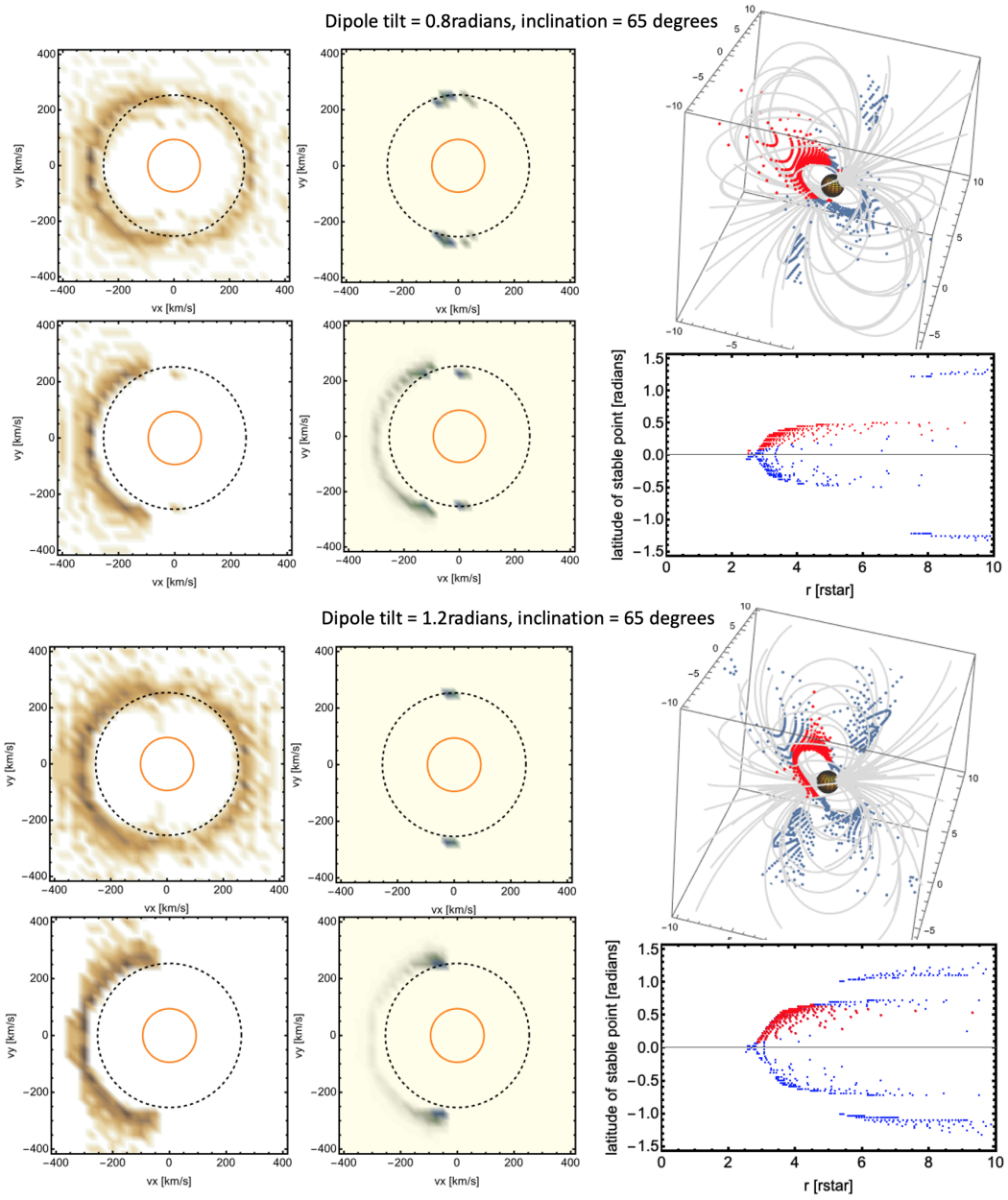

Figure 6.18: As in Figure 6.16 but for an inclination of 65°.

The number of stable points in a region and the mass supported there are both important in order for the region to create a visible feature in the velocity plots. For a dipolar field,

features typically form on either side of the star in two "blobs" around the equatorial co-rotation radius. Similar behaviour can be seen in observations, although others show one or three blobs (eg Figure 6.1). Three blobs can be replicated by this model for a more highly inclined star (65°), suggesting that inclination effects could be responsible. Overall, the velocity plots are quite degenerate.

6.9 Varying the stellar parameters; mass, radius and rotation rate

6.9.1 An M-dwarf

As the smallest stars, M-dwarfs can have different internal structure to larger stars, being fully convective and without the tachocline and radiative envelope that solar-like stars exhibit. For fully convective stars, this results in a different dynamo[160, 161], since the motions of charged particles within the star lead to different electrical currents and magnetic fields. The very low mass M-dwarfs that are fully convective can therefore exhibit different field structures to partially convective stars like the Sun [155].

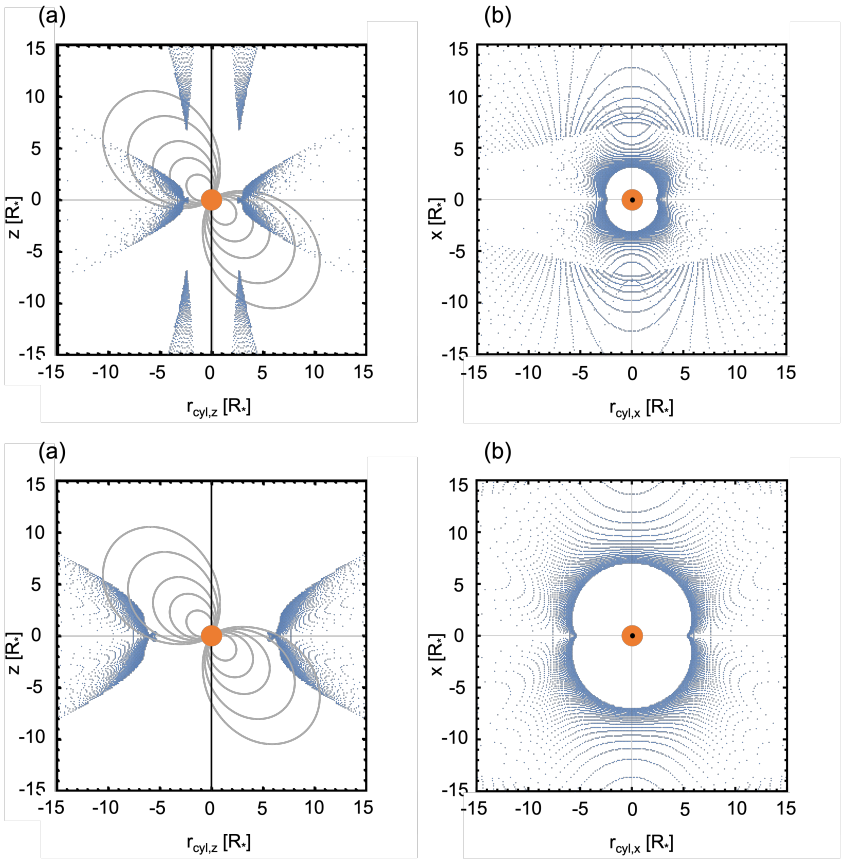

Figure 6.19: Polar plots showing the locations of the stable points for a tilted solar-like star ((a) and (b)) and M-dwarf ((c) and (d)).

Whilst the work above has modelled a young, solar-like star using the stellar parameters of AB Doradus, this small subsection considers the stable points for an M-dwarf of much lower mass but the same rotation rate. Here the parameters used were $M_\star = 0.3 M_\odot$,

$R_\star = 0.3R_\odot$ and $P_\star = 0.515$days. Figure 6.19 shows the stable points on polar plots for the M-dwarf (bottom) compared to the solar-like star (top). Whilst the relative locations of the stable points move outwards for the M-dwarf (with a larger co-rotation radius) the behaviour is still the same. With a mass and radius 0.3 times that of the Sun, this leads to a co-rotation radius about 3 times that of the solar-like star. The figure shows the stable point locations for a dipole tilted at $\pi/4$ radians from the rotation axis. For the solar-like star there are two classes of stable points, those within the wine glass distribution and those at very high latitudes. For the M-dwarf however, all stable points within this volume lie within the wine glass distribution. The high latitude stable points around the pole of the solar-like star could also be found for the M-dwarf, however they would lie at far larger radii from the surface.

The corresponding wine glass plots are shown in Figure 6.20. The M-dwarf is shown in (a) and the solar-like star in (b). The co-rotation radius of the solar-like star lies closer to the star than the M-dwarf and therefore the stable points can also be found closer to the star. The overall behaviour, however, is the same.

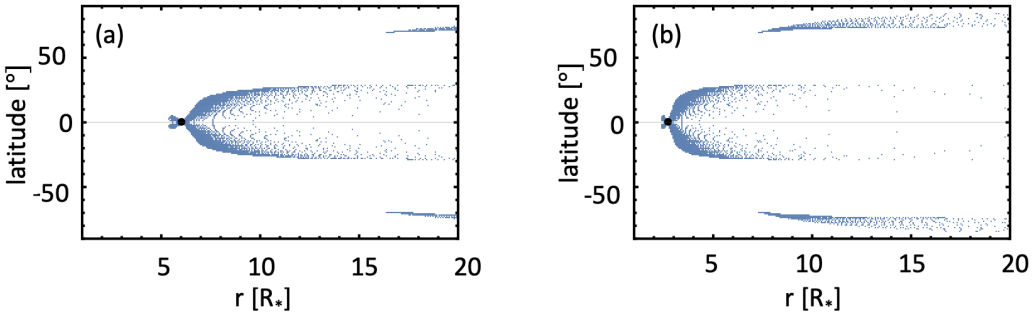

Figure 6.20: Latitude and radial positions of the stable points for (a) an M-dwarf with a tilted dipole and (b) a solar-like star with a tilted dipole.

6.9.2 Altering the stellar mass

Altering the stellar mass alters the effective gravity and the location of the co-rotation radius. This change in effective gravity moves the locations of the stable points. An example is shown in Figure 6.21 for a star with the same mass as AB Doradus (shown in blue) and half this mass (shown in red). The stable points are again shown for a range of dipole tilts. The lower mass star shows stable points closer to the stellar surface than the higher mass

star. This is because decreasing the stellar mass decreases the co-rotation radius:

$$R_k = \frac{GM_\star}{\omega^2 \sin^2\theta}. \tag{6.15}$$

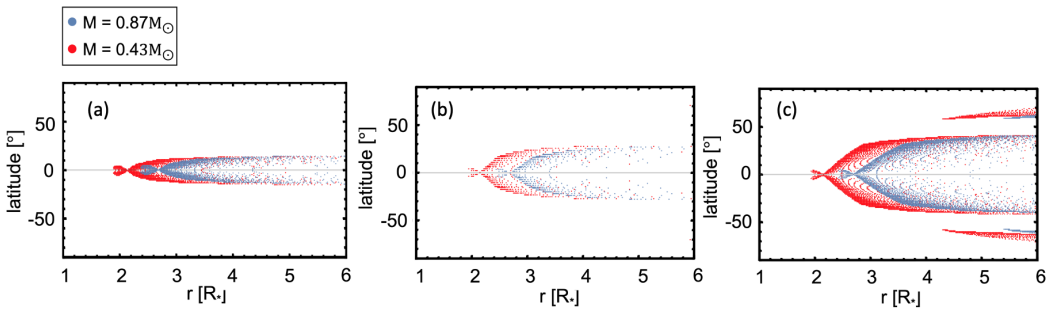

Figure 6.21: Plots showing the locations of the stable points around a star of mass $0.87M_\odot$ (blue) and $0.43M_\odot$ (red). Plots are shown for various dipole tilts: (a) $\pi/8$, (b) $\pi/4$ and (c) $3\pi/8$.

6.9.3 Altering the stellar radius

Figure 6.22 shows the effect of decreasing the stellar radius. Since the effective gravity depends in a complex manner on the stellar radius, it is not immediately apparent what the stable point distribution should look like. The horizontal axis of Figure 6.22 is radius from the star in units of the stellar radius. Since the smaller star has a smaller radius, its co-rotation radius is at a larger radius than for the larger star since

$$r_k = \frac{1}{R_\star}\left(\frac{GM_\star}{\omega^2 \sin^2\theta}\right)^{1/3}, \tag{6.16}$$

where r_k is the co-rotation radius scaled to the stellar radius. This means that the whole distribution moves to the right of the plot. However, it is also apparent that the distribution has altered shape. The distribution is thinner for the smaller star than the larger one, and the lobes found below the equatorial co-rotation radius are larger.

Stellar mass and stellar radius will generally vary together through a mass-radius relation, but it can be helpful to see how individual variables alter the results.

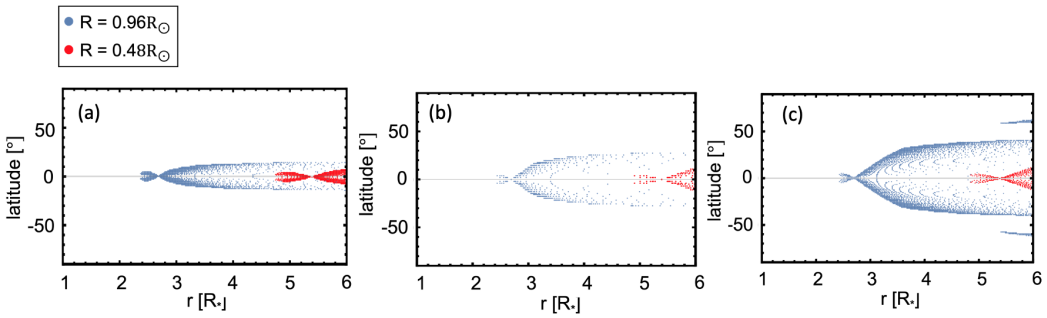

Figure 6.22: Plots showing the locations of the stable points for a star with radius $0.96R_{\odot}$ (blue) and $0.48R_{\odot}$ (red). The dipole tilts are as in Figure 6.21.

6.9.4 Altering the rotation rate

The rotation rate also determines the effective gravity, with an increase in rotation rate increasing the effective gravity. Figure 6.23 shows the locations of the stable points for a fast (blue) and slower (red) star. The stable points move out to larger radii for slower rotating stars, and whilst the shape of the distribution has altered slightly, it is still very similar.

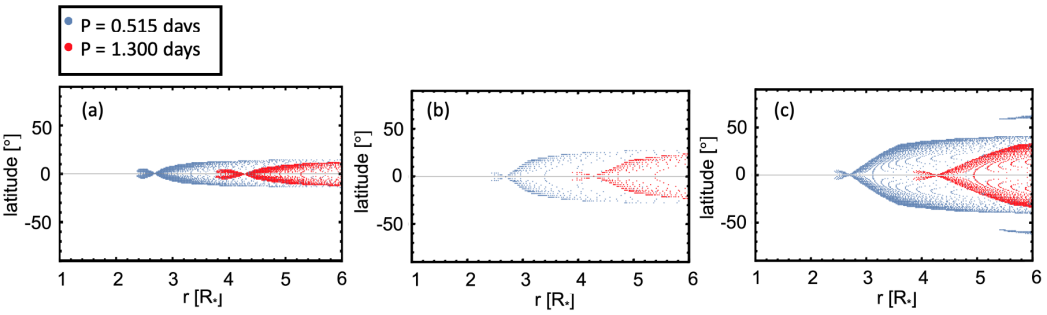

Figure 6.23: Plots showing the locations of the stable points for a fast star with rotation period 0.515days (blue) and a slower star with P= 1.3days (red). The dipole tilts are the same as in Figure 6.21.

6.10 A quadrupolar field

Whilst the dipolar field component is likely to dominate at the heights of most prominences, especially those above the co-rotation radius, the quadrupolar term could also be important [157]. The quadrupole term dies off with height faster than the dipolar term, meaning that it is of particular importance for prominences closer to the stellar surface. Here we consider the stable points around a purely quadrupolar field.

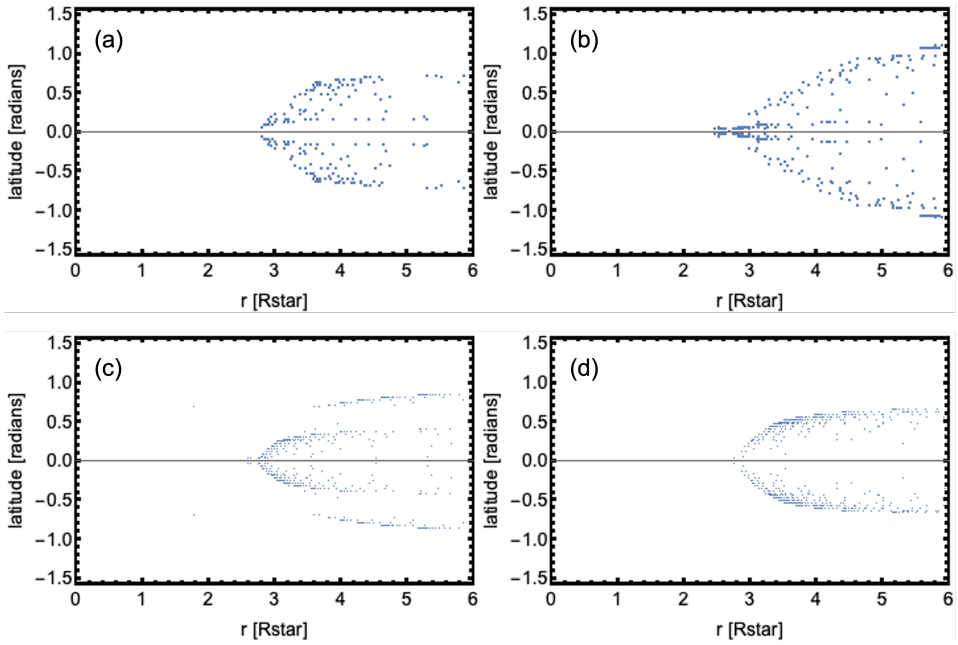

Figure 6.24: Latitude of the stable points within a tilted quadrupolar field. (a) shows the results for a quadrupole tilted at 0.4 radians from the rotation axis, (b) 0.8 radians, (c) 1.2 radians and (d) 1.6 radians.

Figure 6.24 shows a selection of wine glass plots for quadrupolar fields of various tilts. Whilst the shape differs from the dipolar case, the overall "wine glass" spread is the same. Wings are sometimes present, see Figure 6.24 (c), as were present in some of the analogous dipole plots. A small cluster around and just below the equatorial co-rotation radius can be seen in some but not all plots (Figure 6.24 (b) and (c) here).

6.10.1 Stable point distribution

Figure 6.25 shows the stable point distribution with tilt of the quadrupole axis. The left hand side of the horizontal axis represents a quadrupolar axis that is perpendicular to the rotation axis and embedded within the equatorial plane. An aligned quadrupole lies on the right hand side of the plot. Again, dark spots are locations of high density of stable points. The centre of the plot represents a quadrupole tilted by $\pi/4$, where some of the loop summits lie in the equatorial plane and the rotational axis. This leads to a high density region of stable points, focused around the equatorial plane.

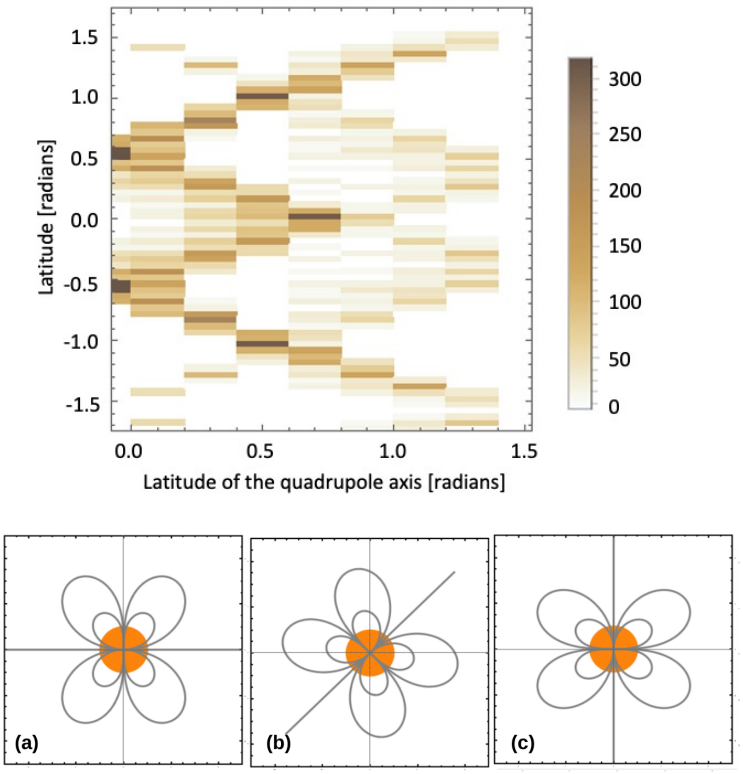

Figure 6.25: The latitudes of stable points against latitude of the quadrupole axis. The colour shows the number density of stable points, with dark showing regions of high density. The bottom row shows (a) a fully misaligned quadrupole, (b) a tilt of $\pi/4$ and (c) a fully aligned quadrupole.

The overall shape of the plot appears as two W shaped curves, mirrored vertically about a quadrupolar tilt of $\pi/4$ radians. Despite the shapes being symmetric, the right hand W appears fainter than the left hand one. This might be due to the slightly different shapes of the quadrupolar field, which can be seen in Figure 6.25. An aligned quadrupole and fully misaligned quadrupole are similar but not identical in shape, and the magnetic field lines point in different directions compared to the direction of the effective gravity. Both of these will have consequences for stable point formation.

Whilst for a dipole, stable points were most easily found around the equatorial plane for an aligned field, with a quadrupole this occurs with a tilt of $\pi/4$ radians. This means that when observing stars with strong quadrupolar components, in order to spot many massive prominences within the equatorial plane the field should be inclined by $\pi/4$ radians in comparison to the rotation axis. Stars with strong quadrupolar components provide more

opportunity for higher latitude prominences than dipolar fields, which can be seen by the double W in Figure 6.25. However, these higher latitude stable points will support less mass than those in the equatorial plane.

6.10.2 Dynamic spectra

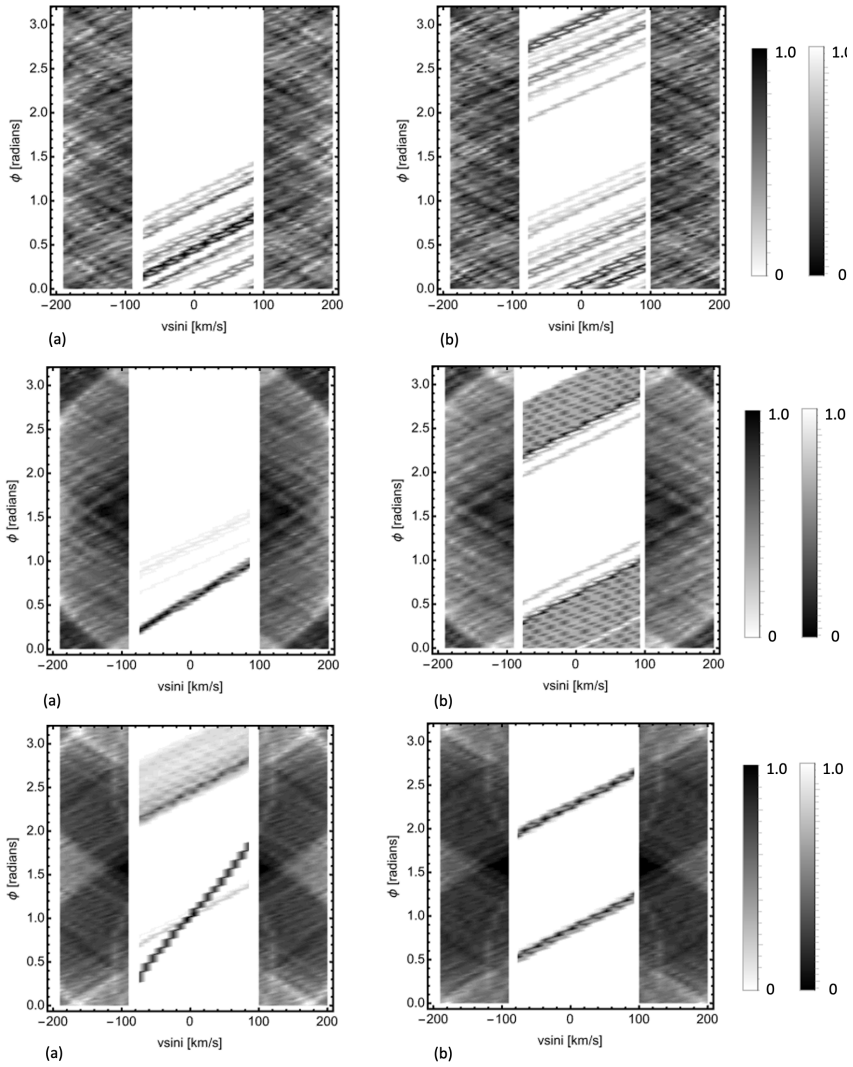

Figure 6.26: Rows: dynamic spectra for a quadrupole tilted by 0.4, 0.8 and 1.2 radians, from top to bottom. The left hand plots show an inclination of 65° and right show 80°. The normalised absorption and emission intensities are shown by the left and right colour bars, respectively.

Figure 6.26 shows the dynamic spectra for a quadrupolar field with various tilts and inclinations. The left hand column shows an inclination of 65° and the right hand column shows 80°. The rows show the quadrupolar tilt, from top to bottom: 0.4, 0.8 and 1.2 radians.

As with the dipole, tilting the quadrupole leads to the thinning of absorption features, but here this leads to two features rather than the one found for a dipole. These two features can both be seen in the highly inclined case ($i = 80°$) but are not always both visible for an inclination of 65°. The emission lines also show similar behaviour to the dipole case - showing more coherence for more inclined quadrupolar fields than aligned ones.

6.10.3 Velocity plots

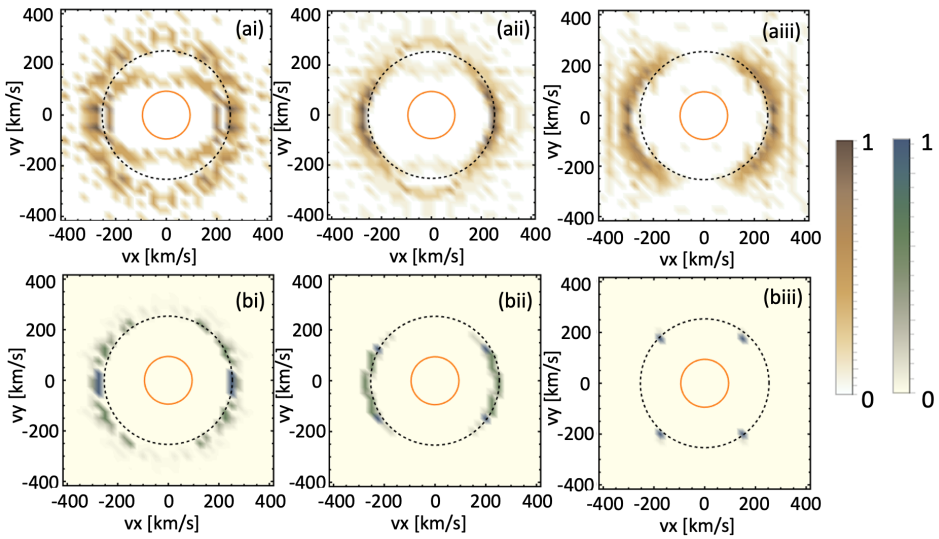

Figure 6.27: Top row: velocity plots showing the density of stable points for a quadrupole tilted by (i) 0.4 radians (ii) 0.8 radians and (iii) 1.2 radians. Bottom row: velocity plots showing the absorption intensity for the material with tilts as above. The colour tables have been normalised, orange circles show the stellar surface and black dashed lines show the co-rotation radius. The normalised intensity of stable point density and absorption are shown by the brown and green colour tables, respectively.

Figure 6.27 shows velocity plots for a quadrupolar field of tilts 0.4, 0.8 and 1.2 radians, from left to right. Again, the top, orange plots show the density of stable points whilst the bottom, green plots are the synthetic observations. As with the dipole, a large number of stable points and mass, congregates around the equatorial co-rotation radius. Again some stable points form within this co-rotation radius, corresponding to the high latitude stable points, with the density of these decreasing as the field is tilted towards the equatorial plane. By (aiii) of the figure, a tilt of 1.2 radians, the stable points no longer form a full ring around the co-rotation radius, showing two gaps separated by $\phi = \pi$ radians. Despite the full ring

in (ai) and (aii), the synthetic plots show broken rings. For a tilt of 0.4 radians (bi) the plots show two gaps in the ring, π radians apart. For a tilt of 0.8 radians, these gaps have grown and the features have shrunk to form two extended blobs. For a tilt of 1.2 radians, only four small features remain.

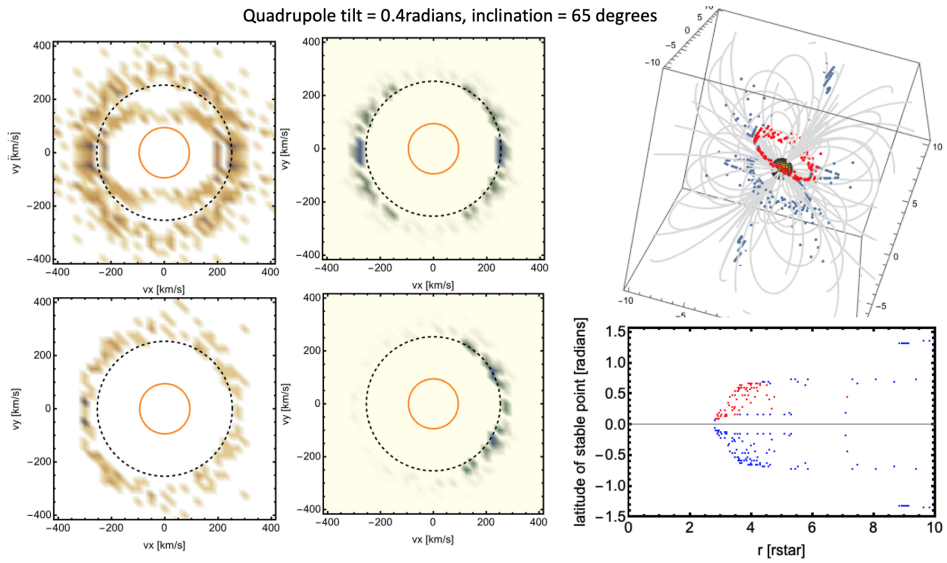

Figure 6.28: Velocity plots for a quadrupole tilted by 0.4 radians and an inclination of 65°. The figure has the same layout as Figure 6.17.

As in the dipole section, the plots shown in Figure 6.27 show the total stable points and material. The material and stable points that are visible to observers will depend on the inclination of the star relative to the observer. Figures 6.28 and 6.29 show the visible material for an inclination of 65°. For the 0.4 radian tilt, only one of the blobs is visible in the synthetic spectra. Many of the stable points, including the high latitude ones, never transit the disc. As can be seen from the 3D stable point plot, most of one of the rings of stable points is visible (red points), with the other hemisphere being invisible in absorption. For an inclination of 0.8 radians and the same inclination, the plane of stable points is more inclined and therefore no longer completely visible. Now only two clumps are visible, and this alters the synthetic spectra so that rather than two extended blobs around co-rotation, only two small features remain in the synthetic spectra. It is apparent from comparison to the corresponding plot for the stable point density that these two features are small compared to the stable points that are visible, and yet they contain most of the mass.
For tilt of 1.2 radians, the stable point distribution becomes more complex. One half of a plane is visible, and a few clumps on the other side of the star, leading to a large

clump and a few specks in the synthetic observations. From comparison to the synthetic observation for the total material, the densities or absorption intensities that would be visible are considerably lower than for the total material.

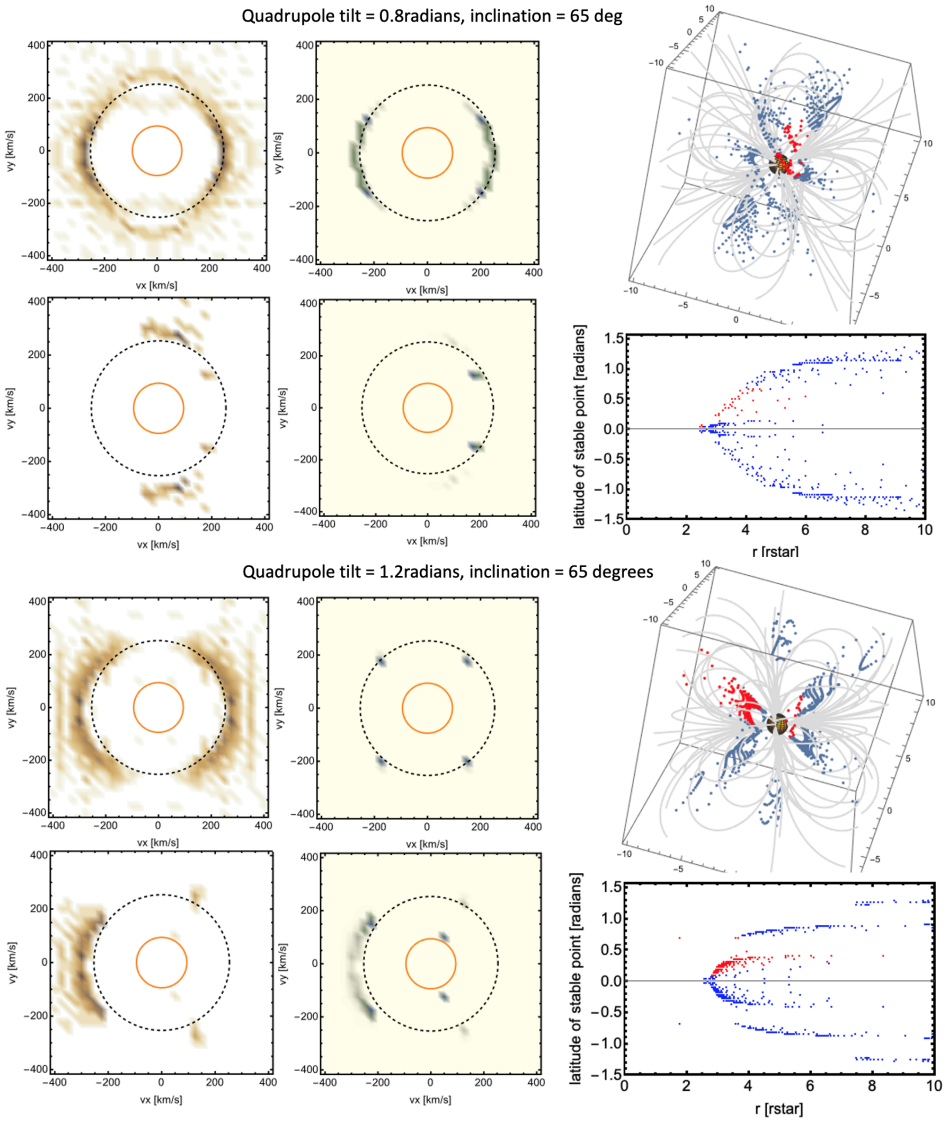

Figure 6.29: As in Figure 6.28 for a quadrupole tilt of 0.8 radians and 1.2 radians.

6.11 Summary and conclusions

This chapter has investigated stable point formation around tilted field structures, particularly dipole fields. As would be expected, the stable points form symmetrically about the equatorial plane of the star. They form in a wine glass shape, that widens in latitude as the dipole tilt becomes more apparent. The distribution of stable points in latitude with

dipole tilt forms a W shape on its side. For fully aligned dipoles (latitude of the dipole axis at π radians), stable points form exclusively within the equatorial plane. As the dipole is tilted over, stable points can be found at a wider range of latitudes about the equatorial plane, with some very high latitude stable points found at large radii. This band around the equatorial plane continues to grow with dipole tilt, and the high latitude stable points move to lower latitudes and radii. This continues until the two sets of solutions merge into a huge band. This band of stable points is not equally spread, with certain latitudes being preferred and leading to the W shape. This behaviour is in keeping with previous work, where bands of stable points were found to vary with dipole tilt [137].
Dynamic spectra for the dipole show the influence of the inclination and dipole tilt on the absorption features in the Hα line. The tilt of the dipole can also be seen to be of importance to the emission part of the spectra, with more highly tilted dipoles producing clearer emission features, for both of the inclinations shown in this work. Therefore the dipole tilt could be an important factor for observing prominences in both absorption and emission around prominence bearing stars. The modelled velocity plots make it apparent that the distribution of stable points need not correlate to the prominence observations. Locations of large numbers of stable points do not necessarily support large amounts of mass, since this is dependant on the effective gravity and local magnetic field strength. The model generates velocity plots that produce two blobs, π radians apart, for a dipole structure. The size of these blobs depends on the tilt of the dipole, with more aligned dipoles producing larger blobs. Once the inclination is accounted for, the appearance of the blobs vary.

The model can be easily adapted for different stars, and increasing the stellar mass, decreasing the stellar radius or increasing the rotation rate all result in the same behaviour but with stable points moving further out from the star.

More complex fields of quadrupoles have been considered, and unsurprisingly result in more complex distributions of stable points. Velocity plots in the quadrupolar case can also result in two blobs, although these blobs can be far more extended and almost ring-like for some tilts. For other quadrupole tilts, four small blobs may be present in the velocity plot. Again, once inclination is considered the velocity plots can look quite different from the total material. In some cases only half a ring remains, in others the two blobs at π radians apart are reduced to two small blobs from one of the original blobs. In the case of the

quadrupole, the velocity plots for inclined fields show less symmetry than the dipolar case. This is a result of the inclination effects which make is impossible to see certain locations around the star in absorption.

With a dipolar field structure, we might expect from this work that such observations to result in velocity plots with two blobs, π radians apart. However, the models here have assumed that all stable points are filled and on a real star this may not be the case at any given time of observation, therefore it would be possible that only one blob (or no blobs!) were present in the observations. With a quadrupolar field, we might expect that observed velocity plots would yield anything from a half ring to four small blobs. By eye it is difficult to pick out any particular trend with field complexity and inclination that would clearly show an observation to correlate to a particular field structure. However, with some sort of machine learning method, it might be possible to compare many generated velocity plots to observations and suggest potential field structures that could produce the observed plots.

Chapter 7

Analysing the observations

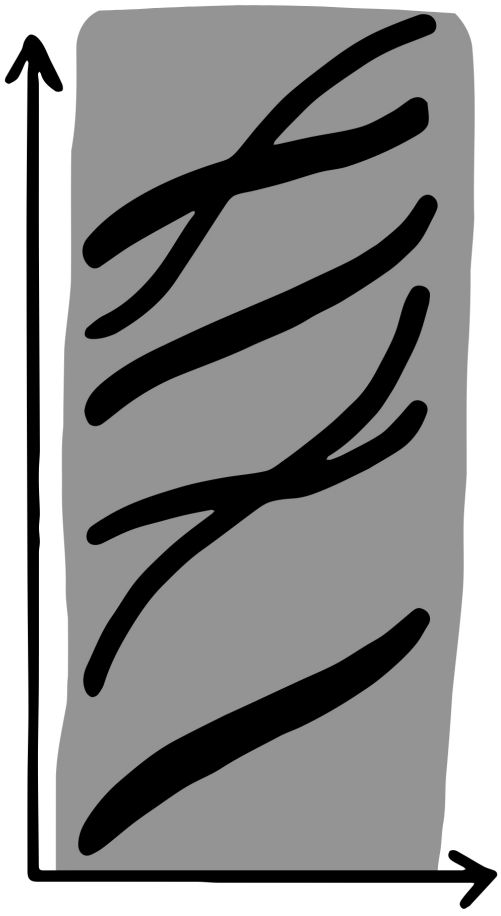

7.1 Introduction

The work within this chapter has not yet been published.

Whilst prominences have been well studied for any given observing run, there has been little work to collate the data available from all prominence observations. In this small chapter, this observational data is collated and compared across the stars for which data could be found in the literature. Since these observations are from a wide range of studies, the data available is not always consistent across stars.

7.1.1 The stellar data

The stars on which there is available data on the prominences observed are given in Table 7.1. For many stars, prominences have been observed but data on masses, distances from the star and/or densities were not reported. This table lists the stars for which data could be found on the prominence distances from the rotation axis.

Star	$M_\star$ [$M_\odot$]	$R_\star$ [$R_\odot$]	$P_\star$ [days]	i [$\circ$]
PZ Tel	1.13	1.23	0.9447	68
HK Aqr	0.4	0.59	0.43122	90
Speedy Mic	0.82	1.06	0.38	69
AB Doradus	0.87	0.96	0.515	58
TWA17	1	1.25	0.685	29
TWA6	0.7	1.05	0.54	47
V410 Tau	1.4	3.1	1.872	59
EY Dra	0.49	0.52	0.459	90
LQ Lup	1.16	1.22	0.31	35
HE373	1	1.11	0.333	61
HE520	1	1.04	0.6079	90
HE622	1	1.09	0.804	70
HE699	1	1.08	0.4908	62
AP149	1	1.29	0.32	30

Table 7.1: A table showing the stellar parameters; mass, radius, rotation period and inclination, for the stars on which there was available data in the literature of prominence locations.

Figure 7.1 gives histograms of the stellar data listed in Table 7.1. Many stars in this sample have a mass of around 1 solar mass and a radius of around 1 solar radius. The smallest star in the sample is the M-dwarf HK Aquarii with the smallest mass and radius at 0.4 solar masses and 0.59 solar radii. The largest star in the sample is V410 Tau, with a

mass of $1.4M\odot$ and a radius of $3.1R_{\odot}$.

The distribution of rotation periods ranges from 0.31 days to 1.872 days. The fastest rotator is LQ Lup and the slowest is V410 Tau. Most stars in the sample have a rotation rate between 0.3 and 1 days.

These stars have a range of inclinations (of the rotation axis to the observer), from 29 to 90 degrees. Stars such as HK Aquarii, EY Dra and HE520 are viewed pole on, whilst TWA17 and AP149 with inclinations of around 30 degrees are viewed closest into the stellar equator. The peak of the distribution lies around 70°, although there is a large spread.

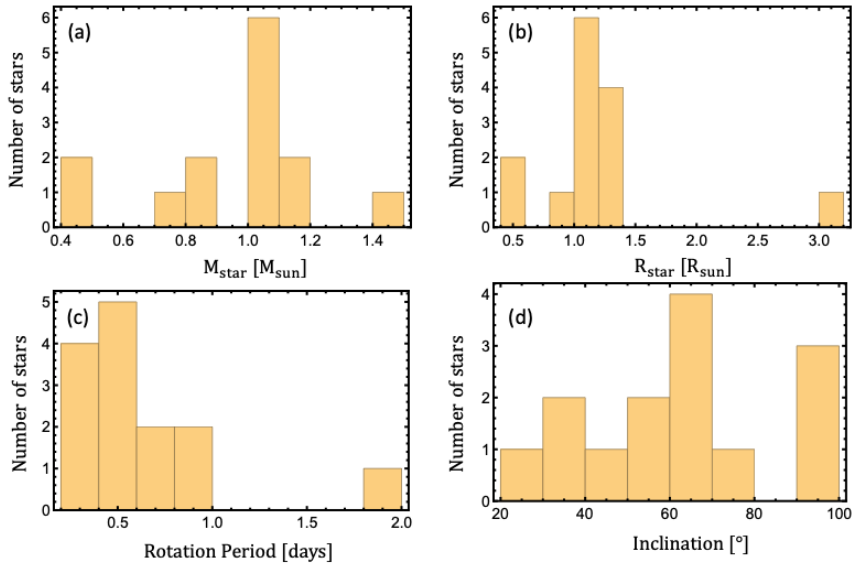

Figure 7.1: Histograms showing the distribution of stellar (a) mass, (b) radius, (c) rotation period and (d) inclination for the stars listed in Table7.1.

7.1.2 The observed prominence data

Prominence distances from the rotation axis

Table 7.2 lists the distances from the rotation axis (ϖ) of prominence observations around these stars, along with the associated references. Distance from the rotation axis is the cylindrical radius, $\varpi = R_p \cos\theta$. For many stars, there are only one or two observations, sometimes given in the literature as a range. For HK Aqr, Speedy Mic and AB Dor however, there are many observations.

Star	ϖ [$R_\star$]	References
PZ Tel	2.3, 4.9, 1.5, 2	Barnes 2000[42]
	1.44, 1.05	Leitzinger 2016[41]
HK Aqr	5.2, 3.4, 3.0, 2.6, 2.1, 2.2, 1.2	van den Oord 1998[43]
	3.75, 0.32, 0.49, 1.67, 2.41, 0.54, 1.35	Leitzinger 2016[41]
	1.34, 1.34, 1.34, 1.35, 1.33, 1.35, 1.34	Byrne 1996[44]
Speedy Mic	2.96, 1.01, 1.36	Jeffries 1993[35]
	1.3, 3.2, 2.4, 3.8	Barnes 2001[54]
	2.79, 3.16, 2.88, 2.4, 3.28, 3.06, 2.82, 1.43, 3.21, 2.32, 3.18, 1.71, 3.31, 3.0, 3.64, 2.1, 2.49, 2.87, 3.48, 3.16, 3.0, 3.09, 2.35, 3.39, 3.24	Dunstone 2006[36]
	2.99, 3.68, 3.72, 3.92, 2.35, 4.67	Dunstone 2006[37]
	3.5, 4.4	Wolter 2008[162]
AB Doradus	7.35, 3.71, 2.87, 1.26, 3.53, 2.29, 2.82, 2.6, 2.32, 6.16	Collier Cameron 1989a[1]
	6.9, 6.2, 2.3, 4.1, 8.1, 5.6, 2.4, 4.4, 3.1, 3.3, 2.9, 2.7, 2.3, 2.7, 4.9, 6.8, 8.5, 2.75, 3.3, 3.7, 3.0, 4.8, 4.1	Collier Cameron 1989b[27]
	2.8, 3.5	Brandt 2001 [30]
	1.9, 2.9, 2.9, 2.7, 3.3, 2.5, 2.3, 2.9, 2.1, 2.3	Donati 1997[25]
	3.1, 3.0, 3.1, 3.45, 4.85, 4, 3.33, 7.96, 3.5	Collier Cameron 1999[31]
	3.0, 4.5, 4.7, 3.2, 4.2, 4.2, 3.1, 3.4, 3.5, 2.7, 4.5, 3.7, 4.5, 4.5, 3.2, 3.8, 2.5, 2.8, 3.8, 4.5, 3.5, 3.8	Donati 2000[53]
	3.1, 3.0	Gomez de Castro 2002 [32]
TWA17	4.0	Skelly 2008[51]
TWA6	4.0	Skelly 2009[52]
V410 Tau	$2.5\cos(\pi/2-\theta)$	Skelly 2010[23]
EY Dra	3.86-3.99, 1.4-1.72, 0.8-1.33, 4	Eibe 1998[48]
LQ Lup	1.3-2	Donati2000[**?**]
HE373	2-2.8	Collier Cameron 1992 [47]
HE520	3.7-5.1	Collier Cameron 1992 [47]
HE622	5.4	Collier Cameron 1992 [47]
HE699	3.8-6.0	Collier Cameron 1992 [47]
AP149	3.23, 3.01, 2.29, 1.58	Barnes 2001[54]

Table 7.2: A table listing the observed distances from the rotation axis of prominences around the stars in Table7.1.

Figure 7.2 shows a histogram generated from this published data. The black dashed line shows the location of the equatorial co-rotation radius. AB Doradus is the most studied star for slingshot prominences, and therefore this histogram has much more data than some of the others, shown in Figure 7.3. For AB Dor, the peak of the distributions can be seen to be at distances around the equatorial co-rotation radius. The distribution is biased to distances beyond this radius, with very few prominences at low distances.

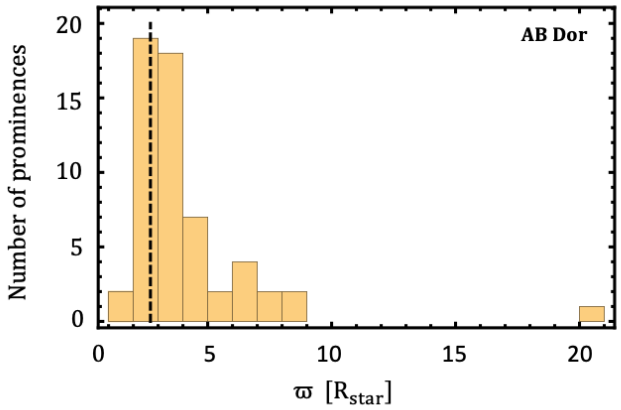

Figure 7.2: Histogram showing the distribution of prominences around AB Doradus for the collated date in Table7.2.

Speedy Mic, another well-observed star, shows a slightly different and more compressed distribution. Rather than the range of $\varpi = 0 - 10R_\star$ that is seen in AB Dor, the distribution for Speedy Mic covers $\varpi = 1 - 5R_\star$. The peak of the distribution is no longer at the equatorial co-rotation radius, but now beyond it. HK Aquarii also has a notable number of observations, and the distribution here is different to both AB Dor and Speedy Mic. The peak of the distribution is below the equatorial co-rotation radius, with prominence numbers decreasing beyond around $2R_\star$. Other stars have low numbers of observations, making extracting anything meaningful from this data difficult, although they are shown in Figure 7.3 for completeness. The histograms shown here collate all the observations of prominences around these stars. For some stars, such as AB Dor, these observations have taken place over many years and the magnetic field structure of the star has likely changed over this time period. Therefore these histograms would show a distribution of prominence locations more like an average, potentially over a stellar cycle, and observations taken in one particular year might look quite different from these distributions.

As discussed in Chapter 2, the distribution of prominence locations can depend on various stellar parameters such as coronal temperature, stellar magnetic field strength, the presence and location of a source surface and the dominating magnetic field topology (e.g. dipolar or quadrupolar). Therefore, that the distributions of prominences on these stars would be different is not surprising but the shapes of the distribution may be expected to

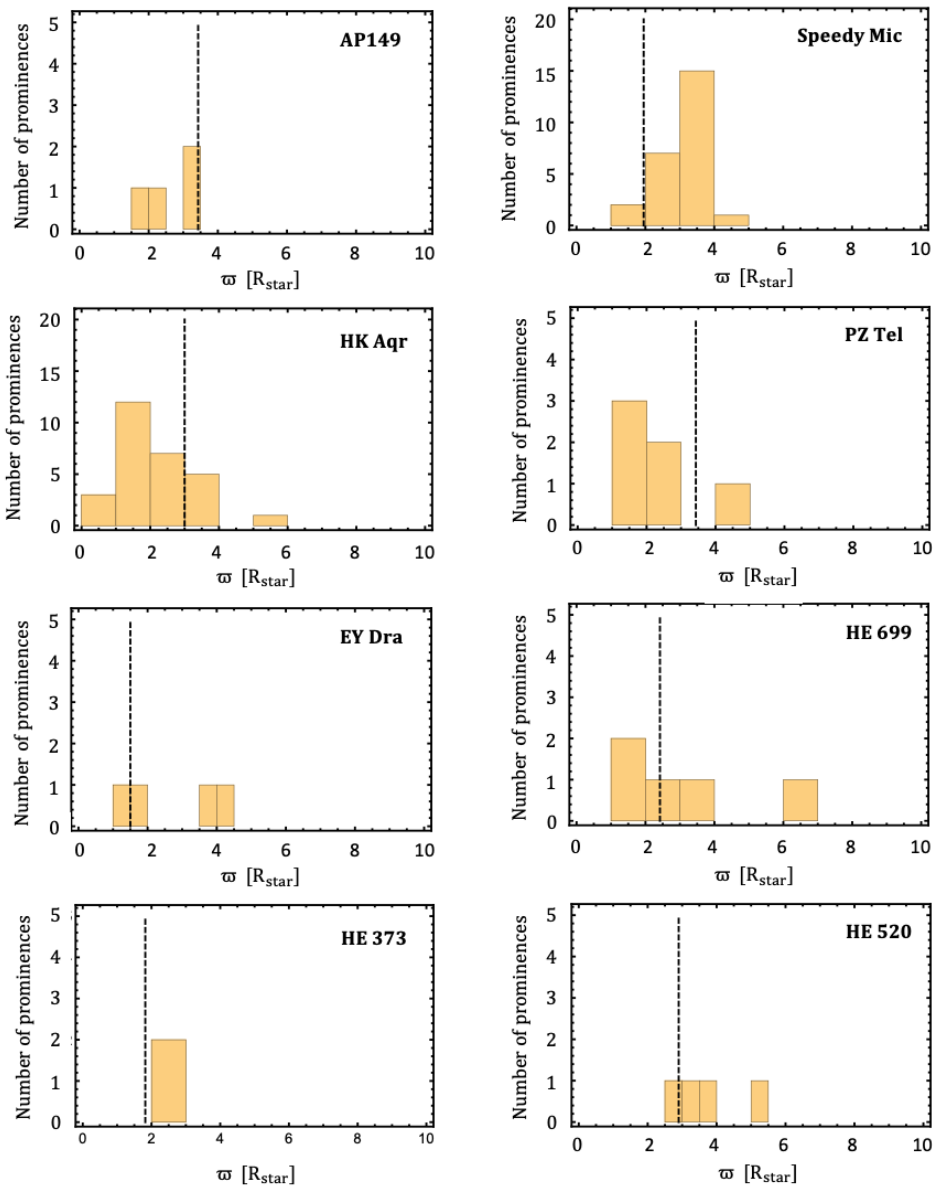

Figure 7.3: Histograms showing the observed prominences distributions. The black dashed line shows the location of the equatorial co-rotation radius.

show the same overall trends. A change in these parameters should not alter the overall shape of the height-width curve that the model in Chapter 2 would generate, and therefore the prominence distributions would be expected to show the same behaviour. However, the distribution from AB Dor looks very different from the distribution for HK Aqr. Work in Chapter 2 showed that the location of the source surface influences the shapes of the distributions and this could be at least partly responsible for the differences seen here in these distributions. Whilst AB Dor and HK Aqr have, relatively speaking, a large number of prominence observations used in generating their histograms, the absolute numbers are still small: 76 and 21 for AB Dor and HK Aqr, respectively. A larger number of observations, especially for HK Aqr, would make it easier to establish if these differences in the histograms are caused by intrinsic differences in the prominence locations, small number statistics, or indeed an inclination effect.

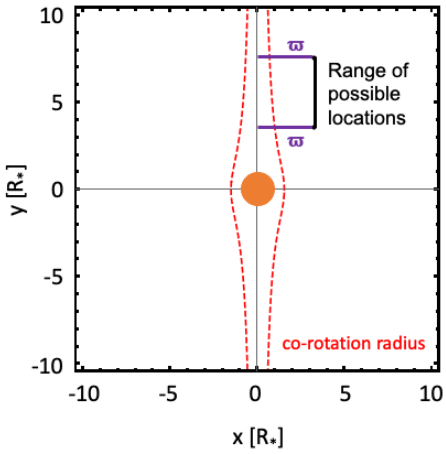

Figure 7.4: Figure showing ϖ, the distance from the rotation axis, which points along the y axis.

Figure 7.4 shows the distance from the rotation axis, ϖ. Because ϖ is a cylindrical radius, a given value of ϖ could correspond to a range of different locations around the star (r_p,θ). As discussed later in this chapter, however, the range of possible locations (r_p,θ) that the prominence could have had is constrained by the fact that the prominence was observed.

Observations of prominences provide the values for ϖ from the drift rate of the promi-

nences in the Hα spectra. In other words, the velocity with which the prominence tracks cross the stellar disc. This can be found from the gradient of the transient. This provides observers with the distance of the prominences from the rotation axis (ϖ) since

$$\varpi = \frac{\dot{v}}{v\Omega^2 \sin(i)}. \tag{7.1}$$

This is distinct from the radial distance of the prominence (r_p), and it's height above the stellar surface:

$$\varpi = r_p \cos\theta \tag{7.2}$$

where θ is the co-latitude of the prominence.

With observationally derived values of ϖ, the possible radii and latitudes of these prominences can be calculated.

7.2 Plotting the potential prominence locations

Potential prominence locations (r, θ) can be found by combining the data from the literature of the prominences distances from the rotation axis (ϖ) with Equation 7.2. This gives a range of possible solutions, examples are shown in Figure 7.5 for AB Dor and Speedy Mic. These plots show the visible locations around a star as the white regions, and the locations that never transit the stellar disc as grey regions. The red line shows the latitude at which a prominence would be visible at any height above the surface, with the equatorial co-rotation radius shown on this line as a red point. The black curves show the possible prominence locations for individual observed prominences.
Given that the prominences were observed and (for almost all stars) transited the stellar disc, the potential prominence locations can be constrained further. The only possible locations for these prominence locations are the sections of the black curves that lie within the white regions of the plot, i.e. transited the disc.
Similar plots for the remaining stars are shown in the appendices (Appendix G).

Observations provide a distance from the rotation axis for prominences, based on the gradient of the curve that the prominence produces in the dynamic spectrum. Whilst this quantity is useful when comparing prominence observations, it can be unsatisfactory since it

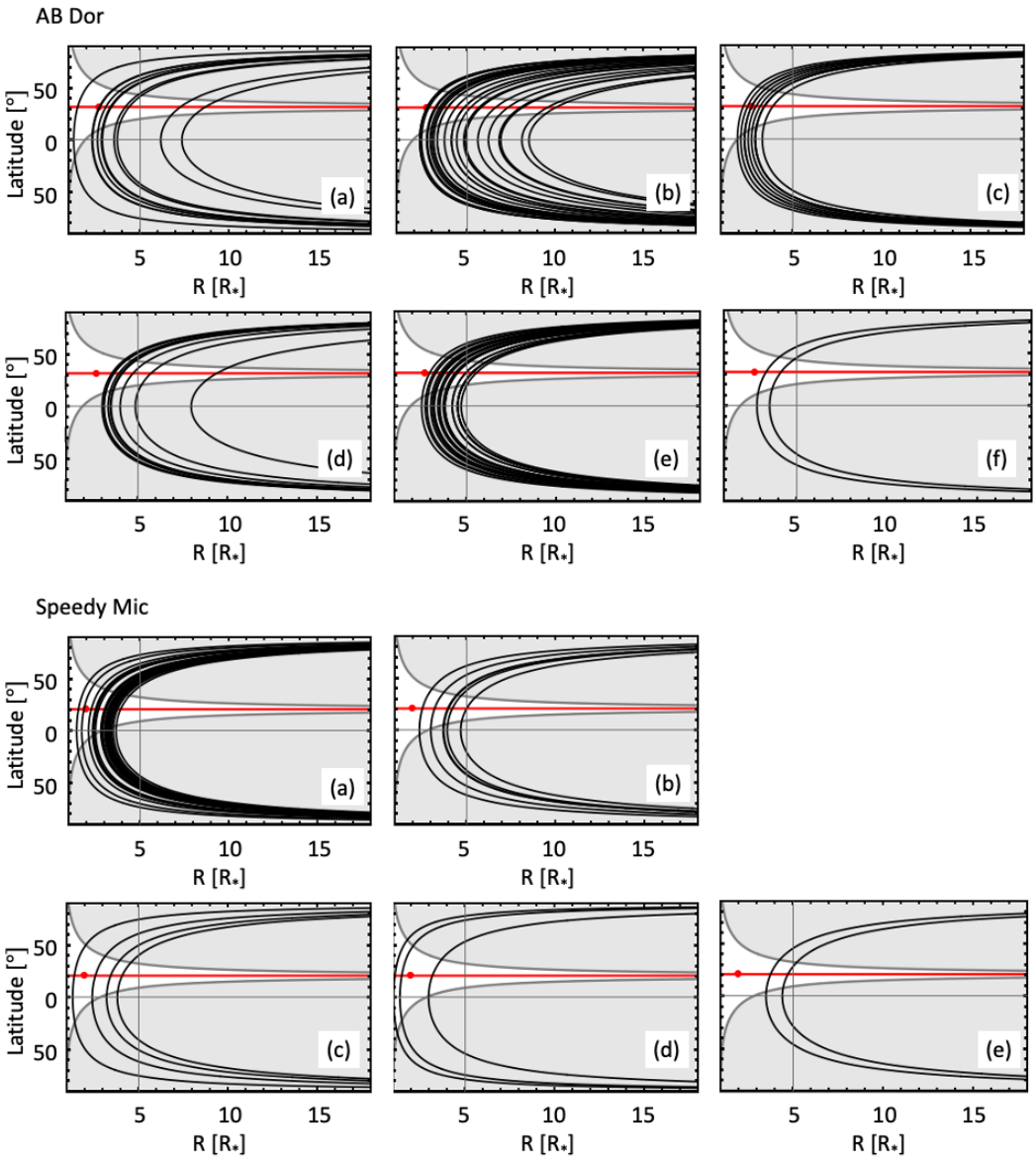

Figure 7.5: Possible prominence locations for the stars AB Doradus and Speedy Mic. The plots show observations from Table7.1. For AB Dor: (a) Collier Cameron 1989a [1] (b) Collier Cameron 1989b [27] (c) Donati 1997 [25] (d) Collier Cameron 1999 [33] (e) Donati 2000 [53] and (f) Brandt 1994 [30]. For Speedy Mic: (a) Dunstone 2006a [36] (b) Dunstone 2006b [37] (c) Barnes 2001 [54] (d) Jefferies 1993 [35] (e) Wolter 2008 [162].

contains within it both the radius and latitude. However, untangling the radius and latitude from ϖ is not straightforward since a range of combinations would produce the same ϖ value. Prominences observed at greater distances from the star have better constrained latitudes. These further out prominences can only have a narrow range of latitudes and still transit the disc. Meanwhile, prominences observed closer to the star have poorer constrained latitudes, since the opposite is true. For constraints on the radius, the stellar inclination is important. An observation of a prominence on a star that is equator on to observers (or has a low inclination) will provide the best constraints on the radius of the prominence. Looking at Figure 7.5, it can be seen from the shape of the black curves that a prominence in the equator with a given ϖ value could have a smaller range of radii whilst still being visible. The black curves of ϖ are very steep around the equator and therefore the radius does not change much. However, because of the flattening of the black curves at large distances, a prominence observed at higher latitudes (for example if the star had a high inclination) could have had a wider range of radii and still been visible.

7.3 How does the maximum radius vary with co-rotation radius?

Figure 7.6 shows the maximum radius at which prominences have been observed, plotted against co-rotation radius. The grey dashed line shows the radius at which the prominence would be at the equatorial co-rotation radius. The solid grey line shows the maximum height a prominence within the equatorial plane could take, as calculated by Jardine and van Ballegooijen 2005 [77]. Speedy Mic, AP149 and AB Dor all lie above this maximum predicted height. This may be that the prominences are being supported at these great distances and that the model can not explain this, or it may be that these prominences are being ejected from the star. Evidence of prominences being ejected has been seen on AB Dor, with some prominences being seen to move further out on consecutive nights of an observing run. Given that AB Dor and Speedy Mic are the most well observed stars for slingshot prominences, it is reasonable that this could be the explanation. For many other stars, prominences are not observed over many nights and are sometimes only observed for one night. Therefore, the chances of seeing a prominence moving out from the star would be lower for the other stars in the sample. Most stars, however, lie between this maximum

predicted height and the co-rotation line. This suggests that prominences typically form up to this maximum height, and beyond the co-rotation radius (grey dashed line). The plot shows quite a lot of scatter, with no obvious trend. Typically, there is a large uncertainty in the maximum height, which comes from the uncertainties provided in the literature for the observed distances from the rotation axis. Not all of the observations provide uncertainties and therefore not all points on the plot have error bars. The horizontal error bars are also associated with the observed uncertainties - the range of potential latitudes of the prominence provides a range of co-rotation radii since the co-rotation radius varies with latitude. The thick black lines show the maximum height for prominences at higher latitudes (latitudes 30°, 50° and 60°, from bottom to top). All stars lie below the maximum height for prominences at a latitude of 50°. Latitudes of prominences are not accounted for in this plot, however the latitude of a prominence will determine its maximum height. Some of the scatter within this plot could be due to differences in latitudes.

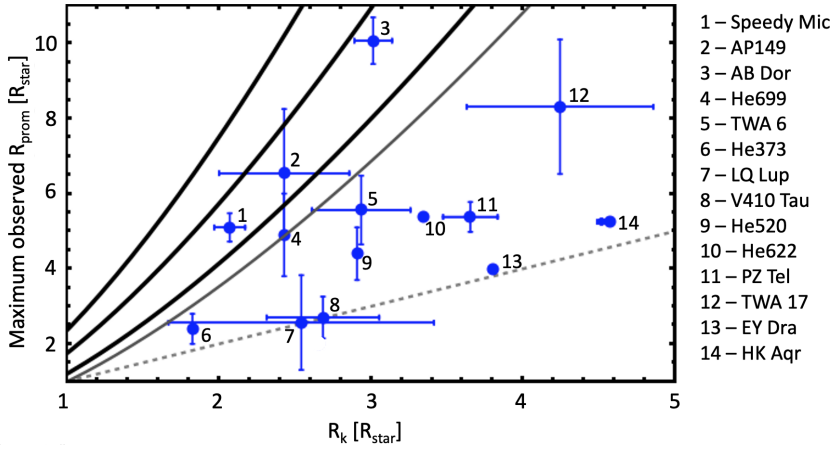

Figure 7.6: Plot showing the maximum radius at which prominences have been observed, against co-rotation radius of the star. The grey dashed line shows where the prominence radius equals the co-rotation radius, and the solid grey line shows the maximum height predicted by Jardine and van Ballegooijen 2005 [77]. The black lines show the maximum radius for higher latitude prominences.

Jardine and van Ballegooijen give the maximum radius as

$$r_{max} = -\frac{1}{2} + \frac{1}{2}\sqrt{(1 + (2r_k)^3)}, \tag{7.3}$$

shown by the solid grey line in the plot. This gives the maximum radius for prominences

within the equatorial plane, and is calculated as the radius at which the gas pressure returns to the same value as it was at the surface. The radius at which this happens is smallest at the equator, where the centrifugal term is maximal. A more general equation can be found to calculate the maximum height at other latitudes and is found from the expression for pressure variation with height, discussed in Chapter 3 as shown by Equation 3.12.

$$r_{max} = -\frac{1}{2} + \frac{1}{2\sin\theta}\sqrt{((\sin\theta)^2 + (2r_k)^3)}, \tag{7.4}$$

For stars with large co-rotation radii, this maximum radius is greater since the gas pressure takes longer to return to its surface value than when the centrifugal force is stronger (i.e. more rapid rotation). However, it is apparent that for very slow rotators like the Sun slingshot prominences can not be formed. Whilst for very rapid rotators the rotational term may dominate and be responsible for the maximum height at which prominences can form, for slower rapid rotators this might not be the case. The rotation alone might not determine the maximum height of prominences and, for example, the magnetic field strength may be an important quantity also. Therefore, it is possible that a plot such as Figure 7.6 might have multiple regimes - one for rapid rotators where this equation holds true, and another regime for the slower of the fast rotators.

7.4 Can the prominence observations help to constrain the field structure?

Chapter 6 investigated the stable point distribution around tilted dipoles and quadrupoles. A question that follows from this is "assuming the observed prominences are supported by a simple field structure, is it possible to constrain what kind of structure this field might have been?". Figure 7.7 shows the locations around AB Dor which transit the stellar disc and are therefore visible in absorption in a dynamic spectrum (white). The grey region shows the locations that do not transit the disc (and therefore are invisible). The black curves show the possible locations of the observed prominences on AB Dor that were published in a paper by Collier Cameron et al in 1989 [1]. Whilst the observations give ϖ, the distance from the rotation axis, it is clear from this plot (and Figure 7.5) that not all of the locations associated with a given ϖ are possible solutions (since some would not transit the disc).

The black curves shown here show only the possible locations.

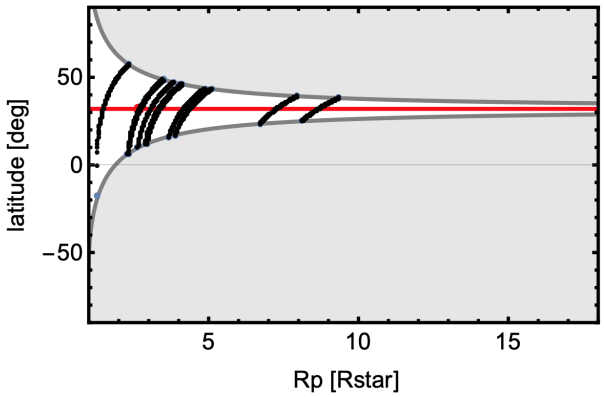

Figure 7.7: A plot showing the possible (r,latitude) locations that prominences observed in 1989 on AB Dor [1] could have had given the reported ϖ values.

In Figure 7.8, the stable points from various tilted dipoles are over-plotted onto these observations. It is immediately clear that even with the largest tilts, the innermost prominence can not be explained by a tilted dipole. From these plots alone, it could be that the second innermost prominence may also be impossible to explain with this field structure. For the remaining prominences, it is clear that the stable points for larger dipole tilts (e.g. (c) in Figure 7.8) could explain the observations better than more aligned dipole fields (Figure 7.8(a)). Larger dipole tilts allow for higher latitude stable points to be formed, which are needed to explain the prominences seen around AB Dor with its inclination of 60°. Whilst not all of the observed prominences could be explained by a tilted dipole field structure, many could. Of these, larger dipole tilts seem the most likely, however, it is likely that many tilts could produce stable points in the necessary locations. This is in part due to the wide range of locations that the observed prominences could have been at (the black curves in Figure 7.8).

Figure 7.9 shows the observed prominence locations and the stable points for a tilted quadrupolar field. The innermost prominence observation could now be explained by a tilted quadrupole, but probably for only a narrow range of quadrupole tilts. The second innermost prominence again can not be described, however, the remaining prominences can be and often by a larger range of tilts than with the dipole, due to the typically wider distribution of stable points for the quadrupole than the dipole.

A simplistic dipole or quadrupole can not alone describe the prominences observed by Collier Cameron et al in their 1989 paper, and therefore likely in other observations also. It

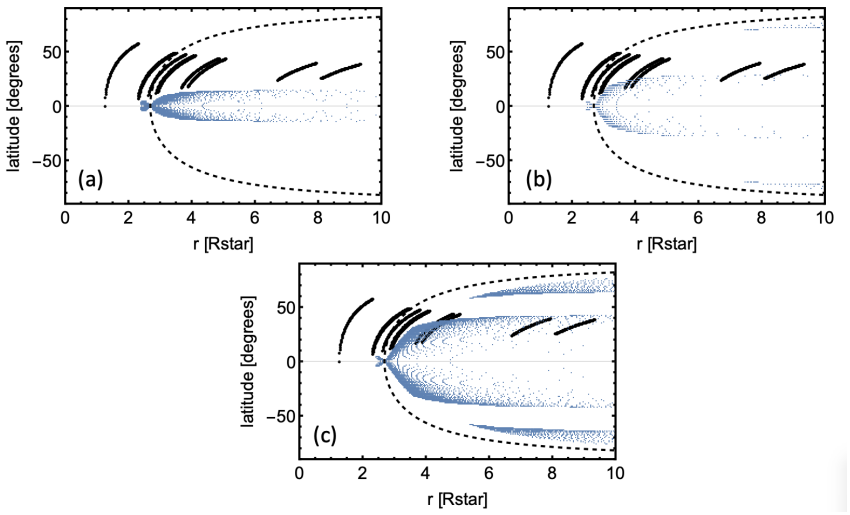

Figure 7.8: Plots showing the possible observed prominence locations (black) and the stable points for dipoles of various tilts (blue). The black dashed line shows the co-rotation radius. (a) has the smallest dipole tilt and (c) has the largest.

is the prominences at very low heights, at least in this example, that are the most difficult to describe, which fits with the magnetic field being more complex close to the stellar surface. A combined field might be more successful in producing stable points which match the observations.

7.4.1 Finding the tilt of AB Dor from prominence observations

Rather than solving for the stable point locations for a fixed dipole tilt as constructed in the previous chapter (Chapter 6) and shown in the plots above (Figures 7.8 and 7.9), we can ask "which dipole tilts are needed to form a stable point at a given location?".

Here, the locations at which prominences were observed are assumed to be stable points. As the observations provide a given value of ϖ, this provides a range of possible (r,θ) values, an example is shown in Figure 7.10 by the black lines for the observed prominences reported in the 1989 paper by Collier Cameron and Robinson [27]. Note that it does not provide any information about the longitude of the prominence.

The equations for stable point formation shown in Chapter 6 can then be used to solve for the dipole tilt (d) and longitude (ϕ) using the prominence location (r, θ) as input parameters. For each prominence (an example is shown in Figure 7.11(a)) there are a range

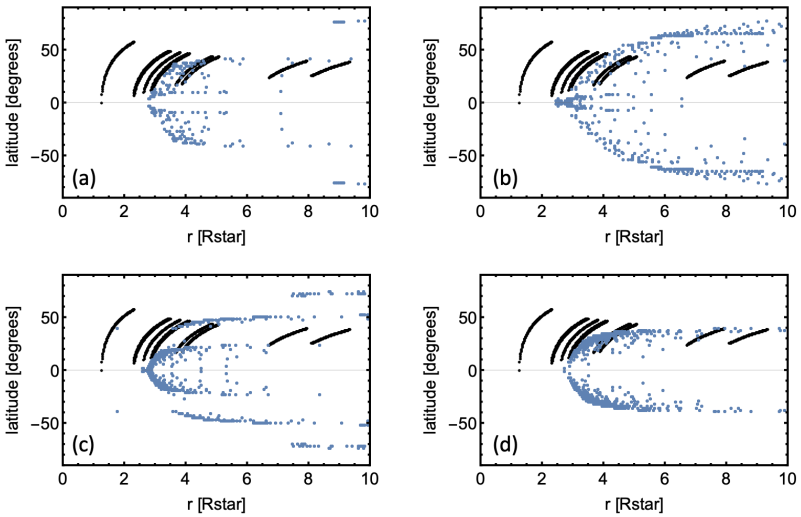

Figure 7.9: Plots showing the possible observed prominence locations (black) and the stable points for quadrupoles of various tilts (blue). (a) has the smallest tilt and (d) the largest.

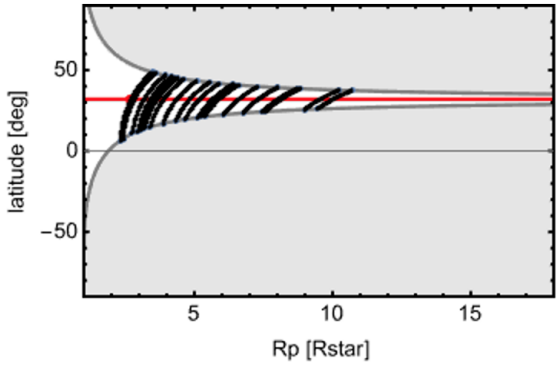

Figure 7.10: Possible (r,θ) locations for the observed prominences reported in Collier Cameron et al 1989b [27].

of different (r, θ) that would match the observed ϖ. Figure 7.11(b) shows the different locations considered here for this prominence. For each of these points, various dipole tilt and longitude values exist for which a stable point could exist at the point. An example is shown in Figure 7.11(c) for the red point shown in (b). This provides a range of dipole tilts for which the prominence could have existed at this location. Figure 7.11(d) shows this range of dipole tilts as a histogram. There is no way from the observations alone to constrain the longitude of the prominence, and therefore the range of possible dipole tilts is the full range plotted in Figure 7.11(c).

Whilst the range of dipole tilts shown in Figure 7.11(c) is only for one possible location of the prominence, a range can be generated in the same method for each point in Figure

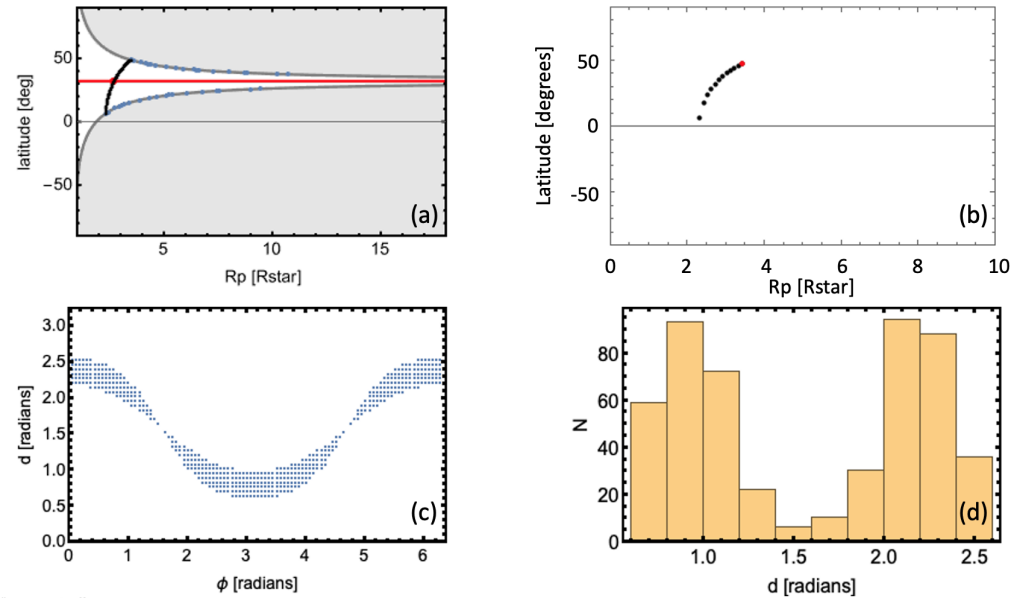

Figure 7.11: (a) shows the range of possible locations for one prominence reported in Collier Cameron et al [27]. (b) the possible locations of the prominence as used here, the red point is associated with plots (c) and (d). (c) the possible dipole tilts and longitude for the stable point and (d) the possible dipole tilts shown as a histogram.

7.11(b). The range of dipole tilts that could have produced the prominence then is the largest range of dipole tilts that comes from the possible locations (an example is shown in Figure 7.12). In this example, the range of dipole tilts that could have produced this prominence is determined by the blue solution, since the other locations resulted in solutions within this range.

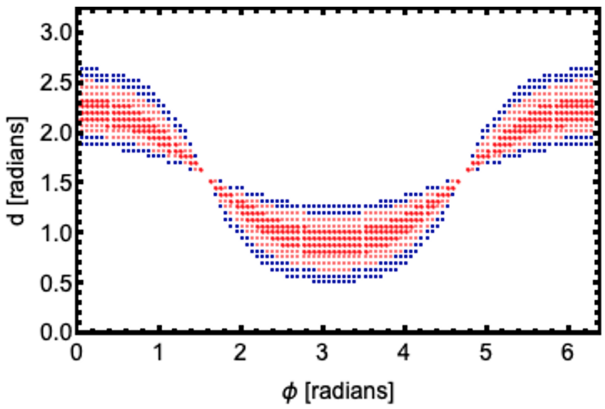

Figure 7.12: An example for one prominence, showing how different possible locations of the stable point lead to different ranges of possible dipole tilts.

This provides the range of dipole tilts that could have produced one prominence, but in

order to constrain the range of dipole tilts of AB Dor at the time of the observations, all of the prominences must be considered. Once a range of dipole tilts is predicted for each prominence, the solution for the star is the narrowest range that would have allowed for all of these prominences to have existed around the star. Figure 7.13 shows the possible range of dipole tilts, calculated by this method from the literature values of the observed prominences. These ranges are shown by the red lines (and black for 1994, in which two different publications provide prominence observations for this year). The blue dots provide the dipole tilt for AB Dor as calculated from the ZDI maps. The range of dipole tilts that is predicted from the prominence observations is typically large and does not constrain the value well. If there was a way to link the observed phases of the prominences to a longitude in the stable point models then this range could be constrained far better. This can be seen from Figures 7.12, because for any given longitude the range of dipole tilts that could produce the prominence is far smaller than the range over all longitudes, being able to constrain this value would lead to better constraints on the dipole tilt. Unfortunately, it is not possible to link the observed phase to a longitude in the stable point coordinate system because this would require knowing a priori how the prominence location relates to the longitude of the dipole axis. Given that we are only working with the observed prominence locations as input parameters into this model, this is not possible. Despite this, whilst the ranges predicted are too large to be of much value, it is comforting that the ranges do lie over the values found from the ZDI maps.

7.5 Future work and conclusions

This chapter has compared the stable points produced in a dipolar and quadrupolar field to the observations of prominences around AB Doradus. It has primarily focussed on a dipolar field, finding the range of dipole tilts that could have produced prominences in the locations in which they were observed.

Not all observed prominences could be generated with a dipolar field, with prominences close to the surface being the hardest to reproduce. It may be that a combined field structure could better replicate the lower lying prominences.

With more time, this chapter would have investigated the range of quadrupole tilts that

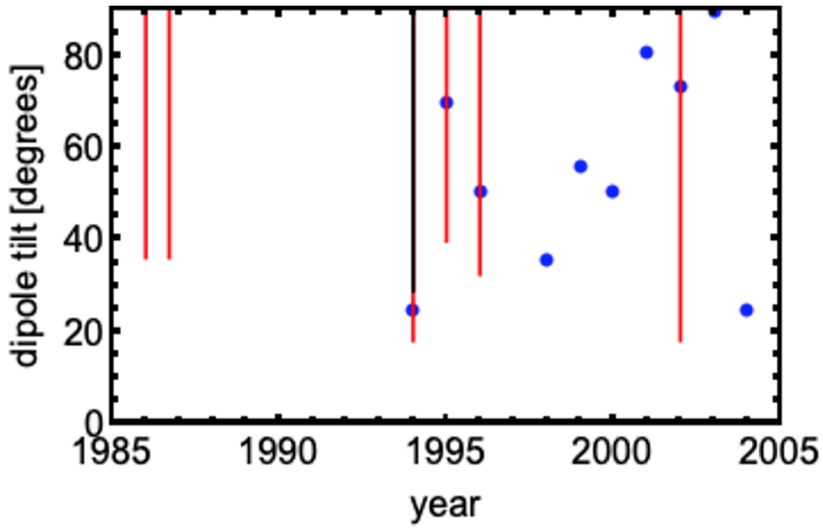

Figure 7.13: Red lines: the predicted range of dipole tilts as calculated here from the prominence observations. A black line is used for one observation in 1994 as there are two publications for this year. Blue dots: the dipole tilt for AB Dor provided from the ZDI maps.

could produce these observations, and compared this to the results for a dipole. It would also have attempted to model the observations from other stars for which there is data, particularly Speedy Mic and HK Aqr where there are more than a handful of prominence observations. It would be interesting to see how well a dipole or indeed quadrupole could describe them and what range of tilts it would give.

Whilst the possible range of dipole tilts predicted from the observed prominences do fit with the results from ZDI maps, the ranges are too large to be very helpful. These ranges could be decreased if the longitude of the prominence could be accounted for. There is no way to link the prominence observations alone to a longitude in the stable point coordinate system, which would constrain the tilt of the dipole axis far better than the radius and latitude alone. Whilst the observations of prominence phases can not be directly mapped to the longitudes used here, the phase of each of the observed prominences are known relative to each other. Whilst outside the scope of this work, it could be possible for the model to be extended and developed in such a way as to include these relative phases as a constraint into the model. This would then help to constrain the dipole tilt and decrease the ranges shown in Figure 7.13. The longitude of the dipole axis can be extracted from ZDI maps, and this could be another way to improve the model. It would be possible to use these values

to map the observed phase of the prominences to longitudes in the stable point coordinate system and therefore better constrain the dipole tilt. It is clear that trying to extract the tilt of the dipolar field from the observations of prominences alone is not very successful, but including some information from the ZDI maps would go some way to improving this. How valuable this would be, however, is unclear.

Chapter 8

Summary

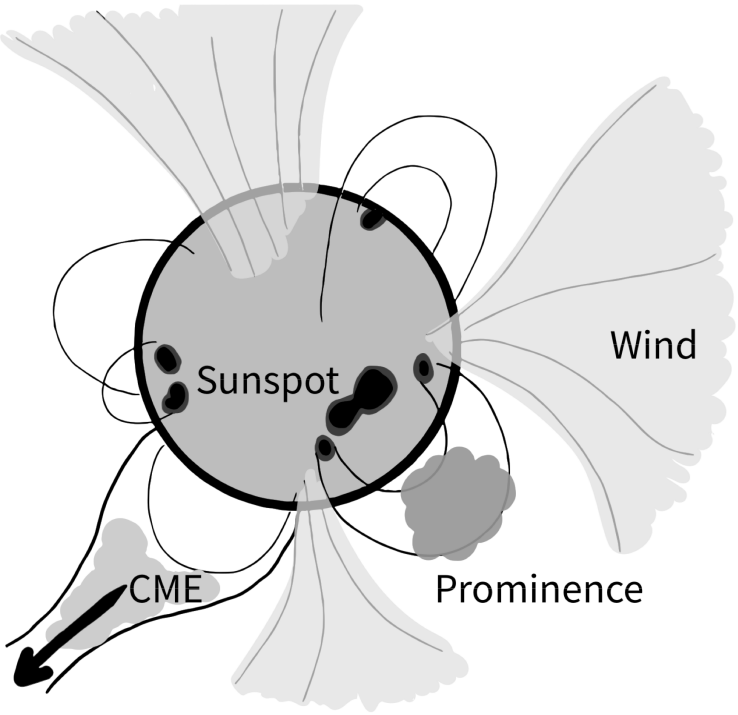

8.1 Introduction

The first and second chapters of this thesis cover a self consistent model of prominences. In these models the prominences are magnetic loops that have cooled compared to the external field and thus have adjusted their shape from this background field. The background field does not adjust shape to account for these loops, which for loops at larger heights from the surface will be more of a limitation than lower loops, since these have diverged most from the coronal field. This model has used basic field structures, i.e. pure spherical harmonics of either a dipole or quadrupole, though in practice this method could be applied to a general magnetic field structure. In the first chapter, the work focused on the magnetic field being embedded within the equatorial plane of the star, with the second chapter developing this model for a magnetic field aligned with the stellar rotation axis. The latter is a more realistic field structure, although the chapters together give the two extremes of such a scenario since most stellar magnetic fields are at some tilt from the rotation axis.

8.2 The equatorial model

The shapes of cooled, prominence bearing loops were found for a variety of field geometries; a dipole, quadrupole, dipole with a source surface (which was placed above and then below the co-rotation radius) and a combined dipole-quadrupole. Families of solutions can be found for a fixed set of parameters (including the stellar parameters, the coronal temperature, prominence temperature and base gas pressures). These families are the set of solutions for all heights above the surface for which an equilibrium is possible. These families are examined as "height-width" plots, in which the "height" is the distance from the stellar surface to the loop summit and the "width" is the angular distance from a footpoint to the loop summit.

The results for a dipole and quadrupole field yield very similar results for the parameters considered here; despite being confined to a smaller angular extent by the background field, the quadrupole shows qualitatively the same shape as the dipole. The maximum loop height, as calculated by the height at which the magnetic field strength of the cooled solutions would tend to zero, is slightly lower for the quarupole than dipole, which would be expected as this field drops off with height quicker.

For a dipolar background field, this was later modified to include a "source surface", a radius at which the field becomes purely radial. This source surface was initially placed above the co-rotation radius, and the behaviour found was very similar to that of a pure dipole but with cooled solutions now being found within the open field region. These solutions are cooled loops supported within the stellar wind. This result is consistent with previous work by Jardine 2005 [77] where similar work was carried out in a Cartesian geometry for a "flat" star.

The source surface, where the magnetic field becomes purely radial, was also placed below the co-rotation radius. Solutions are much more difficult to find in this case, which is partly due to fact that the background field opens before the co-rotation radius, making it difficult to balance the forces and find an equilibrium. However, this may also be influenced by the proximity of the source surface and co-rotation radii. Only two locations for the source surface were investigated here, placed 1 stellar radii away from the co-rotation radius in either direction. From preliminary findings, it appeared that solutions were more difficult to find when the source surface was close and below the co-rotation radius. This would require more investigation however.

The maximum height of these cooled solutions was determined from the expression for the magnetic field strength of these cooled loops. The maximum loop height would occur once this field strength drops to zero at the summit, and the expression for this was determined by the thin flux tube approximation. The influence of various parameters on this maximum loop height was investigated for the field geometries used, namely a dipole, quadrupole and a dipole with a source surface. A hotter loop, that is closer in temperature to the coronal field, can be supported at much larger radii than a cooler one, since less magnetic tension is required to contain this condensation. Increasing the difference in plasma base pressure between outside and inside the loop requires more magnetic tension in order to sustain more material and therefore results in shorter loops than when the loop is in pressure balance with its environment. Decreasing the plasma beta, which here is a proxy for increasing the external field strength, allows for taller loops. This is true for both the dipolar and quadrupolar external field. For the dipole with a source surface, the maximum height is independent of the plasma beta and the temperature. It depends only on the ratio of gas pressures, and varies in a similar way to the pure dipolar field.

This model is compared to the observations using the distributions of prominences with height. Observed data for the stars Speedy Mic and AB Doradus allows prominence distri-

bution with height to be plotted. From the height-width curves of these models, theoretical prominence distribution histograms can be plotted. When compared to the observations, the model using a dipole and source surface above co-rotation matched the observations for AB Doradus better than placing the source surface below co-rotation. The general trend of the modelled histogram matches the observations well, generating three peaks; one at very low heights, one just above co-rotation and one at very large heights. Those at very low heights are not clearly present in the observations, though they would likely be difficult to pick out from background noise due to the small size of these loops. Varying the temperature of the model causes the distribution to be condensed to a smaller range of heights, pushing the peaks to lower heights from the surface. This model has always used families of solutions to generate the distributions (i.e. all loops set to the same temperature) but in reality there is no reason why all prominence bearing loops around a star must take the exact same temperature and it is far more likely that there is a distribution of temperatures contributing to the observed histogram.

Placing the source surface below co-rotation does not match the observations of AB Dor well. This model suggests that the source surface of the star could be beyond the co-rotation radius, if this model accurately replicates the prominences. There is no way to determine for certain the source surface around these stars, and that prominence distributions could provide some constraint on this is interesting. Much more work would need to be done to investigate the combination of parameters that could lead to the model reproducing the trends for the observed data in order to get concrete numbers out of this, however.

For the star Speedy Mic, chosen as a good example of a very rapidly rotating and active star, neither of the source surface locations here generate a histogram which matches the observed trend particularly well. The source surface above co-rotation and at the highest prominence temperature appears closest to the observations, generating the peak at largest heights with ease but struggling to generate the peak just beyond co-rotation. Again a peak is seen at very low heights which is not recovered from the observations. The co-rotation radius of Speedy Mic is much closer to the stellar surface than for AB Doradus and in order to generate this in the modelled histogram, the height-width curve needs to extend outwards in width just beyond co-rotation rather than the tight curves that are seen from these parameters. It may be that a different plasma beta value would produce better results, which is reasonable since the magnetic field strength on Speedy Mic will differ from AB Doradus due to its faster rotation rate. Speedy Mic has a rotation period of about

0.76 times that of AB Doradus, i.e. rotates faster, which assuming a linear dynamo could lead to a an average large scale magnetic field that is 1.3 times that of the field on AB Dor [163]. These values are for the average field strengths alone, and the active regions above which this loops would form might have larger discrepancies between the two stars. The model can be highly sensitive to changes in the input parameters, especially the plasma beta.

8.3 The meridional model

Generalising the model to a dipole aligned with the rotation axis and embedded in a meridional plane makes the model more realistic. The gas pressure variation around a star is dependent on radius from the star and latitude. Thus, whilst the gas pressure is constant at a fixed distance from the star when confined to the equatorial plane, this is no longer the case once out of it. In the case of a dipole in a meridional plane then, the gas pressure varies both in radius and latitude. This alters the shape of the cooled solutions for the meridional dipole when compared to the equatorial dipole. The steepest variation in pressure with height is always found within the equatorial plane, where the centrifugal force is largest. Quantitatively, this change in pressure distribution alters the loop shapes between the equatorial and meridional cases, however this variation is not large. The same behaviour is found in the meridional case as was found in the equatorial case in terms of the family of solutions (i.e. the height-width curves).

A source surface can again be included, and the results are again quantitatively different but qualitatively the same as the equatorial case. Since this work has focused on a dipolar field, this is not surprising. The summit of the loop is still restricted to the equatorial plane, even once the dipole has been aligned with the rotation axis. This is where the majority of the material gathers for tall loops, and for the loops below co-rotation and close to the stellar surface where the magnetic field strength is strong and the loop summits are empty, the cooled field would be expected to follow the background field.

An interesting development of this work would be to extend it to a quadrupolar field. The difference between an equatorial and meridional field would then be more drastic as the pressure distribution in the two cases would be very different. This would also allow for the formation of prominences at higher latitudes, where here all prominences are confined to the equatorial plane. Observations of higher latitude prominences exist on many stars

for which prominences have been observed, and thus this would be a useful development of this work. However, quadrupolar fields drop off with height faster than dipolar fields and at large heights the dipolar field is most likely to be the one dominating.

The masses of flux tubes associated with a family of solutions are calculated, and results show two types of solution, (1) those with summits at low heights (below co-rotation) that have empty summits and heavy footpoints and (2) those with summits above co-rotation with dense summits. These low-lying solutions follow the background field closely, and are more like solar-prominences than the slingshot prominences observed on rapidly rotating young stars. The taller solutions are the slingshot prominences, with dense summits. The masses found are consistent with observations for the star AB Doradus.

Synthetic Hα spectra are generated for a variety of field structures; a dipole embedded within the equatorial plane, an aligned dipole and an aligned dipole with a source surface (placed above and then below co-rotation). The inclination of the star, i.e. the viewing angle of the observer is also investigated.

The inclination of the star has a large effect on if a prominence will transit the stellar disc, and therefore be visible in absorption. Since the prominences always form within the equatorial plane with these field geometries, viewing into the equatorial plane of the star will result in all of the prominences being visible in absorption at some point. However, even with a small change in inclination many prominences will never transit the disc. Prominences at large distances from the surface will not transit the disc with even a slight variation in inclination, and these prominences are the slingshot prominences.

The Hα dynamic spectra generated by an equatorial dipole and aligned dipole are rather different. For an aligned dipole, only one side of the loop is visible for an aligned dipole and therefore the trail produced contains one absorption feature from the leg of the loop, and another one for the loop summit if the dense summit transits. For the equatorial dipole, both legs of the loop transit the disc, producing two (or three) absorption features per loop. However, between a pure dipole and a dipole with a source surface, the Hα trails are more difficult to distinguish. There is some variation in the shapes of the absorption features, based on the shapes of the field lines produced by the different external fields. Ultimately though the overall spectra look similar.

Producing Hα spectra with a similar appearance to the observations is not difficult, with various field structures generating believable synthetic spectra. This is encouraging that the observations do not require a very unique set of parameters, although perhaps disappointing

that recovering the magnetic field structure of the field lines from the dynamic spectra does not appear to be straightforward.

8.4 Prominences around M-dwarfs

The third and fourth chapters use a different method in order to model prominence formation. In this method, the stable points within a field structure are found and associated with a prominence. A prominence can then be modelled as extending about each stable point, with a fixed size. In this model, the field structure is fixed and does not alter in account of the presence of the cooled prominence material that is loaded to the stable point. The field structure is more realistic in this model than the previous, more theoretical chapters, and is generated from observations of the surface magnetic field structure of the stars in the sample.

Stable points are found on all maps, suggesting that prominence formation could be common amongst these kinds of star. Prominences are found to form at a range of latitudes, dependent on the alignment of the magnetic dipole axis and the rotation axis. Whilst a range of latitudes are found, in all cases the preferential latitude is the equatorial plane and is also where the highest mass prominences are supported. Visibility of these prominences is more difficult, because they must transit the stellar disc in order to be visible. Unless the star has an inclination of 90° (viewing into the equatorial plane), the prominences at this latitude and far above the surface will never be visible. In this sample, this often includes the highest mass prominences.

The inclination of a star is fixed, and thus some stars may not seem to be the best candidates for viewing prominences. Chances for viewing prominences around these stars can be increased if the dipole axis of the star tilts. This occurs when the global structure of the coronal field changes, and could occur due to a stellar cycle or just a large scale change in the field structure. Thus a star that is not an ideal candidate one year, could be a possible candidate another. This will rely on the field structure change allowing for stable point formation at higher latitudes that can transit the disc. These prominences are likely to be less massive than the largest prominences around this star, so this is a drawback.

Typically, stars with an aligned dipole field and viewing close to the equatorial plane would be the best candidates for prominence observing. This field structure will produce the most

prominence mass and it will collect about the equatorial plane. Thus, the observer must view into this plane in order to observe this mass. However, in practice this is a challenge. Observing stars directly into their equatorial plane makes the north and south pole indistinguishable from each other and it is unclear which part of the star light has come from. Good stellar candidates for observing prominences are:

- stars that have small co-rotation radii. These stars are able to form slingshot prominences at lower heights than stars that have large co-rotation radii. The most massive prominences typically form around the equatorial co-rotation radius, and thus not only are we more likely to see prominences around these stars in general, but we are also more likely to be able to see the most massive prominences too.

- Stars with high inclinations so that we observe into or close to the equatorial plane. This provides more of a chance of being able to observe the largest massive prominences in absorption.

- Stars that have very misaligned dipole and rotation axes but that have low inclinations. In this case we observe high latitudes of the star, and in order to form high latitude prominences the dipole axis must be very misaligned from the rotation axis.

From the stars examined in this sample, potential candidates for prominence observations are GJ1156, EQ Peg A, GJ1111, GJ9520 and V374 Peg. The proportion of visible prominence mass is far lower than the total mass present however. For those maps in which prominences were visible, this percentage ranged from 0.1% - 50.4% of the mass present.
V374 Peg is especially of importance in this sample as it is the only star for which prominences have been observed. This work found only 13% of the prominence mass predicted to be visible.
Work by Jardine and Collier Cameron [87] used prominences as wind gauges and here the modelled prominences were placed on the Wood plot of mass loss rate per unit area against X-ray flux. The modelled prominences showed a lot of scatter, which is also present in the observations of stellar winds. This scatter was even present amongst stars for which there were maps over consecutive years, suggesting that the scatter is intrinsic, and perhaps related to stellar cycles. The line of best fit for these modelled prominences gives a relation very similar to the relations from observationally derived wind studies. The prominence relation is at the upper end of these literature relations.

If the same plot is made for the observable prominences, there are far fewer points on the plot and the points are up to 3 orders of magnitude lower than the true values. This suggests that whilst prominences are suitable for use as wind gauges to probe the stellar wind, any predictions based from prominence observations alone are likely to greatly underestimate the true value of mass loss rates.

The work in Chapter 4 considered the modelled stellar wind rather than the observations of stellar winds. This preliminary work suggests that the prominence and wind mass loss and angular momentum loss rates may be very similar. This is dependent on the location of the source surface, though the quantitative extent of this was not explored due to time constraints. When plotted on the Wood plot, the modelled wind relation was found to be very similar to the lower end of the literature relations for the observationally derived winds. This fits with the prominence model yielding a relation closer to the upper literature value. Spin-down timescales were calculated for both the modelled prominences and the modelled wind. For the prominences these timescales range from 0.1Gyr to 588.2Gyrs. For the modelled wind this timescale ranged from 0.3Gyr to 2335.0Gyrs.

The reality is that both the prominences and wind remove angular momentum from the star and thus both contribute to the spin-down of the star. Combining the total angular momentum lost and calculating the timescale from this yields spin-down timescales in the range of 0.1Gyr to 469.5Gyrs.

The predictions of angular momentum loss rates from the prominences may be overestimates, and therefore lead to underestimates of the wind angular momentum loss rates in this model. However, this work suggests that the prominences could be having a large contribution to the spin down of some stars. The prominences appear to act as a regulation mechanism in which stars will eventually converge to the same rotation rate, since stars with fast rotation rates tend to lose more angular momentum than their slower counterparts and thus spin-down faster. Since this is also true for the stellar wind, the prominences would be an additional mechanism contributing to this.

The ejection of these prominences into space could also have consequences for any orbiting planets. A thought experiment is proposed by which an Earth-like planet orbits about the equatorial plane of the maps considered here, at a distance of 1AU. The planet is more likely to experience interaction from the ejected prominence material if orbiting about a star with a an aligned dipole and rotation axis. These stars have large proportions of promi-

nence material about the equatorial plane and thus is more likely to impact the planet. For highly misaligned dipoles, the planet is less likely to experience ejected prominence material throughout its orbit. The aligned dipole maps show not only the largest proportion of the planetary orbit in which interception could occur, but also the largest masses of prominence material.

For stars with aligned dipoles, such as EQ Peg B, an orbiting planet will likely experience a lot of ejected prominence material but little wind material. What little wind was experienced would likely be quite constant. This is caused by the prominences dominating the field structure close to the equatorial plane. For a very misaligned dipole such as GJ1156 however, the planet would pass through sections of its orbit where the wind was very strong and regions where the wind was very low. This big fluctuation in wind is caused by the planet passing above regions on the stellar surface of open, wind bearing field and then closed sections. The prominences are spread over a large range of latitudes in this field structure and it is unlikely that many of them would interact with the planetary orbit unless there was a very large number of them. Thus, the planet here would have its orbit dominated by a fluctuating wind and would likely be unaware of the prominences.

8.5 Calculating stable points around tilted field structures

The final two chapters returned to more mathematical work. It combined the theoretical and mathematical modelling in the first few chapters, with the stable point method used within Chapters 3 and 4. Unlike Chapters 1 and 2 where the field is constrained to 2 dimensions and prominences are modelled as field lines that have cooled and adjusted their shape to be in equilibrium with the background field, the final chapters are mostly 3 dimensional work where prominences are modelled as stable points within the background field. In other words, the stable point method assumes that the magnetic field line does not adjust shape once it is mass loaded. This is perhaps cruder but computationally less challenging. The complexity of the magnetic field and its effects on the locations at which prominences could form was investigated in this chapter. This was then used to construct velocity plots that showed the spatial distribution of material around the star, as has been done in observa-

tions [53, 55]. The model was then used to investigate the effects of stellar inclination and orientation of the magnetic field on the velocity plots that would be produced. The velocity plots generated appear similar to the observed velocity plots within the literature, however it is apparent that no one particular field structure is clearly responsible for the observed plots.

The final chapter compared the stable point locations found using the model from Chapter 6 to the observations of prominences found in the literature. It showed that using the reported locations of prominences from the literature to predict the orientation of the dipole axis of the star was not very successful, as many stable point locations are highly degenerate. This is encouraging in that it suggests that such prominences should be common across rapidly rotating stars, regardless of the field orientation, and therefore across stellar cycles also. However it does mean that using prominence locations alone, it is very difficult to extract meaningful information about the field topology of a star and that some more information is necessary. It is clear, however, that some of the observed prominences can not be found even with the most simple field of a dipole. This suggests that the field supporting these prominences is more complex than a dipole and that at low heights we can not rely on a dipole alone to reliably predict prominence locations.

8.6 Further work

The first two chapters are proof of concept of a model. In this work, the stellar magnetic field has been prescribed as a simple field structure (dipole, altered dipole or quadrupole), and in both cases the work has been 2-dimensional. In the first chapter, the model was restricted to the equatorial plane and in the second chapter, restricted to a meridional plane. The next step of this work would be to convert this model to a fully 3-dimensional model. This would likely not yield any new physics, however it would be necessary in order allow for the next logical step with this work. This would be to use a general magnetic field in place of the dipole (or similar) structure used here.

Being able to use a more general field structure would allow for the use of observed magnetic fields as inputs. This would make it easier to compare the model to observations, since maps of stars such as AB Dor could be used and compared directly to prominence observations from the star in the same year. It would also allow for a method in which prominences could be formed in the open field region, whilst allowing the source surface of the star to be closer

to the stellar surface than was possible in chapters 3 and 4.

The work could also be extended to model a tilted dipole, and since the work so far has covered the two limiting cases (equatorial dipole and fully aligned dipole) this would likely not produce a lot of insight in itself. However, it would make for a nice comparison to the work of chapter 5, in which a tilted dipole model is studied using the stable point method.

The main limitation in chapters 3 and 4 is the location of the source surface. Since this model searches for stable points within the coronal magnetic field, prominences can only be found in the closed magnetic field region. In chapters 1 and 2, the models finds equilibrium shapes of cooled loops and thus there can be solutions within the stellar wind, i.e. open field region. This is not possible in this work, and therefore in order to have a possibility of forming prominences at large heights above the surface, the magnetic field must be forced to be closed to large heights.
With more time, an investigation into the importance of source surface location and prominence and wind mass loss rate would be helpful. It was mentioned in chapter 4 that decreasing the source surface for the star V374 Peg from 18 to $9R_\star$ did not increase the area of the stellar surface contributing to the wind mass loss as much as may be expected. However, an investigation to quantify the effect on wind and prominence mass loss could be very valuable here.

To further develop this model, the next obvious and very valuable step would be to use a combined field structure. This could be a combined dipole and quadrupole structure, where the fields may be of equal strength or different strengths and the field axes could be aligned or not. This has not been done here due to time constraints. The current layout of the code is such that calculating the stable points in these structures would likely require more time and computer power than was available. However, this kind of field structure would be far closer to the real fields that most stars have. These more complex field structures would also likely produce more complex velocity plots as the field structures need not be so symmetric and therefore the blobs in the velocity plots could also be asymmetric. In order to make these velocity plots, the method for calculating the radius of curvature of field lines would also likely have to be changed. In the work here the radius of curvature, used to calculate the maximum density that each stable point can support (using the method by Villereal D'Angelo [82]), is calculated analytically from the equation of the field line. This

method may be too computationally expensive with such complex field lines, and another method may need to be implemented in this case.

The magnetic field axis, for both dipole and quadrupole fields, has always been tilted in this work towards the y-axis. With more time, this model would be adapted to vary the direction into which the magnetic axis is tilted. This would not alter the results significantly, but would generalise the model so that the blobs in the velocity plots could be centred at different (v_x, v_y) locations. Alternatively, a relationship could be applied between the rotation of the velocity plots and the rotation in ϕ of the magnetic axis, such that velocity plots could be generated for any geometry of dipole tilt. With these plots, a machine learning approach could be applied to compare observations to many synthetic observations to find the field structure from the prominence observations.

As in previous chapters, the prominence material focused on was that which transmitted the stellar disc. In the vast majority of cases, this is how prominence material is observed. However, it would be interesting to consider stars such as LQ Lup or V530 Per where the inclinations are so low that prominence material is observed in emission. In this case, the velocity plots generated could be compared directly to the few observed velocity plots in the literature.

Appendices

A Co-rotating frame

Although the derivation shown here can be found in many textbooks, it has been included here for completeness. A star can be described in various reference frames. In an inertial reference frame, the star appears to rotate. However, in a rotating reference frame, the star appears stationary as the frame itself constantly rotates in sync with the stellar rotation rate. Forces in an inertial frame can be related to a rotating frame through the following formulae:

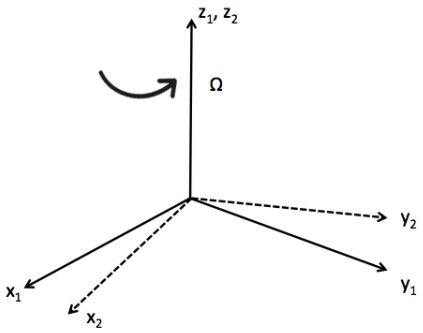

Figure 8.1: A cartoon showing the inertial frame (solid axes) and rotating frame (dashed axes) in Cartesian coordinates. Figure reproduced from Waugh [128].

The second law of Newtonian mechanics is true in both reference frames:

$$\mathbf{F}_{in} = m\mathbf{a}_{in} \tag{8.1}$$

and

$$\mathbf{F}_{rot} = m\mathbf{a}_{rot}. \tag{8.2}$$

Observers in different frames would, however, have different experiences of accelerations and therefore forces on objects. This is described in the following equation:

$$\mathbf{a}_{in} = \mathbf{a}_{rot} + \mathbf{A}. \tag{8.3}$$

Therefore, the force in the rotational frame can be described, as below, in terms of the inertial acceleration (a_{in}) and an additional acceleration (A) which is the acceleration of the rotating frame:

$$\mathbf{F}_{rot} = m(\mathbf{a}_{in} - \mathbf{A}) = \mathbf{F}_{in} + \mathbf{F}_{fict}. \tag{8.4}$$

Here the force experienced in the rotating frame is equal to the force in the inertial frame plus an additional force (F_{fict}). This fictional force is the centrifugal force.

Using $r_1(t + \Delta t) = r_2(t + \Delta t)$ from Figure 8.2 (which can be combined into Figure 8.3) we find,

$$\Delta r_1 = (\Delta r_2 + r_2(t)) - r_1(t). \tag{8.5}$$

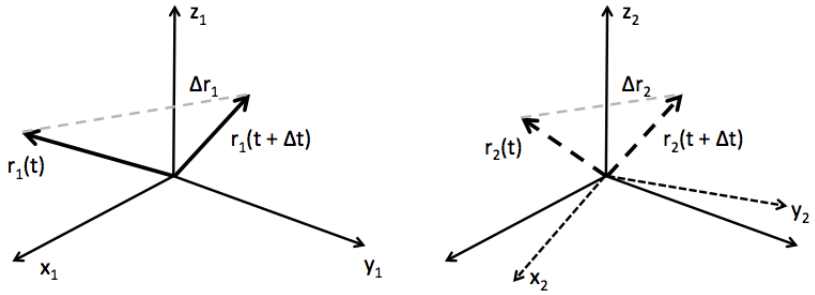

Figure 8.2: Left: Positional vectors in the inertial frame. Right: The corresponding vectors are shown in the rotating frame (dashed axes). The inertial frame is still shown by the solid axes. Figure reproduced from Waugh [128].

And, using

$$\frac{d}{dt}\mathbf{r} = \mathbf{v} = \Omega \times \mathbf{r}, \tag{8.6}$$

which can be rewritten as

$$r_2(t) - r_1(t) = (\Omega \times \mathbf{r})\Delta t, \tag{8.7}$$

Equation 8.5 becomes:

$$\frac{\Delta r_1}{\Delta t} = \frac{\Delta r_2}{\Delta t} + (\Omega \times \mathbf{r}). \tag{8.8}$$

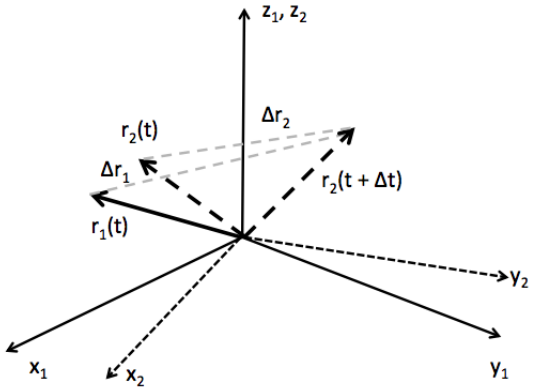

Figure 8.3: Comparing the different frames. Figure reproduced from Waugh [128].

Then, taking the limit of $\Delta t \to 0$, this becomes:

$$\frac{dr}{dt}_{in} = \frac{dr}{dt}_{rot} + \Omega \times \mathbf{r}. \tag{8.9}$$

This is applicable to any vector, and therefore r can be replaced with v_{in}, an expression for the inertial acceleration can then be found:

$$\mathbf{a}_{in} = \frac{dv_{in}}{dt}_{rot} + \Omega \times \mathbf{v}_{in}. \tag{8.10}$$

Substituting $v_{in} = \Omega \times r$ leaves:

$$\mathbf{a}_{in} = \mathbf{a}_{rot} + \frac{d(\Omega \times \mathbf{r})}{dt}_{rot} + \Omega \times \mathbf{v}_{rot} + \Omega \times (\Omega \times \mathbf{r}), \tag{8.11}$$

which, for a constant angular velocity, simplifies to:

$$\mathbf{a}_{in} = \mathbf{a}_{rot} + \Omega \times \frac{d\mathbf{r}}{dt}_{rot} + \Omega \times \mathbf{v}_{rot} + \Omega \times (\Omega \times \mathbf{r}) \tag{8.12}$$

$$\mathbf{a}_{in} = \mathbf{a}_{rot} + 2\Omega \times \mathbf{v}_{rot} + \Omega \times (\Omega \times \mathbf{r}). \tag{8.13}$$

This can be rewritten in terms of gravity, which is the form used in this thesis:

$$\mathbf{g}_{rot} = \mathbf{g} - 2\omega \times \dot{\mathbf{r}} - \omega \times (\omega \times \mathbf{r}). \tag{8.14}$$

When no fluid flows are present, this equation simplifies further:

$$\mathbf{g}_{rot} = \mathbf{g} - \omega \times (\omega \times \mathbf{r}). \tag{8.15}$$

When restricted to the equatorial plane, this equation simplifies further to:

$$\mathbf{g}_{rot} = -\frac{GM}{r^2}\hat{\mathbf{r}} + \omega^2 \mathbf{r} \tag{8.16}$$

B Radius of Curvature

In chapter 1 the standard result

$$\frac{\partial \hat{s}}{\partial s} = (\hat{s}.\nabla)\hat{s} = \frac{\hat{n}}{R_c} = \frac{(rr'' - r^2 - 2(r')^2)}{(r^2 + (r')^2)^{3/2}}\hat{n} \tag{8.17}$$

is quoted. Here this is shown explicitly.

From

$$ds = d\phi\sqrt{r^2 + (r')^2} \tag{8.18}$$

it can be found that

$$\frac{\partial}{\partial s} = \frac{1}{\sqrt{r^2 + (r')^2}}\frac{\partial}{\partial \phi} \tag{8.19}$$

and the unit vector $\hat{s}$ is defined by

$$\hat{s} = \frac{1}{\sqrt{r^2 + (r')^2}}(r'\hat{r} + r\hat{\phi}). \tag{8.20}$$

Thus,

$$\frac{\partial \hat{s}}{\partial s} = \frac{1}{\sqrt{r^2 + (r')^2}}\frac{\partial}{\partial \phi}\Big(\frac{1}{\sqrt{r^2 + (r')^2}}(r'\hat{r} + r\hat{\phi})\Big). \tag{8.21}$$

From here onwards throughout this derivation, $\sqrt{r^2 + (r')^2}$ will simply be denoted by $\sqrt{}$ to make the equations less clunky. Evaluating:

$$\sqrt{}\frac{\partial \hat{s}}{\partial s} = (r'\hat{r} + r\hat{\phi})\frac{\partial}{\partial \phi}\left(\frac{1}{\sqrt{}}\right) + \left(\frac{1}{\sqrt{}}\right)\frac{\partial}{\partial \phi}(r'\hat{r} + r\hat{\phi}) \tag{8.22}$$

$$\sqrt{}\frac{\partial \hat{s}}{\partial s} = (r'\hat{r} + r\hat{\phi})\left(\frac{-1/2}{(\sqrt{})^3}(2rr' + 2r'r'')\right) + \frac{1}{\sqrt{}}(r''\hat{r} + r'\frac{\partial \hat{r}}{\partial \phi} + r'\hat{\phi} + r\frac{\partial \hat{\phi}}{\partial \phi})$$

noting that $\partial\hat{r}/\partial\phi = \hat{\phi}$ and $\partial\hat{\phi}/\partial\phi = -\hat{r}$ this leaves:

$$\sqrt{}\frac{\partial \hat{s}}{\partial s} = (r'\hat{r} + r\hat{\phi})\left(-\frac{(r + r'')r'}{(\sqrt{})^3}\right) + \frac{1}{\sqrt{}}(r''\hat{r} + r'\hat{\phi} + r'\hat{\phi} - r\hat{r})$$

through many lines of algebra, this may be simplified to:

$$(r^2 + (r')^2)^2\frac{\partial \hat{s}}{\partial s} = (rr'' - r^2 - 2(r')^2)(r\hat{r} - r'\hat{\phi})$$

$$\frac{\partial \hat{s}}{\partial s} = \frac{(rr'' - r^2 - 2(r')^2)}{(r^2 + (r')^2)^{3/2}}\left(\frac{(r\hat{r} - r'\hat{\phi})}{\sqrt{r^2 + (r')^2)}}\right)$$

which may equally be written as

$$\frac{\partial \hat{s}}{\partial s} = \frac{(rr'' - r^2 - 2(r')^2)}{(r^2 + (r')^2)^{3/2}}\hat{n}$$

C Source surface magnetic field

At the surface of the star we should have a dipole, i.e.

$$B_r(r = R_\star) = \frac{2M\cos\theta}{r^3} \tag{8.23}$$

where M is the magnetic dipole moment.

We also know that $B_\theta(r = r_{ss}) = 0$, where r_{ss} is the radius of the source surface.

Writing a dipole in terms of spherical harmonics (m=0, l=1):

$$B_r = (-a_{10} + 2b_{10}/r^3)\cos\theta, \tag{8.24}$$

$$B_\theta = (a_{10} + b_{10}/r^3)\sin\theta, \tag{8.25}$$

$$B_\phi = 0. \tag{8.26}$$

at $R_\star$:

$$\frac{2M\cos\theta}{R_\star^3} = (-a_{10} + 2b_{10}/R_\star^3)\cos\theta \tag{8.27}$$

$$2M = -a_{10}R_\star^3 + 2b_{10} \tag{8.28}$$

$$M = -\frac{a_{10}R_\star^3}{2} + b_{10} \tag{8.29}$$

at r_{ss}:

$$B_\theta = 0 \tag{8.30}$$

and therefore

$$a_{10} + b_{10}/r_{ss}^3 = 0 \tag{8.31}$$

$$a_{10} = -b_{10}/r_{ss}^3 \tag{8.32}$$

Combining these,

$$M = frac b_{10} R_\star^3 2 r_{ss}^3 + b_{10} \tag{8.33}$$

$$M = b_{10}\left(\frac{2r_{ss}^3 + R_\star^3}{2r_{ss}^3}\right). \tag{8.34}$$

So,

$$b_{10} = M\left(\frac{2r_{ss}^3}{2r_{ss}^3 + R_\star^3}\right) \tag{8.35}$$

and

$$a_{10} = -M\left(\frac{2}{2r_{ss}^3 + R_\star^3}\right). \tag{8.36}$$

These can be substituted back into the magnetic field equations to give the expression for a dipole with a source surface:

$$B_r \;=\; (-a_{10} \;+\; 2b_{10}/r^3)\cos\theta \;=\left[M\left(\frac{2}{2r_{ss}^3 + R_\star^3}\right) \;+\; \frac{2M}{r^3}\left(\frac{2r_{ss}^3}{2r_{ss}^3 + R_\star^3}\right)\right]\cos\theta \tag{8.37}$$

$$B_r = \frac{2M}{r^3}\cos\theta\left(\frac{r^3 + 2r_{ss}^3}{2r_{ss}^3 + R_\star^3}\right) \tag{8.38}$$

and

$$B_\theta = (a_{10} + b_{10}/r^3)\sin\theta = \left[-2M + \frac{2Mr_{ss}^3}{r^3}\right]\left(\frac{1}{2r_{ss}^3 + R_\star^3}\right)\sin\theta \tag{8.39}$$

$$B_\theta = \frac{M}{r^3}\sin\theta\left(\frac{2r_{ss}^3 - 2r^3}{2r_{ss}^3 + R_\star^3}\right) \tag{8.40}$$

D M-dwarf Prominences

Figures 8.4 to 8.6 show histograms of the; mass, theta location and distance from the rotation axis, of the prominences found from the ZDI maps of the M-dwarf sample. EQ Peg B is given in the text as an example.

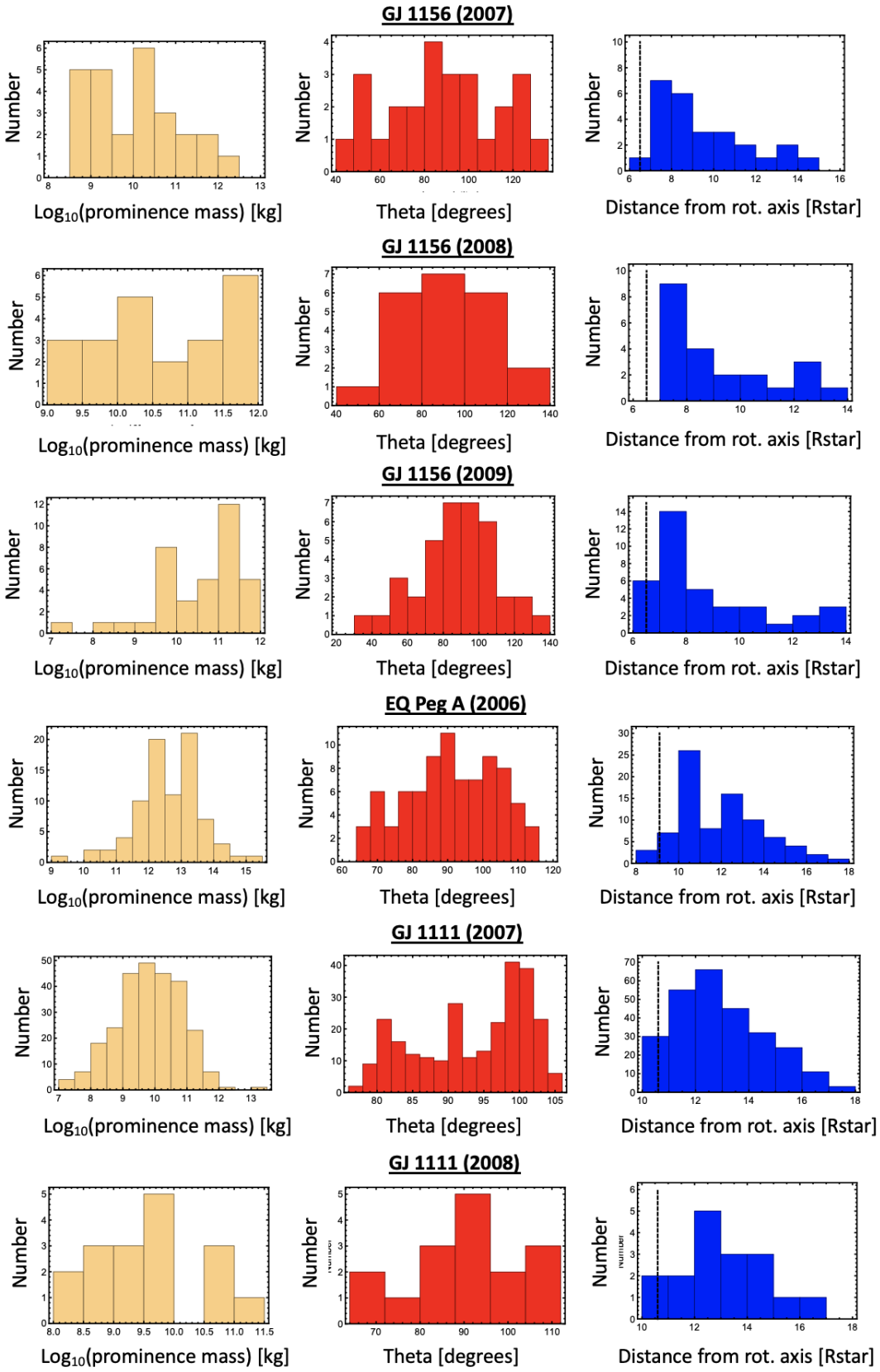

Figure 8.4: prominence data for GJ1156, EQ Peg A and GJ1111

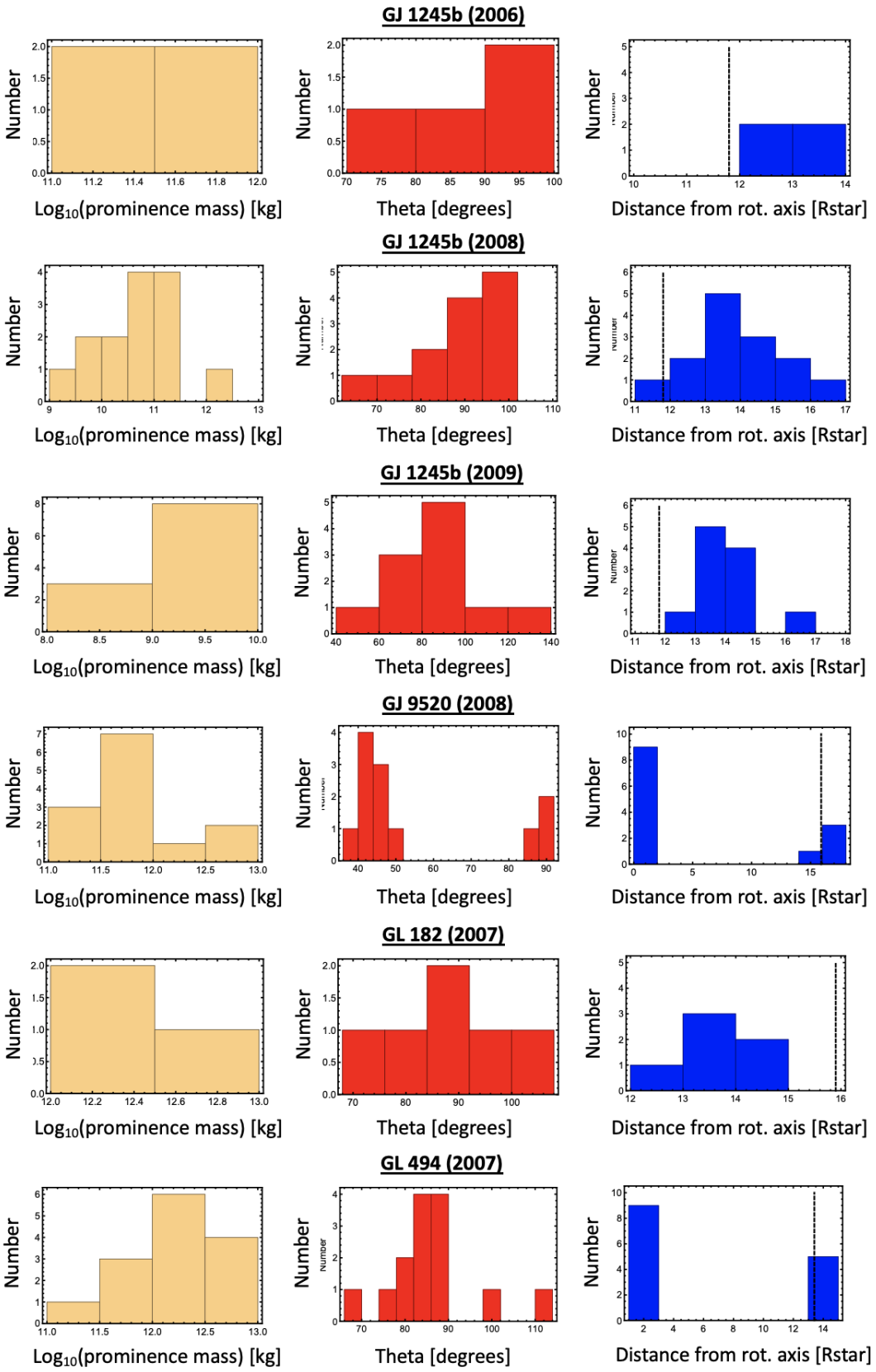

Figure 8.5: prominence data for GJ1245b, GJ9520, GL182 and GL494

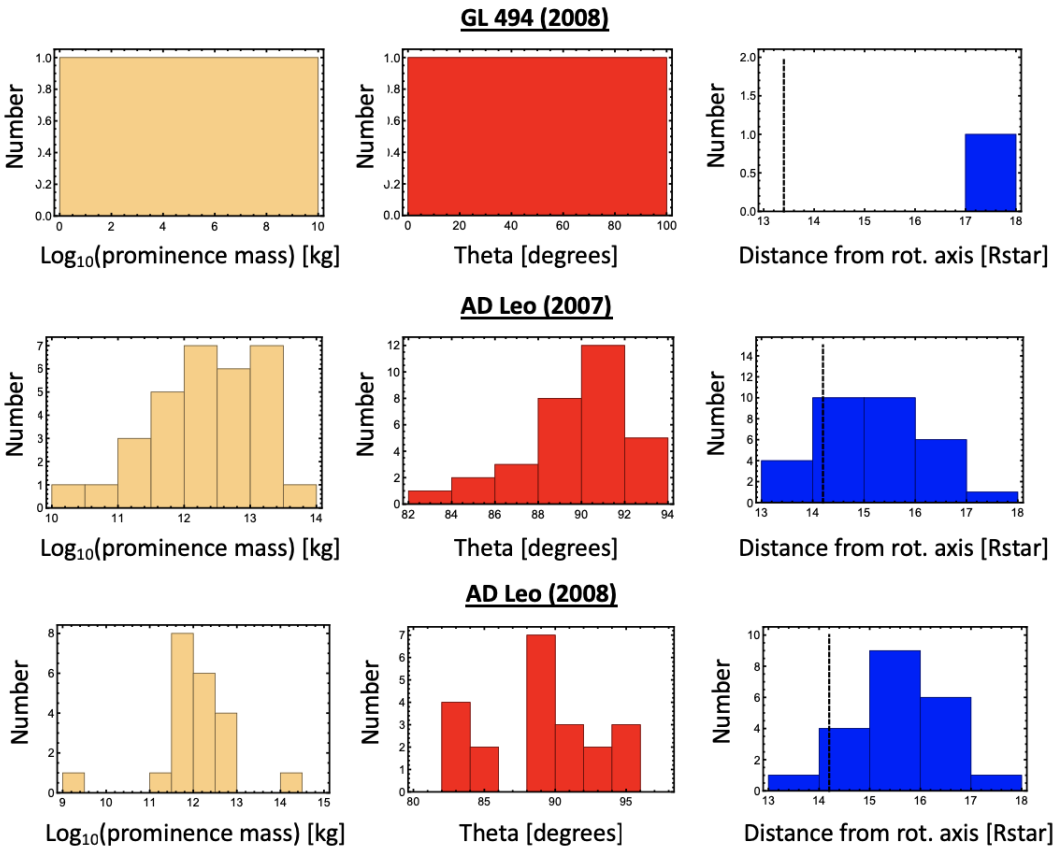

Figure 8.6: prominence data for GL494 and AD Leo

E AB Doradus Prominences from ZDI method

Plots of prominence mass versus polar angle are shown here for the M-dwarfs.

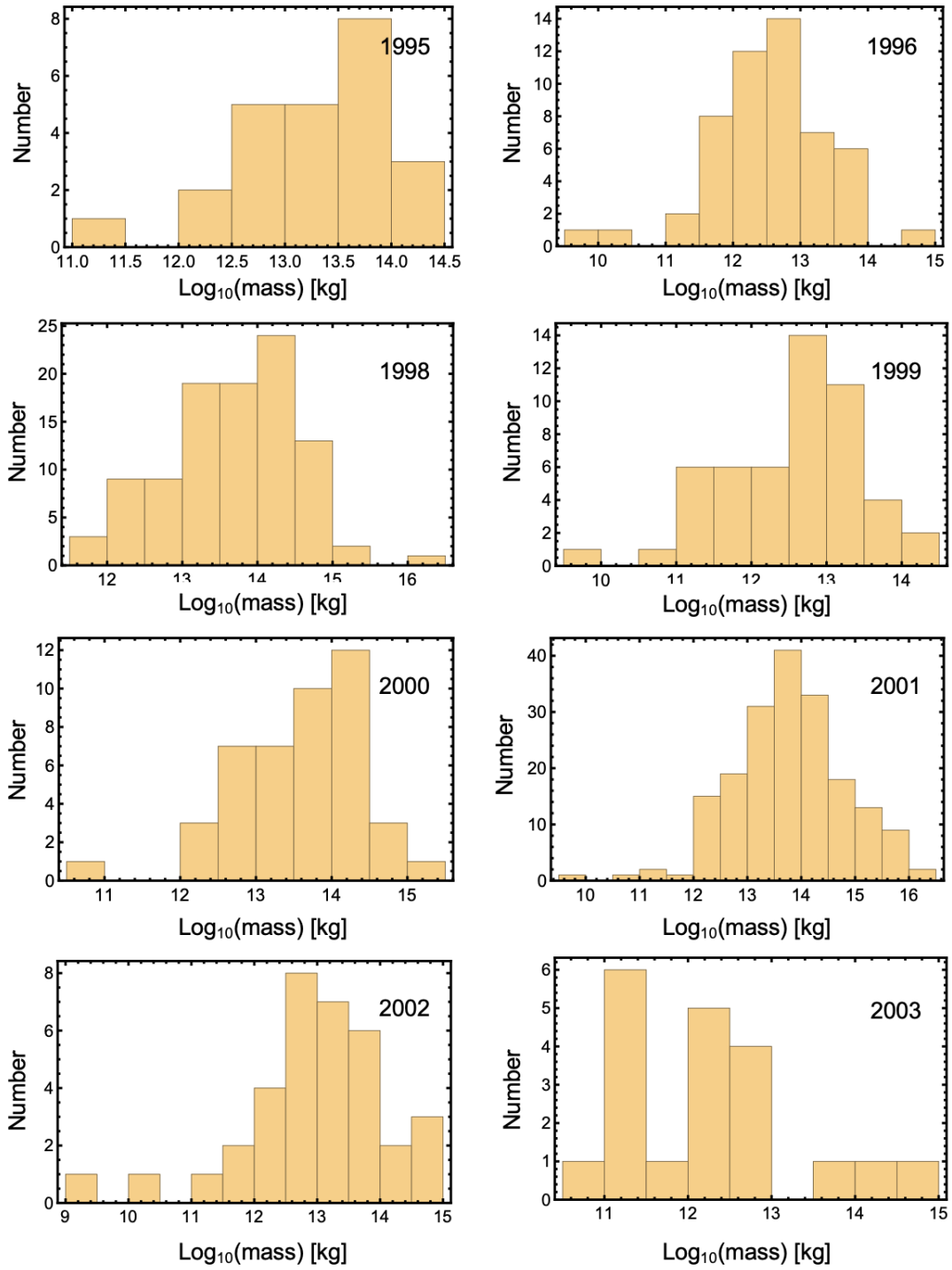

Figure 8.7: Histograms of prominence masses for AB Dor, generated from the ZDI maps.

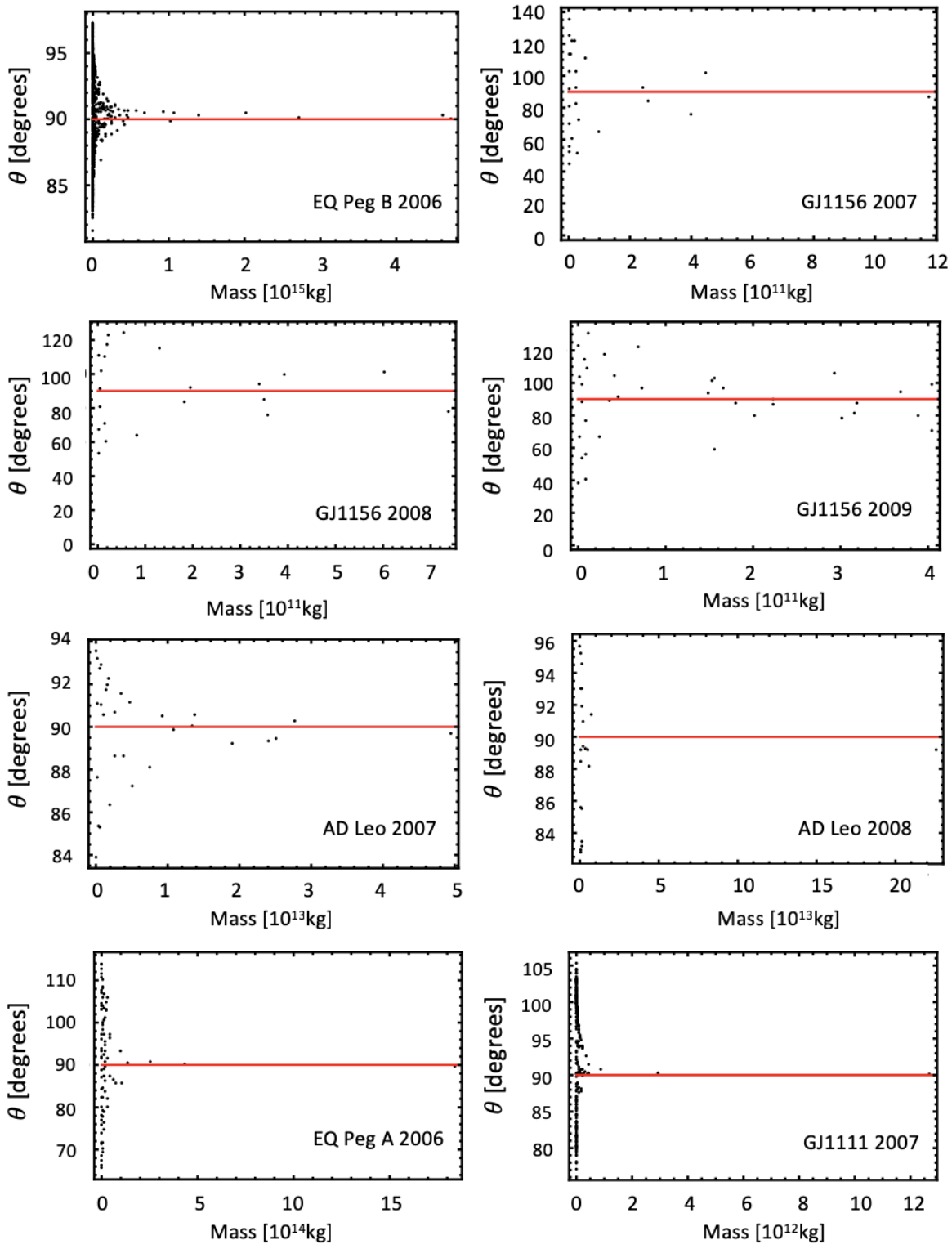

Figure 8.8: Plots of prominence mass versus theta. The red lines in the plots show the equator (i.e. $\theta = 90$degrees)

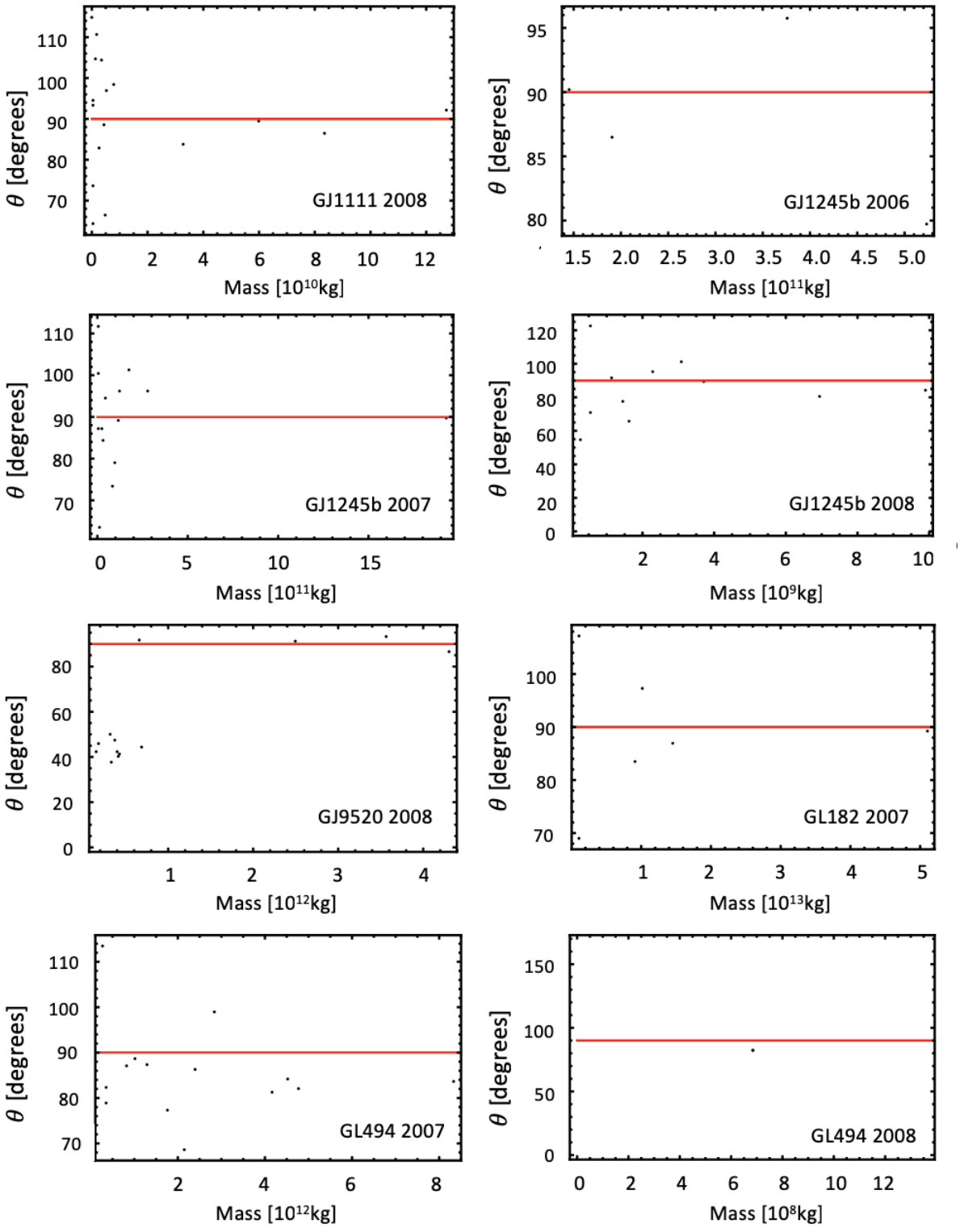

Figure 8.9: Plots of prominence mass versus theta. The red lines in the plots show the equator (i.e. $\theta = 90$degrees)

F Tilting a magnetic field

The following appendix gives the mathematics behind tilting a magnetic field structure from the stellar rotation axis. Here it is discussed in terms of a dipole, although it applies to other structures too.

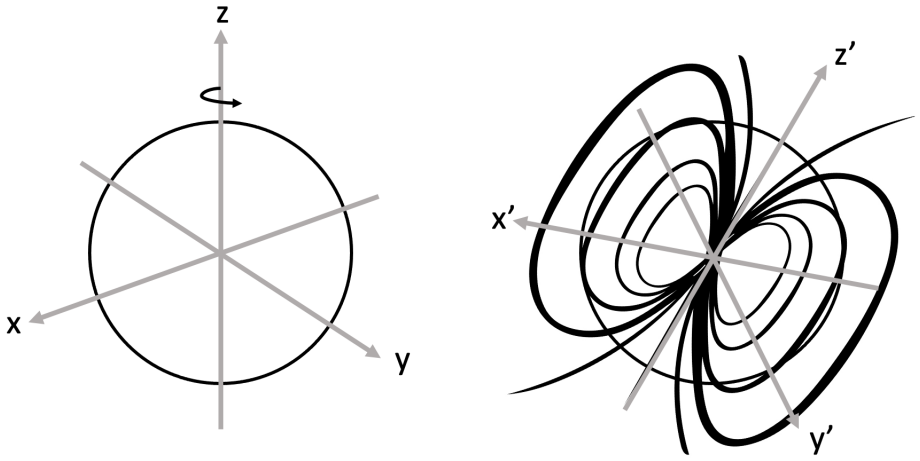

Figure 8.10: Cartoon showing the rotational frame (left) and magnetic frame (right).

The expression for a dipolar magnetic field that is aligned with the rotation axis is

$$\mathbf{B}_d = \frac{2\cos\theta}{r^3}\hat{r} + \frac{\sin\theta}{r^3}\hat{\theta}. \tag{8.41}$$

Two frames can be defined, (1) the frame of the rotation axis and (2) the frame of the tilted magnetic field structure, as shown in Figure 8.10.
In the following, the frame of the rotation axis is denoted as the 'original frame' and the tilted frame is denoted as the primed frame (e.g. $\mathbf{B}'$).
Within the primed frame, the expression for the magnetic field can be written simply as:

$$\mathbf{B}'_d = \frac{2\cos\theta'}{r'^3}\hat{r'} + \frac{\sin\theta'}{r'^3}\hat{\theta'}. \tag{8.42}$$

In order to have generated this expression in terms of the original frame, the magnetic field has been rotated by β. To rotate the field structure around the y-axis, a standard rotation matrix is used:

$$R_y = \begin{pmatrix} \cos\beta & 0 & -\sin\beta \\ 0 & 1 & 0 \\ \sin\beta & 0 & \cos\beta \end{pmatrix}, \tag{8.43}$$

such that $\mathbf{B}'_{cartesian} = [R_y]\mathbf{B}_{cartesian}$.

However, in order to apply this matrix to the magnetic field, the expression for the magnetic field must first be converted into Cartesian coordinates. This can be done with a conversion matrix:

$$\mathbf{B}'_{spherical} = [M]\mathbf{B}'_{cartesian} \tag{8.44}$$

where

$$[M] = \begin{pmatrix} \sin\theta\cos\phi & \sin\theta\sin\phi & \cos\theta \\ \cos\theta\cos\phi & \cos\theta\sin\phi & -\sin\theta \\ -\sin\phi & \cos\phi & 0 \end{pmatrix} \tag{8.45}$$

and thus

$$\mathbf{B}'_{cartesian} = [M]^{-1}\mathbf{B}'_{spherical} \tag{8.46}$$

with $[M]^{-1}$ being the inverse of matrix $[M]$.

Thus, the expression for the magnetic field in the original frame can be found by

$$\mathbf{B}_{cartesian} = [R_y]^{-1}[M]^{-1}\mathbf{B}'_{spherical}. \tag{8.47}$$

The expression for the tilted magnetic field in the original frame can be converted back into spherical coordinates:

$$\mathbf{B}_{spherical} = [M][R_y]^{-1}[M]^{-1}\mathbf{B}'_{spherical}. \tag{8.48}$$

Equation 8.48 is a general expression that can be used to tilt any multipole or magnetic field that can be written in the form of an analytic equation. Due to the matrices manipulation that is required, these expressions used in this thesis were calculated in Mathematica rather than by hand, to eliminate human errors!

G Observed prominences

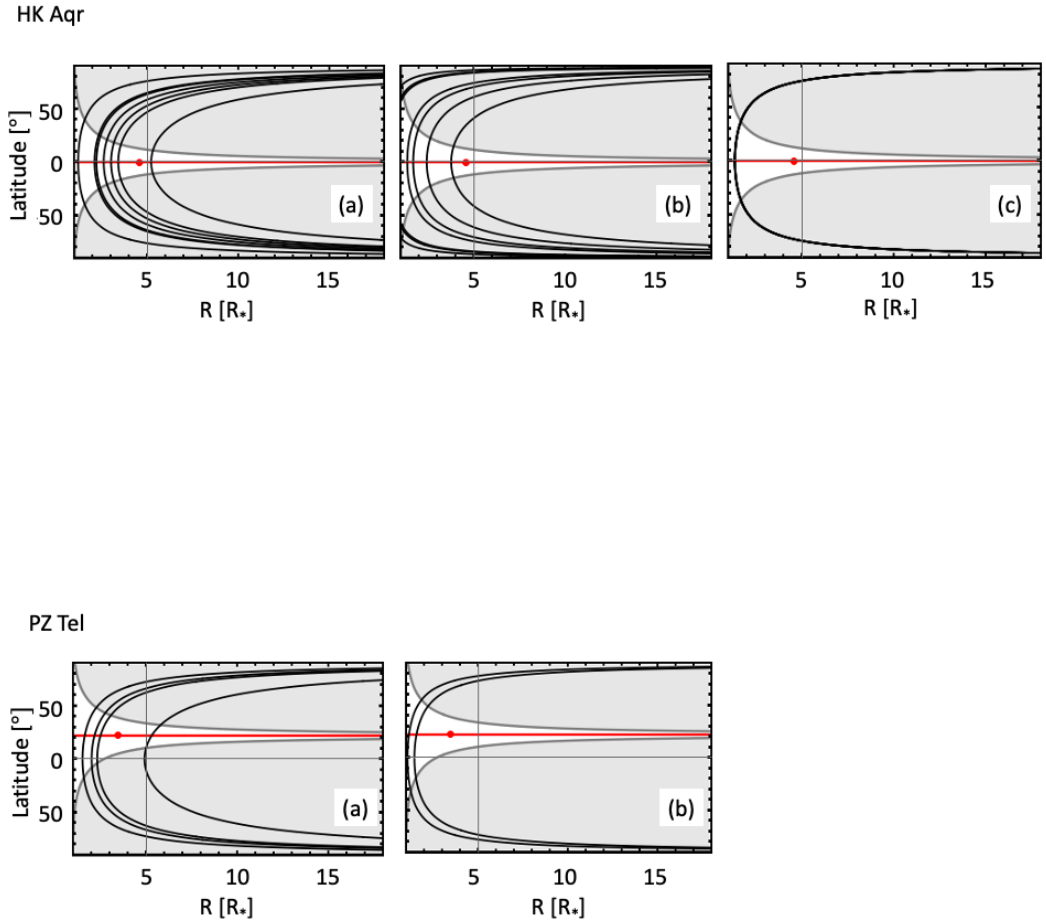

Figure 8.11: Potential prominence locations for the star HK Aqr and PZ Tel. For HK Aqr: (a) van den Ord 1998 [43] (b) Leitzinger 2016 [41] and (c) Byrne 1996 [44]. For PZ Tel: (a) Barnes 2000 [42] and (b) Leitzinger 2016 [41].

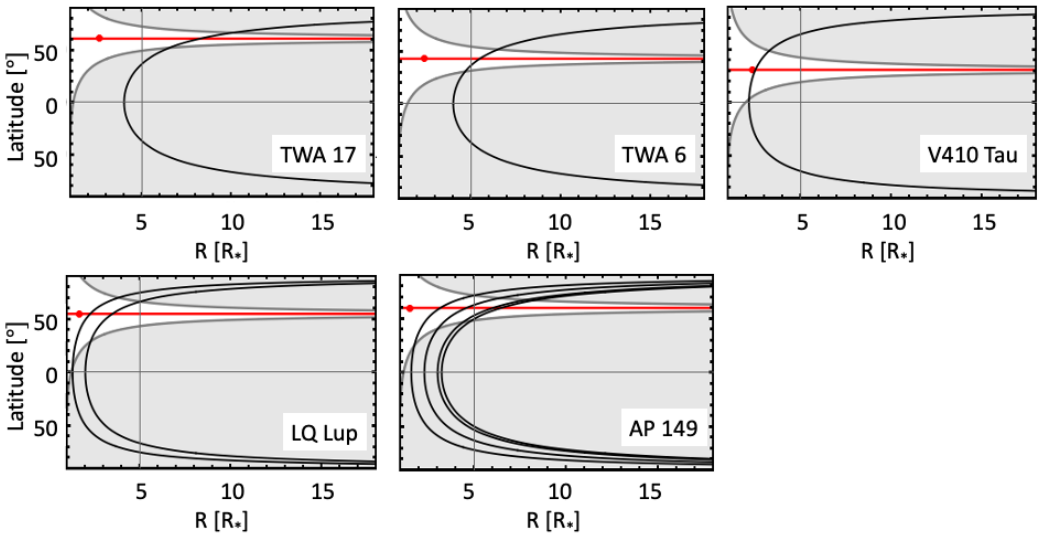

Figure 8.12: Possible prominence locations for the remaining stars, references are given in Table 7.1.

Bibliography

[1] A. Collier Cameron and R.D. Robinson. Fast H-α variations on a rapidly rotating cool main sequence star - I. Circumstellar clouds. *MNRAS*, 236:57–87, 1989. doi: 10.1093/mnras/236.1.57.

[2] J. C. Hall, D. P. Huenemoerder, L. W. Ramsey, and D. L Buzasi. Fiber-optic Echelle CCD observations of SS Bootis. *aap*, 358:610–660, 1990. doi: 10.1086/169013.

[3] J.D. Landstreet and E.F. Borra. The magnetic field of Sigma Orionis E. *ApJ*, 224: L5–L8, 1978.

[4] A. Collier Cameron. Stellar Prominences. *ASP Conference Series*, 158:146–157, 1999.

[5] K-P. Schröder. Detection of a stellar prominence of the K supergiant 32Cyg. *A&A*, 124 (2):16–18, 1983.

[6] K. A. Jensen, J. H. Swank, R. Petre, E. F. Guinan, E. M. Sion, and H. L. Shipman. EXOSAT observations of V471 tauri: a 9.25 minute white dwarf pulsation and orbital phase dependent xray dips. *AJ*, 309:27–31, 1986. doi: 10.1086/184754.

[7] B. Zaire, J. F. Donati, and B. Klein. Magnetic field evolution of the K2 dwarf V471 Tau. *MNRAS*, 513(2):2893–2903, June 2022. doi: 10.1093/mnras/stac721.

[8] J.G. Doyle, G.E. Bromage, A. Collier Cameron, D.W. Kilkenny, J. Krzesinski, H.M. Murphy, J.E. Neff, G. Pajdosz, and F. van Wyk. Short Time-scale Changes in the V-band Light Curve of II Peg: Flare Companion or Prominence? *Surface Inhomogeneities on Late-Type Stars, Proceedings of a colloquium held at Armagh Observatory*, 397:276–, 1992. doi: 10.1007/3-540-55310-X_168.

[9] D. Steeghs, K. Horne, T. R. Marsh, and J.-F. Donati. Slingshot prominences during

dwarf nova outbursts? *MNRAS*, 281 (2):626–636, 1996. doi: 10.1093/mnras/281.2.626.

[10] P.J. Wheatley. ROSAT observations of V471 Tauri, showing that stellar activity is determined by rotation, not age. *MNRAS*, 297:1145–1150, 1998. doi: 10.1046/j.1365-8711.1998.01607.x.

[11] J.C. Hall and L.W. Ramsey. Eclipse observations of RS CVn binaries. I. A survey for extended matter. *ApJ*, 104 (5):1942–1960, 1992. doi: 10.1086/116370.

[12] J.C. Hall and L.W. Ramsey. Eclipse observations of RS CVn binaries. II. A parametric model of extended matter. *ApJ*, 107 (3):1149–1164, 1994. doi: 10.1086/116927.

[13] C.A. Watson, D. Steeghs, V.S. Dhillon, and T. Shahbaz. Imaging the cool stars in the interacting binaries AE Aqr, BV Cen and V426 Oph. *Astronomische Nachrichten*, 328 (8):813–816, 2007. doi: 10.1002/asna.200710800.

[14] C.A. Watson, D. Steeghs, T. Shahbaz, and V.S. Dhillon. Roche tomography of cataclysmic variables – IV. Star-spots and slingshot prominences on BV Cen. *MNRAS*, 382 (3):1105–1118, 2007. doi: 10.1111/j.1365-2966.2007.12173.x.

[15] B.T. Gansicke, D.W. Hoard, K. Beuermann, E.M. Sion, and P. Szkody. HST/GHRS observations of AM Herculis. *A&A*, 338:933–946, 1998.

[16] W. M. Peterson, R. L. Mutel, M. Guedel, and W. M. Goss. A large coronal loop in the Algol system. *Nature letters*, 463:207–209, 2010. doi: 10.1038/nature08643.

[17] S.C. Barden, R.E. Fried, L.W. Ramsey, E.F. Guinan, and S.W. Wacker. The Light Curve, H- Modulation, and Possible Prominences of the Short-Period Binary DH Leo. *Lecture Notes in Physics. Cool Stars, Stellar Systems and the Sun, Proceedings of the Fourth Cambridge Workshop on Cool Stars*, 254:241, 1985.

[18] J.S. Newmark, D.P. Huenemoerder D.L. Buzasi, and L.W. Ramsey. COORDINATED OPTICAL AND ULTRAVIOLET OBSERVATIONS OF DH Leo. *ApJ*, 100 (2):560–568, 1990. doi: 10.1086/115539.

[19] J.S. Newark. PhD thesis, Pensylvania State University, USA. 1990.

[20] D. Cao and G.Shenghong. New observations of chromospheric and prominence activity on the RS CVn-type binary SZ Piscium. *A&A*, 538:4, 2012. doi: 10.1051/0004-6361/201118184.

[21] D. Cao, G.Shenghong, G. Jian, W. Tinggui, Z. Jilin, C. Liang, U. Wolter, M. Mittag, J.H.M.M. Schmitt, and V. Perdelwitz. Prominence activation, optical flare, and post-flare loops on the RS Canum Venaticorum star SZ Piscium. *MNRAS*, 482 (1):988–998, 2019. doi: 10.1093/mnras/sty2768.

[22] P. Petit, J.-F. Donati, M. Jardine, and A. Collier Cameron. Prominence Mapping of the RS CVn system HR 1099. *Coronal and stellar mass ejections*, 226:511–512, 2005. doi: 10.1017/S1743921305001158.

[23] M.B. Skelly, J.-F. Donati, J. Bouvier, K.N. Grankin, Y.C. Unruh, S.A. Artemenko, and P. Petrov. Dynamo processes in the T Tauri star V410 Tau. *MNRAS*, 403 (1): 159–169, 2010. doi: M.B.Skelly,J.-F.Donati,J.Bouvier,K.N.Grankin,Y.C.Unruh,S.A. Artemenko,P.Petrov.

[24] P. Garnavich, C. Littlefield, S. Kafka, M. Kennedy, P. Callanan, D.S. Balsara, and M. Lyutikov. Driving the Beat: Time-resolved Spectra of the White Dwarf Pulsar AR Scorpii. *ApJ*, 872 (1):id. 67, 11 pp., 2019. doi: 10.3847/1538-4357/aafb2c.

[25] J.-F. Donati and A. Collier Cameron. Differential rotation and magnetic polarity patterns on AB Doradus. *MNRAS*, 291:1–19, 1997. doi: 10.1093/mnras/291.1.1.

[26] A. Collier Cameron. Stellar Prominences. *International Astronomical Union*, pages 449–460, 1996.

[27] A. Collier Cameron and R.D. Robinson. Fast H-α variations on a rapidly rotating, cool main- sequence star - II. Cloud formation and ejection. *mnras*, 238:657–674, 1989. doi: 10.1093/mnras/238.2.657.

[28] A. Collier Cameron, P. Ehrenfreund D. K. Duncan, B. H. Foing, K. D. Kuntz, M. V. Pension, R. D. Robinson, and D. R. Soderblom. Fast spectroscopic variations on rapidly rotating, cool dwarfs - III. Masses of circumstellar absorbing clouds on AB Doradus. *mnras*, 247:415–438, 1990. doi: 10.1093/mnrasl/slx206.

[29] O. Vilhu, T. Tsuru, A. Collier Cameron, E. Budding, T. Banks, B. Slee, P. Ehrenfreund, and B.H. Foing. Multifrequency observations of AB Doradus. X-ray flaring and rotational modulation of a young star. *A&A*, 278:467–477, 1993.

[30] J.C. Brandt, S.R. Heap, F.M. Walter, E.A. Beaver, A. Boggess, K.G. Carpenter, D.C. Ebbets, J.B. Hutchings, M. Jura, D.S. Leckrone, J.L. Linsky, S.P. Maran, B. D. Savage, A.M. Smith, L.M. Trafton, R.J. Weymann, D. Norman, and S. Redfield. AB Dor in 94. I. Hubble space telescope goddard high resolution spectrograph observations of the quiescent chromosphere of an active star. *ApJ*, 121 (4):2173–2184, 2001. doi: 10.1086/319958.

[31] J.-F. Donati, A. Collier Cameron, G.A.J. Hussain, and M. Semel. Magnetic topology and prominence patterns on AB Doradus. *MNRAS*, 302:437—-456, 1999. doi: 10.1046/j.1365-8711.1999.02095.x.

[32] A. Gomez de Castro. On the source of the flaring activity in AB Doradus: the UV spectral signatures. *mnras*, 332 (2):409–421, 2002. doi: 10.1046/j.1365-8711.2002.05319.x.

[33] A.Collier Cameron, F.M.Walter, O.Vilhu, T.Böhm, C.Catala, S.Char, F.J.Clarke, P.Felenbok, B.H.Foing, K.K.Ghosh, L.Huang J.Hao, D.A.Jackson, E.Janot Pacheco, S.Jiang, A.-M.Lagrange, N.Suntzeff, and D.S.Zhai. Multisite observations of surface structures on AB Doradus in 1994 November. *MNRAS*, 308:493–509, 1999. doi: 10.1046/j.1365-8711.1999.02771.x.

[34] A. Collier Cameron. Stellar Prominences. *Symposium - International Astronomical Union*, 203:229–236, 2001.

[35] R.D. Jeffries. Prominence activity on the rapidly rotating field star HD197890. *MNRAS*, 262:369–376, 1993. doi: 10.1093/mnras/262.2.369.

[36] N. J. Dunstone, J. R. Barnes, A. Collier Cameron, and M. Jardine. The coronal structure of Speedy Mic - I: A densely packed prominence system beyond co-rotation. *mnras*, 365:530–538, 2006. doi: 10.1111/j.1365-2966.2005.09729.x.

[37] N. J. Dunstone, A. Collier Cameron, J. R. Barnes, and M. Jardine. The coronal structure of Speedy Mic – II. Prominence masses and off-disc emission. *mnras*, 373:1308–1320, 2006. doi: 10.1111/j.1365-2966.2006.11128.x.

[38] K. Vida, L. Kriskovics, K. Olah, M. Leitzinger, P. Odert, Zs. Kova, H. Korhone, R. Greimel, R. Robb, B. Csak, and J. Kovacs. Investigating magnetic activity in very stable stellar magnetic fields. *AAP*, 590:1–12, 2016. doi: 10.1051/0004-6361/201527925.

[39] J-F Donati, T. Forveille, A. Collier Cameron, J.R. Barnes, X. Delfosse, M.M. Jardine, and J.A. Valenti. The Large-Scale Axisymmetric Magnetic Topology of a Very-Low-Mass Fully Convective Star. *Science*, 311(5761):633–635, February 2006. doi: 10.1126/science.1121102.

[40] J. Stauffer, A. Collier Cameron, M. Jardine, T.J. David, L. Rebull, and A.M. Cody et al. Orbiting clouds of material at the keplerian co-rotation radius of rapidly rotating low-mass wtts in upper sco. *ApJ*, 153 (4):34 pp., 2017. doi: 10.3847/1538-3881/aa5eb9.

[41] M. Leitzinger, P. Odert, T. V. Zaqarashvili, R. Greimel A. Hanslmeier, and H. Lammer. Indications of stellar prominence oscillations on fast rotating stars: the cases of HK Aqr and PZ Tel. *MNRAS*, 463 (1):965–979, 2016. doi: 10.1093/mnras/stw1922.

[42] J. R. Barnes, A. Collier Cameron, D. J. James, and J.-F. Donati. Doppler images from dual-site observations of southern rapidly rotating stars ± I. Differential rotation on PZ Tel. *MNRAS*, 314:162–174, 2000. doi: 10.1046/j.1365-8711.2000.03237.x.

[43] G.H.J van den Oord. prominence-like clouds near HK Aqr. *AAP conference series*, 150:251–254, 1998.

[44] P. B. Byrne, M. T. Eibe, and W. R. J. Rolleston. Cool prominences in the corona of the rapidly rotating dMe star, HK Aquarii. *AAP*, 311:651–660, 1996.

[45] J.G. Doyle and A. Collier Cameron. Mass ejections from the rapidly rotating M dwarf star Gl 890. *MNRAS*, 244:291–291, 1990.

[46] A.I. Kolbin and V.V. Tsymbal. Analysis of magnetic activity of the rapidly rotating stars He 373 and AP 225. *Astronomy Reports*, 61 (6):521–532, 2017. doi: 10.1134/S1063772917060063.

[47] A. Collier Cameron and J.A. Woods. Prominence activity in G dwarfs of the alpha Persei cluster. *MNRAS*, 258:360–370, 1992. doi: 10.1093/mnras/258.2.360.

[48] M.T. Eibe. Prominence and plage activity in the recently discovered late-type rapid rotator, RE 1816+541. *A&A*, 337:757–771, 1998.

[49] M.T. Eibe, P.B. Byrne, and R.M. Robb. Indicators of Intense Activity in the Recently Discovered Late-Type Rapid Rotator, RE 1816+541. *ASP Conf. Ser.*, 154, The Tenth Cambridge Workshop on Cool Stars:p.1410, 1998.

[50] P.P. Petrov. 'Prominences' of RY Tauri. *Astrophysics and Space Science*, 169 (1-2): 61–65, 1990. doi: 10.1007/BF0064068.

[51] M. B. Skelly, A. Collier Cameron Y. C. Unruh, J. R. Barnes, J.-F. Donati, W. A. Lawson, and B. D. Carter. Doppler Images and Chromospheric Variability of TWA 6. *MNRAS*, 385:708–718, 2008. doi: 10.1111/j.1365-2966.2008.12917.x.

[52] M. B. Skelly, Y. C. Unruh, J. R. Barnes, W. A. Lawson, J.-F. Donati, and A. Collier Cameron. Doppler images and chromospheric variability of TWA 17. *MNRAS*, 399 (4):1829–1838, 2009. doi: 10.1111/j.1365-2966.2009.15411.x.

[53] J.-F. Donati, M. Mengel, B. D. Carter, S. Marsden, A. Collier Cameron, and R. Wichmann. Surface differential rotation and prominences of the Lupus post T Tauri star RX J1508.6±4423 . *MNRAS*, 316 (3):699–715, 2000. doi: 10.1046/j.1365-8711.2000.03570.x.

[54] J. R. Barnes, A. Collier Cameron, D. J. James, and D. Steeghs. Further images of a Persei G dwarfs. *MNRAS*, 326:1057–1066, 2001. doi: 10.1046/j.1365-8711.2001.04648.x.

[55] T-Q. Cang, P. Petit, J-F. Donati, C.P. Folsom, M. Jardine, C. Villarreal D'Angelo, A.A. Vidotto, S.C. Marsden, F. Gallet, and B. Zaire. Magnetic field and prominences of the young, solar-like, ultra-rapid rotator V530 Persei. *A&A*, 643:16 pp., 2020. doi: 10.1051/0004-6361/202037693.

[56] G.A.J. Hussain, M. Jardine, J.-F. Donati, N.S. Brickhouse, N.J. Dunstone, K. Wood, A.K. Dupree, A. Collier Cameron, and F. Favata. The coronal structure of AB Doradus determined from contemporaneous Doppler imaging and X-ray spectroscopy. *MNRAS*, 377:1488—-1502, 2007. doi: 10.1111/j.1365-2966.2007.11692.x.

[57] N.J. Dunstone. PhD thesis, University of St Andrews, UK. 2008.

[58] G. A. J. Hussain. Observations of stellar coronae and prominences. *Nature of Prominences and their role in Space Weather Proceedings IAU Symposium*, No. 300:309–317, 2014. doi: 10.1017/S1743921313011137.

[59] J-F. Donati M. Jardine and S.G. Gregory. Stellar mass ejections. *Proceedings IAU Symposium No. 257*, pages 201–210, 2009. doi: 10.1017/S1743921309029317.

[60] A.N. Aarnio, K.G. Stassun, and S.P. Matt. Coronal Mass Ejections and Angular Momentum Loss in Young Stars. *Nature of Prominences and their role in Space Weather, Proceedings IAU Symposium No. 300*, pages 318–422, 2014. doi: 10.1017/S1743921313011149.

[61] N. Gopalswamy, S. Akiyama, S. Yashiro, and P. Mäkelä. Coronal Mass Ejections from Sunspot and Non-Sunspot Regions. In *Magnetic Coupling between the Interior and Atmosphere of the Sun*, volume 19 of *Astrophysics and Space Science Proceedings*, pages 289–307, January 2010. doi: 10.1007/978-3-642-02859-5_24.

[62] E. R. Houdebine, B. H. Foing, and M. Rodono. Dynamics of flares on late-type dMe stars. I. Flare mass ejections and stellar evolution. *AAP*, 238:249, November 1990.

[63] K. Vida, M. Leitzinger, L. Kriskovics, B. Seli, P. Odert, O.E. Kovács, H. Korhonen, and L. van Driel-Gesztelyi. The quest for stellar coronal mass ejections in late-type stars. I. Investigating Balmer-line asymmetries of single stars in Virtual Observatory data. *AAP*, 623:A49, Mar 2019. doi: 10.1051/0004-6361/201834264.

[64] B. Fuhrmeister, S. Czesla, J. H. M. M. Schmitt, S. V. Jeffers, J. A. Caballero, M. Zechmeister, A. Reiners, I. Ribas, P. J. Amado, A. Quirrenbach, V. J. S. Béjar, D. Galadí-Enríquez, E. W. Guenther, M. Kürster, D. Montes, and W. Seifert. The CARMENES search for exoplanets around M dwarfs. Wing asymmetries of Hα, Na I D, and He I lines. *AAP*, 615:A14, July 2018. doi: 10.1051/0004-6361/201732204.

[65] M. Leitzinger, P. Odert, R. Greimel, H. Korhonen, E. W. Guenther, A. Hanslmeier, H. Lammer, and M. L. Khodachenko. A search for flares and mass ejections on young late-type stars in the open cluster Blanco-1. *MNRAS*.

[66] H. Korhonen, K. Vida, M. Leitzinger, P. Odert, and O.E. Kovács. Hunting for Stellar Coronal Mass Ejections. In D. Nandy, A. Valio, and P. Petit, editors, *Living Around*

Active Stars, volume 328 of *IAU Symposium*, pages 198–203, Oct 2017. doi: 10.1017/S1743921317003969.

[67] P. Zeeman. The Effect of Magnetisation on the Nature of Light Emitted by a Substance. *Nature*, 55(1424):347, February 1897. doi: 10.1038/055347a0.

[68] G. A. J. Hussain, M. Jardine, and A. Collier Cameron. Mapping potential fields on the surfaces of rapidly rotating starsq. *MNRAS*, 322:681–688, 2001.

[69] G. A. J. Hussain, A. A. van Ballegooijen, M. Jardine, and A. Collier Cameron. The coronal topology of the rapidly rotating K0 dwarf, AB Doradus I. Using surface magnetic field maps to model the structure of the stellar corona. *ApJ*, pages 1–13, 2002. doi: 10.1086/341429.

[70] M. Jardine, A. Collier Cameron, and J.-F. Donati. The global magnetic topology of AB Doradus. *MNRAS*, 333 (2):339–346, 2002. doi: https://doi.org/10.1046/j.1365-8711.2002.05394.x.

[71] M. Jardine, K. Wood, A. Collier Cameron, J.-F. Donati, and D. H. Mackay. Inferring X-ray coronal structures from Zeeman–Doppler images. *MNRAS*, 336:1364–1370, 2002. doi: https://doi.org/10.1046/j.1365-8711.2002.05877.x.

[72] J. B. Climent, J. C. Guirado, R. Azulay, J. M. Marcaide, D. L. Jauncey, J. F. Lestrade, and J. E. Reynolds. The milliarcsecond-scale radio structure of AB Doradus A. *AAP*, 641:A90, September 2020. doi: 10.1051/0004-6361/202037542.

[73] M. Massi, E. Ros, K. M. Menten, M. Kaufman Bernadó, G. Torricelli-Ciamponi, J. Neidhöfer, A. Boden, D. Boboltz, A. Sargent, and G. Torres. Interacting coronae of two T Tauri stars: first observational evidence for solar-like helmet streamers. *AAP*, 480(2):489–494, March 2008. doi: 10.1051/0004-6361:20078637.

[74] M.M. Kao, A.J. Mioduszewski, J. Villadsen, and E.L. Shkolnik. Resolved imaging of an extrasolar radiation belt around an ultracool dwarf, 2023. URL `https://arxiv.org/abs/2302.12841`.

[75] L. K. Harding, G. Hallinan, Q. M. Konopacky, K. M. Kratter, R. P. Boyle, R. F. Butler, and A. Golden. Spin-orbit alignment in the very low mass binary regime. The L dwarf tight binary 2MASSW J0746425+200032AB. *AAP*, 554:A113, June 2013. doi: 10.1051/0004-6361/201220865.

[76] M.M. Jardine and A. Collier Cameron. Magnetostatic equilibria for coronal loops on rotating stars. *Sol. Phys.*, 131:269–289, 1991. doi: 10.1007/BF00151638.

[77] M. Jardine and A.A. van Ballegooijen. Slingshot prominences above stellar X-ray coronae. *MNRAS*, 361:1173–1179, 2005. doi: 10.1111/j.1365-2966.2005.09256.x.

[78] M.D. Altschuler and G. Newkirk. Magnetic fields and the structure of the solar corona. *Sol. Phys.*, 9:131–149, 1969. doi: 10.1007/BF00145734.

[79] H.C. Spruit. Equations for Thin Flux Tubes in Ideal MHD. *A&A*, 102:129–133, 1981.

[80] J.M. Ferreira. A model of slingshot prominences in rapidly rotating stars. *MNRAS*, 316:647–656, 2000.

[81] M. Jardine, A. Collier Cameron, J.-F. Donati, and G.R. Pointer. Prominence support in potential field configurations around rotating stars. *MNRAS*, 324:201–205, 2001. doi: 10.1046/j.1365-8711.2001.04332.x.

[82] C. Villarreal D'Angelo, M. Jardine, and V. See. Prominence formation and ejection in cool stars. *MNRAS*, 475:L25–L29, 2018. doi: 10.1093/mnrasl/slx206.

[83] V. Petit, S. P. Owocki, G. A. Wade, D. H. Cohen, J. O. Sundqvist, M. Gagné, J. Maíz Apellániz, M. E. Oksala, D. A. Bohlender, T. Rivinius, H. F. Henrichs, E. Alecian, R. H. D. Townsend, A. ud-Doula, and MiMeS Collaboration. A magnetic confinement versus rotation classification of massive-star magnetospheres. *MNRAS*, 429(1):398–422, February 2013. doi: 10.1093/mnras/sts344.

[84] V. Reville, A. S. Brun, A. Strugarek S.P. Matt, J Bouvier, C.P. Folsom, and P.Petit. From Solar to Stellar Corona: The Role of Wind, Rotation, and Magnetism. *ApJ*, 814 (2):99–108, 2015. doi: 10.1088/0004-637X/814/2/99.

[85] V. See, M. Jardine, A. A. Vidotto, J.-F. Donati, S. Boro Saikia, R. Fares, C. P. Folsom, S. V. Jeffers, S. C. Marsden, J. Morin, P. Petit, and BCool-Collaboration. The open flux evolution of a solar-mass star on the main sequence. *MNRAS*, 474:536–546, 2018. doi: 10.1093/mnras/stx2599.

[86] M. Jardine, A. Collier Cameron, J-F. Donati, and G.A.J. Hussain. Slingshot prominences: coronal structure, mass loss and spin down. *MNRAS*, 491 (3):4076–4088, 2020. doi: 10.1093/mnras/stz3173.

[87] M. M. Jardine and A. Collier Cameron. Slingshot prominences: nature's wind gauges. *MNRAS*, 482:2853–2860, 2018. doi: 10.1093/mnras/sty2872.

[88] E.J. Weber and L Davis. The Angular Momentum of the Solar Wind. *ApJ*, 148: 217–227, 1967. doi: 10.1086/149138.

[89] L. Mestel. Magnetic breaking by a stellar wind - I. *MNRAS*, 138:359–391, 1968. doi: 10.1093/mnras/138.3.359.

[90] E.N. Parker. Suprathermal Particle Generation in the Solar Corona. *ApJ*, 128:664–676, 1958. doi: 10.1086/146579.

[91] N. Panagia and M. Felli. The spectrum of the free-free radiation from extended envelopes. *A&A*, 39:1–5, 1975.

[92] J. Lim and S.M. White. Limits to Mass Outflows from Late-Type Dwarf Stars. *ApJ letters*, 462:L91, 1996. doi: 10.1086/310038.

[93] G.H.J van den Oord and J.G. Doyle. Constraints on mass loss from dMe stars: theory and observations. *AAP*, 319:578–588, 1997.

[94] J. Villadsen, G. Hallinan, S. Bourke, M. Güdel, and M. Rupen. First Detection of Thermal Radio Emission from Solar-type Stars with the Karl G. Jansky Very Large Array. *ApJ*, 788(2):id 112, 2014. doi: 10.1088/0004-637X/788/2/112.

[95] B.J. Wargelin and J.J. Drake. Stringent X-Ray Constraints on Mass Loss from Proxima Centauri. *ApJ*, 578(1):503–514, 2002. doi: 10.1086/342270.

[96] B. E. Wood, H-R. Muller, G. P. Zank, J. L. Linsky, and S. Redfield. New Mass Loss Measurements from Astrospheric Ly$_\alpha$ Absorption. *ApJ*, 628(2):L143–L146, 2005. doi: 10.1086/432716.

[97] J. Zendejas, A. Segura, and A.C. Raga. Atmospheric mass loss by stellar wind from planets around main sequence M stars. *Icarus*, 210(2):539–544, 2010. doi: 10.1016/j.icarus.2010.07.013.

[98] A. A. Vidotto, J. F. Donati, M. Jardine, V. See, P. Petit, I. Boisse, S. Boro Saikia, E. Hébrard, S. V. Jeffers, S. C. Marsden, and J. Morin. Could a change in magnetic field geometry cause the break in the wind-activity relation? *MNRAS*, 455(1):L52–L56, January 2016. doi: 10.1093/mnrasl/slv147.

[99] V. See, M. Jardine, A. A. Vidotto, J. F. Donati, S. Boro Saikia, R. Fares, C. P. Folsom, É. M. Hébrard, S. V. Jeffers, S. C. Marsden, J. Morin, P. Petit, I. A. Waite, and BCool Collaboration. Studying stellar spin-down with Zeeman-Doppler magnetograms. *MNRAS*, 466(2):1542–1554, April 2017. doi: 10.1093/mnras/stw3094.

[100] J.H. Debes. Measuring M Dwarf Winds with DAZ White Dwarfs. *ApJ*, 652(1):636–642, November 2006. doi: 10.1086/508132.

[101] S. G. Parsons, T. R. Marsh, B. T. Gänsicke, A. Rebassa-Mansergas, V. S. Dhillon, S. P. Littlefair, C. M. Copperwheat, R. D. G. Hickman, M. R. Burleigh, P. Kerry, D. Koester, A. Nebot Gómez-Morán, S. Pyrzas, C. D. J. Savoury, M. R. Schreiber, L. Schmidtobreick, A. D. Schwope, P. R. Steele, and C. Tappert. A precision study of two eclipsing white dwarf plus M dwarf binaries. *MNRAS*, 420(4):3281–3297, March 2012. doi: 10.1111/j.1365-2966.2011.20251.x.

[102] K.G. Kislyakova, M. Holmström, H. Lammer, P. Odert, and M.L. Khodachenko. Magnetic moment and plasma environment of HD 209458b as determined from Lyα observations. *Science*, 346(6212):981–984, November 2014. doi: 10.1126/science.1257829.

[103] V. Bourrier, A. Lecavelier des Etangs, D. Ehrenreich, Y. A. Tanaka, and A. A. Vidotto. An evaporating planet in the wind: stellar wind interactions with the radiatively braked exosphere of GJ 436 b. *AAP*, 591:A121, June 2016. doi: 10.1051/0004-6361/201628362.

[104] A. A. Vidotto and V. Bourrier. Exoplanets as probes of the winds of host stars: the case of the M dwarf GJ 436. *MNRAS*, 470(4):4026–4033, October 2017. doi: 10.1093/mnras/stx1543.

[105] B.E. Wood et al. New Observational Constraints on the Winds of M dwarf Stars. *ApJ*, 915(1):37, July 2021. doi: 10.3847/1538-4357/abfda5.

[106] C.P. McKay. Requirements and limits for life in the context of exoplanets. *PNAS*, 111 (35):12628–12633, 2014. doi: 10.1073/pnas.1304212111.

[107] W. Ludwig, S. Eggl, D. Neubauer, J. Leitner, M.G. Firneis, and R. Hitzenberger. Effective stellar flux calculations for limits of life-supporting zones of exoplanets. *MNRAS*, 458:3752–3759, 2016. doi: 10.1093/mnras/stw509.

[108] D.J. Armstrong, C.E. Pugh, A-M. Broomhall, D.J.A. Brown, M.N. Lund, H.P. Osborn, and D.L. Pollacco. The host stars of Kepler's habitable exoplanets: superflares, rotation and activity. *MNRAS*, 455 (3):3110–3125, 2016. doi: 10.1093/mnras/stv2419.

[109] T. Lüftinger, M. Güdel, and C. Johnstone. Stellar magnetic activity and their influence on the habitability of exoplanets. *Proc. of IAU*, 10 (S305):333–339, 2014. doi: 10.1017/S1743921315005001.

[110] W.D. Gonzalez, J.A. Joselyn, Y. Kamide, H.W. Kroehl, G. Rosoker, B.T. Tsuruani, and V.M. Vasyliunas. What is a geomagnetic storm? *Journal of Geophysical Research*, 99 (A4):5771–5792, 1994. doi: 10.1029/93JA02867.

[111] S.F. Odenwald and J.L. Green. Bracing the Satellite Infrastructure for a Solar Superstorm. *Scientific American*, July 2008.

[112] Earth dodges magnetic storm. *New Scientist*, 1670, June 1989.

[113] J.G. Kappenman, L.J. Zanetti, and W.A. Radasky. Geomagnetic Storms Can Threaten Electric Power Grid. *Space Phys.*, 9 (7):9–11, 1997.

[114] O.C. St. Cyr and D.F. Webb. Activity associated with coronal mass ejections at solar minimum: SMM observations from 1984–1986. *Solar Phys.*, 131 (2):379–394, 1991. doi: 10.1007/BF00146543.

[115] H.R. Gilbert, T.E. Holzer, J.T. Burkepile, and A.J. Hundhausen. Active and Eruptive Prominences and Their Relationship to Coronal Mass Ejections. *ApJ*, 537 (1):503–515, 2000. doi: 10.1086/309030.

[116] P. Subramanian and K.P. Dere. Source Regions of Coronal Mass Ejections. *ApJ*, 561 (1):372–395, 2001. doi: 10.1086/323213.

[117] G. Zhou, J. Wang, and Z. Cao. Correlation between halo coronal mass ejections and solar surface activity. *A&A*, 397:1057–1067, 2003. doi: 10.1051/0004-6361:20021463.

[118] A. Compagnino, P. Romano, and F. Zuccarello. A Statistical Study of CME Properties and of the Correlation Between Flares and CMEs over Solar Cycles 23 and 24. *Solar Phys.*, 292 (5):1–19, 2017. doi: 10.1007/s11207-016-1029-4.

[119] I.F. Shaikhislamov, M.L. Khodachenko, Yu.L. Sasunov, H. Lammer, K.G. Kislyakova, and N.V. Erkaev. Atmosphere expansion and mass loss of close-orbit giant exoplanets

heated by stellar XUV: I. Modeling of hydrodynamic escape of upper atmospheric material. *ApJ*, 795:132:1–15, 2014. doi: 10.1088/0004-637X/795/2/132.

[120] T.T. Koskinen, M.J. Harris, R.V. Yelle, and P. Lavvasc. The escape of heavy atoms from the ionosphere of HD209458b. I. A photochemical–dynamical model of the thermosphere. *Icarus*, 226 (2):1678–1694, 2013. doi: 10.1016/j.icarus.2012.09.027.

[121] H. Lammer, N.V. Erkaev, P. Odert, K.G. Kislyakova, M. Leitzinger, and M.L. Khodachenko. Probing the blow-off criteria of hydrogen-rich 'super-Earths'. *MNRAS*, pages 1247–1256, 2013. doi: 10.1093/mnras/sts705.

[122] L. Sairam, J.H.M.M. Schmitt, and S. Dash. Atmospheric mass loss of extrasolar planets orbiting magnetically active host stars. *MNRAS*, 477 (1):808–815, 2018. doi: 10.1093/mnras/sty732.

[123] M.L. Khodachenko, I. Ribas, H. Lammer, J-M. Griessmeire, M. Leitner, F. Selsis, C. Eiroa, A. Hanslmeier, H.K. Biernat, C.J. Farrugia, and H.O. Rucker. Coronal mass ejection (cme) activity of low mass m stars as an important factor for the habitability of terrestrial exoplanets. i. cme impact on expected magnetospheres of earth-like exoplanets in close-in habitable zones. *Astrobiology*, 7(1):167–184, 2007. doi: 10.1089/ast.2006.0127.

[124] A.A. Vidotto. Stellar magnetic activity and exoplanets. *EPJ Web of Conferences*, 160, 2017. doi: 10.1051/epjconf/201716005011.

[125] A. A. Vidotto, M. Jardine, M. Opher, J. F. Donati, and T. I. Gombosi. Understanding the Angular Momentum Loss of Low-Mass Stars: The Case of V374 Peg. *Astronomical Society of the Pacific Conference Series, 16th Cambridge Workshop on Cool Stars, Stellar Systems, and the Sun.*, 448:1293–, 2011. doi: 10.1111/j.1365-2966.2010.17908.x.

[126] C. Villarreal D'Angelo, M. Jardine, C.P. Johnstone, and V. See. Slingshot prominence evolution for a solar-like star. *MNRAS*, 485(1):1448–1453, 2019. doi: 10.1093/mnras/stz477.

[127]

[128] R.F.P. Waugh. Cool and clumpy: multi-temperature equilibria of plasma in complex stellar magnetic fields. 2016.

[129] D. Kleppner and R.J. Kolenkow. *An Introduction to Mechanics*. Cambridge University Press, 2010.

[130] E. N. Parker. X-ray bright spots on the sun and the nonequilibrium of a twisted flux rope in a stratisfied atmosphere. *ApJ*, 201:494–501, 1975.

[131] D.M. Willis and L.R. Young. Equation for the field lines of an asymmetric magnetic multipole. *Geophys. J.R. astr. Soc.*, (89):1011–1022, 1987.

[132] J. L. Innis, K. Thompson, D. W. Coates, and T. Lloyd Evans. Observations of active chromosphere stars - ii. photometry of ab dor, 1978-1987. *mnras*, 235:1411–1422, 1988. doi: 10.1093/mnras/235.4.1411.

[133] J. C. Guirado, I. Marti-Vidal, J. M. Marcaide, L. M. Close, J. F. Lestrade, D. L. Jauncey, S. Jimenez-Monferrer, D. L. Jones, R. A. Preston, and J. E. Reynolds. The AB Doradus System Revisited: The Dynamical Mass of AB Dor A. *ASSSP*, Highlights of Spanish Astrophysics V:139–145, 2010. doi: 10.1007/978-3-642-11250-8_13.

[134] J. C. Guirado, J. M. Marcaide, I. Marti-Vidal, J. B. Le Bouquin, L. M. Close, W. D. Cotton, and J. Montalban. The size of AB Doradus A from VLTI/AMBER interferometry. *A&A*, 533:A106, 2011. doi: 10.1051/0004-6361/201117426.

[135] R.F.P. Waugh and M.M. Jardine. Magnetic confinement of dense plasma inside (and outside) stellar coronae. *MNRAS*, 514:5465–5477, 2021. doi: 10.1093/mnras/stac1698.

[136] Klaus G. Strassmeier. Starspots. *AAPR*, 17(3):251–308, September 2009. doi: 10.1007/s00159-009-0020-6.

[137] R.F.P Waugh, M.M. Jardine, J. Morin, and J-F Donati. Slingshot prominences: a hidden mass loss mechanism. *MNRAS*, 505 (4):5104–5116, 2021. doi: 10.1093/mnras/stab1709.

[138] J.-F. Donati and J.D. Landstreet. Magnetic fields of nondegenerate stars. *Annual Review of Astronomy and Astrophysics*, 47(1):333–370, 2009. doi: 10.1146/annurev-astro-082708-101833. URL `https://doi.org/10.1146/annurev-astro-082708-101833`.

[139] J. Morin, J. F. Donati, P. Petitand X. Delfosse, T. Forveille, and M. M. Jardine. Large-scale magnetic topologies of late M dwarfs*. *MNRAS*, 407(4):2269–2286, 2010. doi: 10.1111/j.1365-2966.2010.17101.x.

[140] J. Morin, J.-F. Donati, P. Petit, X. Delfosse, T. Forveille, L. Albert, M. Auri‘ere, R. Cabanac, B. Dintrans, R. Fares, T. Gastine, M.M. Jardine, F. Ligni‘eres, F. Paletou, J.C. Ramirez Velez, and S. Theado. Large-scale magnetic topologies of mid M dwarfs. *MNRAS*, 390(2):567–581, 2008. doi: 10.1111/j.1365-2966.2008.13809.x.

[141] J.-F. Donati, J. Morin, P. Petit, X. Delfosse, T. Forveille, M. Auri‘ere, R. Cabanac, B. Dintrans, R. Fares, T. Gastine, M.M. Jardine, F. Ligni‘eres, F. Paletou, J.C. Ramirez Velez, and S. Th ead1. Large-scale magnetic topologies of early M dwarfs. *MNRAS*, 390(2):545–560, 2008. doi: 10.1111/j.1365-2966.2008.13799.x.

[142] A.A. van Ballegooijen, N. P. Cartledge, and E. R. Priest. MAGNETIC FLUX TRANSPORT AND THE FORMATION OF FILAMENT CHANNELS ON THE SUN. *ApJ*, 501:866–881, 1998. doi: 10.1086/305823.

[143] M. Jardine, A. Collier Cameron, J.-F. Donati, and G.A.J. Hussain. Slingshot prominences: coronal structure, mass loss and spin down. *MNRAS*, 491 (3):4076–4088, 2020. doi: 10.1093/mnras/stz3173.

[144] S. V. Jeffers, M. Mengeland C. Moutou, S. C. Marsden, J. R. Barnes, M. M. Jardine, P. Petit, J. H. M. M. Schmitt, V. See, A. A. Vidotto, and BCool Collaboration. The relation between stellar magnetic field geometry and chromospheric activity cycles - II The rapid 120-day magnetic cycle of Bootis. *MNRAS*, 479 (4):5266–5271, 2018. doi: 10.1093/mnras/sty1717.

[145] S. Boro Saikia, T. Lueftinger, S.V. Jeffers, C.P. Folsom, V. See, P. Petit, S.C. Marsden, A.A. Vidotto, J. Morin amd A. Reiners, M. Guedel, and BCool. Direct evidence of a full dipole flip during the magnetic cycle of a sun-like star. *AAP*, 620:L11, 2018. doi: 10.1051/0004-6361/201834347.

[146] K. Vida, L. Kriskovics, K. Olah, M. Leitzinger, P. Odert, Zs. Kova, H. Korhone, R. Greimel, R. Robb, B. Csak, and J. Kovacs. Investigating magnetic activity in very stable stellar magnetic fields. *AAP*, 590:1–12, 2016. doi: 10.1051/0004-6361/201527925.

[147] A. Lavail, O. Kochukhov, and G.A. Wade. A sudden change of the global magnetic field of the active M dwarf AD Leo revealed by full Stokes spectropolarimetric observations. *MNRAS*, 479 (4):4836–4843, 2018. doi: 10.1093/mnras/sty1825.

[148] CDS-Strasbourg. Vizier. 2020. URL https://vizier.u-strasbg.fr/viz-bin/VizieR.

[149] CDS-Strasbourg. Simbad astronomical database. 2020. URL http://simbad.u-strasbg.fr/simbad/.

[150] B. Stelzer, A. Marino, G. Micela, J. Lopez-Santiago, and C. Liefke. The UV and X-ray activity of the M dwarfs within 10pc of the Sun. *MNRAS*, 431 (3):2063–2079, 2013. doi: 10.1093/mnras/stt225.

[151] C.B. Haakonsen and R.E. Rutledge. XID II: statistical cross-association of ROSAT bright source catalog X-ray sources with 2MASS point source catalog near-infrared sources. *The Astrophysical Journal Supplement Series*, ():1–45, 2009. doi: 10.1088/0067-0049/184/1/138.

[152] L. Malo, R. Doyonand D. Lafrenière, E. Artigau, J. Gagné, Frédérique F. Baron, and A. Riedel. Bayesian Analysis to Identify New Star Candidates in Nearby Young Stellar Kinematic Groups. *ApJ*, ():1–43, 2013. doi: 10.1088/0004-637X/762/2/88.

[153] T.K. Suzuki, S. Imada, R. Kataoka, Y. Kato, T. Matsumoto, H. Miyahara, and S. Tsuneta. Saturation of Stellar Winds from Young Suns. *Publications of the Astronomical Society of Japan*, 65(5):id98–, 2013. doi: 10.1093/pasj/65.5.98.

[154] J. Ahuir, A.S. Brun, and A. Strugarek. From stellar coronae to gyrochronology: A theoretical and observational exploration. *AAP*, 635:A170–, 2020. doi: 10.1051/0004-6361/201936974.

[155] J. Morin, E. Dormy, M. Schrinner, and J.-F. Donati. Weak- and strong-field dynamos: from the Earth to the stars. *MNRAS*, 418 (1):L133–L137, 2011. doi: 10.1111/j.1745-3933.2011.01159.x.

[156] V. See, M. Jardine, A.A. Vidotto, J-F Donati, S. Boro Saikia, R. Fares, C.P. Folsom, S.V. Jeffers, S.C. Marsden, J. Morin, P. Petit, and the BCool Collaboration. The open flux evolution of a solar-mass star on the main sequence. *MNRAS*, 474 (1):536–546, 2017. doi: 10.1093/mnras/stx2599.

[157] S.J. Faller and M.M. Jardine. Influence of magnetic cycles on stellar prominences and their mass loss rates. *Monthly Notices of the Royal Astronomical Society*, may

2022. doi: 10.1093/mnras/stac1273. URL https://doi.org/10.1093%2Fmnras%2Fstac1273.

[158] T. R. Marsh and Keith Horne. Images of accretion discs - II. Doppler tomography. *MNRAS*, 235:269–286, November 1988. doi: 10.1093/mnras/235.1.269.

[159] A. Mahdavi and S.J. Kenyon. THE BRIGHT ACCRETION RINGS ON MAGNETIC T TAURI STARS. *ApJ*, 497:342–353, 1998. doi: 10.1086/305443.

[160] G. Chabrier and M. Kuker. Large scale α^2-dynamo in low-mass stars and brown dwarfs. *A&A*, 446(3):1027–1037, 2006. doi: 10.1051/0004-6361:20042475.

[161] M.K. Browning. Simulations of dynamo action in fully convective stars. *ApJ*, 676: 1262, 2008. doi: 10.1086/527432.

[162] U. Wolter, J. Robrade, J.H.M.M. Schmitt, and J.U. Ness. Doppler imaging an X-ray flare on the ultrafast rotator BO Mic. A contemporaneous multiwavelength study using XMM-Newton and VLT. *AAP*, 478 (1):L11–L14, 2008. doi: 10.1051/0004-6361:20078838.

[163] A.A. Vidotto, S.G. Gregory, M.M. Jardine, J-F Donati, P. Petit, J. Morin, C.P. Folsom, J Bouvier, A.C. Cameron, G. Hussain, S. Marsden, I.a¿ Waite, R. Fares, S. Jeffers, and J.D. do Nascimento. Stellar magnetism: empirical trends with age and rotation. *MNRAS*, 441(3):2361–2374, 2014. doi: 10.1093/mnras/stu728.